Title

Probing The Extracellular Space: Development of Molecular Imaging Platforms and Investigations of Metal-Mediated Receptor Signaling

Author

O'Sullivan, Justin James

Publication Date

2022

Probing The Extracellular Space: Development of Molecular Imaging Platforms and Investigations of Metal-Mediated Receptor Signaling

By

JUSTIN JAMES O'SULLIVAN
DISSERTATION

Submitted in partial satisfaction of the requirements for the degree of

DOCTOR OF PHILOSOPHY

in

Chemistry

in the

OFFICE OF GRADUATE STUDIES

of the

UNIVERSITY OF CALIFORNIA
DAVIS

Marie C. Heffern, Chair

Kit Lam

Randy Carney

Committee in Charge

2023

Dedicated to my mom (Gail) who taught me to put my best foot forward no matter what and my dad (Fred) for reminding me never to take life too seriously.

Table of Contents

Abstract of the Dissertation

Probing the Extracellular Space: Development of Molecular Imaging Platforms and Investigations of Metal-Mediated Receptor Signaling

The work described in this dissertation builds upon previous work in chemical biology and molecular imaging. This thesis will touch upon synthetic chemistry, molecular biology, analytical development, and molecular imaging. The works described in general are all centered around developing new tools for monitoring biological analytes with a focus on extracellular applications. Chapter One outlines the history of medical imaging in general and how molecular imaging evolved out of it. This includes information on whole body imaging techniques and how they have been adapted towards imaging biological analytes at the molecular level in living systems. This chapter details the modalities with which we are able to design new imaging probes and discusses the advantages and drawbacks of various modalities.

Chapters Two through four of this dissertation focus on the use of bioluminescence as a powerful imaging platform and details how this natural phenomenon can be modified to produce analyte responsive light emission. Chapter Two describes a novel bioluminescent imaging probe that was developed using a marine luciferin/luciferase system. In particular, the synthesis of a copper(II)-reactive luciferin, picolinic-caged diphenylterazine (Pic-DTZ) is described and its implementation with the engineered Nanoluciferase. The design, synthesis, and characterization of the probe is discussed in detail including its biological relevance and applications in monitoring serum copper status as well as extracellular copper status in high-throughput cellular

assays. Chapter Three outlines a discovery made while working on the copper responsive probe detailed in chapter two. The copper mediated oxidation of imidazopyrazinones and subsequent inactivation of bioluminescence is described. This work details the molecular mechanisms behind how marine luciferases are inhibited by copper. In Chapter Four the development of a second bioluminescent probe, boronate esther-caged diphenylterazine (Bor-DTZ) is described. This caged luciferin is hydrogen peroxide responsive and chapter three outlines its design, synthesis, and characterization. Applications in cell-based assays are also described using breast cancer cells stably expressing Nanoluciferase.

Chapter Five of the dissertation describes work in collaboration with Dr. Randy Carney towards the development of Raman active tags for imaging and characterizing extracellular vesicles using Raman spectroscopy. In particular, the synthesis of Raman active polyynes are described as well as their conjugation to antibodies specific for membrane proteins that are potential biomarkers for ovarian cancer. Subsequent extracellular vesicle capture with the tagged antibodies and Raman spectra analysis are described in detail. The work shows the promise of Raman spectroscopy as a modality for imaging extracellular vesicles as well as for diagnosis of early-stage cancers. It also demonstrates the immense potential extracellular vesicles hold as biomarkers.

Though not directly related to molecular imaging, Chapter Six describes investigations in peptide GPCR interactions in the extracellular space. The chapter details structural and biological assays of oxytocin and related analogs in both apo and metal bound forms and the subsequent effect on bioactivity. Specifically, zinc and copper bound forms of oxytocin and the analogs are studied using electronic absorption spectroscopy and circular dichroism. Receptor activation was monitored by analyzing MAPK activation. The work details how zinc and copper induce different structural changes in oxytocin and analogs and effect receptor activation and downstream signaling.

Lastly, Appendix One details preliminary work on identifying new metal binding peptides using a combinatorial approach in collaboration with Dr. Kit Lam. The design of cysteine and histidine free libraries and their synthesis using the one-bead-one-compound method are described as well as their subsequent screening use live cells and a colorimetric chelator. Though this project is in preliminary stages the work described details a foundation to build open for high throughput screening and identification of unique peptides that are capable of interacting with metal ions.

Acknowledgements

This dissertation is dedicated to many people, family and friends, who without, accomplishing this feat would not have been possible. I have no one to thank more than my mom and dad who have supported me endlessly throughout my life, both in and out of graduate school. From trying to learn how to play the trumpet, to asking for rides to Pine DuBois's cranberry bog, to doing the paleo diet (for one week) with Cody, you've always let me go with whatever flow is pulling me and I am grateful for you both allowing me to explore whatever crazy ideas I've had. I also have my siblings, Patrice, Ryan and Bugsy to thank for their support. Patrice, you've been a consistent support for me. Ryan, you continue to show me that you can always get back up when you fall. Bugsy, never change. Your sense of carefreeness despite what life might throw at you has been a constant inspiration.

I also have my partner, Vanessa, to thank. We've been through thick and thin in graduate school, and I am so fortunate to have found the love of my life here in Davis. You've been my rock through the highs and lows, and I wouldn't have it any other way. I can't wait for us to start the next chapter of our lives.

Ben Bergstrom! Where do I start? You were one of the first people I met in Davis, and we instantly became best friends. I'm having the best time with my best friends! You were a constant source of love and support in Davis, and I am especially grateful for you being my synthesis mentor. I don't think I shared more laughs with anyone in graduate school.

Khaled Jami! You are a gem. I thank you for always being down to talk science and be interested in it. I've learned a lot from you, and I've also laughed a lot with you. I'll see you soon on ISLAND TIME baby… Alameda here we come!!!

Chris Niedek! Thank you for being a great friend and the best board game buddy in Davis! We've shared a ton of great laughs, food, and games throughout the years. One day I will find a sour beer you enjoy.

Angel Cobo! Some of the most fun memories I have in graduate school are hanging out with you. Whether it be cooking a five-star meal or straight partying I thank you for always being down to have a good time.

Nick Mrachek! What a crazy wild man. Although our paths didn't cross for too long, I am so glad you moved into the woods with us. We have some seriously fun times together… banana!

I also have my dissertation committee, Dr. Kit Lam, and Dr. Randy Carney to thank for their support and mentorship. Randy, it's truly been a joy working with you and getting your perspective on things. You're a killer scientist and it was truly to my benefit to learn from you and discuss science with you. Dr. Lam, I thank you for taking me into your lab for a summer to learn all things combinatorial. Working with OBOC was some of the most fun science I did in graduate school.

I'd also like to thank my previous mentors in chemistry. First, my high school chemistry teacher, Mrs. Stanghellini, thank you for instilling a love for science and chemistry in my during highschool that would ultimately carry me to completing a PhD. To my undergraduate mentors, Dr. Kimberley Frederick, Dr. Lisa Quimby, and Kara Cetto Bales, thank you for making me a more competent and confident scientist. I will carry the lessons you gave me forward.

Last but certainly not least, I could not have done this work without the support system that is in the Heffern lab. First and foremost, I have my PhD advisor Dr. Marie Heffern to thank. You have taught me so much about what it means to be a good and rigorous scientist and also person. You’ve led by example and showed me that you don’t have to specialize in any one thing… you’ve allowed me to truly be a multidisciplinary scientist and for that I will be forever grateful. As part of the Heffern original four, Nate, Sam, and Vanessa (and myself), I am so proud of us! We all made it! I have Nate, Sam and Vanessa to thank for being a constant support pillar for me throughout graduate school. We went through the highs and lows together and I’ve learned so much from each of you. You all inspire me in so many different ways and I thank you for being you. I have the rest of the Heffern lab past and present to thank as well for their constant sense of curiosity and support. You all will do great thing

Chapter 1

The Rise of Molecular Imaging for Targeted In Vivo Monitoring of Biomolecules

Let the sun illuminate the words that you could not find.

- Natasha Bedingfield (*Unwritten*, New York, **2004**)

1.1 Introduction: A Brief History of Medical Imaging

In the spirit of understanding how we got to where we are today, though not directly related to the nitty-gritty details of the forthcoming chapters in part one, I'd like to reserve chapter one to provide a bit of context and history on medical imaging in general and how molecular imaging came to be with the advancement of technology. I hope if nothing else it will provide the reader a sense of reflection and wonder on how one experiment, one finding, can unravel an entire field; a notion that any good scientist should remind themselves of regularly.

1.2 Whole Body Imaging

In the late 16th century, the world saw its first great advancement in imaging technology with the invention of the microscope.[1] Although upon its immediate invention the microscope was used as a novelty mainly by the rich, subsequent improvements in lenses allowed for a greater scientific understanding of the composition of life down to scales not previously possible. For example, Robert Hooke used the microscope to identify plant cells in thin slices of cork, coining the term "cell" for the smallest unit of life.[2] Then the development of chemical staining pioneered by Camillo Golgi planted the seeds for histochemical staining, a tool used widely today by medical practitioners and pathologists to detect and diagnose disease.[3,4] Though the microscope proved immensely useful towards better understanding the structure and components of the human body its use required invasive procedures including surgery and biopsy to obtain useful samples.

In November of 1895 the science of medical imaging began. Wilhelm Conrad Roentgen was working with an early cathode ray tube known as a Crooke's tube when he noticed that the invisible waves emitted were able to penetrate various materials (such as his own hand) better than others.[5] It was at this point X-rays were discovered when Roetengen saw the bones of his own hand on a photographic plate on the opposite side of his Crooke's tube. He then would go on to spend over a month in his basement ultimately discovering what the rest of the world would come to known about X-rays for the next two decades. He was awarded the first Nobel Prize in 1901 for these monumental discoveries that would have far reaching implications in fundamental and translational science.[6]

As we now know, the discovery of X-rays set in motion a noninvasive way of viewing the human body that would prove invaluable towards the development of lifesaving technologies. Physicians quickly began to exploit the properties of X-rays towards imaging skeletal trauma in ways that were previously not possible. Quickly the technology became more powerful with the development of "fluoroscopy" in the 1920s.[7] Radiologists would give patients radio visible barium and take films as the barium moved through the gastrointestinal tract. In fact, such methods proved to be some of the first non-invasive diagnostic handle for cancers of the esophagus, stomach, and colons.[7]

Thus the 20th century became the era of medical imaging with one advancement after another, so it seemed. In the 1940's tomography was introduced which allowed for the 3D rendering of X-ray images which was later replaced with computerized axial tomography (CAT) and CT.[8] In the 1950's nuclear medicine ushered in yet another new age of medical imaging with positron emission tomography (PET) which relies on the uptake of radioactive compounds that emit positrons upon decay.[9] Upon emission the positron will collide with an electron after which two photons are emitted in opposite directions which can be detected allowing for the source of emission to be localized in space. Traditionally, most PET imaging was performed using the positron-emitting isotope fluorine-18 that was incorporated into glucose to make, fluorodeoxyglucose (FDG).[10] Because increased glucose uptake is associated with cancerous masses, the use of FDG has become routine to diagnose and monitor cancer.[11,12] The combination of PET with CT resulting in "PET-CT", allowed for substantial increases in the intrinsically low resolution of PET alone thereby facilitating the localization of cancer for subsequent biopsy or removal.[13]

Ultrasound was then first clinically used in the 1970's which is an imaging modality that does not rely on radiation but rather soundwaves.[14] As sound passes through tissue and is reflected back, images can be generated and analyzed. Some of the main uses today for ultrasound are determining mammary masses as cancerous or benign as well as the monitoring of fetus development during the gestation period.[15,16] Notably, today ultrasounds can be recorded with a highly portable machine.

It was also in the 1970's that one of the biggest powerhouses in imaging technologies today began to be developed; magnetic resonance imaging (MRI).[17–19] Of particular importance, MRI generates high-resolution images relative to the other modalities mentioned. Briefly, MRI works by placing a subject within a magnetic field which will align the spins of certain nuclei in said field. Then a radio wave is pulsed at a specific frequency that will resonate with the nuclei of interest. When the radiofrequency is stopped, the spin will return to its relaxed state and a radio-frequency signal is emitted and can be detected. For imaging of the human body, it is typically hydrogen nuclei that are used due to their high abundance in water and fat.

Depending on the environment of the hydrogen nucleus they may have ever so slightly different resonance frequencies even if the magnetic field strength is the same. Indeed, this is the basis of nuclear magnetic resonance (NMR) in chemistry. This principle is harnessed in imaging by making the magnetic field strength more uniform and suppressing water thereby allowing different chemical species with slightly different resonance frequencies to be detected, a process known as magnetic resonance spectroscopy (MRS). A useful example is the detection of N-acetyl aspartate (NAA) which is a biomarker for healthy neurons thereby allowing one to monitor healthy brain tissue from diseased.[20] It is also worth noting that modifications to the radio pulse sequence can produce different magnetic resonance contrasts which can be related to T1 and T2 relaxation times or the diffusion of water or blood for example.[21] Lastly, another notable development is the use of contrast agents, mainly gadolinium based, which serve to lower the T1 relaxation times and improve contrast and visibility of internal body structures.[22] Though much more could be discussed regarding the fundamental principles, the uses, and the variations of MRI methods, they are beyond the scope of this work. I will limit the discussion of MRI to what has already been said here.

1.3 The Development of Molecular Imaging

In contrast to the lengthy and rich history of whole-body medical imaging, molecular imaging is a relatively new field born out of the rapid advancement of scientific technologies within disciplines including but not limited to medical imaging, chemical biology, and engineering. Indeed, molecular imaging has proven to be a massively interdisciplinary field pushed forward by successful collaboration between scientists and engineers with varying expertise. Because the field of molecular imaging falls under such a large umbrella it means different things to different people. For the purposes of the work discussed in this dissertation, the definition of molecular imaging can be stated as the noninvasive, real-time, visualization of biochemical events at the cellular and subcellular level within living cells, tissues, and/or intact subjects.

It typically involves specialized instrumentation (some of which discussed above) sometimes used alone or in conjugation with specialized contrast agents or probes that allow for the direct monitoring of desired analytes or chemical events. Molecular imaging agents can reveal the locations of pathology often with high precision and provide new insights surrounding the mechanisms of physiology and pathology. For example, with molecular imaging agents we can visualize interactions at the molecular scale such as protein-protein interactions, enzymatic turnover, and biomolecule trafficking.[23–27] As such, the molecular imaging tools developed are often of particular importance for both early disease diagnosis, therapeutic intervention, as well as monitoring treatment efficacy to a degree which traditional imaging usually severely lacks.

Though today there are a plethora of modalities that one can choose from to begin developing new molecular imaging agents the genesis of the field has close ties to nuclear medicine.[28] As mentioned previously, nuclear medicine has been interested in the development of noninvasive methods for imaging and monitoring disease in patients through the synthesis and use of radionuclides. Naturally, as our synthetic toolbox and understanding of disease biomarkers and drug targets expanded so did the capabilities of nuclear imaging. The synthesis of novel radionuclides that target specific biomarkers launched the field of nuclear medicine into what would become known as molecular imaging.

PET and SPECT are some of the most widely used molecular imaging techniques that enable visualization of biochemical changes and levels of targets in a living subject. The first step in using PET is to identify a target of interest and then synthesis a radiolabeled imaging agent that is specific and selective for that target. Early on, FDG itself provided a general molecular imaging probe to study a identify and monitor various disease’s such as Alzheimer’s, cardiovascular diseases, and cancer.[29–32] One of the most notable advancements in PET/SPECT molecular imaging is the development of peptide-radionuclides that target specific disease biomarkers.[33–35] In fact, today radiolabeled small peptides are the major class of PET probes used in the diagnosis and therapy of tumors.[36–38] Typically, an over-expressed target receptor is identified on the cancer tissues of interest and a peptide with high specificity and selectivity for that receptor is then used to develop a radiolabeled peptide to target the receptor. In this way, such peptide agents target disease tissue with high specificity and spatial resolution. Some clinically investigated targets using radiolabeled peptides include the somatostatin receptor, prostate-specific membrane antigen, integrins, and chemokine receptors.[39–46]

In addition to PET/SPECT other major modalities used in molecular imaging include MRI. MRI is especially attractive due to its outstanding signal to noise ratio, high spatial resolution, and excellent tissue contrast.[47,48] Aside from providing detailed anatomical information MRI pulse sequences have developed which allow for physiological information to be revealed. Some examples of unique MRI pulse sequences include dynamic contrast-enhanced MRI which can assess the physiological characteristics of the vasculature, and blood oxygen level dependent MRI which can report on the oxygen status of red blood cells in perfused regions of tissue.[49–51] In addition to unique pulse sequences, new contrast agents have also been developed. Like the probes used in PET/SPECT, MRI agents using gadolinium complexes decorated with peptides that target disease tissues selectively and specifically have been developed.[52–54] Examples include superparamagnetic iron oxide (SPIO) nanoparticles functionalized with peptides specific for atherosclerotic events and imaging of integrins using gadolinium-containing liposomes.[55,56]

At this point, I hope to have convinced the reader of how the advent of imaging and molecular imaging have had an enormous impact on both our understanding of human physiology and pathology but also on disease diagnosis and patient outcomes. Although PET and MRI are some of the most used molecular imaging modalities in whole body imaging there are many other modalities I have not discussed. Of these include ultrasound, photoacoustic, and optical. As the following chapters regard the development of molecular imaging probes using some of these modalities, I will take the next section to introduce and discuss some of these in more depth and detail.

1.4 Optical Modalities: Fluorescence, Bioluminescence, and Raman Imaging

Optical methods including both fluorescence and bioluminescence imaging have emerged as powerful new modalities for molecular imaging over the past few decades. For decades now researchers have used optical methods to monitor biochemical processes in live cells assays. For example, using fluorescent proteins we can track cells and proteins at the micrometer scale with microscopy.[57] However, today these methods have been adapted so that scientists can achieve imaging of optical reporters in live animals to the point that we are able to generate whole-body measurements with reasonable resolution.[58] Usually, optical imaging requires the addition of an optical probe that can produce a detectable and targeted signal. The most widely used techniques for optical imaging today are fluorescence and bioluminescence which will be discussed in depth here. Additionally, I will briefly introduce another optical modality, Raman, as it chiefly concerns the project discussed in Chapter five of this work.

Over the past three decades or so the implementation of fluorescence microscopy has revolutionized the field of molecular biology. Fluorescence microscopy is used to increase image contrast and spatial resolution to achieve the previously mentioned goals of successful molecular imaging agents.[59] Generally, fluorescence microscopy utilizes either genetically encoded fluorescent proteins, fluorescent dyes, fluorescently labeled molecules, or even in some cases endogenous fluorescent biomolecules like collagen or hemoglobin. The process of fluorescence involves the absorption of a specific wavelength of light by a chromophore thereby generating an excited state which emits, almost immediately, photons of a longer wavelength and short energy upon relaxation to the ground state (Figure 1.1).

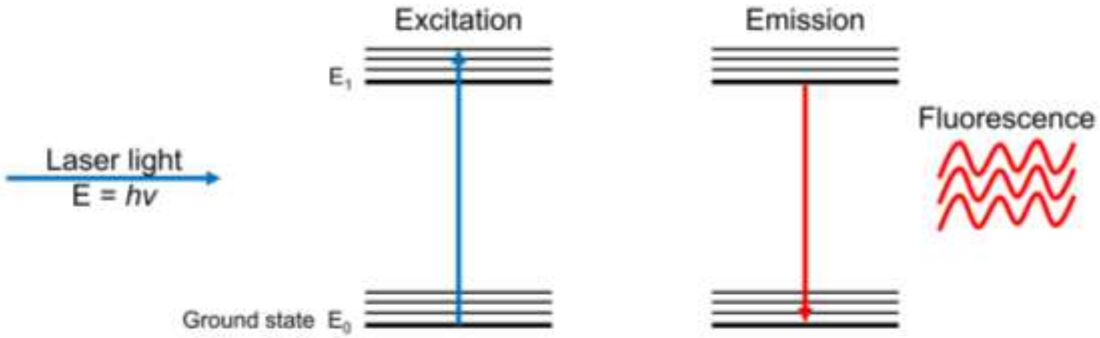

Figure 1.1 Incident light (typically from a laser source) excites an electron from the ground state (E_0) to an excited state (E_1) followed by relaxation and emission of light in the process known as fluorescence.

Some commonly used fluorescent dyes include rhodamines, fluoresceins, and cyanines all of which are resonant dyes characterized by narrow absorption and emission bands. Common charge transfer dyes include coumarins and dansyl fluorophores which are characterized by well separated absorption and emission bands and have large stokes shift relative to resonant dyes. Many of these dyes exist in “click-able” forms with reactive handles used to label functional groups such as amines and thiols on biomolecules such as peptides, antibodies, proteins and DNA/RNA. The discovery of the green fluorescent protein (GFP) revolutionized fluorescent imaging and brought a whole new arsenal of tools used for optical imaging.[60] Protein fluorophores immediately saw success as reporter genes in plasmids providing a facile method of monitoring successful transfection and gene expression through monitoring fluorescence.[61] Other common protein fluorophores derived from GFP include blue, cyan, and yellow fluorescent proteins.

The development of a myriad of microscope options including wide-field, laser scanning confocal, scanning disk confocal and super resolution combined with various emergent methods like fluorescence lifetime imaging, Forster resonance energy transfer, stimulated emission depletion, and fluorescence correlation spectroscopy has allowed researchers to push new boundaries and answer questions that previously had limited tools to aid them. These techniques have been used to study protein-protein interactions, DNA detection and sequencing, cell sorting including flow cytometry, live-cell imaging, and even fluorescence guided surgeries.[62–68] One of the most recent developments using fluorescence imaging is “Cell Painting” which is a high-content image-based assay for morphological profiling using multiplexed fluorescent dyes.[69] The first paper describing such an assay used six fluorescent dyes to stain the nucleus, endoplasmic reticulum, nucleoli, Golgi apparatus and plasma membrane, actin, and the mitochondria.[70] This type of richly multiplexed assay allows researchers to quickly monitor morphological changes in cells thereby providing a new high throughput screening method for drug development.

In addition to organelle targeted dyes researchers have also developed analyte-responsive probes through the chemical modification of small molecule fluorophores. The general design for such probes is to append an analyte-responsive moiety to fluorophore which typically generates a fluorescence “off” analog. However, upon reaction with the analyte of interest the original fluorophore is restored producing an “on” state. These are generally known as “on/off” probes. Such probes have been developed for detecting metal ions, reactive oxygen species, specific functional groups such as thiols, as well as for monitoring pH.[71–76]

On the clinical side, in vivo fluorescence imaging has a wide range of resolution and imaging depths including subcellular with intravital microscopy and whole-animal imaging with 1-3 mm spatial resolution.[77] Endoscopes with confocal or 2-photon laser fluorescence molecular imaging has also been developed allowing clinical use of fluorescence imaging with targeted contrast agents.[78] One major drawback of fluorescence imaging in vivo is that tissue penetration can become an issue due to light scattering and quenching by biomolecules like hemoglobin. To overcome these setbacks researchers have become to develop new, near-infrared dye that have increased tissue penetration. One of the most common near-infrared fluorophores widely used is cyanine-5 (Cy5).[79]

Aside from fluorescence, the other widely used optical modality is bioluminescence. Bioluminescence is a phenomenon observed in nature that involves the oxidation of a small molecule, known generally as a luciferin, by an enzyme, known generally as a luciferase.[80] In this enzymatic oxidation an excited state intermediate is generated which emits a photon upon relaxation to the ground state. While there are more than forty known bioluminescent systems, only eleven of them have been fully characterized to date.[81] Today, uncovering novel pairs and fundamental molecular mechanisms of known systems remains an active area of research. Unlike fluorescence, bioluminescence does not require an excitation light source allowing for extreme sensitivity with high signal to noise ratios and virtually zero background. An additional advantage is controllable localization afforded through tissue/cell line specific genetic encodement of the luciferase. It is commonly used in preclinical cellular and molecular imaging in small animals.

One of the most studied and well used systems is the firefly (*Photinus pyralis*) luciferin/luciferase system where D-luciferin is oxidized by firefly luciferase in a reaction that requires oxygen, adenosine triphosphate (ATP) and magnesium (Figure 1.2). The oxidation of D-luciferin occurs via two key steps, the initial activation of the carboxyl group through adenylation followed by its oxidation to form oxyluciferin as an excited state anionic species via a dioxetanone intermediate.[82,83] The light emitted by this bioluminescent reaction has a broad emission spectrum with a maximum centered around 560 nm.[84]

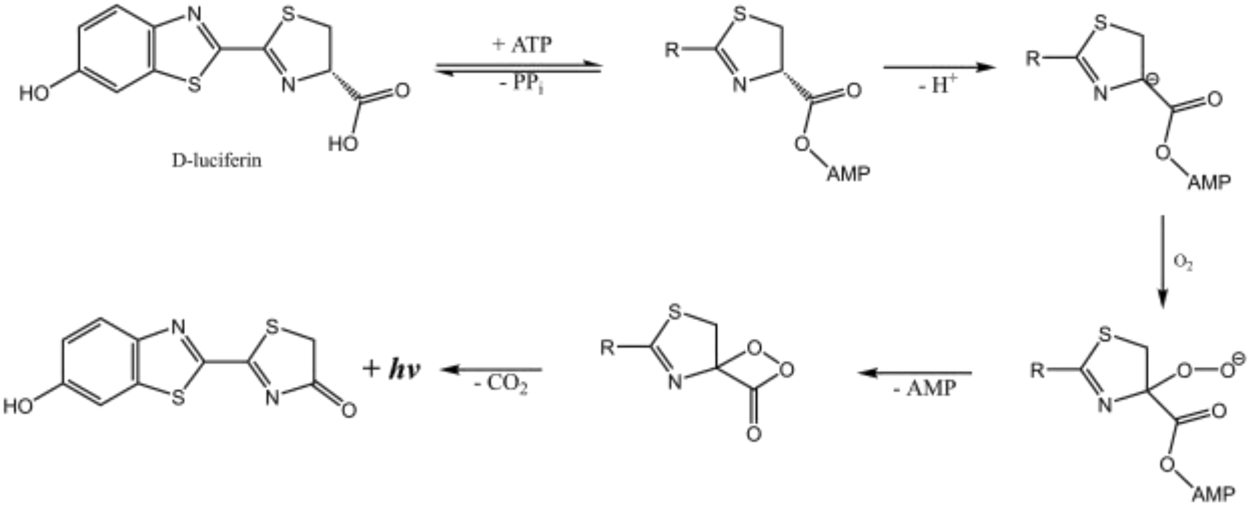

Figure 1.2 Mechanism of D-luciferin oxidation and light emission by firefly luciferase.

Firefly luciferin/luciferase has been used extensively in small animals because of many favorable characteristics. D-luciferin distributes throughout an animal rapidly after injection and can pass through blood-tissue barriers including the brain.[85–87] Furthermore, peak emission lasts for up to an hour providing a wide window for signal acquisition.[88] Indeed, bioluminescence imaging has proven to be one of the most useful tools in basic oncology research for reliably monitoring primary tumor growth.[89] Because of firefly luciferases reliance on ATP for oxidation many in vitro assays have been developed with the firefly system to monitor changes in ATP levels including for hygiene and monitoring bacterial contamination as well as to monitor ATP generating and ATP consuming reactions.[90–99]

There are many known advantages to the firefly system over other luciferin/luciferase pairs. For example, it is well known that firefly luciferin has superior water solubility relative to other small molecule luciferins making it more adaptable to biological fluids.[100] In addition to solubility, it is also established that D-luciferin has much lower toxicity relative to coelenterazine, another luciferin making it ideal for cellular assays and small animal imaging.[101] Furthermore, the firefly system has the highest quantum yield of any luciferin/luciferase pair at around 40% relative to most others at 15-30% as well as the longest wavelength of emission making it ideal for small animal imaging.[84,102]

Although firefly luciferin/luciferase has seen tremendous application in both cellular assays and small animal imaging there are some notable disadvantages for its use in bioluminescent imaging. For small animal imaging, it has been shown that D-luciferin results in nonhomogeneous biodistribution using ^{14}C labelled luciferin.[85] Additionally, uptake is not optimal organ by organ with specifically low uptake in the brain limiting neurological applications.[103] There also limitations in terms of suboptimal cell permeability therefore requiring high D-luciferin doses.[104] Additionally, the requirement of ATP for the enzymatic oxidation limits the use of firefly-based systems to mainly intracellular applications where ATP is abundant and introduces a confounding variable as signal is dependent on ATP concentration. Although one of the most red-shifted systems in vivo imaging applications are still limited especially regarding tissue penetration depth as the light is still strongly absorbed by blood and tissue. It is important to note that a current active area of research is the development of novel luciferins and engineered luciferases for red-shifted emission compatible with deep tissue imaging.[105–109]

The other major class of luciferin/luciferase pairs is marine based systems. Most marine based luciferases have a common imidazopyrazinone substrate called coelenterazine. In fact, to date coelenterazine is the known substrate for roughly fifteen naturally occurring marine luciferases.[110–117] Interestingly, all the marine luciferases, and luciferases in general even, evolved independently and are totally non-homologous.[118,119] Of the marine luciferases some that have seen most notable application in assay development and imaging owing to their early discovery and cloning are *Renilla* luciferase (Rluc), *Gaussia* luciferase (Gluc), and *Metridia longa* luciferase (Mluc).[113–115] Recently, in the past decade the engineered luciferase, Nanoluciferase (Nluc), derived from the deep-sea shrimp, *Oplophorus gracilirostris* has seen enormous use in biochemical research.[120] The general reaction mechanism of coelenterazine to produce blue light occurs via the oxidation of coelenterazine to an excited state coelenteramide through a dioxetanone intermediate (Figure 1.3).[121] This excited state coelenteramide relaxes to ground state through the emission of blue photons in the range of 450-490 nm depending on the luciferase.[81]

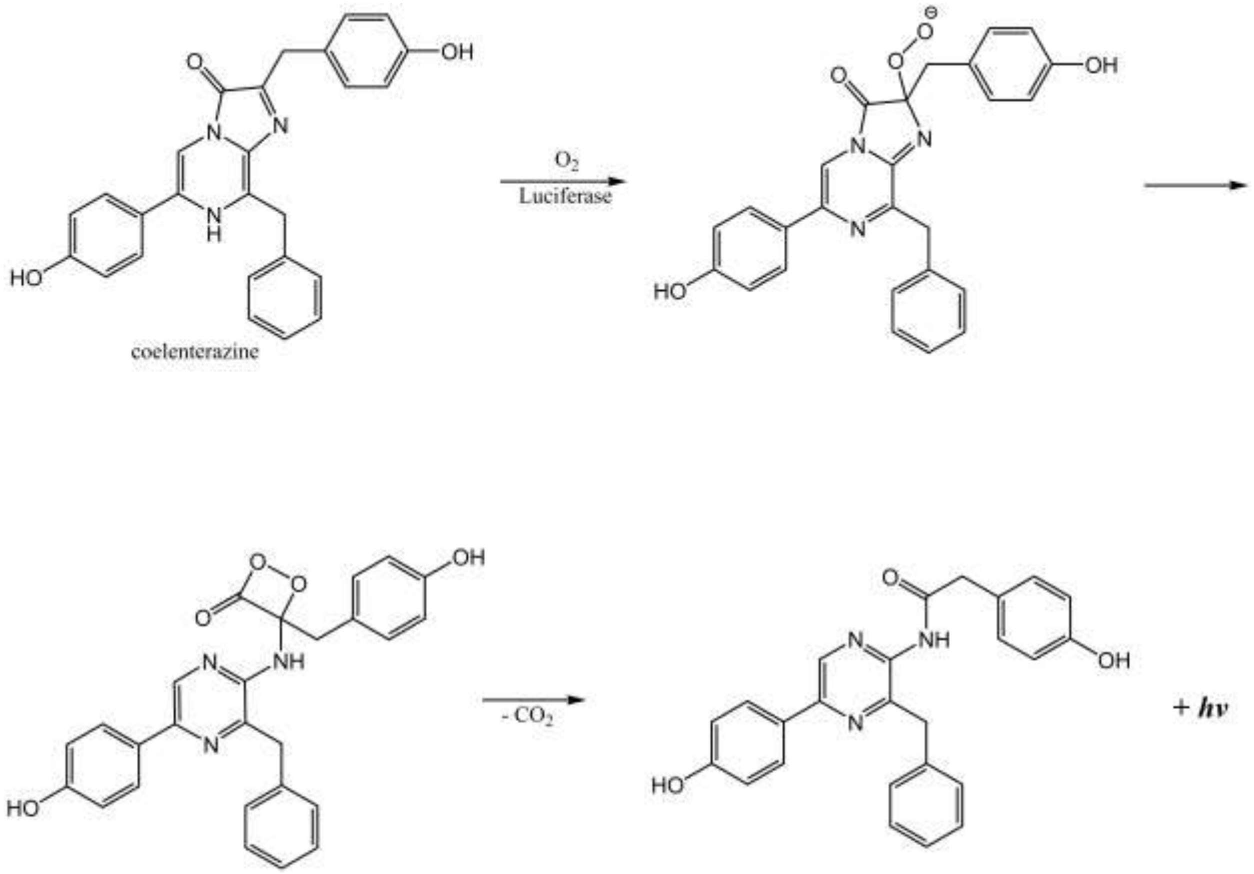

Figure 1.3 The reaction mechanism for the bioluminescent oxidation of coelenterazine, producing blue light.

The bioluminescent oxidation of coelenterazine is only dependent on oxygen and is ATP independent. The ATP independence of marine luciferase systems makes them excellent candidates for extracellular applications where ATP is not abundant. Other favorable characteristics of marine systems include small luciferase size relative to firefly luciferase. Relative to the 62 kDa firefly luciferase, Rluc is 34 kDa, Gluc and Mluc are both around 20 kDa and Nanoluciferase is 19 kDa. The small size of marine based luciferases makes them excellent candidates for use as reporter proteins as their genes can easily be encoded into vectors.

Although the small size, intense light emission, and ATP independence of marine luciferases are of unique advantage over firefly-based systems, the limitations of marine systems should be considered. Some key disadvantages include poor water solubility, increased toxicity relative to firefly luciferin, as well as susceptibility to auto-oxidation leading to chemiluminescence in solution.[100,122,123] Although of chief concern is that the blue shifted emission of coelenterazine utilizing luciferases severely limits applications in vivo as majority of blue shifted photons are absorbed by hemoglobin and tissue. However, it should not be overlooked that because of this researchers are actively developing red-shifted coelenterazine analogs as well as mutant luciferases.[124–128] Additionally, in the sea pansy, Renilla Reniformis, the luciferase Rluc is coupled with GFP where the blue light emitted from Rluc is coupled through resonance energy transfer to the active fluorophore of GFP to form an excited-state species which subsequently emits in the green regions around 510 nm.[129] This has inspired the development of bioluminescent resonance energy transfer (BRET) systems that further red-shift emission.[130–132]

Despite the limitations of marine based luciferin/luciferase systems they have seen widespread use in applications ranging from in vitro assays to live cell assays. Additionally, the development of novel coelenterazine analogs and engineered luciferases like Nluc has increased the space for assay development using marine systems. Table 1.1 shows a representative selection of synthetic coelenterazine analogs with various useful properties.

Table 1.1 Representative synthetic coelenterazine analogs with red-shifted emission spectra.

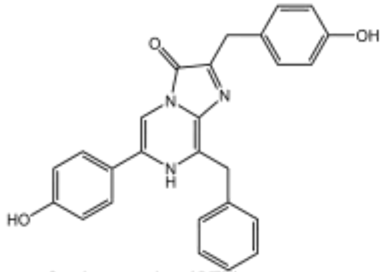

Coelenterazine (CTZ)
λ_{max} 460 nm with Nluc

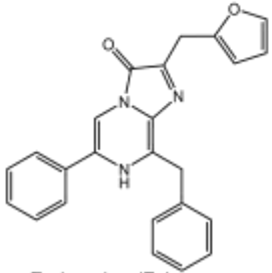

Furimazine (Fz)
λ_{max} 456 nm with Nluc

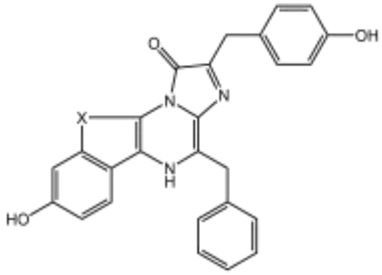

e-CTZ X = CH2CH$_2$
λ_{max} 418/475 nm with Rluc
v-CTZ X = CHCH
λ_{max} 512 nm with Rluc

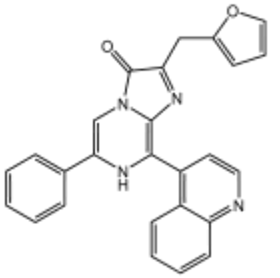

1
λ_{max} 571 nm with Nluc

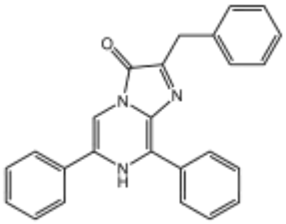

DTZ
λ_{max} 583 nm with Antares2

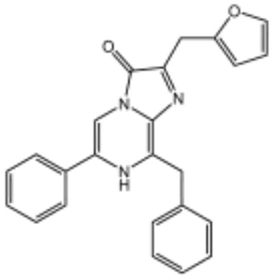

Furimazine (Fz)
λ_{max} 589 nm with Antares

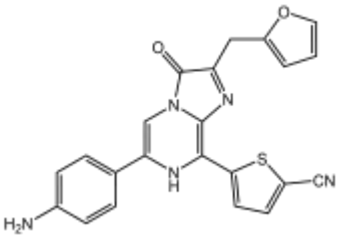

2
λ_{max} 598 nm with Nluc

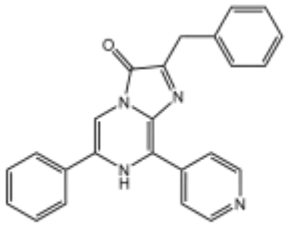

8-PyDTZ
λ_{max} 600 nm with LumiScarlet

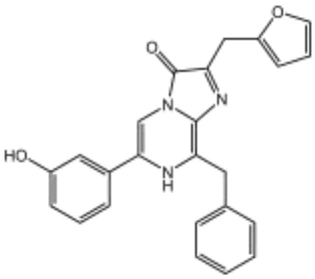

HFz
λ_{max} 650 nm with Antares

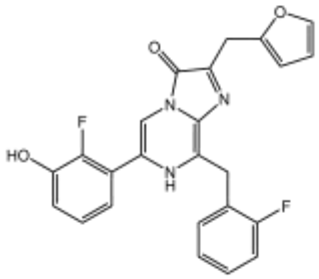

FFz
λ_{max} 650 nm with Nluc

Some of the analogs presented in table one show emission wavelengths when paired to novel engineered luciferases. For the purposes of this dissertation such engineered luciferases, aside from Nluc, will not be discussed in depth as most of the work in the forthcoming chapters uses mainly Nluc in addition to some of the other the already discussed marine luciferases.

Like the applications discussed regarding the firefly systems, the use of marine systems towards biotechnology advancements have been immense. Many marine systems discovered initially, though the exact molecular mechanisms were unknown at the time, included cofactor sensitive photoproteins in addition to luciferases. For example, the discovery of the photoprotein, Aequorin, from the jellyfish, *Aequorea vicotria*, led to the rapid development of calcium sensors for monitoring intracellular calcium fluxes.[133] Today, it is established that in bioluminescent systems of calcium dependence there exists photoproteins (Aequorin in the case of *Aequorea Victoria*) with a coelenterazine derivative, 2-hydroperoxycoelenterazine in the active site.[134,135] Such proteins undergo a conformational change upon calcium binding which triggers decarboxylation and the production of an excited state coelenteramide followed by subsequent light emission upon relaxation.[136] Another unique marine based photoprotein, pholasin, from the luminous seawater mollusk *Pholas dactylus*, was adapted to monitor changes in reactive oxygen species (ROS) production.[137,138] The luminescence reaction of pholasin is triggered by ROS such as superoxide anion and hydroxyl radicals and therefore was adapted into an ROS assay kit. One group led by Shah et al. used pholasin to evaluate ROS production in platelets of patients with heart failure.[139]

Luciferases like Rluc and Gluc saw early uses as reporter fusions after much optimization. For example, Rluc has been used a reporter since 2006 when a variant, Rluc8, with increased stability and more intense light emission was engineered through random mutagenesis.[140] Gluc is a naturally secreted luciferase and therefore resulted in the development of secreted reporter assays. Tannous et al. developed this reporter in mammalian cells where they showed that levels of secreted Gluc were linear in relation to cell number, growth, and proliferation.[141] Furthermore, they demonstrated that the reporter could be used to monitor endoplasmic reticulum stress and the secretory pathway as well as small interference RNA (siRNA) silencing and protein-protein interactions.

Nanoluciferase has gained immense traction as the premier marine system for use in biotechnology and imaging in recent years owing to its small size (19 kDa, which is small even for marine luciferases), intense luminescence, and high thermal stability.[142] It has been engineered into similar reporters like Rluc and Gluc. Additionally, Nluc can be engineered for both intracellular retention and secretion making it particularly useful for both intra- and extracellular applications. In addition to these forms of Nluc there is a third destabilized form of NLuc, Nluc-PEST, which contains a protein degradation signal. This destabilized version provides a coupling to transcriptional activity as Nluc-PEST has a short lifetime (10-30 minutes) therefore rapid changes in expression level are reflective of changes in transcription activity.[143] Promega also offers other Nluc based platforms such as NanoBRET which (perhaps obviously) is a BRET based system that can be used to study protein-protein interactions, ligand-receptor interactions, as well as for stability sensors for signaling proteins.[144,145] Lastly, the split luciferase system, NanoBit, is a highly sensitive system that can be used to study protein-protein interactions where two proteins of interest are tagged with complimentary segments of the Nluc enzyme.[146,147] When said proteins interact the complimentary Nluc "Bits" can fold together into the functioning Nluc enzyme and produce detectable photons.

In addition to the above-mentioned forms and applications of bioluminescent systems available commercially, researchers have adapted them through chemical modification of the luciferins to produce analyte responsive signal like the analyte responsive fluorescent probes previously discussed.[148] Such compounds are typically referred to as "caged" luciferins. The vast majority of such bioluminescent molecular imaging probes to date have been developed based on the firefly luciferase system. Typically, the hydroxyl group on D-luciferin is chemically modified though in some instances the carboxylic acid group was modified. In most cases bioluminescent probes are “turn on” probes where the caged luciferin is luciferase inert. The analyte of interest can chemoselectively remove the cage thereby restoring the native luciferin which can then be oxidized by its luciferase to produce a turn on signal. In this way researchers have used the firefly luciferase system to develop imaging probes for things including but certainly not limited to enzymatic activity, hydrogen peroxide, metal ions, carbon monoxide, glycans, and hydrogen sulphide.[149–158] There are fewer examples of bioluminescent imaging probes using imidazopyraninone based luciferins likely because they are easily auto oxidized and synthetically difficult to handle. Typically, those utilizing imidazopyrazinones cage the luciferin on the carbonyl at the C-3 position. Some such probes reported are for beta-galactosidase and thiophenols.[159,160]

The work in the forthcoming chapters regarding bioluminescent probes seek to expand upon the toolbox for monitoring extracellular (as well as intracellular) analytes of interest, specifically copper and hydrogen peroxide, utilizing marine-based systems (the interest in those analytes will be discussed in more depth in the appropriate chapters). Though the current probes put forth by researchers using firefly-based systems have illuminated much regarding the innerworkings of the cell much less to date is known about biomolecule trafficking and signaling in the extracellular space. The ATP independence of marine systems provides an excellent candidate for monitoring the extracellular milieu in addition to containing all the previously mentioned benefits of bioluminescent based optical imaging.

The last optical modality I will briefly touch on is Raman. Unlike fluorescence and bioluminescence, Raman is not based on the emission of photons but rather the inelastic scattering of light by molecules. Raman scattering occurs when a small fraction of light is scattered by an excitation of molecules which leads to scattered photons with a different frequency of light then the incident photon. For the scope of this work, I will not go in depth on the photophysics and fundamental principles of Raman. For the interested reader they may refer to some advanced primers on the fundamentals of Raman spectroscopy.[161,162] Suffice to say, because the energy levels of every molecule are unique, and the frequency of light scattered is based off the structural characteristics of molecules, Raman spectra are generally highly specific. Because of this specificity Raman has seen many applications across diverse disciplines ranging from geochemistry to materials science to polymer chemistry.[163–165]

Though the theory of Raman scattering was hypothesized in 1923 by Schmekal and then experimentally observed by Raman and Krishna in 1928, it wasn't until recently that the phenomenon began to be used in applications for medicine and biomedical engineering including molecular imaging.[166–168] This is likely because of the development of technology and tools since then that have made the use of Raman spectroscopy more practical. For example, the Raman effect is generally weak and therefore requires a strong, focused beam of light in addition to sensitive detectors. The development of the laser (light amplification by stimulated emission of radiation) and the charge-coupled-device (CCD) are some key technologies that have enabled the implementation of Raman imaging in applications previously inaccessible.[169]

In addition to developments in hardware for collecting Raman spectra there have also been discoveries and development theory surrounding Raman scattering. One such notable advancement is the discovery of surface enhanced Raman spectroscopy (SERS). SERS occurs when incident photons interact with a metallic nanostructure generating a local electric field in the vicinity of the metal surface.[170] When molecules of interest are near the surface of such metallic structures, their Raman scattering is dramatically enhanced. For this reason, SERS has gained increasing traction in biomedical applications because of its high sensitivity and molecular selectivity. Researchers in one group used this phenomenon to develop a SERS active nanoparticle that they tracked inside of a cell.[171] This enabled them to monitor the surroundings of the particle as it traveled inside the cell illuminating structural information regarding cellular transport pathways such as endocytosis.

The use of biorthogonal Raman active tags has also revolutionized researchers' capabilities when it comes to cellular and tissue-based Raman imaging. Because cells are Raman silent in the region of 1,800 to 2,100 cm^{-1} researchers have put forth tags that produce Raman signal in those regions for small molecule imaging in cell-based assays. One example of such a structure is the alkyne functional group which produces a strong signal in the 1,800 to 2,100 cm^{-1} region and does not overlap with any endogenous molecules. Because the alkyne functional group is sufficiently small researchers have been able to append it to various molecules of interest in order to observe their trafficking in living cells.[172,173]

Like the other molecular imaging modalities discussed Raman imaging also comes with its own unique advantages as well as disadvantages. The fact that Raman imaging can provide direct chemical information about cell/tissue samples through the non-invasive collection of a spectra without the addition of probe is one reason it is such an attractive modality. In addition to this Raman possesses high spatiotemporal resolution, high multiplexing ability, and low background noise. However, because of the inherent weakness of Raman scattering, similar to the other optical modalities, tissue penetration is a challenge which can severely limit its use in small animal imaging and clinical settings.

1.5 Conclusions & Outlooks

Molecular imaging has certainly grown drastically in the last three decades and I hope the reader is convinced by now that it provides a powerful means of interrogating living systems to pull new details from out of the shadows. Not only do molecular imaging tools provide new mechanistic insight into physiological and pathological states but it also provides novel tools for diagnosing, monitoring, and even treating disease states. Indeed, the advent of molecular imaging has induced a paradigm shift from whole body medical imaging that provides simply anatomical information to the development of techniques and probes that will provide tissue specific, even molecule specific, biomolecular information. Though traditional anatomical medical imaging, to say, diagnose a broken bone, will always have a place in the clinic, molecular imaging is certainly here to stay with a place in both research and development as well as in the clinic.

As both our understanding of physiology and pathology at the molecular level coupled with the tremendous advancements in technology for imaging have increased over time, new opportunities have arisen for the modern scientist. We now are at a place where we have the necessary tools coupled with new knowledge of disease biomarkers and mechanisms to inspire the development of cutting-edge tools to interrogate biological systems at molecular levels previously unseen. In the first part of this dissertation, I will discuss four projects where I attempt to do just that.

I have alluded to these projects throughout this first chapter. In chapters two and three I will discuss the development of two new bioluminescent based molecular imaging probes to monitor extracellular, labile copper as well as hydrogen peroxide. Following this, in chapter three I will discuss efforts towards the development of a novel class of SERS active tags for characterizing cancer exosomes. Lastly, I will briefly discuss efforts towards the development of novel peptide based fluorescent probes for metal ion detection.

1.6 References

(1) Wollman, A. J. M.; Nudd, R.; Hedlund, E. G.; Leake, M. C.; Leake, M. C. From Animaculum to Single Molecules : 300 Years of the Light Microscope. *Open Biol.* **2015**, No. 5, 150019.

(2) Russinova, E. Have Plant Cells Been Forgotten ? *J. Cell Sci.* **2018**, *131*, 1–2.

(3) Bentivoglio, M.; Cotrufo, T.; Ferrari, S.; Tesoriero, C. The Original Histological Slides of Camillo Golgi and His Discoveries on Neuronal Structure. *Front. Neuroanat.* **2019**, *13*, 1–13.

(4) Alturkistani, H. A.; Tashkandi, F. M.; Mohammedsaleh, Z. M. Histological Stains : A Literature Review and Case Study. *Glob. J. Health Sci.* **2016**, *8* (3), 72–79.

(5) Scatliff, J. H.; Morris, P. J. From Röntgen to Magnetic Resonance Imaging: The History of Medical Imaging. *N. C. Med. J.* **1896**, *75* (2), 111–113.

(6) Lennard, P.; Tesla, N. Wilhelm Conrad Röntgen: Finding X. *Indian J. Ophthalmol.* **2021**, *69* (10), 2570–2572.

(7) Bradley, W. G. History of Medical Imaging. *Am. Philos. Soc.* **2008**, *152* (3), 349–361.

(8) Goldman, L. W. Principles of CT and CT Technology. *J. Nucl. Med. Technol.* **2007**, *35*, 115–128.

(9) Phelps, M. E. Molecular Imaging with Positron Emission Tomography. *Annu. Rev. Nucl. Part. Sci.* **2002**, *52*, 303–338.

(10) Glaudemans, A. W. J. M.; Vries, E. F. J. De; Galli, F.; Dierckx, R. A. J. O.; Slart, R. H. J. A.; Signore, A. The Use of 18 F-FDG-PET/CT for Diagnosis and Treatment Monitoring of Inflammatory and Infectious Diseases. *Clin. Dev. Immunol.* **2013**, *2013*.

(11) Almuhaideb, A.; Papathanasiou, N.; Bomanji, J. 18F-FDG PET/CT Imaging in Oncology. *Ann. Saudi Med.* **2011**, *31*, 3–13.

(12) Zhu, A.; Lee, D.; Shim, H. Metabolic PET Imaging in Cancer Detection and Therapy Response. *Semin. Oncol.* **2012**, *38* (1), 55–69.

(13) Tan, H.; Gu, Y.; Yu, H.; Hu, P.; Zhang, Y.; Mao, W.; Shi, H. Total-Body PET/CT: Current Applications and Future Perspectives. *Am. J. Roentgenol.* **2020**, *215* (2), 325–337.

(14) Kaproth-joslin, K. A.; Dogra, V. S. The History of US: From Bats and Boats to the Bedside and Beyond. *Radiographics* **2015**, *35*, 960–970.

(15) Campbell, S. A Short History of Sonography in Obstetrics and Gynaecology. *ObGyn* **2013**, *5* (3), 213–229.

(16) Sood, R.; Rositch, A. F.; Shakoor, D.; Ambinder, E.; Pool, K.; Pollack, E. Ultrasound for Breast Cancer Detection Globally: A Systematic Review and Meta-Analysis. *J. Glob. Oncol.* **2019**, *5*, 1–17.

(17) Kose, K. Physical and Technical Aspects of Human Magnetic Resonance Imaging : Present Status and 50 Years Historical Review. *Adv. Phys. X* **2021**, *6* (1).

(18) Grover, V. P. B.; Tognarelli, J. M.; Crossey, M. M. E.; Cox, I. J.; Taylor-robinson, S. D.; Mcphail, M. J. W. Magnetic Resonance Imaging: Principles and Techniques: Lessons for Clinicians. *J. Clin. Exp. Hepatol.* **2015**, *5* (3), 246–255.

(19) Smith, H. The History of Magnetic Resonance Imaging and Its Reflections in Acta Radiologica. *Acta radiol.* **2021**, *62* (11), 1481–1498.

(20) Moffett, J. R.; Ross, B.; Arun, P.; Madhavarao, C. N.; Namboodiri, M. A. A. N-

Acetylaspartate in the CNS: From Neurodiagnostics to Neurobiology. *Prog Neurobiol* **2007**, *81* (2), 89–131.

(21) Rydhog, A. S.; Szczepankiewicz, F.; Wirestam, R.; Ahlgren, R.; Westin, C. F.; Knutsson, L.; Pasternak, O. Separating Blood and Water: Perfusion and Free Water Elimination from Diffusion MRI in the Human Brain. *Neuroimage* **2017**, *156*, 423–434.

(22) Wahsner, J.; Gale, E. M.; Caravan, P. Chemistry of MRI Contrast Agents: Current Challenges and New Frontiers. *Chem Rev.* **2020**, *119* (2), 957–1057.

(23) Massoud, T. F.; Paulmurugan, R. Chapter 47 - Molecular Imaging of Protein–Protein Interactions and Protein Folding; Ross, B. D., Gambhir, S. S. B. T.-M. I. (Second E., Eds.; Academic Press, 2021; pp 897–928.

(24) Paulmurugan, R.; Massoud, T. F.; Huang, J.; Gambhir, S. S. Molecular Imaging of Drug-Modulated Protein-Protein Interactions in Living Subjects. *Cancer Res.* **2004**, *64* (6), 2113–2119.

(25) Sellmyer, M. A.; Richman, S. A.; Lohith, K.; Hou, C.; Weng, C.-C.; Mach, R. H.; O'Connor, R. S.; Milone, M. C.; Farwell, M. D. Imaging CAR T Cell Trafficking with EDHFR as a PET Reporter Gene. *Mol. Ther.* **2020**, *28* (1), 42–51.

(26) Shi, H.; Gao, T.; Shi, L.; Chen, T.; Xiang, Y.; Li, Y.; Li, G. Molecular Imaging of Telomerase and the Enzyme Activity-Triggered Drug Release by Using a Conformation-Switchable Nanoprobe in Cancerous Cells. *Sci. Rep.* **2018**, *8* (1), 16341.

(27) Rempel, B. P.; Price, E. W.; Phenix, C. P. Molecular Imaging of Hydrolytic Enzymes Using PET and SPECT. *Mol. Imaging* **2017**, *16*, 1536012117717852.

(28) James, M. L.; Gambhir, S. S. A Molecular Imaging Primer: Modalities, Imaging Agents, and Applications. *Physiol. Rev.* **2012**, *92* (2), 897–965.

(29) Mosconi, L.; Berti, V.; Glodzik, L.; Pupi, A.; De Santi, S.; de Leon, M. J. Pre-Clinical Detection of Alzheimer's Disease Using FDG-PET, with or without Amyloid Imaging. *J. Alzheimers. Dis.* **2010**, *20* (3), 843–854.

(30) Coulden, R. A.; Sonnex, E. P.; Abele, J. T.; Crean, A. M. Utility of FDG PET and Cardiac MRI in Diagnosis and Monitoring of Immunosuppressive Treatment in Cardiac Sarcoidosis. *Radiol. Cardiothorac. imaging* **2020**, *2* (4), e190140.

(31) Skali, H.; Schulman, A. R.; Dorbala, S. 18F-FDG PET/CT for the Assessment of Myocardial Sarcoidosis. *Curr. Cardiol. Rep.* **2013**, *15* (4), 352.

(32) Hildebrandt, M. G.; Lauridsen, J. F.; Vogsen, M.; Holm, J.; Vilstrup, M. H.; Braad, P.-E.; Gerke, O.; Thomassen, M.; Ewertz, M.; Høilund-Carlsen, P. F. FDG-PET/CT for Response Monitoring in Metastatic Breast Cancer: Today, Tomorrow, and Beyond. *Cancers (Basel).* **2019**, *11* (8).

(33) Hu, K.; Ma, X.; Xie, L.; Zhang, Y.; Hanyu, M.; Obata, H.; Zhang, L.; Nagatsu, K.; Suzuki, H.; Shi, R.; Wang, W.; Zhang, M.-R. Development of a Stable Peptide-Based PET Tracer for Detecting CD133-Expressing Cancer Cells. *ACS Omega* **2022**, *7* (1), 334–341.

(34) Rangger, C.; Haubner, R. Radiolabelled Peptides for Positron Emission Tomography and Endoradiotherapy in Oncology. *Pharmaceuticals (Basel).* **2020**, *13* (2).

(35) Sun, X.; Li, Y.; Liu, T.; Li, Z.; Zhang, X.; Chen, X. Peptide-Based Imaging Agents for Cancer Detection. *Adv. Drug Deliv. Rev.* **2017**, *110–111*, 38–51.

(36) Rietschoten, K. Van; Eder, M.; Pavan, S.; Bauder-w, U.; Baranski, A.; Harrison, H.; Campbell, S.; Stace, C. L.; Walker, E. H.; Chen, L.; Bennett, G.; Mudd, G.; Schierbaum, U.; Leotta, K.; Haberkorn, U.; Kopka, K.; Teufel, D. P. Bicyclic Peptides as a New

Modality for Imaging and Targeting of Proteins Overexpressed by Tumors. *Cancer Res.* **2019**, *79* (4), 841–852.

(37) Li, X.; Cai, H.; Wu, X.; Li, L.; Wu, H.; Tian, R. New Frontiers in Molecular Imaging Using Peptide-Based Radiopharmaceuticals for Prostate Cancer . *Frontiers in Chemistry* . 2020.

(38) Charron, C. L.; Farnsworth, A. L.; Roselt, P. D.; Hicks, R. J.; Hutton, C. A. Recent Developments in Radiolabelled Peptides for PET Imaging of Cancer. *Tetrahedron Lett.* **2016**, *57* (37), 4119–4127.

(39) Johnbeck, C. B.; Mortensen, J. Somatostatin Receptor Imaging PET in Neuroendocrine Neoplasm. *PET Clin.* **2021**, *16* (2), 191–203.

(40) Pauwels, E.; Cleeren, F.; Bormans, G.; Deroose, C. M. Somatostatin Receptor PET Ligands - the next Generation for Clinical Practice. *Am. J. Nucl. Med. Mol. Imaging* **2018**, *8* (5), 311–331.

(41) Oh, S. W.; Cheon, G. J. Prostate-Specific Membrane Antigen PET Imaging in Prostate Cancer: Opportunities and Challenges. *Korean J. Radiol.* **2018**, *19* (5), 819–831.

(42) Sheikhbahaei, S.; Werner, R. A.; Solnes, L. B.; Pienta, K. J.; Pomper, M. G.; Gorin, M. A.; Rowe, S. P. Prostate-Specific Membrane Antigen (PSMA)-Targeted PET Imaging of Prostate Cancer: An Update on Important Pitfalls. *Semin. Nucl. Med.* **2019**, *49* (4), 255–270.

(43) Haubner, R.; Maschauer, S.; Prante, O. PET Radiopharmaceuticals for Imaging Integrin Expression: Tracers in Clinical Studies and Recent Developments. *Biomed Res. Int.* **2014**, *2014*, 871609.

(44) Chen, H.; Niu, G.; Wu, H.; Chen, X. Clinical Application of Radiolabeled RGD Peptides for PET Imaging of Integrin Avβ3. *Theranostics* **2016**, *6* (1), 78–92.

(45) Trotta, A. M.; Aurilio, M.; D'Alterio, C.; Ieranò, C.; Di Martino, D.; Barbieri, A.; Luciano, A.; Gaballo, P.; Santagata, S.; Portella, L.; Tomassi, S.; Marinelli, L.; Sementa, D.; Novellino, E.; Lastoria, S.; Scala, S.; Schottelius, M.; Di Maro, S. Novel Peptide-Based PET Probe for Non-Invasive Imaging of C-X-C Chemokine Receptor Type 4 (CXCR4) in Tumors. *J. Med. Chem.* **2021**, *64* (6), 3449–3461.

(46) Alluri, S. R.; Higashi, Y.; Kil, K.-E. PET Imaging Radiotracers of Chemokine Receptors. *Molecules* **2021**, *26* (17).

(47) Hengerer, A.; Grimm, J. Molecular Magnetic Resonance Imaging. *Biomed. Imaging Interv. J.* **2006**, *2* (2), e8.

(48) Gauberti, M.; Fournier, A. P.; Vivien, D.; Martinez de Lizarrondo, S. Molecular Magnetic Resonance Imaging (MMRI). *Methods Mol Bio* **2018**, *1718*, 315–327.

(49) O'Connor, J. P. B.; Tofts, P. S.; Miles, K. A.; Parkes, L. M.; Thompson, G.; Jackson, A. Dynamic Contrast-Enhanced Imaging Techniques: CT and MRI. *Br. J. Radiol.* **2011**, *84 Spec No 2* (Spec Iss 2), S112-20.

(50) Vincent, K.; Moore, J.; Kennedy, S.; Tracey, I. Blood Oxygenation Level Dependent Functional Magnetic Resonance Imaging: Current and Potential Uses in Obstetrics and Gynaecology. *BJOG* **2009**, *116* (2), 240–246.

(51) Gordon, Y.; Partovi, S.; Müller-Eschner, M.; Amarteifio, E.; Bäuerle, T.; Weber, M.-A.; Kauczor, H.-U.; Rengier, F. Dynamic Contrast-Enhanced Magnetic Resonance Imaging: Fundamentals and Application to the Evaluation of the Peripheral Perfusion. *Cardiovasc. Diagn. Ther.* **2014**, *4* (2), 147–164.

(52) Zuo, H. D.; Yao, W. W.; Chen, T. W.; Zhu, J.; Zhang, J. J.; Pu, Y.; Liu, G.; Zhang, X. M. The Effect of Superparamagnetic Iron Oxide with IRGD Peptide on the Labeling of Pancreatic Cancer Cells in Vitro: A Preliminary Study. *Biomed Res. Int.* **2014**, *2014*, 852352.

(53) Sulek, S.; Mammadov, B.; Mahcicek, D. I.; Sozeri, H.; Atalar, E.; Tekinay, A. B.; Guler, M. O. Peptide Functionalized Superparamagnetic Iron Oxide Nanoparticles as MRI Contrast Agents. *J. Mater. Chem.* **2011**, *21* (39), 15157–15162.

(54) Chee, H. L.; Gan, C. R. R.; Ng, M.; Low, L.; Fernig, D. G.; Bhakoo, K. K.; Paramelle, D. Biocompatible Peptide-Coated Ultrasmall Superparamagnetic Iron Oxide Nanoparticles for In Vivo Contrast-Enhanced Magnetic Resonance Imaging. *ACS Nano* **2018**, *12* (7), 6480–6491.

(55) Herranz, F.; Salinas, B.; Groult, H.; Pellico, J.; Lechuga-Vieco, A. V; Bhavesh, R.; Ruiz-Cabello, J. Superparamagnetic Nanoparticles for Atherosclerosis Imaging. *Nanomater. (Basel, Switzerland)* **2014**, *4* (2), 408–438.

(56) Gu, M.-J.; Li, K.-F.; Zhang, L.-X.; Wang, H.; Liu, L.-S.; Zheng, Z.-Z.; Han, N.-Y.; Yang, Z.-J.; Fan, T.-Y. In Vitro Study of Novel Gadolinium-Loaded Liposomes Guided by GBI-10 Aptamer for Promising Tumor Targeting and Tumor Diagnosis by Magnetic Resonance Imaging. *Int. J. Nanomedicine* **2015**, *10*, 5187–5204.

(57) Daniel, M.; Dubreil, L.; Fleurisson, R.; Judor, J.-P.; Bresson, T.; Brouard, S.; Favier, A.; Charreyre, M.-T.; Conchon, S. Multiscale Fluorescent Tracking of Immune Cells in the Liver with a Highly Biocompatible Far-Red Emitting Polymer Probe. *Sci. Rep.* **2020**, *10* (1), 17546.

(58) Yang, M.; Baranov, E.; Jiang, P.; Sun, F.-X.; Li, X.-M.; Li, L.; Hasegawa, S.; Bouvet, M.; Al-Tuwaijri, M.; Chishima, T.; Shimada, H.; Moossa, A. R.; Penman, S.; Hoffman, R. M. Whole-Body Optical Imaging of Green Fluorescent Protein-Expressing Tumors and Metastases. *Proc. Natl. Acad. Sci.* **2000**, *97* (3), 1206–1211.

(59) Pirovano, G.; Roberts, S.; Kossatz, S.; Reiner, T. Optical Imaging Modalities: Principles and Applications in Preclinical Research and Clinical Settings. *J. Nucl. Med.* **2020**, *61* (10), 1419 LP – 1427.

(60) Remington, S. J. Green Fluorescent Protein: A Perspective. *Protein Sci.* **2011**, *20* (9), 1509–1519.

(61) Ghim, C.-M.; Lee, S. K.; Takayama, S.; Mitchell, R. J. The Art of Reporter Proteins in Science: Past, Present and Future Applications. *BMB Rep.* **2010**, *43* (7), 451–460.

(62) Margineanu, A.; Chan, J. J.; Kelly, D. J.; Warren, S. C.; Flatters, D.; Kumar, S.; Katan, M.; Dunsby, C. W.; French, P. M. W. Screening for Protein-Protein Interactions Using Förster Resonance Energy Transfer (FRET) and Fluorescence Lifetime Imaging Microscopy (FLIM). *Sci. Rep.* **2016**, *6* (1), 28186.

(63) Bolger, R.; Lenoch, F.; Allen, E.; Meiklejohn, B.; Burke, T. Fluorescent Dye Assay for Detection of DNA in Recombinant Protein Products. *Biotechniques* **1997**, *23* (3), 532–537.

(64) Smith, L. M.; Sanders, J. Z.; Kaiser, R. J.; Hughes, P.; Dodd, C.; Connell, C. R.; Heiner, C.; Kent, S. B.; Hood, L. E. Fluorescence Detection in Automated DNA Sequence Analysis. *Nature* **1986**, *321* (6071), 674–679.

(65) Liao, X.; Makris, M.; Luo, X. M. Fluorescence-Activated Cell Sorting for Purification of Plasmacytoid Dendritic Cells from the Mouse Bone Marrow. *J. Vis. Exp.* **2016**, No. 117.

(66) McKinnon, K. M. Flow Cytometry: An Overview. *Curr. Protoc. Immunol.* **2018**, *120*, 5.1.1-5.1.11.

(67) Ettinger, A.; Wittmann, T. Fluorescence Live Cell Imaging. *Methods Cell Biol.* **2014**, *123*, 77–94.

(68) Nagaya, T.; Nakamura, Y. A.; Choyke, P. L.; Kobayashi, H. Fluorescence-Guided Surgery. *Front. Oncol.* **2017**, *7*, 314.

(69) Bray, M.-A.; Singh, S.; Han, H.; Davis, C. T.; Borgeson, B.; Hartland, C.; Kost-Alimova, M.; Gustafsdottir, S. M.; Gibson, C. C.; Carpenter, A. E. Cell Painting, a High-Content Image-Based Assay for Morphological Profiling Using Multiplexed Fluorescent Dyes. *Nat. Protoc.* **2016**, *11* (9), 1757–1774.

(70) Gustafsdottir, S. M.; Ljosa, V.; Sokolnicki, K. L.; Anthony Wilson, J.; Walpita, D.; Kemp, M. M.; Petri Seiler, K.; Carrel, H. A.; Golub, T. R.; Schreiber, S. L.; Clemons, P. A.; Carpenter, A. E.; Shamji, A. F. Multiplex Cytological Profiling Assay to Measure Diverse Cellular States. *PLoS One* **2013**, *8* (12), e80999.

(71) Wu, L.; Sedgwick, A. C.; Sun, X.; Bull, S. D.; He, X.-P.; James, T. D. Reaction-Based Fluorescent Probes for the Detection and Imaging of Reactive Oxygen, Nitrogen, and Sulfur Species. *Acc. Chem. Res.* **2019**, *52* (9), 2582–2597.

(72) Gomes, A.; Fernandes, E.; Lima, J. L. F. C. Fluorescence Probes Used for Detection of Reactive Oxygen Species. *J. Biochem. Biophys. Methods* **2005**, *65* (2–3), 45–80.

(73) Carter, K. P.; Young, A. M.; Palmer, A. E. Fluorescent Sensors for Measuring Metal Ions in Living Systems. *Chem. Rev.* **2014**, *114* (8), 4564–4601.

(74) Sumalekshmy, S.; Fahrni, C. J. Metal Ion-Responsive Fluorescent Probes for Two-Photon Excitation Microscopy. *Chem. Mater.* **2011**, *23* (3), 483–500.

(75) Tang, B.; Yu, F.; Li, P.; Tong, L.; Duan, X.; Xie, T.; Wang, X. A Near-Infrared Neutral PH Fluorescent Probe for Monitoring Minor PH Changes: Imaging in Living HepG2 and HL-7702 Cells. *J. Am. Chem. Soc.* **2009**, *131* (8), 3016–3023.

(76) Wang, S.; Huang, Y.; Guan, X. Fluorescent Probes for Live Cell Thiol Detection. *Molecules* **2021**, *26* (12).

(77) Luker, G. D.; Luker, K. E. Optical Imaging: Current Applications and Future Directions. *J Nucl Med* **2008**, *49* (1), 1–4.

(78) Polglase, A. L.; McLaren, W. J.; Skinner, S. A.; Kiesslich, R.; Neurath, M. F.; Delaney, P. M. A Fluorescence Confocal Endomicroscope for in Vivo Microscopy of the Upper- and the Lower-GI Tract. *Gastrointest. Endosc.* **2005**, *62* (5), 686–695.

(79) Gong, Y.-J.; Zhang, X.-B.; Mao, G.-J.; Su, L.; Meng, H.-M.; Tan, W.; Feng, S.; Zhang, G. A Unique Approach toward Near-Infrared Fluorescent Probes for Bioimaging with Remarkably Enhanced Contrast. *Chem. Sci.* **2016**, *7* (3), 2275–2285.

(80) Fleiss, A.; Sarkisyan, K. S. A Brief Review of Bioluminescent Systems. *Curr. Genet.* **2019**, *65* (4), 877–882.

(81) Syed, A. J.; Anderson, J. C. Applications of Bioluminescence in Biotechnology and Beyond. *Chem. Soc. Rev.* **2021**, *50* (9), 5668–5705.

(82) Branchini, B. R.; Behney, C. E.; Southworth, T. L.; Fontaine, D. M.; Gulick, A. M.; Vinyard, D. J.; Brudvig, G. W. Experimental Support for a Single Electron-Transfer Oxidation Mechanism in Firefly Bioluminescence. *J. Am. Chem. Soc.* **2015**, *137* (24), 7592–7595.

(83) Koo, J. A.; Schmidt, S. P.; Schuster, G. B. Bioluminescence of the Firefly: Key Steps in

the Formation of the Electronically Excited State for Model Systems. *Proc. Natl. Acad. Sci. U. S. A.* **1978**, *75* (1), 30–33.

(84) Ando, Y.; Niwa, K.; Yamada, N.; Enomoto, T.; Irie, T.; Kubota, H.; Ohmiya, Y.; Akiyama, H. Firefly Bioluminescence Quantum Yield and Colour Change by PH-Sensitive Green Emission. *Nat. Photonics* **2008**, *2* (1), 44–47.

(85) Berger, F.; Paulmurugan, R.; Bhaumik, S.; Gambhir, S. S. Uptake Kinetics and Biodistribution of 14C-D-Luciferin--a Radiolabeled Substrate for the Firefly Luciferase Catalyzed Bioluminescence Reaction: Impact on Bioluminescence Based Reporter Gene Imaging. *Eur. J. Nucl. Med. Mol. Imaging* **2008**, *35* (12), 2275–2285.

(86) Evans, M. S.; Chaurette, J. P.; Adams, S. T. J.; Reddy, G. R.; Paley, M. A.; Aronin, N.; Prescher, J. A.; Miller, S. C. A Synthetic Luciferin Improves Bioluminescence Imaging in Live Mice. *Nat. Methods* **2014**, *11* (4), 393–395.

(87) Bakhsheshian, J.; Wei, B.-R.; Chang, K.-E.; Shukla, S.; Ambudkar, S. V; Simpson, R. M.; Gottesman, M. M.; Hall, M. D. Bioluminescent Imaging of Drug Efflux at the Blood-Brain Barrier Mediated by the Transporter ABCG2. *Proc. Natl. Acad. Sci. U. S. A.* **2013**, *110* (51), 20801–20806.

(88) Paroo, Z.; Bollinger, R. A.; Braasch, D. A.; Richer, E.; Corey, D. R.; Antich, P. P.; Mason, R. P. Validating Bioluminescence Imaging as a High-Throughput, Quantitative Modality for Assessing Tumor Burden. *Mol. Imaging* **2004**, *3* (2), 15353500200403172.

(89) Jenkins, D. E.; Oei, Y.; Hornig, Y. S.; Yu, S.-F.; Dusich, J.; Purchio, T.; Contag, P. R. Bioluminescent Imaging (BLI) to Improve and Refine Traditional Murine Models of Tumor Growth and Metastasis. *Clin. Exp. Metastasis* **2003**, *20* (8), 733–744.

(90) Lundin, A.; Hasenson, M.; Persson, J.; Pousette, A. Estimation of Biomass in Growing Cell Lines by Adenosine Triphosphate Assay. *Methods Enzymol.* **1986**, *133*, 27–42.

(91) Lundin, A.; Rickardsson, A.; Thore, A. Continuous Monitoring of ATP-Converting Reactions by Purified Firefly Luciferase. *Anal. Biochem.* **1976**, *75* (2), 611–620.

(92) Lundin, A. Optimization of the Firefly Luciferase Reaction for Analytical Purposes. *Adv. Biochem. Eng. Biotechnol.* **2014**, *145*, 31–62.

(93) Scheuerbrandt, G.; Lundin, A.; Lövgren, T.; Mortier, W. Screening for Duchenne Muscular Dystrophy: An Improved Screening Test for Creatine Kinase and Its Application in an Infant Screening Program. *Muscle Nerve* **1986**, *9* (1), 11–23.

(94) Lundin, A.; Jäderlund, B.; Lövgren, T. Optimized Bioluminescence Assay of Creatine Kinase and Creatine Kinase B-Subunit Activity. *Clin. Chem.* **1982**, *28* (4), 609–614.

(95) Branchini, B. R.; Southworth, T. L.; Fontaine, D. M.; Kohrt, D.; Talukder, M.; Michelini, E.; Cevenini, L.; Roda, A.; Grossel, M. J. An Enhanced Chimeric Firefly Luciferase-Inspired Enzyme for ATP Detection and Bioluminescence Reporter and Imaging Applications. *Anal. Biochem.* **2015**, *484*, 148–153.

(96) Nakamura, M.; Mie, M.; Funabashi, H.; Yamamoto, K.; Ando, J.; Kobatake, E. Cell-Surface-Localized ATP Detection with Immobilized Firefly Luciferase. *Anal. Biochem.* **2006**, *352 1*, 61–67.

(97) Zhang, Y.; Phillips, G. J.; Li, Q.; Yeung, E. S. Imaging Localized Astrocyte ATP Release with Firefly Luciferase Beads Attached to the Cell Surface. *Anal. Chem.* **2008**, *80* (23), 9316–9325.

(98) Cruz-Aguado, J. A.; Chen, Y.; Zhang, Z.; Elowe, N. H.; Brook, M. A.; Brennan, J. D. Ultrasensitive ATP Detection Using Firefly Luciferase Entrapped in Sugar-Modified

Sol−Gel-Derived Silica. *J. Am. Chem. Soc.* **2004**, *126* (22), 6878–6879.
(99) Berg, J.; Hung, Y. P.; Yellen, G. A Genetically Encoded Fluorescent Reporter of ATP:ADP Ratio. *Nat. Methods* **2009**, *6* (2), 161–166.
(100) Morse, D.; Tannous, B. A. A Water-Soluble Coelenterazine for Sensitive in Vivo Imaging of Coelenterate Luciferases. *Mol Ther.* April 2012, pp 692–693.
(101) Dubuisson, M. L. N.; Wergifosse, B. de; Trouet, A.; Baguet, F.; Marchand-Brynaert, J.; Rees, J.-F. Antioxidative Properties of Natural Coelenterazine and Synthetic Methyl Coelenterazine in Rat Hepatocytes Subjected to Tert-Butyl Hydroperoxide-Induced Oxidative Stress. *Biochem. Pharmacol.* **2000**, *60* (4), 471–478.
(102) Roda, A.; Guardigli, M.; Michelini, E.; Mirasoli, M. Bioluminescence in Analytical Chemistry and in Vivo Imaging. *Trends Anal. Chem.* **2009**, *28* (3), 307–322.
(103) Iwano, S.; Sugiyama, M.; Hama, H.; Watakabe, A.; Hasegawa, N.; Kuchimaru, T.; Tanaka, K. Z.; Takahashi, M.; Ishida, Y.; Hata, J.; Shimozono, S.; Namiki, K.; Fukano, T.; Kiyama, M.; Okano, H.; Kizaka-Kondoh, S.; McHugh, T. J.; Yamamori, T.; Hioki, H.; Maki, S.; Miyawaki, A. Single-Cell Bioluminescence Imaging of Deep Tissue in Freely Moving Animals. *Science (80-.).* **2018**, *359* (6378), 935–939.
(104) Shinde, R.; Perkins, J.; Contag, C. H. Luciferin Derivatives for Enhanced in Vitro and in Vivo Bioluminescence Assays. *Biochemistry* **2006**, *45* (37), 11103–11112.
(105) Conley, N. R.; Dragulescu-Andrasi, A.; Rao, J.; Moerner, W. E. A Selenium Analogue of Firefly D-Luciferin with Red-Shifted Bioluminescence Emission. *Angew. Chemie* **2012**, *51* (14), 3350–3353.
(106) Weihs, F.; Dacres, H. Red-Shifted Bioluminescence Resonance Energy Transfer: Improved Tools and Materials for Analytical in Vivo Approaches. *Trends Anal. Chem.* **2019**, *116*, 61–73.
(107) Kuchimaru, T.; Iwano, S.; Kiyama, M.; Mitsumata, S.; Kadonosono, T.; Niwa, H.; Maki, S.; Kizaka-Kondoh, S. A Luciferin Analogue Generating Near-Infrared Bioluminescence Achieves Highly Sensitive Deep-Tissue Imaging. *Nat. Commun.* **2016**, *7* (1), 11856.
(108) Viviani, V. R.; Bevilaqua, V. R.; Souza, D. R. De; Pelentir, G. F.; Kakiuchi, M.; Hirano, T. A Very Bright Far-Red Bioluminescence Emitting Combination Based on Engineered Railroad Worm Luciferase and 6 -Amino-Analogs for Bioimaging Purposes. *Int. J. Mol. Sci.* **2021**, *22*, 303.
(109) Mofford, D. M.; Reddy, G. R.; Miller, S. C. Aminoluciferins Extend Firefly Luciferase Bioluminescence into the Near-Infrared and Can Be Preferred Substrates over d-Luciferin. *J. Am. Chem. Soc.* **2014**, *136* (38), 13277–13282.
(110) Lorenz, W. W.; McCann, R. O.; Longiaru, M.; Cormier, M. J. Isolation and Expression of a CDNA Encoding Renilla Reniformis Luciferase. *PNAS* **1991**, *88* (10), 4438–4442.
(111) Inouye, S.; Watanabe, K.; Nakamura, H.; Shimomura, O. Secretional Luciferase of the Luminous Shrimp Oplophorus Gracilirostris: CDNA Cloning of a Novel Imidazopyrazinone Luciferase(1). *FEBS Lett.* **2000**, *481* (1), 19–25.
(112) Takenaka, Y.; Yamaguchi, A.; Tsuruoka, N.; Torimura, M.; Gojobori, T.; Shigeri, Y. Evolution of Bioluminescence in Marine Planktonic Copepods. *Mol. Biol. Evol.* **2012**, *29* (6), 1669–1681.
(113) Takenaka, Y.; Masuda, H.; Yamaguchi, A.; Nishikawa, S.; Shigeri, Y.; Yoshida, Y.; Mizuno, H. Two Forms of Secreted and Thermostable Luciferases from the Marine Copepod Crustacean, Metridia Pacifica. *Gene* **2008**, *425* (1–2), 28–35.

(114) Markova, S. V; Golz, S.; Frank, L. A.; Kalthof, B.; Vysotski, E. S. Cloning and Expression of CDNA for a Luciferase from the Marine Copepod Metridia Longa. A Novel Secreted Bioluminescent Reporter Enzyme. *J. Biol. Chem.* **2004**, *279* (5), 3212–3217.
(115) Titushin, M. S.; Markova, S. V; Frank, L. A.; Malikova, N. P.; Stepanyuk, G. A.; Lee, J.; Vysotski, E. S. Coelenterazine-Binding Protein of Renilla Muelleri: CDNA Cloning, Overexpression, and Characterization as a Substrate of Luciferase. *Photochem. Photobiol. Sci.* **2008**, *7* (2), 189–196.
(116) Verhaegen, M.; Christopoulos, T. K. Recombinant Gaussia Luciferase. Overexpression, Purification, and Analytical Application of a Bioluminescent Reporter for DNA Hybridization. *Anal. Chem.* **2002**, *74* (17), 4378–4385.
(117) Stepanyuk, G. A.; Liu, Z.-J.; Markova, S. S.; Frank, L. A.; Lee, J.; Vysotski, E. S.; Wang, B.-C. Crystal Structure of Coelenterazine-Binding Protein from Renilla Muelleri at 1.7 Å: Why It Is Not a Calcium-Regulated Photoprotein. *Photochem. Photobiol. Sci.* **2008**, *7* (4), 442–447.
(118) Delroisse, J.; Duchatelet, L.; Flammang, P.; Mallefet, J. Leaving the Dark Side? Insights Into the Evolution of Luciferases . *Frontiers in Marine Science* . 2021.
(119) Davis, M. P.; Sparks, J. S.; Smith, W. L. Repeated and Widespread Evolution of Bioluminescence in Marine Fishes. *PLoS One* **2016**, *11* (6), e0155154.
(120) Hall, M. P.; Unch, J.; Binkowski, B. F.; Valley, M. P.; Butler, B. L.; Wood, M. G.; Otto, P.; Zimmerman, K.; Vidugiris, G.; Machleidt, T.; Robers, M. B.; Benink, H. A.; Eggers, C. T.; Slater, M. R.; Meisenheimer, P. L.; Klaubert, D. H.; Fan, F.; Encell, L. P.; Wood, K. V. Engineered Luciferase Reporter from a Deep Sea Shrimp Utilizing a Novel Imidazopyrazinone Substrate. *ACS Chem. Biol.* **2012**, *7* (11), 1848–1857.
(121) Ohmiya, Y.; Hirano, T. Shining the Light: The Mechanism of the Bioluminescence Reaction of Calcium-Binding Photoproteins. *Chem. Biol.* **1996**, *3* (5), 337–347.
(122) Hughes, C.; Rabinowitz, A.; Tate, M.; Birrell, L.; Allsup, J.; Billinton, N.; Walmsley, R. M. Development of a High-Throughput Gaussia Luciferase Reporter Assay for the Activation of the GADD45a Gene by Mutagens, Promutagens, Clastogens, and Aneugens. *J. Biomol. Screen.* **2012**, *17* (10), 1302–1315.
(123) Zhao, H.; Doyle, T. C.; Wong, R. J.; Cao, Y.; Stevenson, D. K.; Piwnica-Worms, D.; Contag, C. H. Characterization of Coelenterazine Analogs for Measurements of Renilla Luciferase Activity in Live Cells and Living Animals. *Mol. Imaging* **2004**, *3* (1), 15353500200403180.
(124) Xiong, Y.; Zhang, Y.; Li, Z.; Reza, M. S.; Li, X.; Tian, X.; Ai, H. Engineered Amber-Emitting Nano Luciferase and Its Use for Immunobioluminescence Imaging In Vivo. *J. Am. Chem. Soc.* **2022**, *144* (31), 14101–14111.
(125) Grinstead, K. M.; Rowe, L.; Ensor, C. M.; Joel, S.; Daftarian, P.; Dikici, E.; Zingg, J.-M.; Daunert, S. Red-Shifted Aequorin Variants Incorporating Non-Canonical Amino Acids: Applications in In Vivo Imaging. *PLoS One* **2016**, *11* (7), e0158579.
(126) Yeh, H.; Karmach, O.; Ji, A.; Carter, D.; Martins-green, M. M.; Ai, H. Red-Shifted Luciferase – Luciferin Pairs for Enhanced Bioluminescence Imaging. *Nat. Methods* **2017**, *14* (10), 971–978.
(127) Giuliani, G.; Molinari, P.; Ferretti, G.; Cappelli, A.; Anzini, M.; Vomero, S.; Costa, T. New Red-Shifted Coelenterazine Analogues with an Extended Electronic Conjugation.

Tetrahedron Lett. **2012**, *53* (38), 5114–5118.

(128) Shakhmin, A.; Hall, M. P.; Machleidt, T.; Walker, J. R.; Wood, K. V; Kirkland, T. A. Coelenterazine Analogues Emit Red-Shifted Bioluminescence with NanoLuc. *Org. Biomol. Chem.* **2017**, *15* (40), 8559–8567.

(129) Kricka, L. J. BIOLUMINESCENCE. In *Encyclopedia of Analytical Science*; Worsfold, P., Townshend, A., Poole, C. B. T.-E. of A. S. (Second E., Eds.; Elsevier: Oxford, 2005; pp 277–284.

(130) Endo, M.; Ozawa, T. Advanced Bioluminescence System for In Vivo Imaging with Brighter and Red-Shifted Light Emission. *International Journal of Molecular Sciences*. 2020.

(131) Xu, Y.; Piston, D. W.; Johnson, C. H. A Bioluminescence Resonance Energy Transfer (BRET) System: Application to Interacting Circadian Clock Proteins. *PNAS* **1999**, *96* (1), 151–156.

(132) Nishihara, R.; Paulmurugan, R.; Nakajima, T.; Yamamoto, E.; Natarajan, A.; Afjei, R.; Hiruta, Y.; Iwasawa, N.; Nishiyama, S.; Citterio, D.; Sato, M.; Kim, S. B.; Suzuki, K. Highly Bright and Stable NIR-BRET with Blue-Shifted Coelenterazine Derivatives for Deep-Tissue Imaging of Molecular Events in Vivo. *Theranostics* **2019**, *9* (9), 2646–2661.

(133) Blinks, J. R. Use of Photoproteins as Intracellular Calcium Indicators. *Environ. Health Perspect.* **1990**, *84*, 75–81.

(134) Head, J. F.; Inouye, S.; Teranishi, K.; Shimomura, O. The Crystal Structure of the Photoprotein Aequorin at 2.3 A Resolution. *Nature* **2000**, *405* (6784), 372–376.

(135) Liu, Z.-J.; Vysotski, E. S.; Deng, L.; Lee, J.; Rose, J.; Wang, B.-C. Atomic Resolution Structure of Obelin: Soaking with Calcium Enhances Electron Density of the Second Oxygen Atom Substituted at the C2-Position of Coelenterazine. *Biochem. Biophys. Res. Commun.* **2003**, *311* (2), 433–439.

(136) Vysotski, E. S.; Lee, J. Ca2+-Regulated Photoproteins: Structural Insight into the Bioluminescence Mechanism. *Acc. Chem. Res.* **2004**, *37* (6), 405–415.

(137) Nourooz-Zadeh, J.; Ziegler, D.; Sohr, C.; Betteridge, J. D.; Knight, J.; Hothersall, J. The Use of Pholasin as a Probe for the Determination of Plasma Total Antioxidant Capacity. *Clin. Biochem.* **2006**, *39* (1), 55–61.

(138) Kuse, M.; Tanaka, E.; Nishikawa, T. Pholasin Luminescence Is Enhanced by Addition of Dehydrocoelenterazine. *Bioorg. Med. Chem. Lett.* **2008**, *18* (20), 5657–5659.

(139) Shah, A.; Passacquale, G.; Gkaliagkousi, E.; Ritter, J.; Ferro, A. Platelet Nitric Oxide Signalling in Heart Failure: Role of Oxidative Stress. *Cardiovasc. Res.* **2011**, *91* (4), 625–631.

(140) Loening, A. M.; Fenn, T. D.; Wu, A. M.; Gambhir, S. S. Consensus Guided Mutagenesis of Renilla Luciferase Yields Enhanced Stability and Light Output. *PEDS* **2006**, *19* (9), 391–400.

(141) Tannous, B. A. Gaussia Luciferase Reporter Assay for Monitoring Biological Processes in Culture and in Vivo. *Nat. Protoc.* **2009**, *4* (4), 582–591.

(142) England, C. G.; Ehlerding, E. B.; Cai, W. NanoLuc: A Small Luciferase Is Brightening Up the Field of Bioluminescence. *Bioconjug. Chem.* **2016**, *27* (5), 1175–1187.

(143) Berry, S. L.; Hameed, H.; Thomason, A.; Maciej-Hulme, M. L.; Saif Abou-Akkada, S.; Horrocks, P.; Price, H. P. Development of NanoLuc-PEST Expressing Leishmania Mexicana as a New Drug Discovery Tool for Axenic- and Intramacrophage-Based

Assays. *PLoS* **2018**, *12* (7), e0006639.
(144) Dale, N. C.; Johnstone, E. K. M.; White, C. W.; Pfleger, K. D. G. NanoBRET: The Bright Future of Proximity-Based Assays . *Frontiers in Bioengineering and Biotechnology* . 2019.
(145) Machleidt, T.; Woodroofe, C. C.; Schwinn, M. K.; Méndez, J.; Robers, M. B.; Zimmerman, K.; Otto, P.; Daniels, D. L.; Kirkland, T. A.; Wood, K. V. NanoBRET—A Novel BRET Platform for the Analysis of Protein–Protein Interactions. *ACS Chem. Biol.* **2015**, *10* (8), 1797–1804.
(146) Cooley, R.; Kara, N.; Hui, N. S.; Tart, J.; Roustan, C.; George, R.; Hancock, D. C.; Binkowski, B. F.; Wood, K. V; Ismail, M.; Downward, J. Development of a Cell-Free Split-Luciferase Biochemical Assay as a Tool for Screening for Inhibitors of Challenging Protein-Protein Interaction Targets. *Wellcome open Res.* **2020**, *5*, 20.
(147) Shetty, S. K.; Walzem, R. L.; Davies, B. S. J. A Novel NanoBiT-Based Assay Monitors the Interaction between Lipoprotein Lipase and GPIHBP1 in Real Time[S]. *J. Lipid Res.* **2020**, *61* (4), 546–559.
(148) Li, J.; Chen, L.; Du, L.; Li, M. Cage the Firefly Luciferin! - A Strategy for Developing Bioluminescent Probes. *Chem. Soc. Rev.* **2013**, *42* (2), 662–676.
(149) Mofford, D. M.; Adams, S. T.; Reddy, G. S. K. K.; Reddy, G. R.; Miller, S. C. Luciferin Amides Enable in Vivo Bioluminescence Detection of Endogenous Fatty Acid Amide Hydrolase Activity. *J. Am. Chem. Soc.* **2015**, *137* (27), 8684–8687.
(150) Dragulescu-Andrasi, A.; Liang, G.; Rao, J. In Vivo Bioluminescence Imaging of Furin Activity in Breast Cancer Cells Using Bioluminogenic Substrates. *Bioconjug. Chem.* **2009**, *20* (8), 1660–1666.
(151) Yao, H.; So, M.; Rao, J. A Bioluminogenic Substrate for in Vivo Imaging of Beta-Lactamase Activity. *Angew. Chem. Int. Ed. Engl.* **2007**, *46* (37), 7031–7034.
(152) Zhou, W.; Shultz, J. W.; Murphy, N.; Hawkins, E. M.; Bernad, L.; Good, T.; Moothart, L.; Frackman, S.; Klaubert, D. H.; Bulleit, R. F.; Wood, K. V. Electrophilic Aromatic Substituted Luciferins as Bioluminescent Probes for Glutathione S-Transferase Assays. *Chem. Commun.* **2006**, No. 44, 4620–4622.
(153) Wang, A.; Li, X.; Ju, Y.; Chen, D.; Lu, J. Bioluminescence Imaging of Carbon Monoxide in Living Cells Based on a Selective Deiodination Reaction. *Analyst* **2020**, *145* (2), 550–556.
(154) Tian, X.; Li, Z.; Lau, C.; Lu, J. Visualization of in Vivo Hydrogen Sulfide Production by a Bioluminescence Probe in Cancer Cells and Nude Mice. *Anal. Chem.* **2015**, *87* (22), 11325–11331.
(155) Cohen, A. S.; Dubikovskaya, E. A.; Rush, J. S.; Bertozzi, C. R. Real-Time Bioluminescence Imaging of Glycans on Live Cells. *J. Am. Chem. Soc.* **2010**, *132* (25), 8563–8565.
(156) Van de Bittner, G. C.; Bertozzi, C. R.; Chang, C. J. Strategy for Dual-Analyte Luciferin Imaging: In Vivo Bioluminescence Detection of Hydrogen Peroxide and Caspase Activity in a Murine Model of Acute Inflammation. *J. Am. Chem. Soc.* **2013**, *135* (5), 1783–1795.
(157) Tian, X.; Liu, X.; Wang, A.; Lau, C.; Lu, J. Bioluminescence Imaging of Carbon Monoxide in Living Cells and Nude Mice Based on Pd(0)-Mediated Tsuji-Trost Reaction. *Anal. Chem.* **2018**, *90* (9), 5951–5958.
(158) Heffern, M. C.; Min, H.; Au-yeung, H. Y.; Bittner, G. C. Van De; Ackerman, C. M. In

Vivo Bioluminescence Imaging Reveals Copper Deficiency in a Murine Model of Nonalcoholic Fatty Liver Disease. *PNAS* **2016**, *113* (50), 14219–14224.

(159) Lindberg, E.; Mizukami, S.; Ibata, K.; Miyawaki, A.; Kikuchi, K. Development of Luminescent Coelenterazine Derivatives Activatable by β-Galactosidase for Monitoring Dual Gene Expression. *Chem. – A Eur. J.* **2013**, *19* (44), 14970–14976.

(160) Yuan, M.; Ma, X.; Jiang, T.; Zhang, C.; Chen, H.; Gao, Y.; Yang, X.; Du, L.; Li, M. A Novel Coelenterate Luciferin-Based Luminescent Probe for Selective and Sensitive Detection of Thiophenols. *Org. Biomol. Chem.* **2016**, *14* (43), 10267–10274.

(161) Jones, R. R.; Hooper, D. C.; Zhang, L.; Wolverson, D.; Valev, V. K. Raman Techniques: Fundamentals and Frontiers. *Nanoscale Res. Lett.* **2019**, *14* (1), 231.

(162) Dietzek, B.; Cialla, D.; Schmitt, M.; Popp, J. Introduction to the Fundamentals of Raman Spectroscopy BT - Confocal Raman Microscopy; Toporski, J., Dieing, T., Hollricher, O., Eds.; Springer International Publishing: Cham, 2018; pp 47–68.

(163) Nasdala, L.; Schmidt, C. Applications of Raman Spectroscopy in Mineralogy and Geochemistry. *Elements* **2020**, *16* (2), 99–104.

(164) Cantarero, A. Raman Scattering Applied to Materials Science. *Procedia Mater. Sci.* **2015**, *9*, 113–122.

(165) Wang, W.; Shao, F.; Kröger, M.; Zenobi, R.; Schlüter, A. D. Structure Elucidation of 2D Polymer Monolayers Based on Crystallization Estimates Derived from Tip-Enhanced Raman Spectroscopy (TERS) Polymerization Conversion Data. *J. Am. Chem. Soc.* **2019**, *141* (25), 9867–9871.

(166) Smekal, A. Zur Quantentheorie Der Dispersion. *Naturwissenschaften* **1923**, *11* (43), 873–875.

(167) Raman, C. V. A Change of Wave-Length in Light Scattering. *Nature* **1928**, *121* (3051), 619.

(168) Raman, C. V; Krishnan, K. S. A New Type of Secondary Radiation. *Nature* **1928**, *121* (3048), 501–502.

(169) Bocklitz, T. W.; Guo, S.; Ryabchykov, O.; Vogler, N.; Popp, J. Raman Based Molecular Imaging and Analytics: A Magic Bullet for Biomedical Applications!? *Anal. Chem.* **2016**, *88* (1), 133–151.

(170) Li, P.; Long, F.; Chen, W.; Chen, J.; Chu, P. K.; Wang, H. Fundamentals and Applications of Surface-Enhanced Raman Spectroscopy–Based Biosensors. *Curr. Opin. Biomed. Eng.* **2020**, *13*, 51–59.

(171) Kneipp, K.; Haka, A. S.; Kneipp, H.; Badizadegan, K.; Yoshizawa, N.; Boone, C.; Shafer-Peltier, K. E.; Motz, J. T.; Dasari, R. R.; Feld, M. S. Surface-Enhanced Raman Spectroscopy in Single Living Cells Using Gold Nanoparticles. *Appl. Spectrosc.* **2002**, *56* (2), 150–154.

(172) Chen, Y.; Ren, J.-Q.; Zhang, X.-G.; Wu, D.-Y.; Shen, A.-G.; Hu, J.-M. Alkyne-Modulated Surface-Enhanced Raman Scattering-Palette for Optical Interference-Free and Multiplex Cellular Imaging. *Anal. Chem.* **2016**, *88* (12), 6115–6119.

(173) Yamakoshi, H.; Dodo, K.; Palonpon, A.; Ando, J.; Fujita, K.; Kawata, S.; Sodeoka, M. Alkyne-Tag Raman Imaging for Visualization of Mobile Small Molecules in Live Cells. *J. Am. Chem. Soc.* **2012**, *134* (51), 20681–20689.

Chapter 2

A Caged Imidazopyrazinone for Selective Bioluminescence Detection of Labile Extracellular Copper(II)*

---

* This chapter is a modified version of the following published article: O'Sullivan, J.J.; Medici, V.; Heffern, M.C. A Caged Imidazopyrazinone for Selective Bioluminescence Detection of Labile, Extracellular Copper(II), *Chemical Science* **2022**, *13*, 4352.

2.1 Abstract

Copper is an essential redox-active metal that plays integral roles in biology ranging from enzymatic catalysis to mitochondrial respiration. However, if not adequately regulated, this redox activity has the potential to cause oxidative stress through the production of reactive oxygen species. Indeed, the dysregulation of copper has been associated with a variety of disease states including diabetes, neurodegenerative disorders, and multiple cancers. While increasing tools are being developed for illuminating labile intracellular copper pools and the trafficking pathways in which they are involved, significantly less attention has been given to the analogous extracellular labile pool. To address this gap, we have developed a bioluminescence-based imaging probe, picolinic ester caged-diphenylterazine (pic-DTZ) for monitoring labile, extracellular copper using a coelenterazine-like imidazopyrazinone and the genetically - engineered, marine-based luciferase, Nanoluciferase. Unlike the more commonly-used firefly luciferase, Nanoluciferase does not require ATP to allow its application to the extracellular milieu. Pic-DTZ demonstrates high metal and oxidation state selectivity for Cu(II) in aqueous buffer as well as selectivity for labile pools over protein bound Cu(II). We demonstrate the potential of pic-DTZ as a diagnostic tool in human serum and plasma for copper-associated diseases. Additionally, we apply pic-DTZ to lend insight into the extracellular copper dynamic in anticancer treatments.

2.2 Introduction

2.2.1 Copper in Biological Systems

Copper is a trace micronutrient required for proper physiological function in all living organisms.[1,2] Nature harnesses its accessible Cu(II) and Cu(I) oxidation states for essential roles in enzymatic catalysis, mitochondrial respiration, and cell proliferation.[3–7] Dysregulated copper biology has been associated with both aberrant redox activity and unwanted protein aggregation,[8] implicating it in disease states that include obesity-associated metabolic disorders, neurodegeneration, and a variety of cancers.[9–11] For this reason, biology has evolved complex systems to tightly regulate and traffic copper.

Increasing studies point to the importance in regulating not only the overall levels and redox states of biological copper, but its localization between the intra- and extracellular space. For example, Finney et al. used X-ray fluorescence spectroscopy to reveal large-scale relocalization and extracellular translocation of cellular copper during tumor angiogenesis.[12] Widely studied yet still debated is the putative role of mislocalized extracellular copper in Alzheimer's disease and amyloid-beta aggregation.[13] However, many of these studies are limited to structural studies with isolated proteins in buffer, snapshots of copper localization in fixed tissues and cells, or indirect measures via tracking of copper-dependent proteins and enzymes.[14–17] The ability to target and monitor the copper pools in both the intracellular and extracellular milieu would provide valuable insight into copper dynamics in both normal physiological and pathological states.

Researchers have put forth powerful imaging probes for tracking intracellular copper that have illuminated the importance of the labile copper pool in dynamic cellular signaling.[18]

Distinct from the static copper pool, which is tightly bound within protein pockets, the labile pool is loosely-bound to its ligands, allowing for exchange between biomolecules and low-molecular-weight chelates. Indeed, changes in the labile pool in extracellular fluids, such as blood and urine, have been observed in copper-associated disease states. For instance, in Wilson disease (WD), a genetic disease resulting from pathogenic variants of the ATP7B copper transporter, serum samples exhibit elevation of non-ceruloplasmin-bound copper while total serum copper levels are not significantly affected.[19] Acquiring knowledge to track both tissue and extracellular copper fluxes in cases such as this would have diagnostic potential and will shed light on the systemic manifestations of the disease.

2.2.2 Current Methods for Monitoring Copper in Biological Systems

Despite the advances in probe development for visualizing intracellular labile Cu(I) pools, tools for directly monitoring the labile, extracellular copper pool remain scarce.[17] Extracellular copper measurements typically rely on either quantification of total copper levels by analytical techniques such as ICP-MS or monitoring blood levels of the major copper chaperone protein, ceruloplasmin.[20,21] Though these methods can provide useful information particularly to total copper levels, they do not capture real-time changes in localization or cycling between the copper pools.[17] To investigate the labile pool, researchers have paired the existing techniques with pre-analysis separation steps, such as chelation followed by size-exclusion enrichment.[22,23] While these approaches have indeed expanded our understanding of the labile pool, they may perturb the native copper speciation.[24] Thus, chemo-responsive imaging agents that directly target extracellular labile copper would preserve and inform on the copper dynamics outside of the cell and offer a platform for copper-associated diagnostics. An ideal probe would be selective for Cu(II), the expected oxidation state in the extracellular space, target labile rather than tightly-bound pools, generate signal corresponding to extracellular rather than intracellular populations, and provide a turn-on a response, which can be a challenge due to the high fluorescence quenching ability of Cu(II).[17]

Here we report the design, synthesis, and biological applications of a bioluminescent probe for monitoring labile, extracellular Cu(II) pools with high selectivity and sensitivity. The picolinic ester-caged diphenylterazine (pic-DTZ) is a copper-responsive caged imidazopyrazinone probe that generates diphenylterazine (DTZ) upon ester hydrolysis by Cu(II) for subsequent enzymatic conversion by the Nanoluciferase (Nluc) enzyme to produce light (Scheme 2.1). Extracellular targeting can be achieved by the selective localization of Nluc. We demonstrate the selectivity of the probe for Cu(II) over other relevant biological metals and for chelatable pools over tightly-bound copper. We show the potential of the probe as a diagnostic tool for serum and plasma copper levels, including its ability to distinguish elevated labile Cu(II) levels in the plasma of individuals with WD relative to the plasma from healthy individuals. Finally, we employ the probe to directly assess changes in labile extracellular Cu(II) levels in a breast cancer cell line treated with various anti-cancer agents that are known or reported to perturb intracellular copper trafficking pathways.

Scheme 2.1 Design of pic-DTZ for Cu(II)-responsive Bioluminescence[a]

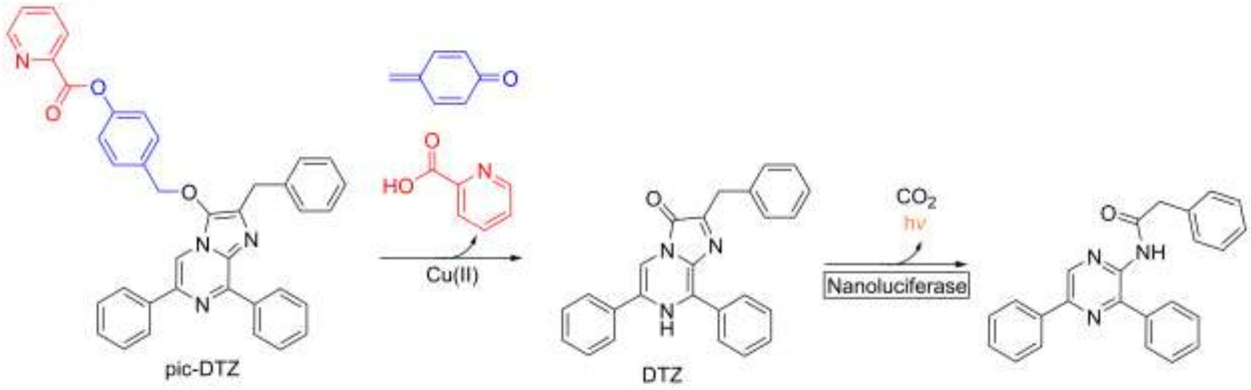

[a] Red: Cu(II)-responsive cage, blue: self-immolative linker, black: diphenylterazine (DTZ) core.

2.3 Results and Discussion

2.3.1 Design and Synthesis of Probes

Bioluminescence, which involves the enzymatic conversion of luciferin substrates by luciferase enzymes to produce light, is an attractive imaging modality for its high signal-to-noise ratio. Additionally, probes developed on this platform can be endowed with cell and tissue specificity through genetically encoding luciferase expression and localization.[25] Caged luciferins are inert, chemically-modified derivatives of luciferin substrates that chemo-selectively react with the analyte of interest to restore the native luciferin which can then react with its cognate luciferase to produce a bioluminescent signal. Researchers have successfully developed a number of caged D-luciferins, the substrate of firefly luciferase.[18,26–28] However, to the best of our knowledge, only three caged luciferins have been reported using a marine bioluminescent luciferin/luciferase pair.[29–31] Marine bioluminescent systems all share the common imidazopyrazinone luciferin, coelenterazine, that can react with a variety of marine luciferases such as *Renilla*, *Gaussia*, and the engineered Nanoluciferase.[32]

To generate a copper-responsive bioluminescent agent that is compatible with the extracellular environment, we turned to agents derived from the marine bioluminescent systems as they operate independent of ATP, in contrast with the firefly luciferase/luciferin pair which requires ATP as a cofactor. As ATP is in low abundance in the extracellular space, eliminating ATP dependence is for signal sensitivity. Among the marine luciferases and its derivatives, both the naturally-occurring *Gaussia* luciferase and the engineered Nanoluciferase are significantly brighter than firefly luciferase by about 1000 times and 100 times respectively.[32,33] This feature is especially useful when developing probes for analytes that are present in trace amounts like the labile copper pool. Additionally both of these luciferases have been applied to extracellular applications using secreted forms of the enzymes.[34] One the one hand, the intensely bright, *Gaussia* luciferase has extremely low substrate tolerance, only accepting native coelenterazine.[34] On the other hand, a variety of coelenterazine derivatives have been synthesized that are accepted by Nanoluciferase in addition to its engineered substrate, furimazine.[35] We thus explored three different imidazopyrazinone-type compounds as cores for our probe: native coelenterazine (CTZ), coelenterazine 400a (CTZ400a) and diphenylterazine (DTZ) (Figure 2.1).

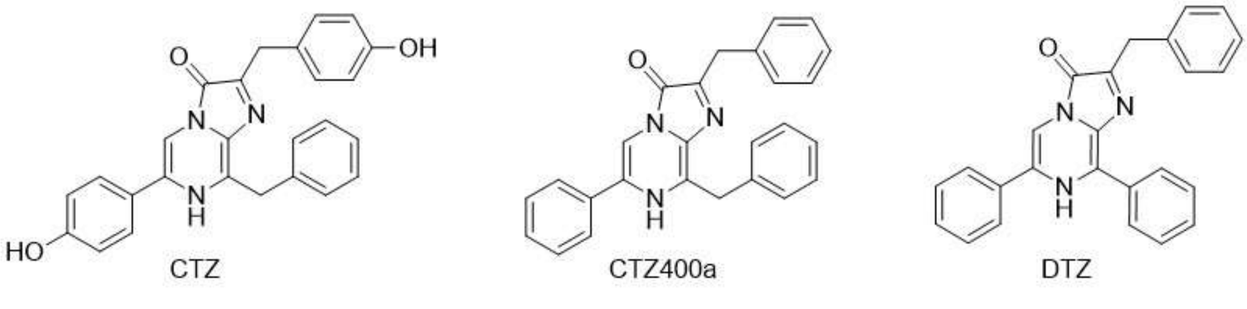

Figure 2.1 Chemical structures of coelenterazine, coelenterazine 400a, and diphenylterazine.

For our cage design we adapted a previously-reported picolinic ester susceptible to hydrolysis by Cu(II).[36] We also explored the potential for other heterocyclic esters, furan and thiophene, to undergo metal mediated hydrolysis. The three heterocyclic ester cage precursors were synthesized as shown in Scheme 2.2 (synthesis for pyridine ester cage is shown in Scheme 2.3) and were subsequently tested for their response to metals by UV-Vis spectroscopy (Figure 2.2).

Scheme 2.2 Synthesis of heterocyclic ester cages.[a]

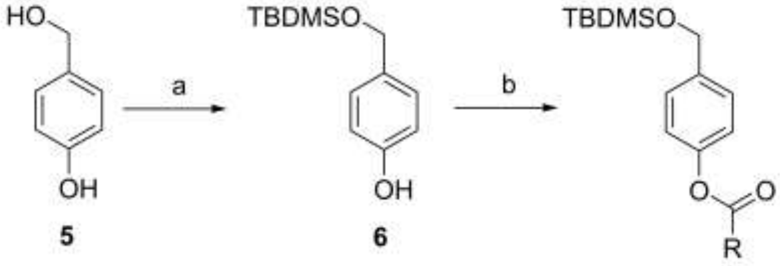

7a: R = 2-thiophene
7b: R = 2-furan

a. Reagents and conditions: (a) TBDMS-Cl, imidazole, DMF, r.t., 30 min; (b) furan-2-carbonyl chloride or thiophene-2-carbonyl chloride, anhyd. pyridine/DMF, r.t., 2 hours.

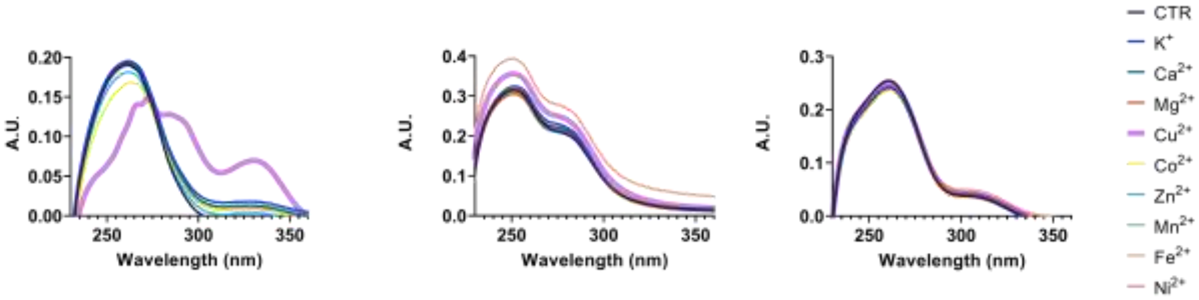

Figure 2.2 UV-Vis spectra of 10 µM (a) pyridine ester 7 (b) thiophene ester 7a, and (c) furan ester 7b in 15 mM MOPS buffer at pH 7.4 in the presence of 25 µM metal salts or a no-metal control (CTR). The marked shift in the spectra of the pyridine ester suggests hydrolysis in the presence of Cu^{2+}; while no distinct reactions are observed with the other two esters.

Consistent with the previous literature, we observed a distinct shift in the spectra of the picolinic ester upon addition of Cu(II) suggesting that the proposed Cu(II)-mediated hydrolysis occurs. However, we saw no changes to the spectra of either the thiophene or the furan ester upon the addition of any of the tested metals. With this information in hand, we proceeded with synthesis of the picolinic ester-caged imidazopyrazinones using the aforementioned cores (Scheme 2.3). It is well-known that these coelenterazine-like compounds readily degrade at ambient temperatures and in the presence of air likely due to the anti-aromatic nature of the lower pyrazine-like ring. To overcome this, researchers have been able to stabilize these compounds while maintaining bioluminescent activity by nucleophilic addition to the carbonyl thereby achieving complete aromaticity of the core.[37] Thus, we chose to conjugate the picolinic ester cage at the carbonyl position. For chemical compatibility, we employed a benzyl ether self-immolative linker.[29]

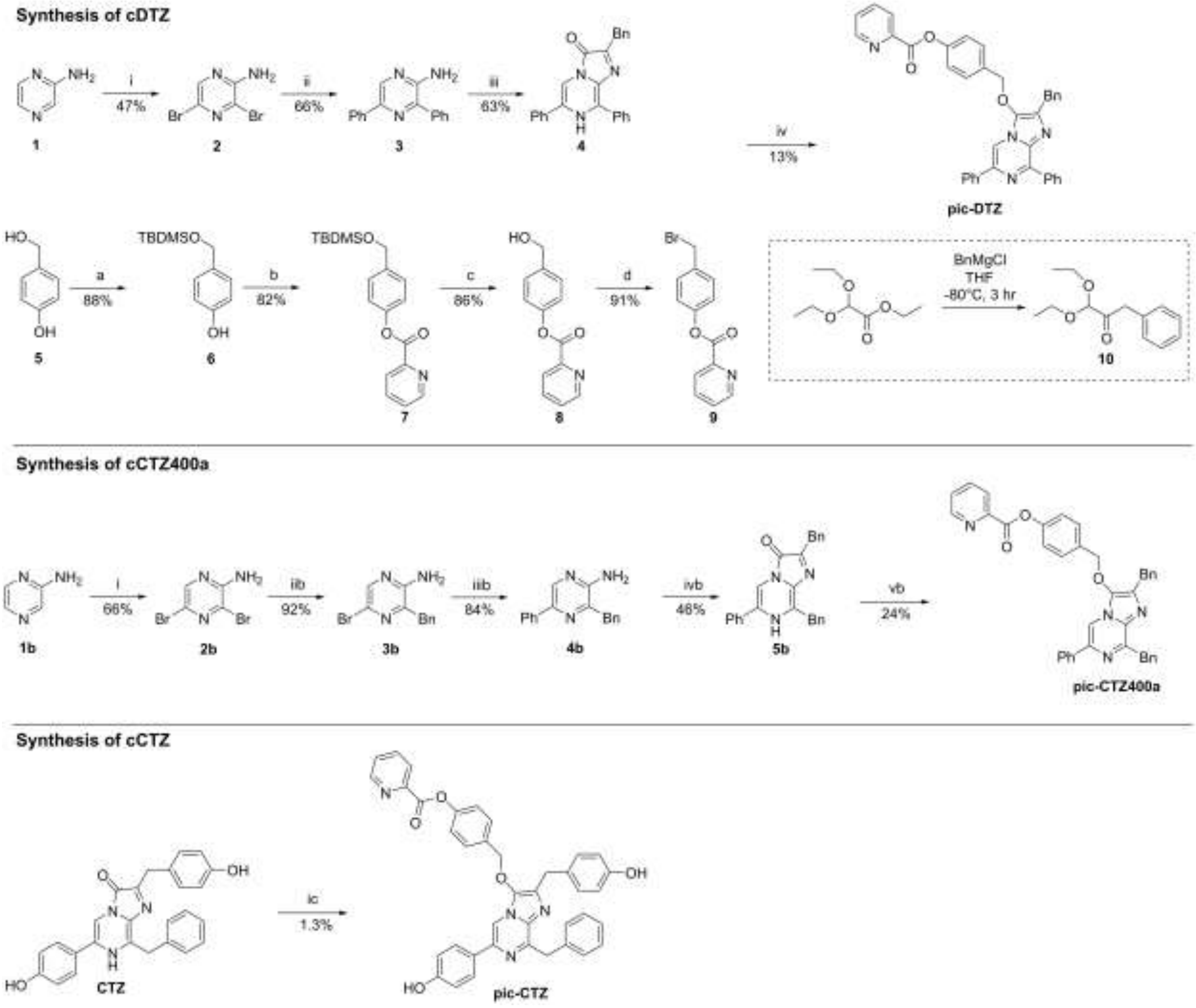

Scheme 2.3 Synthesis of pic-DTZ reagents and conditions: (i) NBS, $CHCl_3$, 3 h; (ii) Phenylyboronic acid, $Pd(PPh_3)_4$, K_2CO_3, Dioxane, H_2O, 80°C, 12 h; (iii) **10**, EtOH, H_2O, cat. HCl, 80°C, 12 h; (a) TBDMS-Cl, imidazole, DMF, r.t., 30 min; (b) 2-picolinic acid, EDCI, cat. DMAP, CH_2Cl_2. r.t., 3 h; (c) MeOH, cat. HCl, r.t., 30 min; (d) PBr_3, THF, r.t., 2 h; (iv) **9**, Cs_2CO_3, KI, MeCN, r.t., 12 h. **Synthesis of pic-CTZ400a reagents and conditions:** (iib) BnBr, Zn, I_2, $Pd(Cl)_2(PPh3)_2$, r.t. 12 h; (iiib) Phenylyboronic acid, $Pd(PPh_3)_4$, K_2CO_3, Dioxane, H_2O, 80°C, 12 h; (ivb) **10**, EtOH, H_2O, cat. HCl, 80°C, 12 h; (vb) MeOH, cat. HCl, r.t., 30 min. **Synthesis of pic-CTZ reagents and conditions:** (ic) MeOH, cat. HCl, r.t., 30 min.

With the three caged imidazopyrazinone compounds in hand we moved on to evaluating their response and selectivity towards Cu(II) in the presence of their cognate luciferases (Figure 2.3).

We assessed pic-DTZ and pic-CTZ400a with recombinant Nanoluciferase (rNluc) and pic-CTZ with *Gaussia* luciferase.

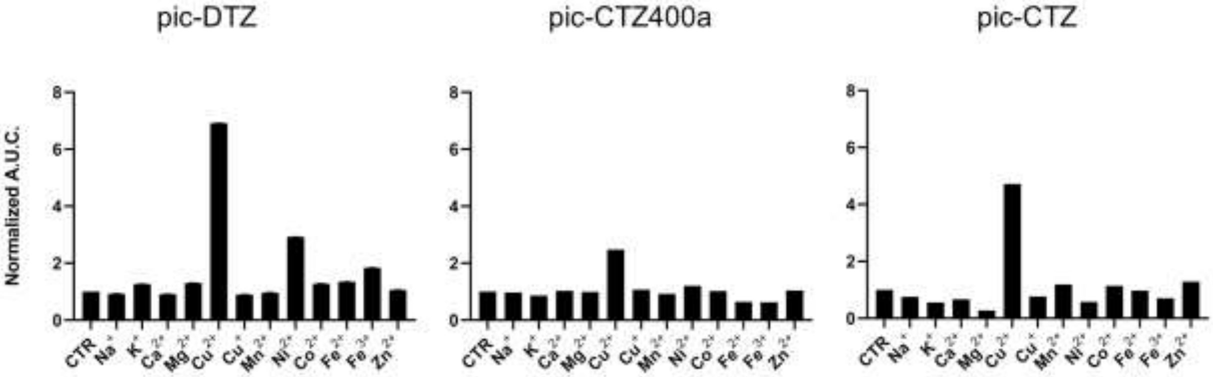

Figure 2.3 Calculated area under the curve of luminescence measured over 20 minutes with 5 µM caged probes in the presence of biologically-relevant d-block (5 µM) and s-block (1 mM) metals. For pic-DTZ and pic-CTZ400a, 120 nM rNluc was used. For pic-CTZ, 425 nM recombinant *Gaussia* luciferase was used.

pic-DTZ in the presence of rNluc exhibits a stronger intensity in signal (recorded over 20 minutes) relative to either pic-CTZ400a and pic-CTZ. Additionally, although pic-CTZ400a did show Cu(II)-selective light output, the signal-to-background ratio is much lower compared to either pic-DTZ or pic-CTZ. It should also be noted that access to native coelenterazine is more synthetically challenging relative to the other two imidazopyrazinones tested. Indeed, the yield for the caged CTZ was so low we were unable to get a reasonable carbon NMR spectra and even the proton NMR displayed low signal to noise. For these reasons, we chose to move forward with pic-DTZ as the probe of choice

2.2.2 Reactivity and Cu(II) Selectivity of pic-DTZ in Aqueous Buffer with Recombinant Nluc (rNluc)

The chemo-selectivity of pic-DTZ was evaluated by reacting various analytes with the probe in aqueous buffer (DPBS, pH 7.4), then monitoring enzymatic conversion with recombinant Nluc (rNluc). Figure 2.4 shows both the kinetic luminescence spectra as well as the selecitivity panel shown in Figure 2.3.

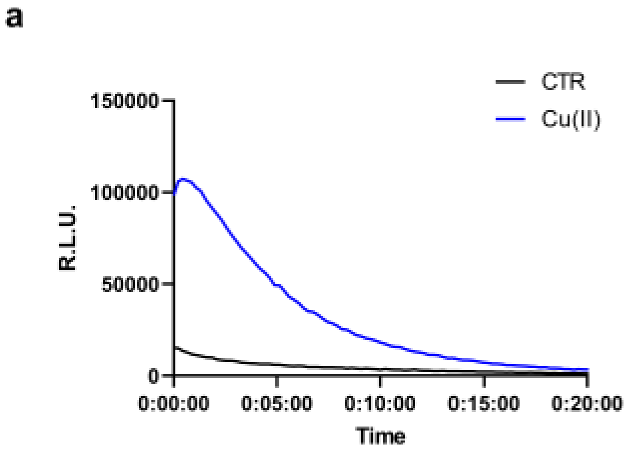

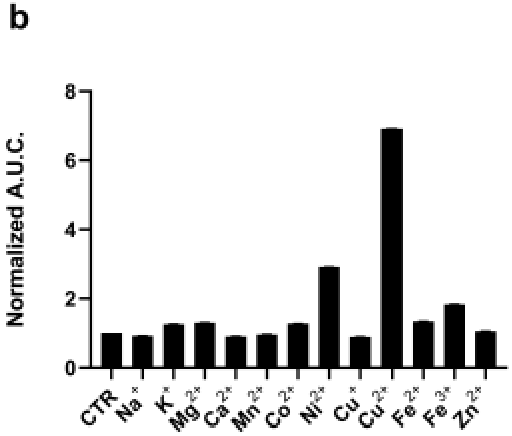

Figure 2.4 (a) Representative kinetic curve of luminescence of 5 µM pic-DTZ with or without the addition of 5 µM Cu(II) in the presence of 120 nM rNluc. The control treatment (CTR) refers to the same conditions but with no metal salt added (b) Calculated area under the curve for luminescence over 20 minutes of 5 µM pic-DTZ in the presence of biologically relevant d-block (5 µM) and s-block (1 mM) metals. Data points are normalized to signal of pic-DTZ without metal addition. Error bar denotes SEM, n=3.

When exposed to Cu(II), pic-DTZ exhibits an immediate seven-fold increase in luminescence relative to control treatment with no metal (CTR), demonstrating efficient uncaging in the presence of free Cu(II) (Figure 2.4). When monitoring the reactivity of the cage by ultraviolet-visible (UV-Vis) spectrophotometry, we observe a distinct change of the peak at 266 nm towards a spectrum with two absorbance maxima at 280 nm and 345 nm, suggesting hydrolysis of the picolinic ester (Figure 2.2). We further validated that Cu(II)-mediated hydrolysis of pic-DTZ releases the parent DTZ by monitoring the reaction using liquid chromatography (Figure 2.5).

We observe that in the presence of excess $CuSO_4$, pic-DTZ is immediately hydrolyzed to DTZ. Furthermore, in the presence of sub-stoichiometric amounts of $CuSO_4$ (1:10 Cu(II):pic-DTZ) we also observe partial conversion to native DTZ albeit over four hours suggesting that Cu(II) is not acting catalytically.

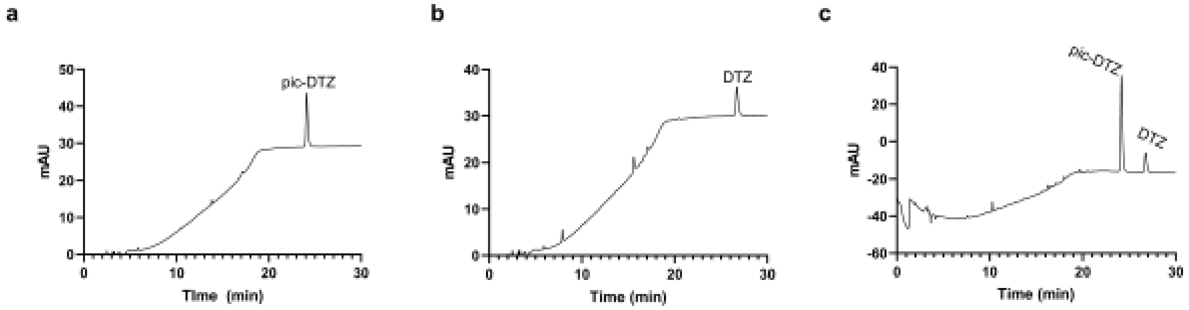

Figure 2.5 LCMS chromatograms of (a) pic-DTZ (50 µM) alone (b) pic-DTZ (50 µM) immediately after addition of 1 mM Cu(II) and (c) pic-DTZ (50 µM) 4 hours after addition of 5 µM Cu(II), monitored at 250 nm. All LCMS samples were prepared methanol. A gradient was run from 90:10 H_2O:MeCN + 0.1% FA to 10:90 H_2O:MeCN + 0.1% FA over 15 minutes, then held at 10:90 H_2O:MeCN + 0.1% FA for 15 minutes. Peak labeled "pic-DTZ" corresponds to m/z of 589.2 corresponding to $[M+H]^+$ and peak labeled "DTZ" corresponds to m/z of 376.2 corresponding to a salt form of DTZ.

Furthermore, a dose dependence is observed of pic-DTZ from 0 to 10 µM Cu(II) until signal saturation is reached (Figure 2.6). Taken together, these results provide evidence for pic-DTZ applicability towards monitoring low concentrations of copper. In line with previously suggested mechanisms of copper-induced hydrolysis, pic-DTZ turn-on likely results from Cu(II) coordination to the pyridine nitrogen, with the carbonyl acting as a Lewis acid thereby increasing the susceptibility of the ester to nucleophilic attack.[38]

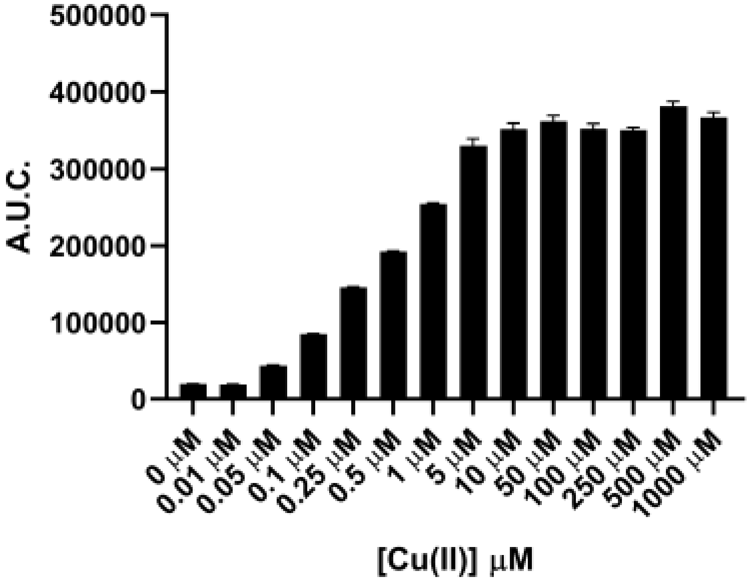

Figure 2.6 Dose-dependence of pic-DTZ (1 µM) with varying concentrations of Cu(II) in the presence of 120 nM rNluc.

Next we evaluated the selectivity of pic-DTZ for Cu(II) over other biologically-relevant metals including transition, alkali, and alkaline earth metals (Figure 2.4 b). The data shows that pic-DTZ demonstrates selectivity for Cu(II) over any of the other metals. Although a slight turn-on is observed in the presence of Ni(II). serum levels of Ni(II) are estimated from 4 nM to 0.8 µM relative to Cu(II) at 16 µM.[17,39] Additionally, a labile nickel pool has not yet been observed or characterized in mammalian systems. In addition to metal selectivity, pic-DTZ exhibits an oxidation-state specific response to Cu(II) with no detectable turn-on in the presence of Cu(I). Lastly, we investigated the effect of pH on the efficiency of Cu(II)-mediated uncaging. Because conversion from pic-DTZ to DTZ requires self-immolation of the phenolate generated upon hydrolysis of the picolinate we suspected that this would be a pH-sensitive process. We observed Cu(II)-induced turn on at pH 6.2, 7.0, and 8.8 with increasing light output with increases in pH likely due to stabilization of the phenolate and subsequent self-immolation (Figure 2.7).

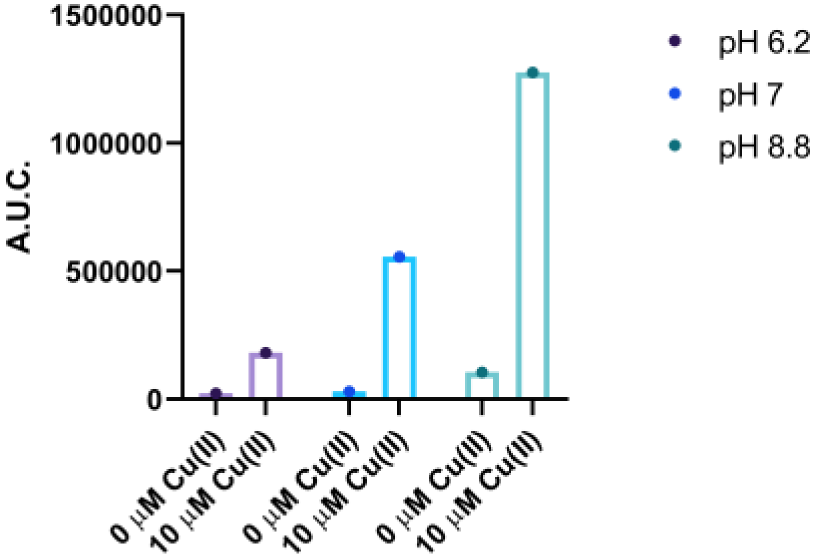

Figure 2.7 Calculated area under the curve for luminescence over 20 minutes of 1 µM pic-DTZ in the presence of 120 nM rNluc at various pHs in DPBS.

2.2.3 Application of pic-DTZ to Measure Copper Levels in Human Serum and Plasma

We next evaluated the capacity of pic-DTZ to detect labile Cu(II) pools over tightly-bound populations in serum and plasma (Figure 2.8 a). Detection of Cu(II) in biological fluids by optical methods are challenging due to the high background of these media from autofluorescence of its components in the UV/visible excitation and emission ranges.[17] We reasoned that our system could overcome these challenges given the near-zero background signal of bioluminescence imaging.[40] We first determined whether holo-ceruloplasmin (copper-bound form of the protein), the major carrier of Cu(II) in the blood, would interfere with labile Cu(II) detection by pic-DTZ. While ceruloplasmin carries anywhere from 50-90% of serum copper, they are tightly-bound.[41] When pic-DTZ is added to holo-ceruloplasmin at a physiologically relevant concentration in the presence of rNluc, only a slight turn-on response was observed relative to the control (Figure 2.8 a), suggesting that pic-DTZ does not detect static copper pools. We also assessed the response of pic-DTZ to serum albumin. While Cu(II)-bound albumin contributes to the labile extracellular pool, copper-free albumin has been shown to non-specifically oxidize coelenterazine, the core from which DTZ is derived.[42] However, pic-DTZ again displayed only a slight turn-on response with copper-free albumin in the presence of rNluc, showing that this particular system is not susceptible to significant auto-oxidation by albumin.

We then applied pic-DTZ to a 10% solution of pooled human serum. A strong luminescent response was observed, suggesting that pic-DTZ can detect a copper pool that is distinct from that of ceruloplasmin. To characterize this pool, we performed a study with copper-loaded biological chelators to assess if pic-DTZ can turn-on in the presence of bound-copper species (Figure 2.8 b). We loaded the tripeptide GHK (10 μM), histidine (10 μM), and albumin (100 μM) with Cu(II) in a 1:1 molar ratio and observed in all cases that pic-DTZ was still able to turn on suggesting that pic-DTZ is able to detect reactive copper species that are bound by these chaperones.

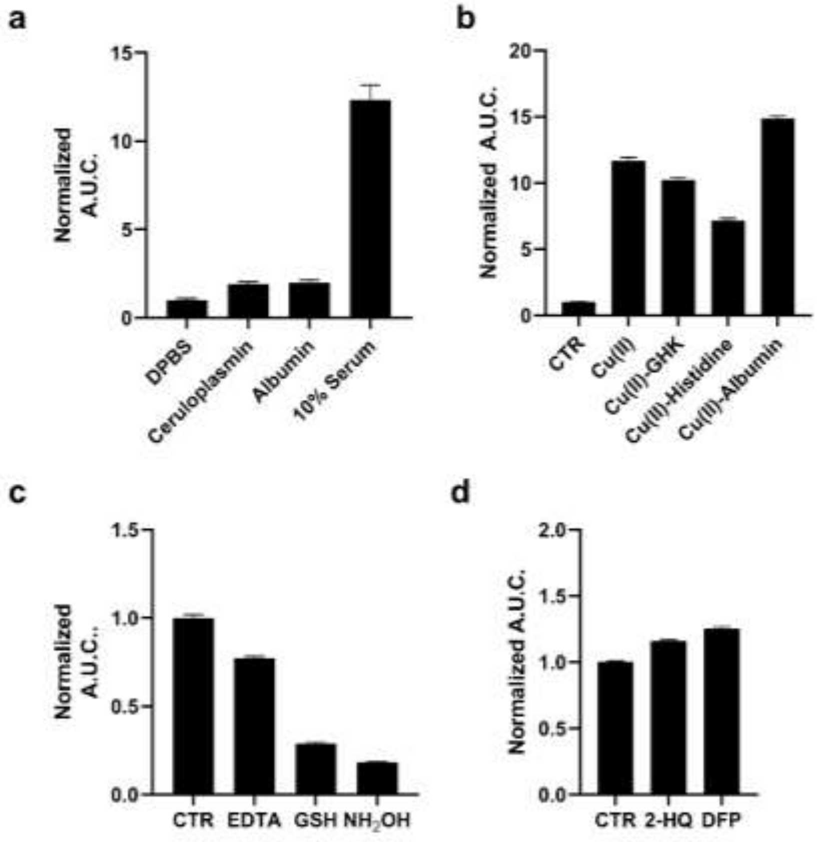

Figure 2.8 (a) Calculated area under the curve of luminescence taken over 20 minutes of 1 µM pic-DTZ in the presence of holo-ceruloplasmin (1000 mU/mL), albumin (645 µM), or 10% pooled human serum in DPBS with 100 nM rNluc. (b) Calculated area under the curve of luminescence taken over 20 minutes of 1 µM pic-DTZ in the presence of Cu(II) (10 µM), Cu(II)-GHK (10:10 µM), Cu(II)-Histidine (10:10 µM), and Cu(II)-Albumin (100:100 µM) with 100 nM rNluc. (c) Calculated area under the curve of luminescence taken over 20 minutes of 1 µM pic-DTZ in 10% pooled human serum with EDTA (1 mM), GSH (200 µM), or NH$_2$OH (200 µM) with 100 nM rNluc. (d) Calculated area under the curve of luminescence taken over 20 minutes of 1 µM pic-DTZ in 10% pooled human serum with esterase inhibitors 2-HQ and DFP (5 µM) with 100 nm rNluc. For a-d above error bars denote SEM, n=3.

Controls with GHK and histidine alone at this concentration showed little to no effect relative to the control (Figure 2.9). Although a slight turn-on is observed at the concentration of apo-albumin tested for this particular experiment (100 µM), the turn-on of pic-DTZ by holo-albumin at this same concentration is significantly higher (Figure 2.10).

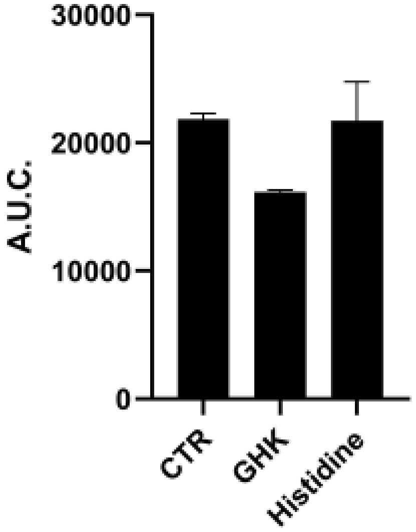

Figure 2.9 Calculated area under the curve over 20 minutes of 1 µM pic-DTZ in the presence of GHK and histidine (10 µM) with 120 nM rNluc. Error bars denote SEM, n = 3.

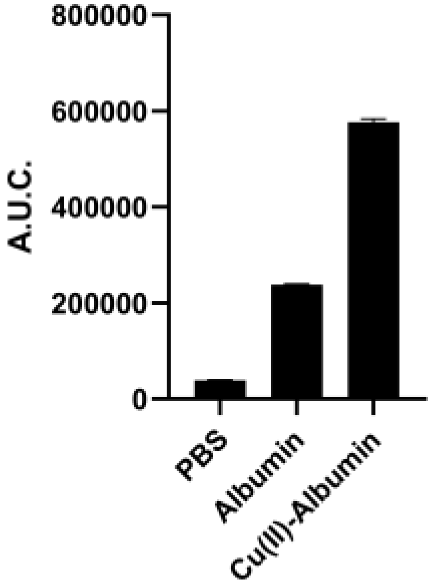

Figure 2.10 Calculated area under the curve over 20 minutes of 1 µM pic-DTZ in the presence of albumin (100 µM) or copper loaded albumin (1:1 molar ratio, 100 µM) with 120 nM rNluc. Error bars denote SEM, n = 3.

To further validate that the observed signal in pooled human serum is resulting from reaction of pic-DTZ with Cu(II) we used the chelator, EDTA, and two reductants, glutathione (GSH) and hydroxylamine (NH_2OH), to reduce Cu(II) to Cu(I) as Cu(I) would not readily hydrolyze the picolinate cage (Figure 2.8 c). As expected, EDTA and both reductants attenuated the turn-on response. Similar assays in buffer alone (in the absence of serum) had no effect on pic-DTZ activity, showing that EDTA and the reductants affect a pool of analytes that is present in serum (Figure 2.11).

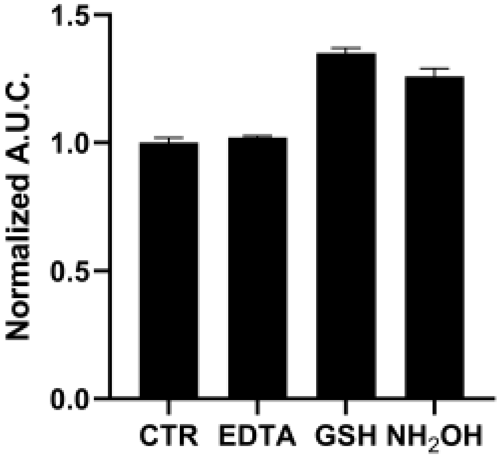

Figure 2.11 Calculated area under the curve over 20 minutes of 1 µM pic-DTZ in the presence of EDTA (1 mM), GSH (200 µM), or NH_2OH (200 µM) with 120 nM rNluc. Error bars denote SEM, n = 3.

Lastly, as esterases are present in serum, we assessed whether such enzymes could interfere with pic-DTZ. We tested pic-DTZ's susceptibility to esterase activity by evaluating pic-DTZ signal in serum in the presence of diisopropylfluorophosphate (DFP) and 2-hydroxyquinoline (2-HQ), inhibitors for the two major plasma esterase's, butyrylcholinesterase (BChE) and paraoxonase (PON1), respectively (Figure 2.8 d).[43] The inhibitors did not decrease light output relative to the control serum, suggesting that the esterase activity does not interfere with pic-DTZ reactivity.

Taken together, this data further suggests that the observed signal in serum is resulting from reaction of pic-DTZ with a pool of copper that is coordinatively unsaturated and accessible for reaction with pic-DTZ, which we term here as “reactive”.

Having observed the applicability of pic-DTZ for detecting reactive copper in serum, we assessed whether the probe could distinguish differences in labile plasma copper levels between individuals with WD and healthy individuals (Figure 2.12). In WD, due to the absence of functional ATP7B, copper-free ceruloplasmin fails to mature properly in the hepatocytes and is rapidly degraded. Elevated levels of non-ceruloplasmin-bound copper is secreted from the hepatocytes into systemic circulation.[44] The beneficial effects of chelation therapy in patients with WD suggest that this secreted copper is a labile pool. Serum ceruloplasmin levels are widely used as a screening and diagnostic test in WD, but this can lead to false negatives as most of these clinically-available assays do not distinguish between copper-bound and copper-free forms of the protein.[45] Other diagnostic methods include determination of 24-hour urinary copper excretion and serum "free" copper levels. Serum "free" copper has classically been estimated via The Walshe’s index by calculating the difference between total copper, determined by ICP-MS, and ceruloplasmin-bound copper.[46] This index assumes that the measured ceruloplasmin is fully loaded with 6 copper atoms, and is therefore susceptible to over-estimation of copper-bound ceruloplasmin and underestimation of serum "free" copper. We reasoned that pic-DTZ could overcome these challenges by providing a direct means for detecting reactive copper(II) in human plasma. Addition of pic-DTZ to the plasma of healthy controls and individuals with WD resulted in a significant ($P < 0.05$) elevation in bioluminescent response in the plasma of WD individuals (Figure 2.12 c).

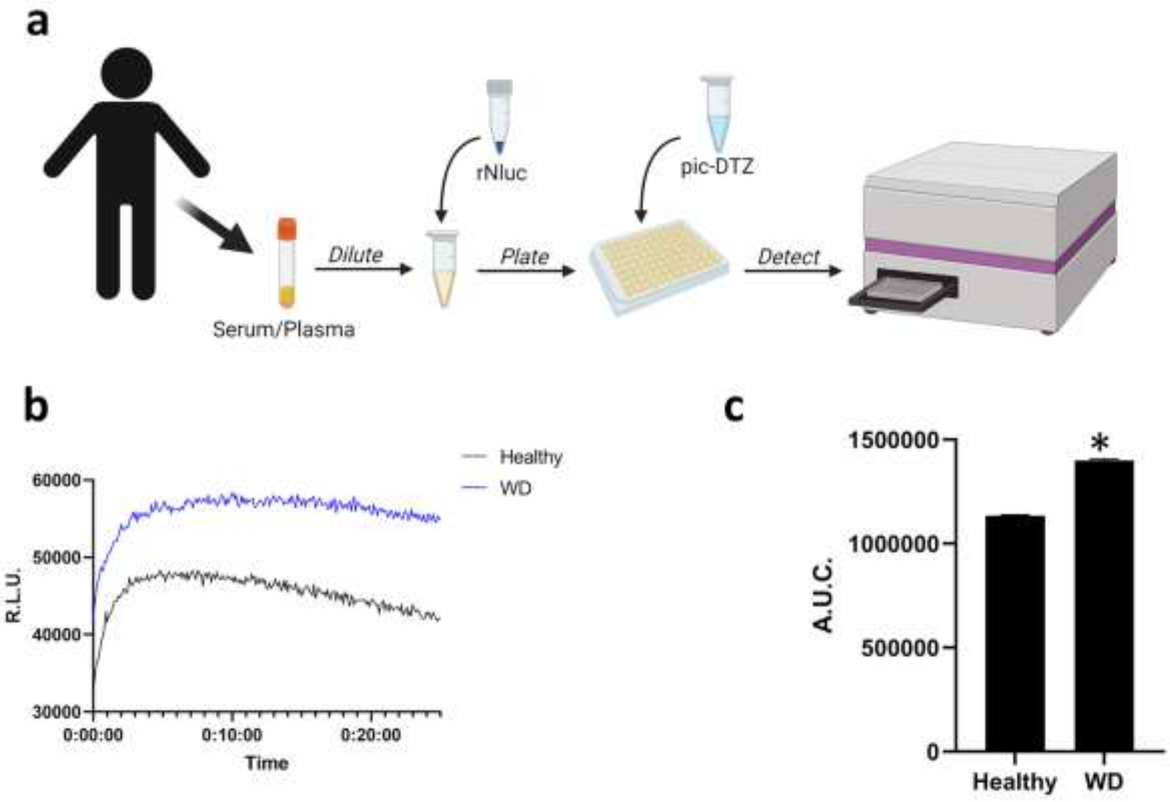

Figure 2.12 (a) Workflow for applying pic-DTZ for monitoring of labile copper status in human serum samples (figured created with BioRender.com) (b) Representative kinetic curve of luminescence and (c) calculated area under the curve of luminescence over 20 minutes of plasma (diluted to 10% in DPBS) from healthy individuals or patients with Wilson disease analyzed by addition of 1 µM pic-DTZ and 100 nM recombinant Nanoluciferase. Error bar denotes SEM, n=3. Statistical significance was assessed by calculating *p*-values using unpaired t-test, * $p < 0.05$

Notably, the serum albumin levels as well as overall protein levels between cohorts remained the same as would be expected suggesting that the observed changes in light output with pic-DTZ are indeed copper-dependent and not due to global changes (Figure 2.13). This demonstrates the probe's potential utility as a direct means of monitoring labile copper in serum and its potential as an alternative diagnostic tool for copper metabolism disorders.

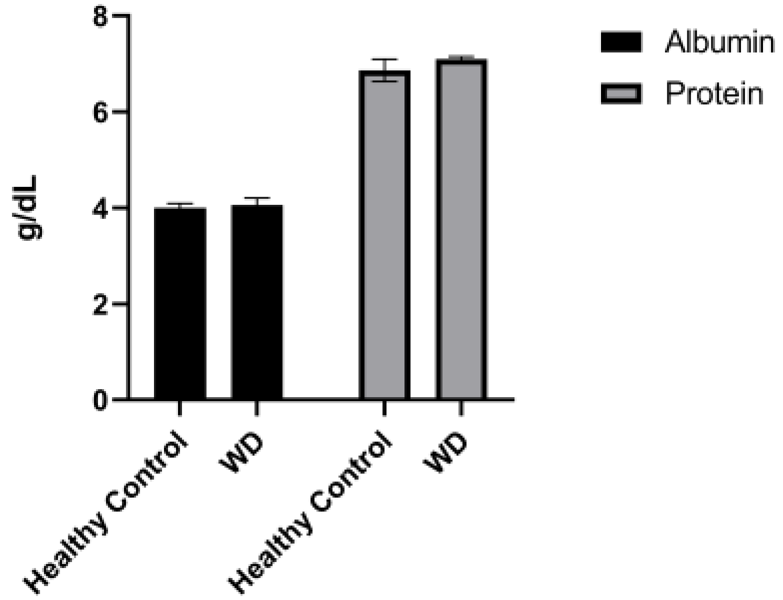

Figure 2.13 Clinically determined albumin and overall protein levels of healthy control and Wilson's diseased (WD) cohorts. Error bars denote SEM, n=3.

2.2.4 Monitoring Extracellular Copper(II) in Response to Anti-cancer Agents

Copper has long been connected to cancer, with recent years identifying molecular mechanisms responsible for this interplay in a framework termed cuproplasia (copper-dependent cell proliferation).[47] Stemming from these connections, chemicals that can chelate copper or modify copper trafficking pathways are emerging as potential cancer therapeutic agents.[48,49,50,51,52] These copper-associated anticancer agents have been proposed to work via different mechanisms that perturb overall copper bioavailability to the cell, including extracellular chelation, intracellular depletion, and disrupting molecular pathways to alter metal distribution.[53] However, studies that directly monitor the extracellular copper availability with these treatments remain sparse, and research has primarily focused on monitoring intracellular copper concomitant with tumor growth. We therefore explored the utility of pic-DTZ towards monitoring extracellular copper status of a metastatic breast cancer cell line, MDA-MB-231, stably expressing secreted Nluc (secNluc MDA-MB-231) in response to these agents (Figure 2.14).

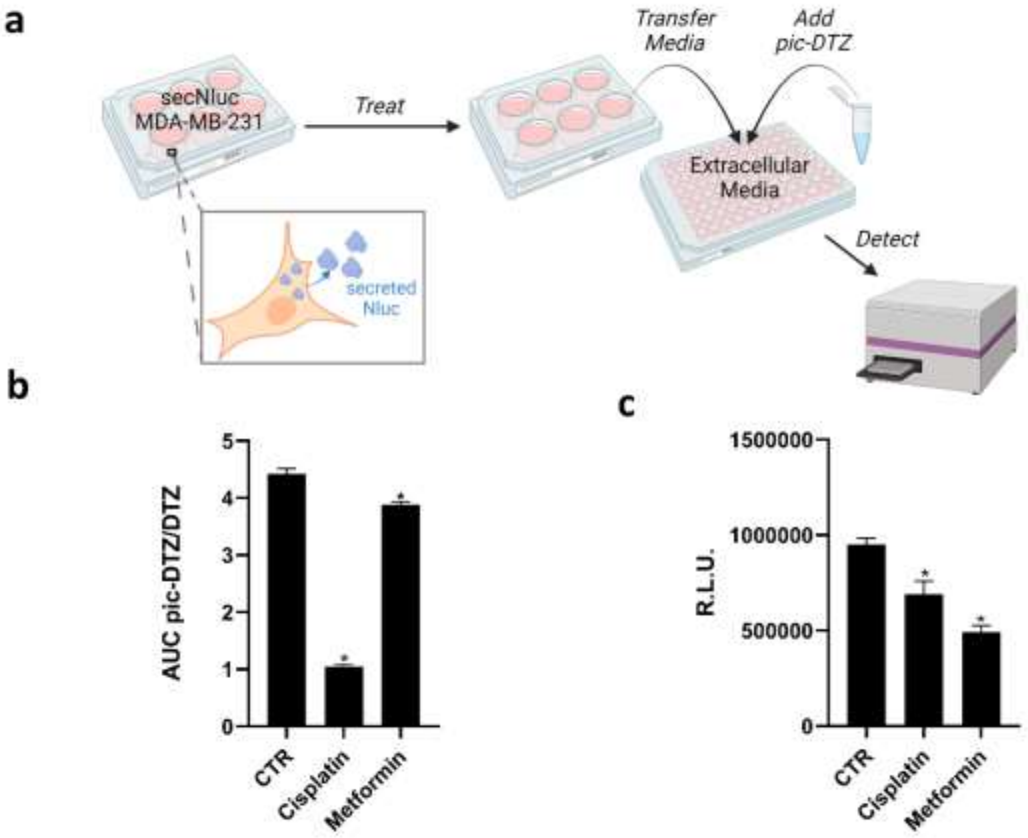

Figure 2.14 (a) Experimental workflow for applying pic-DTZ to monitoring extracellular copper in a breast cancer cell model. (Figure created with BioRender.com) (b) Calculated ratio of the area under the curve over 20 minutes of pic-DTZ:DTZ luminescence from secNluc MDA-MB-231 cells treated with a screen of cancer-associated agents reported to perturb copper metabolism: 30 µM cisplatin and 5 mM metformin. Error bars denote SEM, n=3. Statistical significance was assessed by calculating *p*-values using unpaired t-test, * $p < 0.05$. (c) Cell viability in response to the cancer-associated agents in Figure 4b as determined by CellTiter-Glo assay (Promega). Error bars denote SEM, (n=4). Statistical significance was assessed by calculating *p*-values using unpaired t-test, * $p < 0.05$.

Specifically, we assessed response to cisplatin, a well-established chemotherapy drug that has been shown to interfere with and hijack intracellular copper trafficking mechanisms;[54,55] and metformin, an antidiabetic agent under consideration for cancer therapy and prevention, that has been shown to complex to and potentially rely on copper for its drug action.[56] Although these agents have been associated with copper, little is known about their effects on extracellular copper populations. We treated cells with these agents using concentrations based on previous reports[56,57,58] for 18 hours in a 96-well plate, followed by addition of either pic-DTZ or the parent DTZ. Luminescence was recorded and the area under the curve (AUC) was calculated. The data was analyzed using the ratios of the AUC pic-DTZ:DTZ to normalize any effects the treatments may have on cell viability or secNluc expression. (Figure 2.14 b). We confirmed that neither compound interfered with pic-DTZ signal in the presence or absence of exogenous Cu(II) (Figure 2.15).

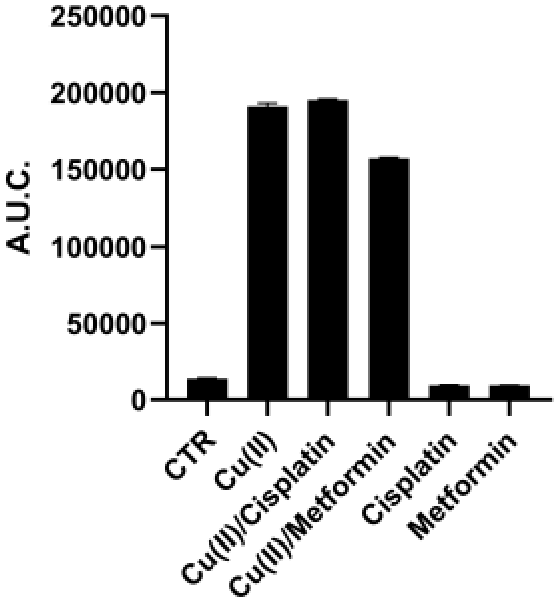

Figure 2.15 Calculated area under the curve over 20 minutes of 1 µM pic-DTZ in the presence of Cu(II) (10 µM) or cisplatin and metformin (30 µM and 5 mM respectively) with or without 10 µM Cu(II) and 125 nM rNluc. Error bars denote SEM, n = 3.

Both treatments showed significant decreases in extracellular copper-dependent signal but cisplatin treatment exhibited the most notable decrease in signal. Recent work by Akerfeldt et al. showed that the complex increases cytosolic copper availability.[50] Our findings may complement this observation if this increase in intracellular copper stems from increased trafficking of copper from the extracellular to intracellular space. We further characterized the effects of the tested treatments by monitoring changes in protein expression of various copper-trafficking proteins via western blotting (Figure 2.16) and observed that cisplatin induced the strongest changes in protein expression relative to the untreated control in line with the observed drastic decrease in light output observed with pic-DTZ of cisplatin treated cells.

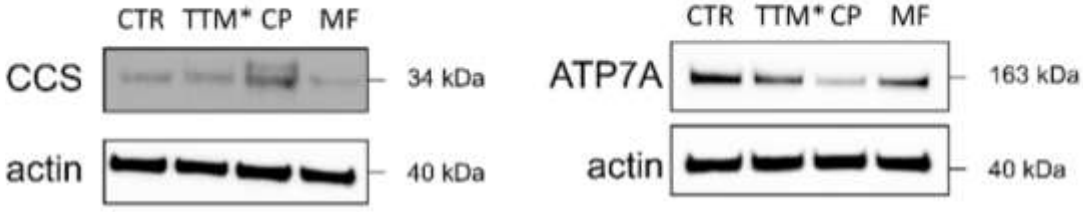

Figure 2.16 Western blot analysis of the copper chaperone for superoxide dismutase (CCS), and the copper transporter ATP7A, from cell lysates of secNluc MDA-MB-231 cells treated with 30 μM cisplatin (CP) or 5 mM metformin (MF) compared to untreated control (CTR). *TTM is included as a copper chelation control for the western blot experiments, but is not assessed with pic-DTZ as we observed light inhibition with native DTZ in the presence of TTM.

Interestingly, analysis of the cell media after treatment by ICP-MS showed no significant changes in total copper levels between the treated cells and untreated controls (Figure 2.17), suggesting that while total copper levels may not be significantly altered, the treatments may perturb a subpopulation of copper that is detectable with pic-DTZ.

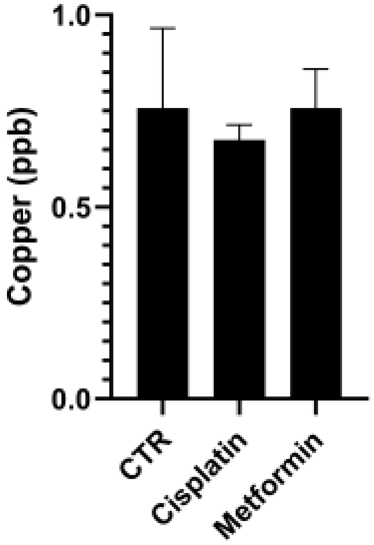

Figure 2.17 ICP-MS quantification of copper from cell media removed from secNluc MDA-MB-231 cells after treatment for 18 hours by cisplatin (30 µM) or metformin (5 mM) relative to untreated control (CTR). Error bars denote SEM, n=3.

Lastly, the copper-responsive signals were distinct from bioluminescent response from the same treatments monitored with CellTiter Glo (Figure 2.14 c). CellTiter Glo is a widely used assay for measuring cell viability using the firefly luciferase system. The differential response between this bioluminescence-based cell viability assay and our pic-DTZ system shows the potential for bioluminescence multiplexing for high-throughput screening of copper-perturbing agents.

2.4 Conclusions and Outlook

We have demonstrated the design, synthesis, characterization, and biological application of pic-DTZ, a new bioluminescent imaging probe for labile, extracellular Cu(II) pools. To the best of our knowledge, the pic-DTZ/Nluc system is the first such caged imidazopyrazinone probe paired with the bright, thermostable Nluc as well as the first bioluminescent imaging probe for directly monitoring Cu(II) in the extracellular space. pic-DTZ is metal- and redox state-specific for Cu(II) in aqueous buffer with rNluc and can differentiate plasma copper levels in clinical samples. Additionally, the probe system can be easily applied to a 96-well format for cell-based assaying of extracellular copper. We also show that that pic-DTZ can be integrated into existing workflows and be multiplexed with existing firefly luciferase-based assays.

pic-DTZ offers unique advantages over traditionally explored methods of monitoring labile, extracellular copper. For example, pic-DTZ requires no excitation light source resulting in high signal-to-background ratios that are ideal for monitoring trace analytes like labile metal micronutrient pools. The reaction-based nature of pic-DTZ allows for signal amplification through the catalytic use of Cu(II) relative to turn-on/turn-off probes. Paired with the locale-specificity afforded by genetically encoding Nluc we envision that pic-DTZ has immense potential for application in live-animal models alongside emerging Nluc applications.

2.5 Materials and Methods

General Methods. Reactions using moisture- or air-sensitive reagents were carried out in dried glassware under an inert N_2 atmosphere . Dry solvents were all purchased from Sigma-Aldrich (St. Louis, MO) and used immediately. All commercially purchased chemicals were used as received without further purification. 2-aminopyrazine was purchased from Oakwood Products, Inc. (Estill, SC); all other chemicals were purchased from Sigma-Aldrich. Silica Gel 60 F254 (precoated sheets, 200 µm thickness, MilliporeSigma) were used for analytical thin layer chromatography. Silica gel sorbent (230-400 mesh, grade 60, ThermoFisher) or aluminum oxide (neutral, Brockmann I, 50-200 µm, grade 60, Sigma-Aldrich) were used for column chromatography. ^{1}H and ^{13}C NMR spectra were collected at room temperature in $CDCl_3$, DMSO-d_6 or CD_2Cl_2 (Sigma-Aldrich) on a 400 or 800 MHz Bruker or 600 MHz Varian NMR spectrometer. All chemical shifts are reported as δ parts per million relative to the residual solvent peak at 7.26 ($CDCl_3$), 2.50 (DMSO-d_6), or 5.32 (CD_2Cl_2) for ^{1}H and 77.16 ($CDCl_3$), 39.52 (DMSO-d_6) or 53.84 (CD_2Cl_2) for ^{13}C. Multiplicities are reported as s (singlet), d (doublet), t (triplet), q (quartet), p (pentet), h (hextet), m (multiplet), dt (doublet of triplets), or br (broad). Electrospray ionization mass spectral analyses were performed using an LC-MSD system (Agilent Technologies 1260 Infinity II coupled with an Agilent Technologies InfinityLab LC/MSD).

2.5.1 Synthesis of pic-DTZ

2-amino-3,5-dibromopyrazine, 2. 2-aminopyrazine (2.00 g, 21.92 mmol, 1 equiv.) and N-bromosuccinimide (7.86 g, 44.14 mmol, 2.1 equiv.) were dissolved in chloroform (45 mL). The reaction was allowed to stir at room temperature for three hours. It was then quenched with water and extracted with EtOAc (3 X 25 mL), washed with saturated sodium bicarbonate (5 X 100 mL), dried over Na_2SO_4, and concentrated in vacuo to yield **3** (2.51 g, 47%) as a pale brown solid. ^{1}H NMR (400 MHz, $CDCl_3$) δ 8.04 (s, 1H), 5.05 (br, 2H). Low-resolution mass spectrometry (LRMS) (*m/z*): $[M+H]^+$ calculated for : $C_4H_4Br_2N_3$, 253.88; found, 253.8

3,5-diphenyl-2-aminopyrazine, 3. 2-amino-3,5-dibromopyrazine, **2**, (812 mg, 3.22 mmol, 1 equiv.), phenylboronic acid (863 mg, 7.08 mmol, 2 equiv), $Pd(PPh_3)_4$ (373 mg, 0.322 mmol, 0.1 equiv.), and K_2CO_3 (1.450 g, 10.5 mmol, 3.25 equiv.) were added to a flame-dried 250 mL round- bottom flask purged with N_2. 1,4-dioxane (65 mL) and water (15 mL) were added to the flask and the reaction mixture was heated to 80 ºC. The reaction was allowed to stir for 12 hours before being quenched with water and extracted with DCM (3 X 25 mL), washed with brine, dried over), dried over Na_2SO_4, and concentrated in vacuo. The crude product was then purified by silica gel chromatography (60/40 Heptanes/EtOAc). Combined product fractions were concentrated under reduced pressure to yield **4** (525 mg, 66%) as a green-brown solid. ^1H NMR (400 MHz, $CDCl_3$) δ 8.46 (s, 1H), 7.98 (d, 2H), 7.84 (d, 2H), 7.53 (t, 2H), 7.50 – 7.41 (m, 3H), 7.41 – 7.35 (m, 1H), 4.84 (s, 2H). Low-resolution mass spectrometry (LRMS) (*m/z*): $[M+H]^+$ calculated for : $C_{16}H_{14}N_3$, 248.12; found, 248.1.

1,1-diethoxy-3-phenylpropan-2-one, 10. Ethyl diethoxyacetate (1.00 g, 5.68 mmol, 1 equiv.) was dissolved in THF (12 mL) and added to a flame-dried round-bottom flask purged with N_2. It was then cooled to -78 ºC (dry ice-acetone bath). To the mixture was added benzyl magnesium chloride (2 M solution in THF, 1.28 g, 4.26 mL, 1.5 equiv.) dropwise. The reaction was allowed to stir for two hours and then quenched with saturated NH_4Cl solution. The reaction was then extracted with ethyl acetate (3 X 25 mL). The combined organic extract was washed with brine, dried over Na_2SO_4, and concentrated in vacuo. The crude product was used without further purification.

Diphenylterazine, 4. 3,5-diphenyl-2-aminopyrazine, **3**, (0.240 g, 0.889 mmol, 1 equiv.) and 1,1-diethoxy-3-phenylpropan-2-one, **10**, were added to a N2-purged round-bottom flask followed by ethanol (11 mL), water (2 mL), and hydrochloric acid (0.2 mL). The reaction was then refluxed overnight. The reaction was then concentrated under reduced pressure and purified on an alumina gel column (gradient 0-10% MeOH in DCM) to afford **4** (211 mg, 63%) of pure product as a pale brown solid. ^1H NMR (400 MHz, DMSO) δ 8.73 (s, 1H), 8.54 (s, 2H), 8.19 (d, 2H), 7.57-7.64 (m, 3H) 7.51-.755 (t, 2H), 7.42-7.46 (t, 1H), 7.27-7.33 (m, 4 H), 7.16-7.20 (t, 1 H), 4.24 (s, 2H). Low-resolution mass spectrometry (LRMS) (*m/z*): $[M+H]^+$ calculated for : $C_{25}H_{20}N_3O$, 378.16; found, 378.1.

4-(((tert-butyldimethylsilyl)oxy)methyl)phenol, 6. 4-hydroxybenzyl alcohol (1.00 g, 8.06 mmol, 1 equiv.), TBDMS-Cl (1.58 g, 10.47 mmol, 1.3 equiv.) and imidazole (1.31 g, 19.3 mmol, 2.6 equiv.) were added to a dry round-bottom flask and dissolved in DMF (5 mL) and allowed to stir under ambient conditions for 1 hour. The reaction was then quenched in water and extracted with ethyl acetate (3 x 25 mL). The combined ethyl acetate extracts were then washed with 0.1 M HCl (1X 50 mL), sat. $NaHCO_3$ (1 X 50 mL) and then brine (1 X 50 mL) and then dried over Na_2SO_4 and concentrated under reduced pressure. The crude product was then purified by silica gel column chromatography (50/50 hexanes/EtOAc) to afford **6** (1.7 g, 88% yield) as a pale-yellow oil. ^1H NMR (400 MHz, $CDCl_3$) δ 7.18 (d, 2H), 6.79 (d, 2H), 4.67 (s, 2H), 0.94 (s, 9H), 0.10 (s, 6H). ^{13}C NMR (100 MHz, $CDCl_3$) δ 155.01, 133.27, 127.99, 115.29, 77.48, 65.02, 26.12, 18.99, -5.04. Low-resolution mass spectrometry (LRMS) (*m/z*): $[M+H]^+$ calculated for : $C_{13}H_{23}O_2Si$, 239.15; found, 239.1.

4-(((tert-butyldimethylsilyl)oxy)methyl)phenyl picolinate, 7. 4-(((tert-butyldimethylsilyl)oxy)methyl)phenol, **6**, (1.46 g, 5.71 mmol, 1 equiv.), 2-picolinic acid (0.878 g, 7.13 mmol, 1.25 equiv.), EDCI (1.37 g, 7.13 mmol, 1.25 equiv.), and DMAP (0.261 g, 2.14 mmol, 0.375 equiv.) were added to a dry round-bottom flask and dissolved in DCM (8 mL). The reaction was allowed to stir for three hours under ambient conditions until complete conversion was observed by LCMS. The reaction mixture was quenched in 100 mL of water and extracted with ethyl acetate (3 X 25 mL) and the combined ethyl acetate extracts were washed with brine, dried over Na_2SO_4, and then concentrated under reduced pressure. The crude product was purified by silica gel column chromatography (50/50 hexanes/EtOAc) to afford **7** (1.6 g, 82%) as a pale-yellow oil. ^1H NMR (400 MHz, $CDCl_3$) δ 8.2-8.5 (d, 1H), 8.26 (d, 1H), 7.88-7.92 (dt, 1H), 7.52-7.56 (m, 1H), 7.37-7.39 (d, 2H), 7.20-7.22 (d, 2H), 4.76 (s, 2H), 0.94 (s, 9H), 0.11 (s, 6H). ^{13}C NMR (100 MHz, $CDCl_3$) δ 164.00, 150.12, 149.73, 147.56, 139.38, 137.22, 127.41, 127.08, 125.87, 121.39, 120.15, 64.43, 25.97, 25.67, 18.43, -5.24. Low-resolution mass spectrometry (LRMS) (*m/z*): $[M+H]^+$ calculated for : $C_{19}H_{26}NO_3Si$, 344.17; found, 344.2.

4-(hydroxymethyl)phenyl picolinate, 8. 4-(((tert-butyldimethylsilyl)oxy)methyl)phenyl picolinate, **7**, (1.6 g, 4.66 mmol) was dissolved in 0.1% HCl in methanol (10 mL) and was allowed to stir under ambient conditions for 30 minutes. The reaction mixture was then quenched with 100 mL of water and extracted into ethyl acetate (3 X 25 mL), washed with brine, dried over Na_2SO_4 and concentrated under reduced pressure. The product **8** (920 mg, 86%) was obtained as a white powder and used without further purification. ^1H NMR (400 MHz, $CDCl_3$) δ 8.74-8.76 (d, 1H), 8.22-8.24 (d, 1H), 7.86-7.90 (dt, 1H), 7.50-7.54 (m, 1H), 7.36-7.38 (d, 2H), 7.16-7.18 (d, 2H), 4.65 (s, 2H). ^{13}C NMR (100 MHz, $CDCl_3$) δ 163.93, 156.27, 150.05, 147.29, 139.17, 137.43, 128.79, 128.12, 127.62, 125.95, 121.66, 115.55, 77.16, 63.93. Low-resolution mass spectrometry (LRMS) (*m/z*): $[M+H]^+$ calculated for : $C_{13}H_{12}NO_3$, 230.08; found, 230.1.

4-(bromomethyl)phenyl picolinate, 9. 4-(hydroxymethyl)phenyl picolinate, **8**, (856 mg, 3.73 mmol, 1 equiv.) was added to a flame-dried round-bottom flask and the flask was purged with N_2. DCM (7 mL) was then added to the flask followed by PBr_3 (1.3 g, 4.85 mmol, 1.2 equiv.). The reaction was allowed to stir at room temperature under a N_2 atmosphere for two hours and was then quenched with water (100 mL) and extracted into ethyl acetate (3 X 25 mL). The combined ethyl acetate extract was then washed with brine and dried over Na_2SO_4 and then concentrated under reduced pressure. The crude product was then purified by silica gel column chromatography (25/75 petroleum ether/ethyl acetate) to obtain **9** (990 mg, 91%) as a white solid. ^1H NMR (400 MHz, $CDCl_3$) δ 8.80-8.82 (d, 1H), 8.22-8.24 (d, 1H), 7.86-7.90 (dt, 1H), 7.50-7.54 (m, 1H), 7.42-7.44 (d, 2H), 7.20-7.22 (d, 2H), 4.48 (s, 2H). ^{13}C NMR (100 MHz, $CDCl_3$) δ 163.71, 150.77, 150.17, 147.24, 137.33, 135.70, 130.36, 127.60, 125.96, 122.08, 32.71. Low-resolution mass spectrometry (LRMS) (*m/z*): $[M+H]^+$ calculated for $C_{13}H_{11}BrNO_2$, 292.00; found 292.0.

pic-DTZ. Diphenylterazine, **4**, (72 mg, 0.19 mmol, 1 equiv.), 4-(bromomethyl)phenyl picolinate, **9**, (112 mg, 0.38 mmol, 2 equiv.), Cs_2CO_3 (25 mg, 0.076 mmol, 0.4 equiv.), and KI (35 mg, 0.21 mmol, 1.1 equiv.) were added to a flame-dried round-bottom flask that was then purged with N_2. The reagents were then dissolved in anhydrous acetonitrile (2 mL) and the reaction was allowed to stir overnight. The reaction mixture was subsequently quenched in 20 mL of water and extracted in DCM (3 x 10 mL). The combined DCM extract was then washed with brine, dried over Na_2SO_4, and concentrated under reduced pressure. The crude product was then purified by reverse-phase HPLC (gradient, 70%:30% H_2O/MeCN to 100% MeCN over 50 min on a T3 Atlantis column (Waters) and dried under reduced pressure to obtain **pic-DTZ** (14 mg, 13% yield) as a brown-red solid. ^1H NMR (600 MHz, CD_2Cl_2) δ 8.86-8.88 (d, 2H), 8.79-8.81 (d, 1H), 8.22-8.24 (d, 1H), 8.09 (s, 1H), 8.01-8.03 (d, 2H), 7.91-7.94 (t, 1H), 7.49-7.58 (m, 6H), 7.36-7.44 (m, 5H), 7.27-7.32 (m, 4H), 7.20-7.23 (t, 1H), 5.08 (s, 2H), 4.18 (s, 2H). ^{13}C NMR (150 MHz, CD_2Cl_2) δ 164.02, 151.92, 150.49, 147.68, 139.79, 138.37, 137.59, 137.39, 137.29, 136.73, 134.19, 134.16, 132.36, 130.59, 130.50, 130.14, 129.17, 128.90, 128.83, 128.55, 127.91, 126.76, 126.53, 126.15, 122.54, 109.89, 76.99, 33.82. Low-resolution mass spectrometry (LRMS) (*m/z*): $[M+H]^+$ calculated for : $C_{38}H_{29}N_4O_3$, 589.22; found, 589.2.

2.5.2 Synthesis of pic-CTZ400a

3-benzyl-5-bromopyrazin-2-amine, 3b. Zinc mesh 20-30 (1.18 g, 18 mmol, 3.5 equiv.), zinc dust (1.18 g, 18 mmol, 3.5 equiv.), and iodine (70 mg, 0.9 mmol, 5 mol%) were added to a flame-dried round-bottom flask purged with N_2. Benzyl bromide (967 mg, 5.65 mmol, 1.1 equiv.) in N,N-DMA (8 mL) was then added to the round-bottom flask and the reaction was heated to 80 ºC and allowed to stir for three hours. A suspension of 3,5-dibromo-2-aminopyrazine (1.3 g, 5.14 mmol, 1 equiv.) and $PdCl_2(PPh_3)_2$ (180 mg, 0.257 mmol, 5 mol%) in N,N-DMA (8 mL) was added to the reaction mixture. The reaction was allowed to stir for 72 hours. The reaction was quenched in water (100 mL) and extracted with ethyl acetate (3 X 25 mL). The combined ethyl acetate extract was washed with brine, dried over Na_2SO_4, and concentrated under reduced pressure. The crude product was then purified by silica gel column chromatography (60/40 hexanes/EtOAc) to afford **3b** (1.25 g, 92%) as a brown solid. ^1H NMR (400 MHz, $CDCl_3$) δ 8.02 (s, 1H), 7.26-7.36 (m, 5H), 4.40 (bs, 2H), 4.08 (s, 2H). Low-resolution mass spectrometry (LRMS) (*m/z*): $[M+H]^+$ calculated for $C_{11}H_{10}BrN_3$, 264.0; found $[M+H]^+$ 264.0.

3-benzyl-5-phenylpyrazin-2-amine, 4b. 3-benzyl-5-bromopyrazin-2-amine, **3b**, (339 mg, 1.283 mmol, 1 equiv.), phenylboronic acid (188 mg, 1.54 mmol, 1.2 equiv.), $Pd(PPh_3)_4$ (148 mg, 0.128 mmol, 0.1 equiv.), and K_2CO_3 (310 mg, 2.25 mmol, 1.75 equiv.) were all added to a round-bottom flask purged with N_2, then water (5 mL) and 1,4-dioxane (25 mL) were added. The reaction was heated to 80 ºC and was allowed to stir overnight. The reaction was then quenched in water (100 mL) and extracted into ethyl acetate (3 X 25 mL). The combined ethyl acetate extract was then washed with brine, dried over Na_2SO_4, and concentrated under reduced pressure. The crude product was then purified by silica gel column chromatography (70/30 pet. ether/hexanes) to afford **3c** (282 mg, 84%) as a brown solid.^{1}H NMR (400 MHz, DMSO) δ 8.43 (s, 1H), 7.90-7.92 (d, 2H), 7.27-7.43 (m, 7H), 7.20 (t, 1H), 6.40 (s, 2H), 4.09 (s, 2H). Low-resolution mass spectrometry (LRMS) (*m/z*): $[M+H]^+$ calculated for $C_{17}H_{16}N_3$, 262.1; found 262.2.

CTZ400a, 5b. 3-benzyl-5-phenylpyrazin-2-amine, **4b,** (217 mg, 0.830 mmol, 1 equiv.) and 1,1-diethoxy-3-phenylpropan-2-one, **10**, (277 mg, 1.246 mmol, 1.5 equiv.) were added to a N_2-purged round-bottom flask followed by ethanol (16 mL), water (2 mL), and hydrochloric acid (0.4 mL). The reaction was then refluxed overnight. The reaction was then concentrated under reduced pressure and purified on alumina gel column (gradient 0-10% MeOH in DCM) to afford **5b** (150 mg, 46%) of pure product as a bright yellow solid. ^{1}H NMR (400 MHz, DMSO) δ 7.16-7.92 (m, 16H), 4.34 (s, 2H), 4.09 (s, 2H). Low-resolution mass spectrometry (LRMS) (*m/z*): $[M+H]^+$ calculated for: $C_{26}H_{22}N_3O$, 392.18; found $[M+H]^+$ 392.1.

pic-CTZ400a. CTZ400a, **5b**, (86 mg, 0.219 mmol, 1 equiv.), 4-(bromomethyl)phenyl picolinate, **9**, (128 mg, 0.439 mmol, 2 equiv.), Cs_2CO_3 (30 mg, 0.087 mmol, 0.4 equiv.), and KI (40 mg, 0.241 mmol, 1.1 equiv.) were added to a flame-dried round-bottom flask that was then purged with N_2. The reagents were then dissolved in anhydrous MeCN (2 mL) and the reaction was allowed to stir overnight. The following morning the reaction mixture was quenched in 20 mL of water and extracted in DCM (3 x 10 mL). The combined DCM extract was then washed with brine, dried over Na_2SO_4, and concentrated under reduced pressure. The crude product was then purified by reverse-phase HPLC (gradient, 70% H_2O/30% MeCN to 100% MeCN over 50 minutes on an Agilent C3 column) and dried under reduced pressure to obtain **pic-CTZ400a** (31 mg, 24% yield) as a brown-red solid. ^1H NMR (800 MHz, CD_2Cl_2) δ 8.80-8.82 (d, 1H), 8.22-8.24 (d, 1H), 7.87-7.97 (m, 4H), 7.54-7.58 (m, 3H), 7.17-7.47 (m, 15H), 5.03 (s, 2H), 4.55 (s, 2H), 4.13 (s, 2H). ^{13}C NMR (200 MHz, CD_2Cl_2) δ 152.54, 151.48, 139.40, 138.31, 138.17, 137.14, 136.99, 133.80, 133.62, 132.53, 130.82, 130.34, 129.99, 129.55, 128.97, 128.79, 128.70, 128.43, 128.29, 128.20, 127.52, 126.82, 126.35, 126.32, 126.11, 125.72, 124.98, 122.11, 109.32, 76.57, 39.32, 33.34, 29.68. Low-resolution mass spectrometry (LRMS) (*m/z*): $[M+H]^+$ calculated for: $C_{39}H_{31}N_4O_3$, 603.24; found $[M+H]^+$ 603.2.

2.5.3 Synthesis of pic-CTZ

pic-CTZ Coelenterazine (Goldbio), (25 mg, 0.06 mmol, 1 equiv.), 4-(bromomethyl)phenyl picolinate, **9**, (20 mg, 0.07 mmol, 1.1 equiv.), Cs_2CO_3 (8 mg, 0.02 mmol, 0.4 equiv.), and KI (10 mg, 0.07 mmol, 1.1 equiv.) were added to a flame dried round-bottom flask that was then purged with nitrogen. The reagents were then dissolved in anhydrous acetonitrile (0.5 mL) and the reaction was allowed to stir overnight. The following morning the reaction mixture was quenched in 20 mL of water and extracted in DCM (3 x 10 mL). The combined DCM extract was then washed with brine, dried over Na_2SO_4, and concentrated under reduced pressure. The crude product was then purified by reverse-phase HPLC (gradient, 70% H_2O/30%MeCN over 50 minutes 100% MeCN on a T3 Atlantis column) and dried under reduced pressure to obtain **pic-**

CTZ (0.5 mg, 1.3% yield) as a brown-red solid. Low-resolution mass spectrometry (LRMS) (*m/z*): $[M+H]^+$ calculated for: $C_{39}H_{30}N_4O_5$, 635.23; found $[M+H]^+$ 635.3.

2.5.4 Synthesis of Heterocyclic Esters

Thiophene ester, 7a. Phenol **6** (200 mg, 0.840 mg, 1 equiv.) and thiophene-2-carbonyl chloride (148 mg, 1.01 mmol, 1.2 equiv.) were added to a flame-dried round-bottom flask purged with N_2 and then dissolved in anhydrous pyridine/DMF (1:1, 2 mL) and allowed to stir at room temperature for three hours. The reaction was then quenched in water and extracted into ethyl acetate (3 X 10 mL). The combined ethyl acetate extract was then washed with brine, dried over Na_2SO_4 and concentrated under reduced pressure. The crude product was purified by silica gel column chromatography (70/30 hexanes/EtOAc) to obtain the desired product **7b** (224 mg, 77%) as a yellow oil. ^{1}H NMR (400 MHz, CDCl3) δ 7.98-8.00 (dd, 1H), 7.64-7.66 (dd, 1H), 7.37-7.39 (d, 2H), 7.16-7.20 (m, 3H), 4.72 (s, 2H), 0.97 (s, 9H), 0.13 (s, 6H). 13C NMR (100 MHz, $CDCl_3$) δ 160.82, 149.51, 139.32, 134.75, 133.56, 133.06, 128.12, 127.80, 127.16, 121.48, 115.16, 64.87, 64.55, 26.07, 18.52, -5.12. Low-resolution mass spectrometry (LRMS) (*m/z*): $[M+H]^+$ calculated for: $C_{18}H_{25}O_3SSi$, 349.1; found $[M+H]^+$ 349.1.

Furan ester, 7b. Phenol **6** (200 mg, 0.840 mg, 1 equiv.) and furan-2-carbonyl chloride (132 mg, 1.01 mmol, 1.2 equiv.) were added to a flame-dried round-bottom flask purged with N_2 and then dissolved in anhydrous pyridine/DMF (1:1, 2 mL) and allowed to stir at room temperature for three hours. The reaction was then quenched in water and extracted into ethyl acetate (3 X 10 mL). The combined ethyl acetate extract was then washed with brine, dried over Na_2SO_4, and concentrated under reduced pressure. The crude product was purified by silica gel column chromatography (70/30 hexanes/EtOAc) to obtain the desired product **7b** (230 mg, 83%) as a white solid. ^{1}H NMR (400 MHz, CDCl3) δ 7.66 (s, 1H), 7.36-7.38 (m, 3H), 7.16-7.18 (d, 2H), 4.75 (s, 2H), 0.95 (s, 9H), 0.11 (s, 6H). 13C NMR (100 MHz, CDCl3) δ 159.77, 149.11, 147.22, 144.57, 139.44, 127.19, 121.85, 119.92, 112.30, 64.52, 26.54, 17.19, -5.13. Low-resolution mass spectrometry (LRMS) (*m/z*): $[M+H]^+$ calculated for $C_{18}H_{25}O_4Si$, 331.15; found $[M+H]^+$ 331.1.

2.5.5 Luminescence Assays

***In Vitro* Luminescence Assays.** Milli-Q water (18.2 MΩ) was used to prepare all aqueous solutions. Metal ion solutions were prepared to 15 µM in water ($MgCl_2$, NaCl, KCl, $CaCl_2$, $MnCl_2$, $(NH_4)_2Fe(SO_4)\cdot 6H_2O$, $FeCl_3$, $CoCl_2$, $NiCl_2$, $Cu(MeCN)_4(PF_6)$, $CuCl_2$ and $ZnCl_2$). A 15 µM solution of pic-DTZ was prepared by initially dissolving pic-DTZ in 5% pure ethanol of the total volume and bringing it up in DPBS (Gibco) at pH 7.4 to a final concentration of 15 µM. A 120 nM solution of rNluc was prepared by adding 4 µL of 0.4 mg/mL stock solution (Promega, Nano-Glo Assay Kit) into 699 µL of DPBS at pH 7.4. 25 µL of rNluc solution was added to the wells of a white, opaque, flat-bottom 96-well plate followed by 25 µL of metal solution. Finally, pic-DTZ (25 µL) was added to all the wells using a multi-channel pipette and mixed well. The bioluminescent signal was immediately measured using a Molecular Devices SpectraMax i3x plate reader at 37 ºC for 1 hour. For *in vitro* assays using albumin, ceruloplasmin and pooled human serum, a 645 µM solution of albumin (Fatty Acid Free, ThermoFisher) was prepared in DPBS, a 1000 mU/mL solution of ceruloplasmin was prepared from a stock solution (ceruloplasmin colorimetric activity kit, ThermoFisher), and a 10% pooled human serum solution was prepared in DPBS from a stock solution (Sigma-Aldrich). A 1 µM solution of pic-DTZ was prepared in 5% pure ethanol in DPBS from a frozen aliquot and a 100 nM solution of rNluc was prepared in DPBS from a frozen stock solution (0.4 mg/mL, Promega, Nano-glo assay kit). For experiments using EDTA, GSH, and NH_2OH (Sigma-Aldrich) solutions were prepared in DPBS (pH 7.4). For experiments using GHK (Bachem), histidine (Sigma-Aldrich) and albumin (Sigma-Aldrich), stock solutions were prepared in water with or without $CuSO_4$ and allowed to incubate for 15 minutes before measuring luminescence. For experiments using 2-HQ and DFP (Sigma-Aldrich), stock solutions were prepared in ethanol and were added to 10% serum to a final concentration of 5 µM (ethanol final concentration was less than 5%) and incubated for 15 minutes before reading the luminescence. When reporting area under the curve, these values were calculated using GraphPad Prism software.

Bioluminescent Response to Copper in Plasma. Human plasma samples from healthy individuals (n=3) and individuals with Wilson disease (n=3) were obtained from Dr. Valentina Medici (UC Davis). All subjects provided written informed consent prior to participation following the Declaration of Helsinki. The protocol was approved by UCD Institutional Review Board (protocol # 818454). A 10% sample of plasma for each condition was prepared in DPBS and rNluc (Promega, 0.4 mg/mL) from a frozen stock solution was added to obtain a final concentration of 100 nM enzyme. 100 µL of each sample was added into wells of a 96-well, white, flat-bottom opaque plate and 1 µL of a 100 µM pic-DTZ (5% pure ethanol in DPBS) solution was added to each well using a multi-channel pipette. Luminescence was immediately measured as described previously.

Evaluation of pH responsiveness of pic-DTZ. DPBS solutions were prepared from a stock commercial solution to desired pH using either 6 M HCl or NaOH and then 125 nM rNluc solutions were made from a stock solution of rNluc (Promega) and these were plated in a 96-well white, opaque plate. To the wells were added Cu(II) to a final concentration of 10 µM when appropriate. Lastly, 1 µL of a 100 µM pic-DTZ (in ethanol) solution was added to all wells and the luminescence was measured immediately as previously described.

2.5.6. Cell Culture and Cellular Luminescent Assays

Cell Culture Procedures. MDA-MB-231 cells stably expressing secreted Nanoluciferase (secNluc MDA-MB-231) were a kind gift from Drs. Gary and Kathy Luker (University of Michigan). Cells were maintained in Dulbecco's modified medium (DMEM) supplemented with 10% fetal bovine serum (FBS) (Gibco) 1x penicillin-streptomycin (Corning), 2 mM L-glutamine (Gibco), 1 mM sodium pyruvate (Gibco) at 37 ºC and 5% CO_2.

Bioluminescent Response to Copper in secNluc MDA-MB-231 cells. Cells were plated at 10,000 cells per well in a 96-well, white, opaque flat-bottom plate. Eight hours later, the media was removed and the cells were washed with pre-warmed (37 ºC) DPBS and 100 µL of OptiMem (Gibco) was added to each well. A 3 mM solution of cisplatin and 500 mM solution of metformin were prepared in water. 1 µL of these solutions were added to the wells for final concentrations of 30 µM cisplatin and 5 mM metformin. At the 18-hour time point solutions of 100 µM pic-DTZ and 100 µM DTZ (5% pure ethanol in DPBS) were prepared and 1 µL was added per well per treatment (n=3). Luminescence was immediately recorded as previously described. The area under the curve was calculated using GraphPad Prism software and the ratio of the A.U.C. from pic-DTZ to DTZ was calculated.

2.5.7 ICP-MS Analysis

Cells were plated at 100,000 cells per well in a 12-well clear, flat-bottom plate. Eight hours later, the media was removed and the cells were washed with pre-warmed (37 ºC) DPBS and 100 µL of OptiMem (Gibco) was added to each well. A 3 mM solution of cisplatin and 500 mM solution of metformin were prepared in water. 10 µL of these solutions were added to the wells for final concentrations of 30 µM cisplatin and 5 mM metformin. At the 18-hour time point cell media was removed and was digested in concentrated acid overnight. The following morning the solutions were diluted in 2% (v/v) aqueous nitric acid. Metal analysis was performed at the Northwestern University Quantitative Bio-element Imaging Center generously supported by NASA Ames Research Center NNA06CB93G.

2.5.8 Cell Stimulations & Western Blot Analysis

secNluc MDA-MB-231 cells were plated in a 6 well plate at 200,000 cells per well. 6 hours after plating the media was removed, the cells were washed with prewarmed (37°C) DPBS, and fresh OptiMem was added. TTM, Cis-platin, and metformin solutions were prepared in water and added to wells at a final concentration of 30 µM, 30 µM, and 5 mM, respectively. At the 18-hour time point cells were lysed in RIPA buffer (150 mM NaCl, 1% NP-40, 0.5% sodium deoxycholate, 0.1% SDS, 50 mM Tris pH 7.4) with EDTA free protease inhibitor (ThermoFisher) and phosphatase inhibitor (Sigma). Lysates were put one ice for 15 minutes before being vortexed and centrifuged at 15000 x G at 4°C. Protein was quantified after freezing the lysates by BCA assay (Invitrogen). For Ctr1, ATP7A, and CCS, samples were made using 10 µg of protein with PBS (Gibco), sample buffer (Invitrogen), and 2-mercaptoethanol (BioRad). Samples were loaded into a 4-12% bis-tris 10 well gel (Invitrogen) and run for one hour at 100V and then was transferred on to a PVDF membrane using a Trans-Blot Turbo Transfer System (BioRad). The membranes were blocked for one hour in 5% milk in TBST buffer. Membranes were then incubated overnight at 4°C with primary antibodies and washed three times the following day with TBST buffer before incubating secondary antibodies for one hour. Membranes were imaged on a Chemidoc MP Imager (BioRad). Primary antibodies used were Anti-Ctr1 (1:2,000 Cell Signaling Technologies), Anti-ATP7A (1:2,000 Santa Cruz Biotechnology), Anti-CCS (1:1,000 Santa Cruz Biotechnology), and Anti-Actin (Ms IgG and Rb IgG, 1:5000 or 1,10,000 respectively, Santa Cruz Biotechnology and Cell Signaling Technologies respectively). Secondary antibodies used were anti-rabbit IgG HRP-conjugated antibody (1:2,000 Cell Signaling Technologies) for Ctr1, anti-mouse IgG HRP-conjugated antibody (1:2,000 Cell Signaling Technologies) for ATP7A and CCS, anti-rabbit IgG Alexafluor 800 (1:10,000 Invitrogen) for actin and anti-mouse IgG Alexafluor 800 (1:5,000 Invitrogen) for actin.

2.6 References

(1) Chen, J.; Jiang, Y.; Shi, H.; Peng, Y.; Fan, X.; Li, C. The Molecular Mechanisms of Copper Metabolism and Its Roles in Human Diseases. *Eur. J. Physiol.* **2020**, *472*, 1415–1429.

(2) Tapiero, H.; Townsend, D. M.; Tew, K. D.; Chase, F. Trace Elements in Human Physiology and Pathology. Copper. *Biomed Pharmacother.* **2019**, *57* (9), 386–398.

(3) Ferguson-miller, S.; Babcock, G. T. Heme / Copper Terminal Oxidases B . Insights from the Atomic Resolution Structures of Cytochrome c Oxidases. *Chem. Rev.* **1996**, *96* (7), 2889–2907.

(4) Horn, D.; Barrientos, A. Mitochondrial Copper Metabolism and Delivery to Cytochrome c Oxidase. *IUBMB Life* **2010**, *60* (7), 421–429.

(5) Ashino, T.; Sudhahar, V.; Urao, N.; Oshikawa, J.; Chen, G.; Wang, H.; Huo, Y.; Finney, L.; Vogt, S.; Mckinney, R. D.; Maryon, E. B.; Kaplan, J. H.; Ushio-fukai, M.; Fukai, T. Unexpected Role of the Copper Transporter ATP7A in PDGF-Induced Vascular Smooth Muscle Cell Migration. *Circ. Res.* **2010**, *107* (6), 787–799.

(6) Turski, M. L.; Thiele, D. J. New Roles for Copper Metabolism in Cell Proliferation , Signaling , and Disease *. *J. Biol. Chem.* **2009**, *284* (2), 717–721.

(7) Kardos, J.; Héja, L.; Simon, Á.; Jablonkai, I.; Kovács, R.; Jemnitz, K. Copper Signalling : Causes and Consequences. *Cell Commun. Signal.* **2018**, *16* (71).

(8) Alinas, J. V. Í. C. A.; Lbores, A. R. A. Copper Increases the Damage to DNA and Proteins Caused by Reactive Oxygen Species. *Biol. Trace Elem. Res.* **2005**, *103*, 229–248.

(9) Gu, K.; Li, X.; Xiang, W.; Jiang, X. The Relationship Between Serum Copper and Overweight / Obesity : A Meta-Analysis. *Biol. Trace Elem. Res.* **2020**, *194*, 336–347.

(10) Denoyer, D.; Masaldan, S.; Fontaine, L.; Cater, M. A. Targeting Copper in Cancer Therapy : ‘ Copper That Cancer .’ *Metallomics* **2015**, *7*, 1459–1476.

(11) Tanaka, A.; Kaneto, H.; Miyatsuka, T.; Yamamoto, K.; Yoshiuchi, K. Role of Copper Ion in the Pathogenesis of Type 2 Diabetes. *Endocr. J.* **2009**, *56* (5), 699–706.

(12) Finney, L.; Mandava, S.; Ursos, L.; Zhang, W.; Rodi, D.; Vogt, S.; Legnini, D.; Maser, J.; Ikpatt, F.; Olopade, O. I.; Glesne, D. X-Ray Fluorescence Microscopy Reveals Large-Scale Relocalization and Extracellular Translocation of Cellular Copper during Angiogenesis. *PNAS* **2007**, *104* (7), 2247–2252.

(13) Ejaz, H. W.; Wang, W. Copper Toxicity Links to Pathogenesis of Alzheimer ’ s Disease and Therapeutics Approaches. *Int. J. Mol. Sci.* **2020**, *21* (20), 7660–7693.

(14) Bossak-ahmad, K.; Fra, T.; Bal, W.; Drew, S. C. The Sub-Picomolar Cu 2 + Dissociation Constant of Human Serum Albumin. *ChemBioChem* **2020**, *21* (1), 331–334.

(15) Morgan, M. T.; Bourassa, D.; Harankhedkar, S.; Mccallum, A. M.; Zlatic, S. A. Ratiometric Two-Photon Microscopy Reveals Attomolar Copper Buffering in Normal and Menkes Mutant Cells. *PNAS* **2019**, *116* (25), 12167–12172.

(16) Blockhuys, S.; Zhang, X.; Wittung-stafshede, P. Single-Cell Tracking Demonstrates Copper Chaperone Atox1 to Be Required for Breast Cancer Cell Migration. *PNAS* **2020**, *117* (4), 2014–2019.

(17) Falcone, E.; Okafor, M.; Vitale, N.; Raibaut, L.; Sour, A.; Faller, P. Extracellular Cu 2 + Pools and Their Detection : From Current Knowledge to next-Generation Probes. *Coord.*

Chem. Rev. **2021**, *433*, 213727.

(18) Heffern, M. C.; Park, H. M.; Au-Yeung, H. Y.; Van de Bittner, G. C.; Ackerman, C. M.; Stahl, A.; Chang, C. J. In Vivo Bioluminescence Imaging Reveals Copper Deficiency in a Murine Model of Nonalcoholic Fatty Liver Disease. *Proc. Natl. Acad. Sci.* **2016**, *113* (50), 14219–14224.

(19) Patil, M.; Sheth, K. A.; Krishnamurthy, A. C.; Devarbhavi, H. A Review and Current Perspective on Wilson Disease. *J. Clin. Exp. Hepatol.* **2013**, *3* (4), 321–336.

(20) Laur, N.; Kinscherf, R.; Pomytkin, K.; Kaiser, L.; Knes, O.; Id, P. D. ICP-MS Trace Element Analysis in Serum and Whole Blood. *PLoS One* **2020**, *15* (5), 1–14.

(21) Jain, S.; Cohen, J.; Ward, M. M.; Kornhauser, N.; Chuang, E.; Cigler, T.; Moore, A.; Donovan, D.; Lam, C.; Cobham, M. V; Schneider, S.; Rúa, S. M. H.; Benkert, S.; Greenwood, C. M.; Zelkowitz, R.; Warren, J. D.; Lane, M. E.; Mittal, V.; Ra, S.; Vahdat, L. T. Tetrathiomolybdate-Associated Copper Depletion Decreases Circulating Endothelial Progenitor Cells in Women with Breast Cancer at High Risk of Relapse. *Ann. Oncol.* **2013**, *25*, 1491–1498.

(22) Ramirez, A. G.; Bohrer, D.; Cı, P.; Mendonc, J. K. A.; Carvalho, L. M. De; Cristina, S.; Pomblum, G. Comparison of Ultrafiltration and Solid Phase Extraction for the Separation of Free and Protein-Bound Serum Copper for the Wilson ’ s Disease Diagnosis. *Clin. Chim. Acta* **2004**, *345*, 113–121.

(23) Inagaki, K.; Mikuriya, N.; Morita, S.; Haraguchi, H. Speciation of Protein-Binding Zinc and Copper in Human Blood Serum by Chelating Resin Pre-Treatment and Inductively Coupled Plasma Mass Spectrometry. *Analyst* **2000**, *125*, 197–203.

(24) Buckley, W. T.; Vanderpool, Æ. R. A. Analytical Variables Affecting Exchangeable Copper Determination in Blood Plasma. *Biometals* **2008**, *21*, 601–612.

(25) Mezzanotte, L.; van ‘t Root, M.; Karatas, H.; Goun, E. A.; Löwik, C. W. G. M. In Vivo Molecular Bioluminescence Imaging: New Tools and Applications. *Trends Biotechnol.* **2017**, *35* (7), 640–652.

(26) Aron, A. T.; Heffern, M. C.; Lonergan, Z. R.; Vander Wal, M. N.; Blank, B. R.; Spangler, B.; Zhang, Y.; Park, H. M.; Stahl, A.; Renslo, A. R.; Skaar, E. P.; Chang, C. J. In Vivo Bioluminescence Imaging of Labile Iron Accumulation in a Murine Model of Acinetobacter Baumannii Infection. *Proc. Natl. Acad. Sci.* **2017**, *114* (48), 12669–12674.

(27) Bittner, G. C. Van De; Dubikovskaya, E. A.; Bertozzi, C. R.; Chang, C. J. In Vivo Imaging of Hydrogen Peroxide Production in a Murine Tumor Model with a Chemoselective Bioluminescent Reporter. *PNAS* **2010**.

(28) Jr, S. T. A.; Miller, S. C. Beyond D-Luciferin : Expanding the Scope of Bioluminescence Imaging in Vivo. *Curr. Opin. Chem. Biol.* **2014**, *21*, 112–120.

(29) Lindberg, E.; Mizukami, S.; Ibata, K.; Miyawaki, A. Development of Luminescent Coelenterazine Derivatives Activatable by b -Galactosidase for Monitoring Dual Gene Expression. *Chem. - A Eur. J.* **2013**, *19*, 14970–14976.

(30) Yang, X.; Li, Z.; Jiang, T.; Du, L.; Li, M. A Coelenterazine-Type Bioluminescent Probe for Nitroreductase Imaging. *Org. Biomol. Chem.* **2018**, *16*, 146–151.

(31) Nishihara, R.; Kurita, R. Mix-and-Read Bioluminescent Copper Detection Platform Using a Caged Coelenterazine Analogue. *Analyst* **2021**, *146*, 6139–6144.

(32) Hall, M. P.; Unch, J.; Binkowski, B. F.; Valley, M. P.; Butler, B. L.; Wood, M. G.; Otto, P.; Zimmerman, K.; Vidugiris, G.; Machleidt, T.; Robers, M. B.; Benink, H. A.; Eggers,

C. T.; Slater, M. R.; Meisenheimer, P. L.; Klaubert, D. H.; Fan, F.; Encell, L. P.; Wood, K. V. Engineered Luciferase Reporter from a Deep Sea Shrimp Utilizing a Novel Imidazopyrazinone Substrate. *ACS Chem. Biol.* **2012**, *7* (11), 1848–1857.

(33) Tannous, B. A.; Kim, D.; Fernandez, J. L.; Weissleder, R.; Breakefield, X. O. Codon-Optimized Gaussia Luciferase CDNA for Mammalian Gene Expression in Culture and in Vivo. *Mol. Ther.* **2005**, *11* (3), 435–443.

(34) Markova, S. V; Larionova, M. D.; Vysotski, E. S. Shining Light on the Secreted Luciferases of Marine Copepods : Current Knowledge and Applications. *Photochem. Photobiol.* **2019**, *95* (2), 705–721.

(35) Shakhmin, A.; Hall, M. P.; Machleidt, T.; Walker, J. R.; Wood, V.; Kirkland, T. A. Biomolecular Chemistry Bioluminescence with NanoLuc †. **2017**, 8559–8567.

(36) Kierat, R. M.; Kra, R. A Fluorogenic and Chromogenic Probe That Detects the Esterase Activity of Trace Copper (II). **2005**, *15*, 4824–4827.

(37) Yuan, M.; Ma, X.; Jiang, T.; Gao, Y.; Cui, Y.; Zhang, C.; Yang, X.; Huang, Y.; Du, L.; Yampolsky, I.; Li, M. Biomolecular Chemistry and Mice Using Novel Pro-Substrates for Renilla. **2017**, 10238–10244.

(38) Kierat, R. M.; Kra, R. A Fluorogenic and Chromogenic Probe That Detects the Esterase Activity of Trace Copper (II). *Bioorg. Med. Chem. Lett.* **2005**, *15*, 4824–4827.

(39) Quarles, C. D.; Kenneth, J. R.; Brumaghim, J. L. Competitive Binding of Fe 3 + , Cr 3 + , and Ni 2 + to Transferrin. *J. Biol. Inorg. Chem.* **2011**, *16*, 913–921.

(40) Rathbun, C. M.; Prescher, J. A. Bioluminescent Probes for Imaging Biology beyond the Culture Dish. *Biochemistry* **2017**, *56*, 5178–5184.

(41) Kirsipuu, T.; Zadoro, A.; Smirnova, J.; Friedemann, M.; Plitz, T. Copper (II) -Binding Equilibria in Human Blood. *Sci. Rep.* **2020**, *10*.

(42) Vassel, N.; Cox, C. D.; Naseem, R.; Morse, V.; Evans, R. T.; Power, R. L. Enzymatic Activity of Albumin Shown by Coelenterazine Chemiluminescence. *J. Biol. Chem. Lumin.* **2012**, *27*, 234–241.

(43) Li, B.; Sedlacek, M.; Manoharan, I.; Boopathy, R. Butyrylcholinesterase, Paraoxonase, and Albumin Esterase, but Not Carboxylesterase, Are Present in Human Plasma. *Biochem. Pharmacol.* **2005**, *70*, 1673–1684.

(44) Stremmel, W.; Weiskirchen, R. Therapeutic Strategies in Wilson Disease : Pathophysiology and Mode of Action. *Ann. Transl. Med.* **2021**, *9* (8).

(45) Rodriguez-castro, K. I.; Hevia-urrutia, F. J.; Sturniolo, G. C.; Rodriguez-castro, K. I.; Terme, P. A.; Terme, A.; Rodriguez-castro, K. I.; Hevia-, F. J.; San, H.; Dios, J. De; José, S.; Rica, C.; Rodriguez-castro, K. I.; Sturniolo, G. C.; Hevia-urrutia, F. J.; Cima, H.; Postal, A.; José, S.; Rica, C. Wilson ’ s Disease : A Review of What We Have Learned. *World J. Hepatol.* **2015**, *7* (29), 2859–2870.

(46) Walshe, J. M. Wilson ’ s Disease : The Importance of Measuring Serum Caeruloplasmin Non-Immunologically. *Ann. Clin. Biochem.* **2003**, *40*, 115–121.

(47) Ge, E. J.; Bush, A. I.; Casini, A.; Cobine, P. A.; Cross, J. R.; Denicola, G. M.; Dou, Q. P.; Franz, K. J.; Gohil, V. M.; Petris, M. J.; Polishchuk, R.; Ralle, M.; Schilsky, M. L.; Tonks, N. K.; Vahdat, L. T.; Aelst, L. Van; Xi, D.; Yuan, P.; Brady, D. C.; Chang, C. J. Connecting Copper and Cancer: From Transition Metal Signalling to Metalloplasia. *Nat. Rev. Cancer* **2021**.

(48) Khan, G.; Merajver, S. Copper Chelation in Cancer Therapy Using Tetrathiomolybdate :

An Evolving Paradigm Copper Chelation in Cancer Therapy Using Tetrathiomolybdate : An Evolving Paradigm. *Expert Opin. Investig. Drugs* **2009**, *18* (4), 541–548.

(49) Fatfat, M.; Merhi, R. A.; Rahal, O.; Stoyanovsky, D. A.; Zaki, A.; Haidar, H. Copper Chelation Selectively Kills Colon Cancer Cells through Redox Cycling and Generation of Reactive Oxygen Species. *BMC Cancer* **2014**, *14*.

(50) Versini, A.; Sindikubwabo, F.; Belthier, G.; Niyomchon, S.; Pannequin, J.; Grimaud, L.; Ca, T. Metformin Reveals a Mitochondrial Copper Addiction of Mesenchymal Cancer Cells. *PLoS One* **2018**, *13* (11).

(51) Wang, J.; Luo, C.; Shan, C.; You, Q.; Lu, J.; Elf, S.; Zhou, Y.; Wen, Y.; Vinkenborg, J. L.; Fan, J.; Kang, H.; Lin, R.; Han, D.; Xie, Y.; Karpus, J.; Chen, S.; Ouyang, S.; Luan, C.; Zhang, N.; Ding, H.; Merkx, M.; Liu, H.; Chen, J.; Jiang, H.; He, C. Inhibition of Human Copper Trafficking by a Small Molecule Significantly Attenuates Cancer Cell Proliferation. *Nat. Chem.* **2015**, *7*, 968–979.

(52) Wang, Q.; Franz, K. J. Stimulus-Responsive Prochelators for Manipulating Cellular Metals. *Acc. Chem. Res.* **2016**, *49*, 2468–2477.

(53) Gaur, K.; Alexandra, M. V; Duran-camacho, G.; Vega-cartagena, M.; Loza-rosas, S. A.; Acevedo, X. R. Iron and Copper Intracellular Chelation as an Anticancer Drug Strategy. *Inorganics* **2018**, *6* (126).

(54) Polishchuk, R. S. Activity and Trafficking of Copper-Transporting ATPases in Tumor Development and Defense against Platinum-Based Drugs. *Cells* **2019**, *8*, 1080.

(55) Akerfeldt, M. C.; Tran, C. M. N.; Shen, C.; Hambley, T. W.; New, E. J. Interactions of Cisplatin and the Copper Transporter CTR1 in Human Colon Cancer Cells. *J. Biol. Inorg. Chem* **2017**, *22*, 765–774.

(56) Bizjak, M.; Malavašič, P.; Dolinar, K.; Pohar, J.; Pirkmajer, S. Combined Treatment with Metformin and 2-Deoxy Glucose Induces Detachment of Viable MDA-MB-231 Breast Cancer Cells in Vitro. *Sci. Rep.* **2017**, *7* (1761).

(57) Czarnomysy, R.; Bielawski, K.; Bielawska, A. Synergistic Action of Cisplatin and Echistatin in MDA-MB-231 Breast Cancer Cells. *Mol. Cell Biochem* **2017**, *427*, 13–22.

(58) Karginova, O.; Weekley, C. M.; Raoul, A.; Alsayed, A.; Wu, T.; Lee, S. S.; He, C.; Olopade, O. I. Inhibition of Copper Transport Induces Apoptosis in Triple-Negative Breast Cancer Cells and Suppresses Tumor Angiogenesis. *Mol. Cancer Ther.* **2019**, No. 17, 873–886.

Chapter 3

Copper Mediated Oxidation of Imidazopyrazinones Inhibits Marine Luciferase Activity*

---

*This chapter is adapted from a submitted manuscript for publication entitled: Copper Mediated Oxidation of Imidazopyrazinones Inhibits Marine Luciferase Activity. Vanessa Lee collected all spectroscopic data including the electronic absorption spectra.

3.1 Abstract

The development of bioluminescent based tools has seen steady growth in the field of chemical biology over the past few decades ranging in uses from reporter genes to assay development and targeted imaging. More recently marine based luciferases such as *Gaussia*, *Renilla*, and the engineered Nano- luciferases have been utilized due to their intense luminescence relative to firefly luciferin/luciferase. The emerging importance of these systems warrants investigations into the components that affect their light production. Previous work has reported that one marine luciferase, *Gaussia*, is potently inhibited by copper salt. The mechanism for inhibition was not elucidated but was hypothesized to occur via binding to the enzyme. In this study, we provide the first report of a group of non-homologous marine luciferases also exhibiting marked decreases in light emission in the presence of copper(II). We investigate the mechanism of action behind this inhibition and demonstrate that the observed copper inhibition does not stem from a luciferase interaction but rather the chemical oxidation of imidazopyrazinone luciferins generating inert, dehydrated luciferins.

3.2 Introduction

Bioluminescence is a natural phenomenon where a small molecule substrate, luciferin, is oxidized by its enzyme, luciferase. This enzyme-catalyzed reaction results in the production of photons through relaxation of an excited state intermediate. Though observed in nature for thousands of years, it was not until the second half of the 20th century that scientists began to fully characterize and elucidate the molecular mechanisms of bioluminescence.1 Since then, bioluminescent systems have steadily gained popularity as a unique tool in biochemical research ranging in uses from reporter genes to molecular imaging probes.[2,3,4,5,6] Compared to other optical modalities such as fluorescence, bioluminescence-based platforms find a key advantage in requiring no excitation light, affording near-zero background signal and minimizing phototoxicity.[7]

The three most well-studied classes of bioluminescent systems are insect, bacterial, and marine luciferin/luciferases.[8] The marine ecosystems in particular contain a vast diversity of luminescent organisms. For example, in one study about 76% of individuals in the water column were observed to have luminescent capability.[9] Currently known marine-based bioluminescent systems are representative of different taxa, are of various complexity, and are of different molecular mechanisms. Interestingly, while diverse in the structures of their enzymes, most of these systems show similarities in their substrates, utilizing luciferins with a shared imidazopyrazinone core, with coelenterazine (CTZ, Figure 3.1) being the most well-studied and commonly used.[10]

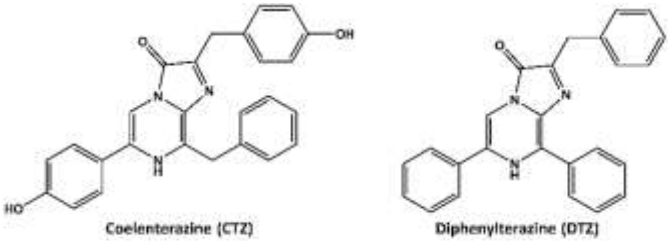

Figure 3.1 Chemical structures of native marine luciferin, coelenterazine, and synthetic analog, diphenylterazine.

3.3 Results and Discussion

Biochemical research on coelenterazine-utilizing organisms to date have primarily focused on the *Renilla reniformis, Gaussia princeps,* and *Oplophorus gracilirostis* organisms.[11,12,13] Additionally, Nanoluciferase (Nluc), a recently engineered luciferase derived from *Oplophorus* luciferase, has gained notable traction due to its small size, high thermal stability, and intense light emission in the presence of its partner imidazopyrazinone, furimazine.[14] It has previously been reported that *Gaussia* luciferase is potently inhibited by Cu(II) ions.[15,16] Inhibition was posited to occur via direct interactions with the enzyme. However, in our previous work developing a copper-responsive bioluminescent imaging probe based on the imidazopyrazinone, diphenylterazine (DTZ, Figure 3.1), and luciferase, Nluc, we observed bioluminescence inhibition at high Cu(II) concentrations despite the dissimilarities between the *Gaussia* luciferase and Nluc structure.[17] This led us to the hypothesis that copper-mediated inhibition of marine luciferase bioluminescence may actually arise from transformation of the imidazopyrazinone substrate core.

We validated that Cu(II) ions could alter the activity of a series of imidazopyrazinone-based luciferases. We investigated the effects of Cu(II) on the bioluminescence of *Renilla,* Nano-, and *Gaussia* luciferases. These marine luciferases are non-homologous as they evolved independently.[18] For these studies we used CTZ for all three luciferases (Figure 3.2a-c) as well as DTZ with Nanoluciferase (Figure 3.2d) as *Renilla* and *Gaussia* luciferases do not accept DTZ. In all cases, bioluminescence was potently inhibited by Cu(II).

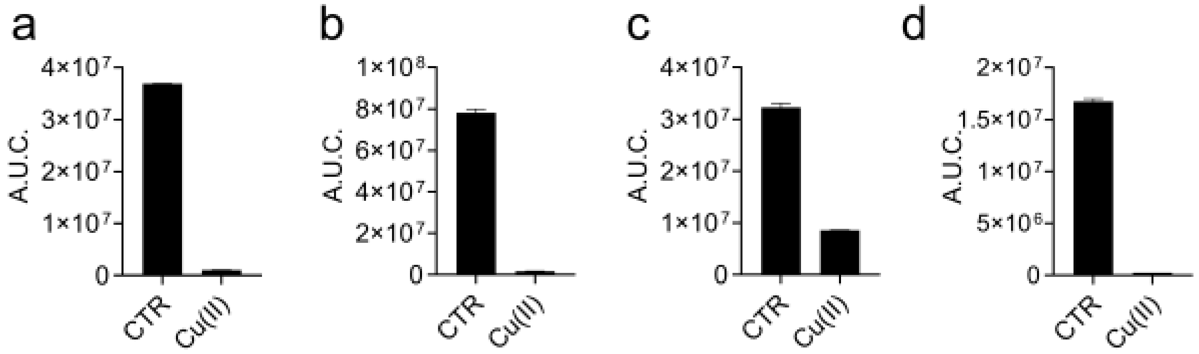

Figure 3.2 Calculated area under the curve over twenty minutes of kinetic luminescence measurements of CTZ (10 µM) in the absence or presence of Cu(II) ions (100 µM) with A) *Renilla*, B) Nano- or C) *Gaussia* luciferases (0.4 µg/mL), or D) of DTZ (10 µM) in the absence or presence of Cu(II) ions (100 µM) with Nanoluciferase (0. 4 µg/mL).

We therefore aimed to determine the structural impact of Cu(II) on the partner luciferins (DTZ and CTZ) by Cu(II) as the driver of bioluminescence inhibition. As inhibition was observed with both substrates, we chose to use DTZ for the majority of studies due to its increased stability relative to CTZ and its facile synthesis. The conjugated nature of marine luciferins lends itself to study by electronic absorption spectroscopy. To begin understanding the interactions between the luciferins and Cu(II), we performed a metal screen with CTZ and DTZ in the presence and absence of a panel of biologically relevant metals (Figure 3.3). We noted significant spectral changes upon addition of both copper(II) and iron(III).

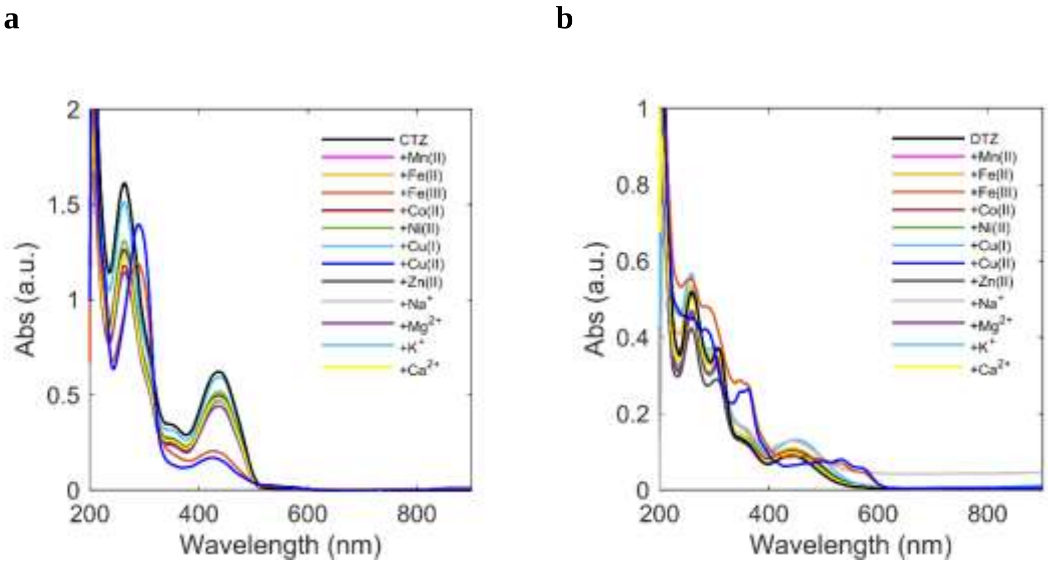

Figure 3.3 Electronic absorption spectra of 50 µM (A) CTZ and (B) DTZ alone (black) and upon addition of 50 µM biologically relevant metal ions. Significant spectral changes occur in both CTZ and DTZ spectra upon addition of Cu(II) and Fe(III) ions indicating interactions between the luciferins and these metal ions.

Interestingly, in enzyme studies analogous to those presented in Figure 3.2 but performed with Fe(III), no inhibition of light output was observed (Figure 3.4). This could mean that the interaction with Fe(III) is either not as strong as in the case with Cu(II) or may have slower kinetics than the enzymatic oxidation reaction.

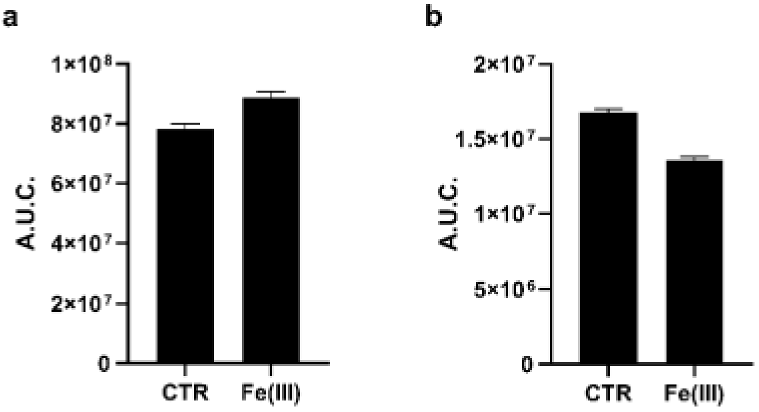

Figure 3.4 Calculated area under the curve over twenty minutes of kinetic luminescence measurements of 10 µM (A) CTZ or (B) DTZ in the absence or presence of Fe(III) ions (100 µM) with recombinant Nluc (0.4 µg/mL).

Furthermore, the original spectrum was not able to be restored after addition of the non-specific chelator EDTA (Figure 3.5). This would suggest that the interaction occurring is non-reversible and therefore would be unlikely to be a metal-coordination complex.

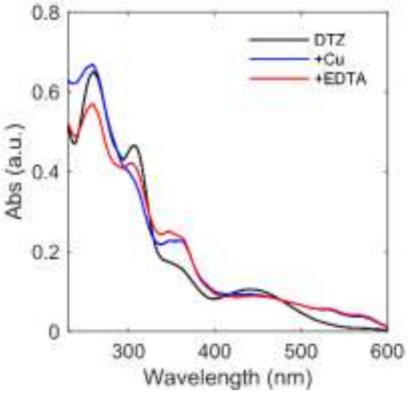

Figure 3.5 Electronic absorption spectrum of 50 µM DTZ with and without addition of 50 µM $CuSO_4$ in ethanol. Spectral changes suggest oxidation of DTZ upon interaction with copper. Upon addition of 500 µM EDTA, the DTZ spectrum is not restored which confirms that the interaction is irreversible by chelation of the metal ion.

The same electronic absorption spectroscopy studies were performed with CTZ resulting in similar spectral changes (Figure 3.3a), suggesting the Cu(II) interaction is not a DTZ dependent effect and is likely occurring at the shared imidazopyrazinone core. The irreversible nature of the interaction as well as the similarity in effect with Fe(III) led us to investigate potential redox events involving Cu(II). To determine if Cu(II) is reduced to Cu(I) in the presence of DTZ, we used a colorimetric Cu(I) chelator, bathocuproine disulfonic acid (BCS), to confirm the presence of Cu(I) in solution (Figure 3.6).

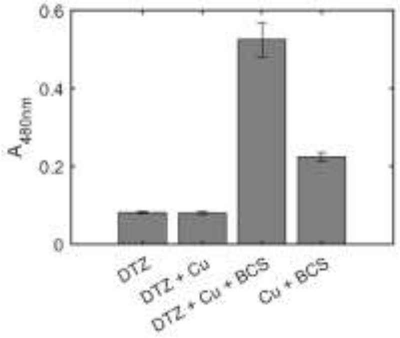

Figure 3.6 Bathocuproine disulfonic acid (BCS) is a copper(I)-specific colorimetric chelator that absorbs at 480 nm when complexed. Addition of 500 µM BCS to a solution of 50 µM DTZ and 50 µM $CuSO_4$ results in increased absorbance at 480 nm indicating reduction of Cu(II) by DTZ.

Indeed BCS shows a significant increase in absorption at 480 nm in the presence of DTZ and $CuSO_4$ suggesting that DTZ is able to reduce Cu(II) to Cu(I). These spectroscopic data point to a redox-driven chemical reaction over Cu(II) coordination as the cause of the observed enzyme inhibition.

We thus tested the hypothesis that Cu(II) addition may drive DTZ oxidation towards a luciferase-inert compound. Reverse-phase LC-MS analysis of DTZ in the presence of Cu(II) showed the emergence of a peak exhibiting a ten-minute increase in retention time relative to DTZ alone (Figure 3.7). The increased retention time suggests that the oxidized product is more non-polar than DTZ. The mass of the species in this peak (m/z = 376.1, Figure 3.8), corresponds to a loss of 2 protons corroborating an oxidation reaction.

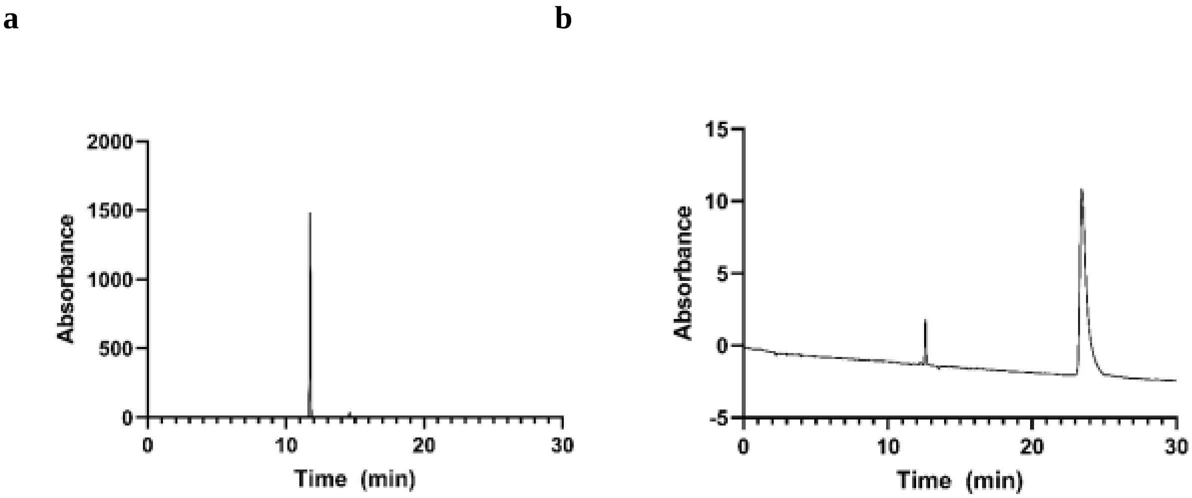

Figure 3.7 Chromatograms of (a) DTZ and (b) DTZ after reaction with Cu(II) reveal a 10 minute longer retention time.

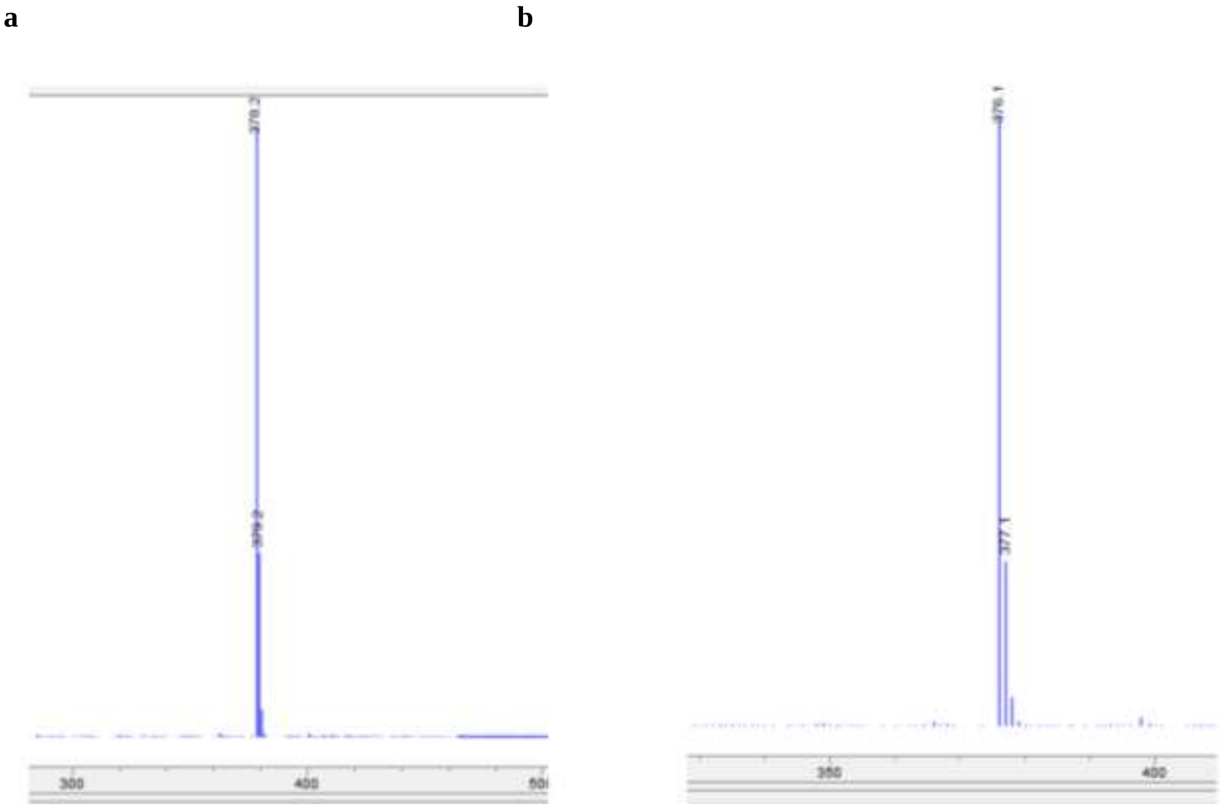

Figure 3.8 Mass spectra of (a) DTZ and (b) DTZ after reaction with Cu(II) show an m/z of 378.2 and 376.1 for DTZ and Cu(II) reacted DTZ respectively.

We applied NMR spectroscopy to observe any changes in the 1H spectra (Figure 3.9). DTZ was reacted with excess Cu(II) until full conversion to oxidized DTZ was observed by LC-MS. As Cu(II) is paramagnetic and may cause universal peak broadening, a liquid extraction with DCM/H_2O was performed to remove the metal ion from the sample prior to NMR analysis.

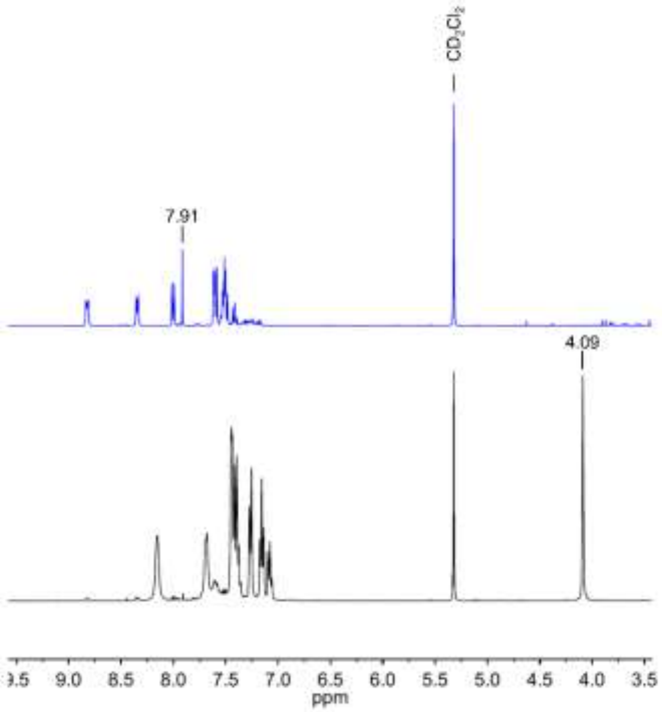

Figure 3.9 ^{1}H NMR spectra of oxidized DTZ (top) and DTZ (bottom) measured in CD2Cl2 as solvent shows a loss of methylene proton signals at 4.09 ppm and appearance of a vinyl proton signal at 7.91 ppm after oxidation by Cu(II).

The most notable changes in the NMR spectra were the absence of methylene proton signals from the benzyl group of DTZ at 4.09 ppm and the appearance of a peak at 7.91 ppm. This coupled with the LC-MS data suggests the formation of a vinyl proton which could only occur at the benzylic carbon of DTZ. Therefore, we hypothesized that Cu(II) oxidized DTZ to dehydrated DTZ (dhDTZ, Figure 3.10).

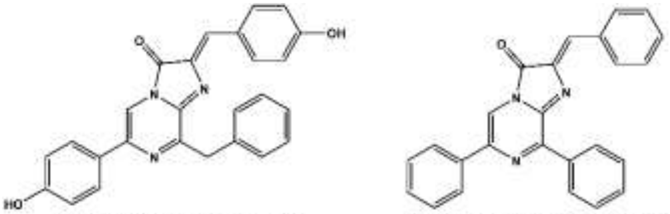

Dehydrated coelenterazine (dhCTZ)

Dehydrated diphenylterazine (dhDTZ)

Figure 3.10 Structure of dehydrated diphenylterazine (dhDTZ) and dehydrated coelenterazine (dhCTZ).

Indeed, copper mediated oxidation of similar molecules containing dihydropyrazine moieties have been previously reported in the literature.[19,20] Brook et al. noted the structural uniqueness of 1,4-dihydropyrazines related to the cyclic 8π electron system they possess imparting antiaromatic character.[19] This electron richness allows them to readily undergo the loss of an electron generating a radical cation. In 2016, Li et al. reported a new Cu(II) sensor that is based on the oxidation of a dihyropyrazine containing compound.[20] Taken together, this strongly supports the hypothesis that Cu(II) is able to oxidize coelenterazine and related marine luciferases generating the dehydrated forms depicted in Figure 3.10.

Interestingly, dehydrated coelenterazine (dhCTZ) has previously been observed in nature and reported in the literature independent of any Cu(II)-mediated mechanism. The first report of a dehydrated coelenterazine was in 1977 from Inouye et. al where dhCTZ was isolated from the liver of the squid, Watasenia scintillans, suggesting perhaps the dehydrated form plays a role in storage.[20] Here researchers noticed that the isolated compound was two mass units less then CTZ and found that reduction with $NaBH_4$ restored CTZ. Similarly, when we treated dhDTZ with $NaBH_4$, we were able to restore light output with Nanoluciferase (Figure 3.11).

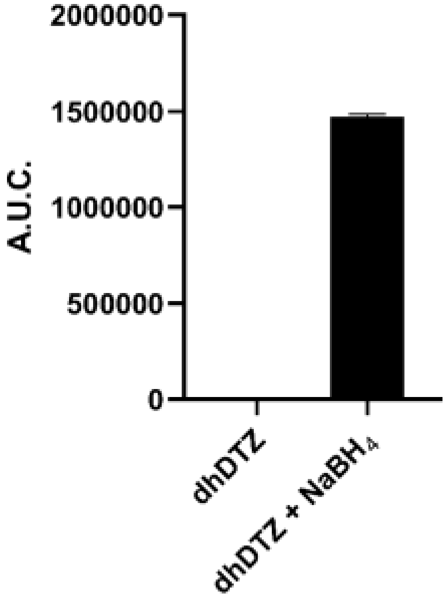

Figure 3.11 Calculated area under the curve over fifteen minutes of kinetic luminescence measurements of 10 µM dhDTZ with or without preincubation with $NaBH_4$ (100 µM) in the presence of recombinant Nluc (0.4 µg/mL)

Furthermore, in 1993, dehydrated coelenterazine was found in the light organs of another luminous squid, Symplectoteuthis oualaniensis.[22] In this report, the authors further found that dehydrocoelenterazine had no luminescent activity but acetone and dithiothreitol adducts formed by addition to the vinyl group had luminescent activity. Thus, the authors proposed a mechanism in which protein-dhCTZ adducts served to stabilize the chromophore in the protein binding pocket. Indeed, fifteen years later in 2008 Isobe et al. confirmed that cysteine-390 is the binding site of the photoprotein symplectin where Cys390 forms an adduct at the vinyl group of dhCTZ to yield the luminescent chromophore.[23]

More recently in 2008, a second marine organism, Pholas dactylus, which is a marine bivalve mollusk was proposed to utilize dhCTZ for its luminescent activity.[24] Indeed, a year later the same group successfully showed that similar to symplectin, pholasin's prosthetic group was also formed through an adduct formation of dhCTZ at a free cysteine in the protein.[25] Interestingly the luciferase is a 150-kDa copper containing enzyme characterized as a peroxidase.[26] Taken together with our findings, we propose that the copper center may have functions beyond peroxidase activity. For example, it is possible that CTZ is converted to dhCTZ by the copper-containing luciferase before being loaded into pholasin to form the active adduct.

3.4 Conclusion & Outlooks

In conclusion, we have determined for the first time that the copper-dependent inhibition of non-homologous marine luciferases originates from Cu(II)-mediated oxidation of the shared imidazopyrazinone structure rather than from interactions with the enzyme. This is, to our knowledge, the first example of a metal mediated transformation of marine luciferin substrates. This information not only provides valuable insight towards the development of future biotechnologies with said marine luciferin/luciferase systems but also opens the door to further questions and possibilities for the evolution and molecular mechanisms surrounding native marine bioluminescent systems.

3.5 Materials & Methods

Materials. *Gaussia*, *Renilla*, and Nano- luciferases were all purchased commercially (Promega, Raybiotech, & Nanolight technologies). Diphenylterazine (DTZ) was synthesized as previously described.[16] Coelenterazine (CTZ) was purchased from GoldBio. ^{1}H and ^{13}C NMR spectra were collected at room temperature in CD_2Cl_2 on a 400 Bruker Varian NMR spectrometer. All chemical shifts are reported as δ ppm relative to the residual solvent peak at 5.32 (CD_2Cl_2) for 1H. Electrospray ionization mass spectral analyses were performed using an LC-MSD system

(Agilent Technologies 1260 Infinity II coupled with an Agilent Technologies InfinityLab LC/MSD).

Luminescence Measurments. All luminescence measurements were performed similarly to previously reported methods.[16] In short, metal ion solutions were prepared in water, luciferin stock solutions were prepared in pure ethanol and diluted in phosphate buffer, and luciferase solutions were prepared freshly in phosphate buffer. Readings were measured on a SpectraMax i3x plate reader.

Reaction of DTZ with Cu(II). DTZ (245 mg, 0.650 mmol) was dissolved in methanol and to this was added $CuSO_4$ (161 mg, 0.650 mmol). The solution was stirred at room temperature until complete conversion was observed by LCMS. After this the reaction was poured into water and extracted into dichloromethane. The combined dichloromethane extracts were then washed with saturated sodium chloride, collected, and dried over magnesium sulfate. After filtration, the crude product was concentrated under reduced pressure. The crude mixture was then purified by silica gel column chromatography using DCM as eluent and was subsequently recrystallized in acetonitrile to afford dhDTZ as dark purple powder (100 mg, 40% yield). ^{1}H NMR (400 MHz, CD_2Cl_2) δ 8.81- 8.83 (m, 2H), 8.33-8.35 (m, 2H), 7.99-8.01 (d, 2H), 7.91 (s, 1H), 7.60-7.62 (t, 3H), 7.58 (s, 1H), 7.48-7.55 (m, 5H), 7.39-7.43 (m, 1H). Low-resolution mass spectrometry (LRMS) (m/z): $[M+H]^+$ calculated for $C_{25}H_{17}N_3O$ 376.1; found, 376.1.

Electronic absorption spectroscopy. UV-Vis studies were performed on a Shimadzu UV-1900i at room temperature using quartz cuvettes (Starna) with a pathlength of 1 cm. All spectra were referenced to water and buffer subtracted. Stock solutions of 1 mM luciferin in ethanol, 1 mM metal salts in water, 10 mM EDTA in water, and 10 mM BCS in water were prepared. The final concentrations were 50 μM luciferin, 50 μM metal salts, 500 μM EDTA, and 500 μM BCS using ethanol as the buffer to prevent precipitation of the luciferin. Excess BCS was used to detect the presence of copper(I) in solution, and excess EDTA chelated free copper ions in solution

3.6 References

(1) Roda, A. Chemiluminescence and Bioluminescence: Past, Present and Future. Royal Society of Chemistry Publishing. 2011.

(2) Moroz, M. A.; Zurita, J.; Moroz, A.; Nikolov, E.; Likar, Y.; Dobrenkov, K.; Lee, J.; Shenker, L.; Blasberg, R.; Serganova, I.; et al. Mol. Ther. Oncolytics 2021, 21, 15.

(3) Neefjes, M.; Housmans, B. A. C.; Akker, G. G. H. Van Den; Rhijn, L. W. Van. Sci. Rep. 2021, 11, 1.

(4) Aron, A. T.; Heffern, M. C.; Lonergan, Z. R.; Vander, M. N.; Blank, B. R.; Spangler, B.; Zhang, Y.; Min, H.; Stahl, A.; Renslo, A. R.; et al. PNAS. 2017, 114, 12669.

(5) Van de Bittner, G. C.; Bertozzi, C. R.; Chang, C. J. J. Am. Chem. Soc. 2013, 135, 1783.

(6) Rathbun, C.; Prescher, J. Biochemistry. 2017. 56, 5178-5184.

(7) Serganova, I.; Blasberg, R. J. Nucl. Med. 2019, 60, 1665.

(8) Fleiss, A.; Sarkisyan, K. S. Curr. Genet. 2019, 65, 877.

(9) Martini, S.; Haddock, S. H. D. Sci. Rep. 2017, 7, 1.

(10) Krasitskaya, V. V; Bashmakova, E. E.; Frank, L. A. Int. J. Mol. Sci. 2020, 21, 1.

(11) Jiang, T.; Yang, X.; Zhou, Y.; Yampolsky, I.; Du, L.; Li, M. Org. Biomol. Chem. 2017, 15, 7008.

(12) Tannous, B. A.; Kim, D.; Fernandez, J. L.; Weissleder, R.; Breakefield, X. O. Mol. Ther. 2005, 11, 435.

(13) Satoshi, I.; Watanabe, K.; Nakamura, H.; Shimomura, O. Fed. Eur. Biochem. Sci. 2000, 481, 19.

(14) Hall, M. P.; Unch, J.; Binkowski, B. F.; Valley, M. P.; Butler, B. L.; Wood, M. G.; Otto, P.; Zimmerman, K.; Vidugiris, G.; Machleidt, T.; et al. 2012.

(15) Inouye, S.; Sahara, Y. Biochem. Biophys. Res. Commun. 2008, 365, 96.

(16) Galaway, F.; Wright, G. J. Sci. Rep. 2020, 10, 1.

(17) O'Sullivan, J. J.; Medici, V.; Heffern, M. C. Chem. Sci. 2022, 13, 4352.

(18) Delroisse, J.; Duchatelet, L.; Flammang, P.; Mallefet, J. Front. Mar. Sci. 2021, 8, 1.

(19) Brook, D. J. R.; Haltiwanger, R. C.; Koch, T. H. J. Am. Chem. Soc. 1992, 114, 6017.

(20) Li, J.; Chen, S.; Zhang, P.; Wang, Z.; Long, G.; Ganguly, R. Chem. Asian. J. 2016, 11, 136.

(21) Inoue, S.; Taguchi, H.; Murata, M.; Kakoi, H.; Goto, T. Chem. Lett. 1977, 3, 259.

(22) Takahashi, H.; Isobe, M. Bioorg. Med. Chem. Lett. 1993, 3, 2647–2652.

(23) Isobe, M.; Kuse, M.; Tani, N.; Fujii, T.; Matsuda, T. Proc. Japanese Acad. Sci. 2008, 84.

(24) Kuse, M.; Tanaka, E.; Nishikawa, T. Bioorg. Med. Chem. Lett. 2008, 18, 5657.

(25) Tanaka, E.; Kuse, M.; Nishikawa, T. ChemBioChem 2009, 10, 2725.

(26) Dunstan, S. L.; Sala-newby, G. B.; Bermu, A.; Taylor, K. M.; Campbell, A. K. J. Biol. Chem. 2000, 275, 9403.

Chapter 4

Development of an ATP-Independent Bioluminescent Probe for Detection of Extracellular Hydrogen Peroxide*

---

* This chapter is a modified version of the following published article: O'Sullivan, J.J.; Heffern, M.C. Development of an ATP-independent bioluminescent probe for detection of extracellular hydrogen peroxide, *Organic & Biomolecular Chemistry*, **2022**, *20*, 6231-6238.

4.1 Abstract

This work reports a new ATP-independent bioluminescent probe (bor-DTZ) for detecting hydrogen peroxide that is compatible with the Nanoluciferase enzyme. The probe is designed with an arylboronate ester protecting group appended to a diphenylterazine core via a self-immolative phenolate linker. Reaction with hydrogen peroxide reveals diphenylterazine, which can then react with Nanoluciferase to produce a detectable bioluminescent signal. Bor-DTZ shows a dose-dependent response to hydrogen peroxide and selectivity over other biologically relevant reactive oxygen species and can be applied to detect either intra- or extracellular species. We further demonstrate the ability of this platform to monitor fluxes in extracellular hydrogen peroxide in a breast cancer cell line in response to the anticancer treatments, cisplatin.

4.2 Introduction

Hydrogen peroxide (H_2O_2) is a key molecule in biological redox metabolism and stress.[1] On the one hand, H_2O_2 is a hallmark of oxidative stress[2] whereby its generation alongside other reactive oxygen species results in direct or indirect oxidation of various biomolecules such as lipids[3], DNA[4], RNA[5], and proteins[6]. On the other hand, endogenous levels of H_2O_2 have been shown to play important roles in cellular signaling in processes ranging from immune response to cell proliferation.[7,8,9,10,11] For example, neutrophils have been shown to utilize NADPH oxidase systems to generate millimolar quantities of H_2O_2 as a defense against foreign microbes.[12] H_2O_2 imbalances have been implicated in variety of disease pathologies such as cancer,[13,14] diabetes,[15,16] inflammation[17,18] and cardiovascular diseases[19,20]. Tools for monitoring H_2O_2 fluxes are vital for understanding the molecular mechanisms at play regarding both the physiological and pathological roles H_2O_2 plays in biological systems.

Small molecules[21,22,23,24,25] employing various reaction triggers such as sulfonic esters[22], diketones[26,27], and arylboronates[28] have been widely employed for fluorescence-based sensing of H_2O_2. In particular, the arylboronate reaction-based triggers have been extensively adopted mainly owing to their high selectivity and sensitivity in addition to their fast reaction kinetics relative to other H_2O_2 reactive moieties.[29,30,31,32,33] Although fluorescence-based imaging probes have provided valuable insight into H_2O_2 dynamics, they are primarily applied to monitoring intracellular H_2O_2 dynamics, given that the larger volume and diffuse nature of the extracellular space and extracellular fluids can lead to signal dilution. Aside from fluorescence-based imaging probes researchers have also turned to the development of alternative modalities with improved sensitivity, such as such as electrochemical sensors, but many of these are not amenable to *in vivo* work.[34,35,36]

To fill this gap, bioluminescence has become an increasingly favorable candidate for molecular imaging platforms.[37] Bioluminescence results in the emission of photons via the enzymatic oxidation of a small molecule luciferin by its cognate luciferase enzyme. Imaging with this technique offers the benefits of high signal-to-noise ratio as well as the ability to endow cell and tissue specificity through the genetic encoding of the luciferase.[38] The phenomenon has been adapted for sensing molecular analytes of interest by chemical modification of the luciferin, termed “caging”, which precludes interaction with its luciferase pair.[39,40] Upon chemo-selective reaction with the analyte the native luciferin is restored and subsequent oxidation by its luciferase results in the production of detectable photons. This strategy has been successfully employed for the detection of intracellular H_2O_2 using a firefly luciferin caged with an arylboronic acid.[41,42] While capable of detecting intracellular H_2O_2 and in the tissues of living mice, an inherent property of the firefly luciferin/luciferase system is its dependence on ATP, therefore limiting the probes’ applicability to intracellular applications and regimes where ATP levels are not significantly perturbed. Development of probes for the extracellular space are of particular interest due to the transient nature of signaling biomolecules like H_2O_2. The ability to monitor extracellular H_2O_2 would provide valuable insight into both the physiological roles that this oxidative metabolite plays in extracellular signaling as well as a means to monitor oxidative stress in disease progression. Unlike the firefly luciferases, marine luciferases and their derivatives do not require ATP, making these platforms adaptable to extracellular applications.[43,44]

To this end, we report the design, synthesis, and evaluation of a new bioluminescent based probe for detecting H_2O_2 in the extracellular space using a marine luciferin/luciferase pair. We report a boronate ester caged diphenylterazine (bor-DTZ), a small molecule luciferin with an H_2O_2 reactive boronate ester and self-immolative linker attached to the carbonyl of the parent diphenylterazine (DTZ). Upon H_2O_2 induced oxidative hydrolysis and subsequent self-immolation, DTZ is generated which can then interact with the engineered marine luciferase, Nanoluciferase (Nluc)[45], to produce a detectable bioluminescent signal. We demonstrate the ability of bor-DTZ to selectively detect H_2O_2 over other biologically relevant ROS and show that it can detect exogenous and endogenous H_2O_2 in live cells. We further show the probes utility in monitoring changes to extracellular H_2O_2 in response to a clinically relevant cancer treatment in a human breast cancer cell model.

Scheme 3.1 Design of bor-DTZ for H_2O_2-responsive Bioluminescence[a]

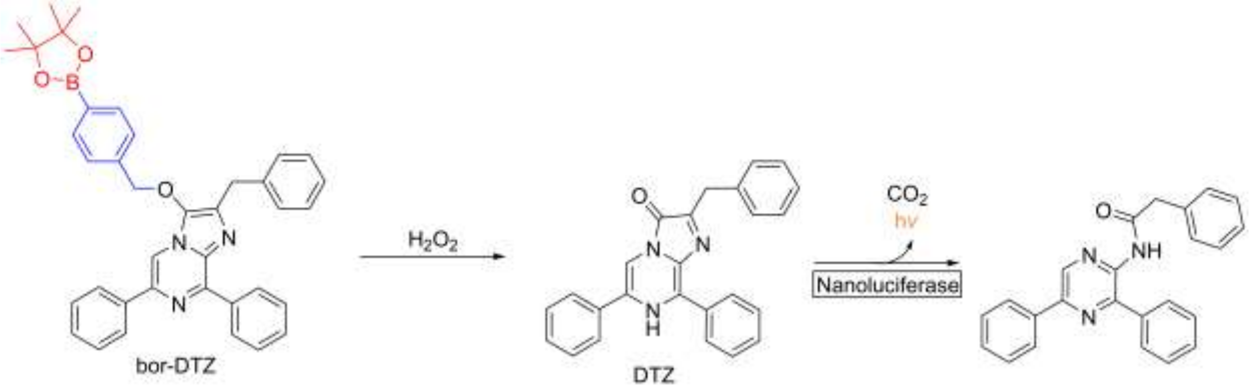

[a] Red: H_2O_2-responsive cage, blue: self-immolative linker, black: diphenylterazine (DTZ) core.

4.3 Results and Discussion

4.3.1 Synthesis and reactivity of bor-DTZ

The recently engineered Nanoluciferase (Nluc) is a marine based luciferase derived from a deep sea shrimp which has gained attention due to its small size, high thermal stability, and highly intense luminescence in the presence of its engineered substrate, furimazine, relative to firefly luciferase.[46] We recently demonstrated that modifying imidazopyrazinone substrates at the imidazoyl carbonyl with a reactive group responsive to copper(II) could yield caged luciferins compatible with Nluc, with the synthetic imidazopyrazinone, diphenylterazine (DTZ), yielding optimal response among a series of caged imidazopyrazinone derivatives.[47] Thus, to design a bioluminescence agent for the Nluc system that could respond to hydrogen peroxide, we paired the well-studied arylboronate ester cage to diphenylterazine (DTZ) with a self-immolating phenolate linker (scheme 2). The arylboronate ester cage is expected to undergo selective oxidative hydroxylation by H_2O_2, which in turn triggers an electron cascade to reveal the parent DTZ for recognition by Nluc. We synthesized the native DTZ according to previously published methods[47,48] and then performed a nucleophilic substitution with 4-bromomethylphenylboronic acid pinacol ester under basic conditions to afford bor-DTZ in 18% yield. We attributed the relatively low yield due to a side product where the pinacol ester adds to the alkene at the C2 position as well as DTZ being inherently prone to oxidation. However, it is important to note that for subsequent biological assays bor-DTZ can be used in concentrations as low as 1 µM such that low milligram quantities of bor-DTZ can be used for hundreds of assays depending on sample size.

Scheme 3.2 Synthesis of bor-DTZ

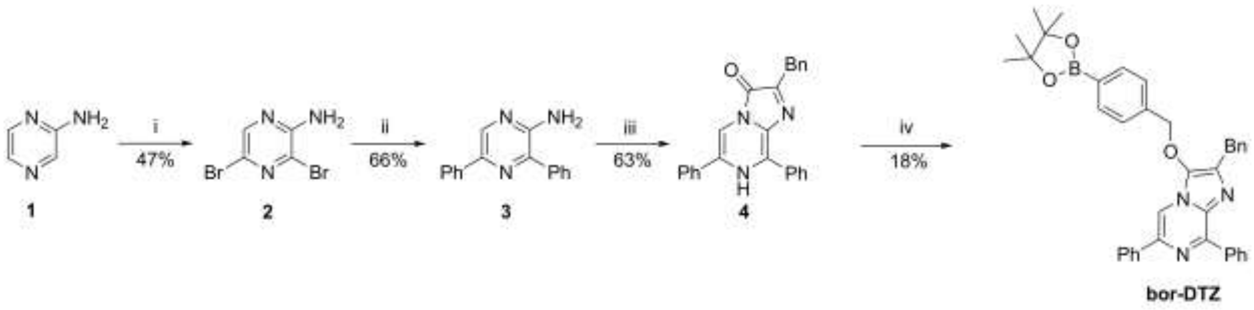

^{a}**Reagents and conditions:** (i) NBS, $CHCl_3$, 3 h; (ii) Phenylboronic acid, $Pd(PPh_3)_4$, K_2CO_3, 1,4-dioxane, H_2O, 80 ºC, 12 h; (iii) 1,1-diethoxy-3-phenylpropan-2-one, EtOH, H_2O, cat. HCl, 80 ºC, 12 h; (iv) 4-Bromomethylphenylboronic acid pinacol ester, Cs_2CO_3, KI, MeCN, 12 h.

To evaluate the reactivity of bor-DTZ, its luminescence output was measured upon addition of analytes of interest in the presence of purified recombinant Nanoluciferase (rNluc) in aqueous buffer. Selectivity was assessed by comparing reactivity with H_2O_2 to a panel of reactive oxygen species as well as glutathione, a biologically relevant reducing agent. The normalized total photon flux was determined by calculating the area under the curve of the kinetic reading over 30 minutes and normalizing values from all ROS tested to that of bor-DTZ alone (Figure 3.1 a).

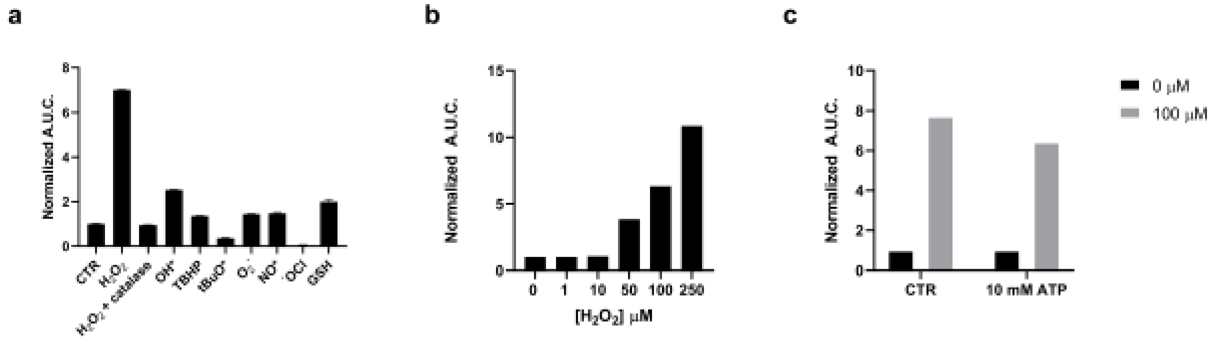

Figure 3.1 Reactivity of bor-DTZ (1µM) reported as calculated area under the curve of luminescence output over 20 minutes in the presence of analytes and rNluc (0.4 µg/mL), normalized to bor-DTZ in the absence of analytes; all solutions in DPBS, pH 7.4, 37°C, emission range: 300-850 nm. (a) Reactivity of bor-DTZ in the presence of various biologically relevant ROS (100 µM) and glutathione (GSH, 10 mM) . Error bars denote n=3, SEM. (b) Light output of bor-DTZ in the presence of various concentrations of H_2O_2 (0-250 µM) and rNluc (0.4 µg/mL).

(c) Responsiveness of bor-DTZ to H_2O_2 (100 µM) in the presence of ATP (10 mM). Data points are normalized to the control without H_2O_2 added.

A representative kinetic curve for bor-DTZ in the presence of 100 µM H_2O_2 can be seen in Figure 3.2. We observed that bor-DTZ exhibits exceptional selectivity towards H_2O_2 relative to the other ROS tested. We confirmed that the turn-on response was due to H_2O_2 by observing a loss in signal upon addition of catalase, an enzyme that rapidly degrades H_2O_2. Moreover, bor-DTZ demonstrated a dose-dependent response to the H_2O_2 from 50-250 µM (Figure 3.1 b), which is within a biologically-relevant range in the context of the tumor microenvironment.[49,50,51]

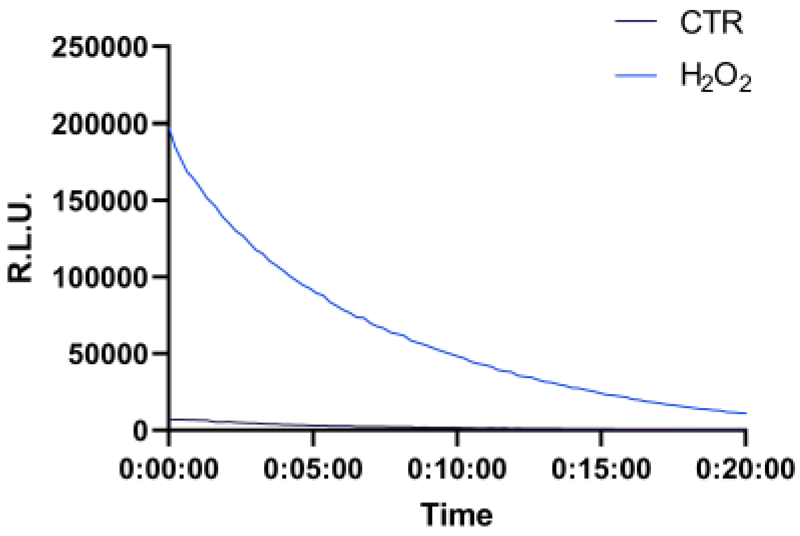

Figure 3.2 Representative kinetic curve of luminescence of bor-DTZ (1 µM) with rNluc (0.4 µg/mL) measured over twenty minutes in the presence and absence of H_2O_2 (100 µM). All solutions in DPBS, pH 7.4, 37°C, emission range: 300-850 nm.

We next assessed whether the signal produced by bor-DTZ was affected by ATP. Previously reported bioluminescence probes for H_2O_2 rely on the firefly luciferase enzyme, which utilizes ATP as a cofactor. The need for ATP limits the probe to mainly intracellular applications where ATP is abundant; additionally, various cellular processes can result in significant changes to

ATP levels, making this cofactor a confounding variable for firefly luciferase-based sensors. Comparison of light output of bor-DTZ to 100 µM H_2O_2 in the presence and absence of 10 mM ATP showed little to no difference (Figure 3.1 c), demonstrating that the probe is indeed ATP-independent, permitting its application to extracellular environments and systems where ATP levels are perturbed.

4.3.2 Detection of Intracellular H_2O_2 by bor-DTZ

Having established the selectivity and sensitivity of bor-DTZ towards H_2O_2 in buffer we next evaluated the H_2O_2 responsiveness in cells. We utilized a breast cancer cell line, MDA-MB-231, engineered to express Nluc intracellularly. To stimulate an increase in intracellular H_2O_2 we treated cells with 500 µM paraquat for 24 hours, which generates intracellular ROS through disruption of mitochondrial respiration.[52] We monitored light output in the presence of both bor-DTZ, and analogous experiments were performed using the parent DTZ. The data is presented as the ratio of the area under the curve of the 1 hour luminescence of bor-DTZ:DTZ in order to normalize for any changes in Nluc expression or cell proliferation due to paraquat treatment (Figure 3.3 a). Representative kinetic curves for the luminescence of both bor-DTZ and DTZ are presented in Figure 3.4.

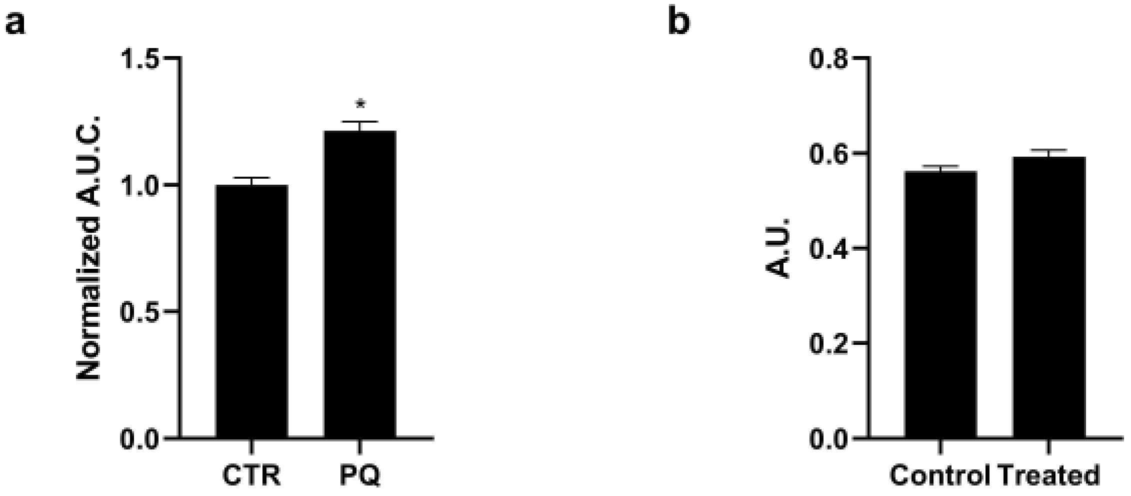

Figure 3.3 (a) Calculated ratio of the area under the curve over 1 hour of bor-DTZ:DTZ (10 µM for both) luminescence from MDA-MB-231 cells expressing Nluc in the absence (control, CTR) or presence of 500 µM paraquat (PQ) for 24 hours. Error bars denote n=3, SEM. Statistical significance was assessed by calculating *p*-values using unpaired t-test, * $p < 0.005$. Measurements performed in DPBS, pH 7.4, 37°C, emission range: 300-850 nm. (b) Average absorbance at 490 nm of Nluc MDA-MB-231 cells after an 8-hour incubation with bor-DTZ followed by the addition of MTS for one hour. Error bars denote n=6.

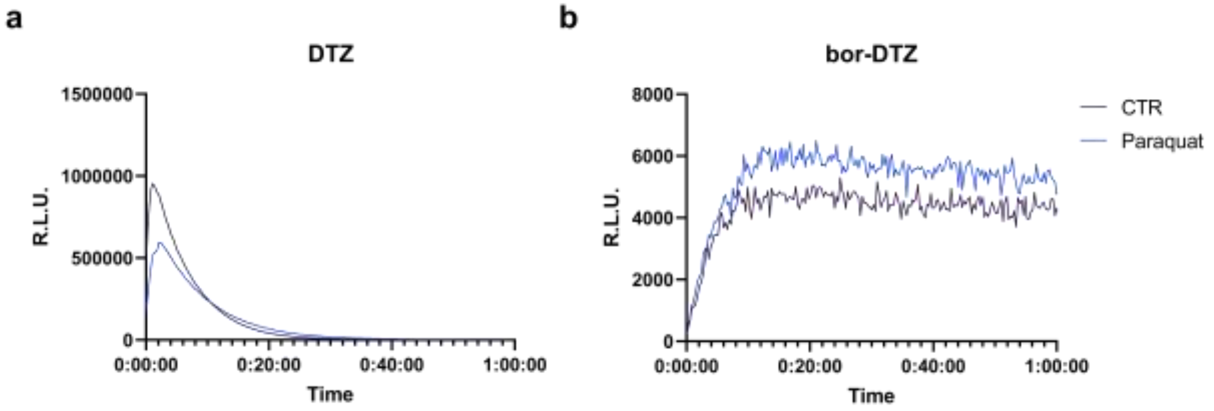

Figure 3.4 Representative kinetic curves of intracellular luminescence of (a) DTZ (10 µM) or (b) Bor-DTZ (10 µM) in Nluc MDA-MB-231 cells that have either been untreated (CTR) or treated with paraquat (500 µM) for 24 hours. All solutions in DPBS, pH 7.4, 37°C, emission range: 300-850 nm.

Indeed, bor-DTZ detected a significant ($p < 0.005$) increase in signal of paraquat-treated cells relative to untreated cells showing the biological utility of this probe in cell-based models. As this particular cell-line is expressing a form of Nluc without a secretion signaling domain the observed signal indicates that bor-DTZ is able to diffuse through the cell membrane. Additionally, the cells are washed with PBS prior to imaging in order to remove any extracellular hydrogen peroxide or Nluc that may be present. We also performed an experiment to assess the toxicity of bor-DTZ towards the cells using an MTS assay where cell viability is measured through reduction of the MTS tetrazolium compound by viable cells to form a colorimetric compound. We found that when Nluc MDA-MB-231 cells are incubated with bor-DTZ (10 µM) for 8 hours there is no significant effect on cell viability (Figure 3.3 b) suggesting minimal to no toxicity.

4.3.3 Detection of extracellular H_2O_2 by bor-DTZ

To determine the ability of bor-DTZ to detect changes in extracellular H_2O_2, we applied bor-DTZ in the media of MDA-MB-231 cells engineered to stably express and secrete Nanoluciferase (secNluc MDA-MB-23). Cells were plated and cultured in Optimem media for 24 hours, then media was removed and placed in a new well plate, H_2O_2 was spiked in and the samples were treated with bor-DTZ, then analyzed for light output over a 20-minute period. As the cells secrete Nluc, no addition of rNluc was required for these experiments. Furthermore, media was removed from cells and the assay was done in the absence of cells to prevent any signal occurring from intracellular activation. We observed slight increases in light output in the 0-10 µM range followed by large increases from 50-250 µM (Figure 3.5 a). This range is in line with physiologically-relevant levels of tumor microenvironments wherein H_2O_2 concentrations can reach as high as 50-100 µM.[49,50,51]

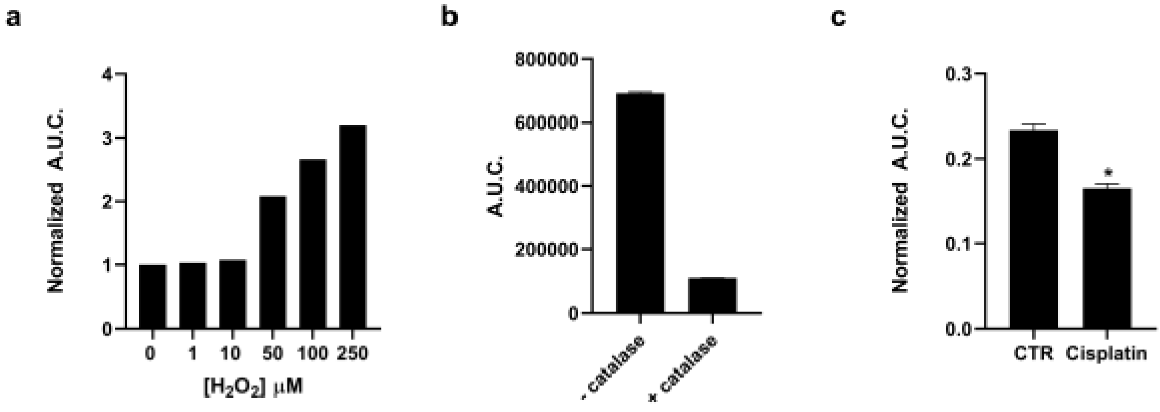

Figure 3.5 (a) Dose-dependent light output as monitored by calculated area under the curve for luminescence over 20 minutes of bor-DTZ (1 µM) in the presence of various concentrations of H_2O_2 (0-250 µM) in cell media removed from secNluc MDA-MB-231 cells. Data points are normalized to the control without H_2O_2 added. (b) Calculated area under the curve of luminescence over 20 minutes of cell media from secNluc MDA-MB-231 cells in the presence or absence of catalase (1 x 10^4 U/L) with 1 µM bor-DTZ. Error bars denotes SEM, n=3. (c) Calculated ratio of the area under the curve over 20 minutes of bor-DTZ:DTZ luminescence from secNluc MDA-MB-231 cells treated with cisplatin (30 µM). Error bars denote SEM, n=3. Statistical significance was assessed by calculating *p*-values using unpaired t-test, * $p < 0.05$. Measurements performed in Optimem, pH 7.4, 37°C, emission range: 300-850 nm.

To determine if bor-DTZ could detect endogenous levels of H_2O_2 in the media, the bioluminescent response of the media was measured in the absence or presence of catalase without addition of exogenous H_2O_2 (Figure 3.5 b). We observe a drastic decrease in light output in cell media that had been spiked with catalase suggesting bor-DTZ could detect basal levels of H_2O_2 in the media. Notably, catalase has little to no effect on the native DTZ/Nluc system (Figure 3.6).

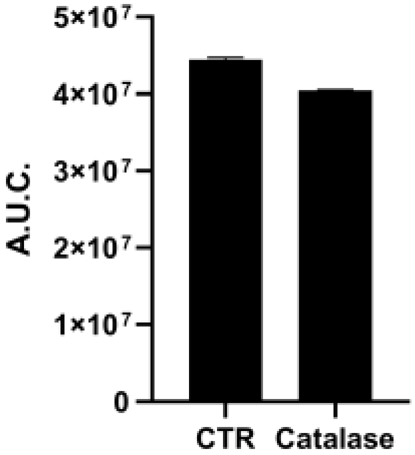

Figure 3.6 Calculated area under the curve of luminescence over 30 minutes of cell media from secNluc MDA-MB-231 cells in the presence or absence of catalase (1 x 10^4 U/L) with 1 µM DTZ. Error bars denotes SEM, n=3.

As oxidative stress and ROS production is a hallmark of breast cancer,[53] we applied bor-DTZ to assess how extracellular H_2O_2 levels are perturbed in the presence of cisplatin, a well-studied anti-cancer agent.[54] The secNluc MDA-MB-231 cells were plated and treated with cisplatin for 16 hours before removing the media from the cells and monitoring luminescence in the presence of bor-DTZ or the parent DTZ for 20 minutes. The ratio of the area under the curve for bor-DTZ:DTZ was calculated in order to account for any effects that the treatments had on secNluc expression or cell proliferation (Figure 3c). We observe that cisplatin treatment induces a decrease in light output relative to the control. Interestingly, our previous report on a copper(II) responsive DTZ showed that cisplatin also decreases extracellular levels of copper(II). These findings provide a basis and tool for further investigations into the interplay between trafficking of H_2O_2 and copper in both physiological and pathological states. The above study also demonstrates the high-throughput and accessible nature that the bor-DTZ probe offers through use of a 96-well plate and luminometer or plate reader. This lays the foundation for a unique new tool for future high-throughput studies investigating the effect of external stimuli on H_2O_2 dynamics.

4.4 Conclusions and Outlook

We have demonstrated the design, synthesis, and evaluation of a new bioluminescent probe, bor-DTZ, for monitoring H_2O_2 in vitro in an ATP-independent manner. Bor-DTZ shows a high level of selectivity towards H_2O_2 over other biologically relevant reactive oxygen species and shows sensitivity down to the low-mid µM range. The probe can detect H_2O_2 in either intracellular or extracellular environments based on where the Nluc enzyme is expressed. We also demonstrate that bor-DTZ can be applied to a 96 well-plate for cell-based assays for high-throughput analysis of H_2O_2 dynamics in a cancer cell line.

Bioluminescence-based sensing of H_2O_2 offers the advantages of in vivo compatibility as well as high sensitivity due to near-zero background and signal output that does not require an excitation light source. Among the caged bioluminescence agents that have been reported, bor-DTZ is one of the first diphenylterazine-based imaging probes to be paired with the bright, thermostable Nluc. The ATP-independent nature of Nluc allows bor-DTZ to be used in both intracellular and extracellular applications broadening the scope of currently available tools for H_2O_2. Paired with Nluc and emerging analogs for deep-tissue imaging, bor-DTZ has broad potential for investigating oxidative biology in both cell-based and live-animal studies.

4.5 Materials and Methods

General Methods. Reactions using moisture- or air-sensitive reagents were carried out in dried glassware under an inert N_2 atmosphere. DTZ (**4)** was synthesized according to previously published methods.[47,48] Dry solvents were all purchased from Sigma-Aldrich and used immediately. All commercially purchased chemicals were used as received without further purification. 2-aminopyrazine was purchased from Oakwood Products. All other chemicals were purchased from Sigma-Aldrich unless otherwise noted. Silica Gel 60 F254 (precoated sheets, 200 µm thickness, MilliporeSigma) were used for analytical thin layer chromatography. Silica gel sorbent (230-400 mesh, grade 60, ThermoFisher) or aluminum oxide (neutral, Brockmann I, 50-200 µm, grade 60, Sigma-Aldrich) were used for column chromatography. ^{1}H and ^{13}C NMR spectra were collected at room temperature in DMSO-d6 (Sigma-Aldrich) on a 600 MHz Varian NMR spectrometer. All chemical shifts are reported as δ parts per million relative to the residual solvent peak at 2.50 (DMSO-d6) for 1H and 39.52 (DMSO-d6) for 13C. Multiplicities are reported as s (singlet), d (doublet), t (triplet), q (quartet), p (pentet), h (hextet), m (multiplet), dt (doublet of triplets), or br (broad). Electrospray ionization mass spectral analyses were performed using a Thermo Q-Exactive HF Orbitrap.

Synthesis of bor-DTZ. Diphenylterazine, **4**, (14 mg, 0.037 mmol, 1 equiv.), 4-bromomethylphenylboronic acid pinacol ester (11 mg, 0.037 mmol, 1 equiv.), Cs_2CO_3 (5 mg, 0.015 mmol, 0.4 equiv.), and KI (7 mg, 0.041 mmol, 1.1 equiv.) were added to a flame-dried round-bottom flask that was then purged with N_2. The reagents were then dissolved in anhydrous acetonitrile (1 mL) and the reaction was allowed to stir overnight. The reaction mixture was subsequently quenched in 10 mL of water and extracted in DCM (3 x 5 mL). The combined DCM extract was then washed with brine, dried over Na_2SO_4, and concentrated under reduced pressure. The crude product was then purified by reverse-phase HPLC (isochratic, 80/20 MeCN:H_2O over 2 hours on a T3 Atlantis column (Waters)) and dried under reduced pressure to obtain **bor-DTZ** (4 mg, 18% yield) as a yellow-brown solid. ^{1}H NMR (600 MHz, DMSO-d6) δ

8.83-8.85 (d, 2H), 8.44 (s, 1H), 8.09-8.11 (d, 2H), 7.68-7.70 (d, 2H), 7.50-7.60 (m, 5H), 7.46-7.47 (d, 2H), 7.41-7.43 (t, 1H), 7.27 (m, 4H), 7.18 (m, 1H), 5.25 (s, 2H), 4.07 (s, 2H), 1.27 (s, 12H). ^{13}C NMR (151 MHz, DMSO-d6) δ 146.08, 139.64, 139.59, 137.25, 137.11, 136.84, 136.19, 135.09, 134.15, 131.55, 130.77, 129.75, 129.17, 129.13, 129.03, 128.88, 128.86, 128.82, 128.74, 126.62, 126.48, 110.99, 84.18, 77.02, 32.95, 25.11. . High-resolution mass spectrometry (HRMS) (m/z): $[M+H]^+$ calculated for : $C_{38}H_{37}BN_3O_3$, 594.2927; found, 594.2915

***In Vitro* Luminescence Assays.** Milli-Q water (18.2 MΩ) was used to prepare all aqueous solutions. Reactive oxygen species solutions were prepared to 10 mM in water. Hydrogen peroxide (H_2O_2), *tert*-butyl hydroperoxide (TBHP), and hypochlorite (OCl^-) stock solutions were prepared from 30%, 70%, and 2-3% aqueous solutions, respectively. Hydroxyl radical (*OH) and *tert*-butoxy radical (*OtBu) were generated in situ by reaction with excess Fe(II). Nitric oxide (NO*) was generated using PROLI NONOate (Cayman Chemical). Superoxide (O_2^-) was delivered from a stock solution of potassium superoxide (KO_2) in DMSO. A 100 µM solution of bor-DTZ was prepared by dissolving bor-DTZ in pure ethanol. A 0.4 µg/mL solution of rNluc was prepared by adding 1 µL of 0.4 mg/mL stock solution (Promega, Nano-Glo Assay Kit) into 999 µL of DPBS at pH 7.4. 100 µL of rNluc solution was added to the wells of a white, opaque, flat-bottom 96-well plate followed by 1 µL of ROS 10 mM stock solution. Finally, bor-DTZ (1 µL) was added to all the wells using a multi-channel pipette and mixed well. The bioluminescent signal was immediately measured using a Molecular Devices SpectraMax i3x plate reader at 37 ºC for 1 hour. For dose-dependence studies 100x stock solutions of H_2O_2 were prepared in Millipore water from a 30% (w/w/) aqueous solution and 1 µL of these stock solutions were added to 100 uL of rNluc solution in wells of a 96-well white plate. Bor-DTZ (1 µL of a 100 µM solution) was added via a multichannel pipette and the luminescence was immediately measured.

For ATP studies a 10 mM solution of ATP was prepared in DPBS pH 7.4 by adding 100 µL of a 100 mM stock (ThermoScientific) into 900 µL of DPBS. To this was added 1 µL of 0.4 mg/mL rNluc (Promega) to get a final volume of 0.4 µg/mL rNluc. The control rNluc solution was prepared to 0.4 µg/mL as described previously and 100 µL aliquots of control and ATP containing solutions were plated in 96-well white plate. Bor-DTZ (1 µL of a 100 µM solution) was added to the wells and the luminescence was measured immediately. When reporting area under the curve, these values were calculated using GraphPad Prism software.

Cell Culture. MDA-MB-231 cells stably expressing secreted or intracellular Nanoluciferase (secNluc MDA-MB-231 or Nluc MDA-MB-231 respectively) were a kind gift from Drs. Gary and Kathy Luker (University of Michigan). Cells were maintained in Dulbecco's modified medium (DMEM, 4.5 g/L glucose) supplemented with 10% fetal bovine serum (FBS) (Gibco) 1x penicillin-streptomycin (Corning), 2 mM L-glutamine (Gibco), 1 mM sodium pyruvate (Gibco) at 37 ºC and 5% CO_2.

Detecting H_2O_2 intracellularly in Nluc MDA-MB-231 Cells. Cells were plated at 10,000 cells per well in a 96-well white, opaque, flat bottom plate. Twenty-four hours later media was replaced with fresh media and paraquat was added from a freshly prepared stock solution to a final concentration of 500 µM. Cells were then incubated for 24 hours and then the media was removed and washed with warm DPBS before adding 100 µL of fresh DPBS to wells. Bor-DTZ (1 µL of a 1 mM solution) was added to wells and luminescence was measured immediately over one hour.

Detecting H_2O_2 in Media of secNluc MDA-MB-231 Cells. Cells were plated at 10,000 cells per well in a 96-well black clear bottom plate. Twenty-four hours later the media was removed from the wells and added to a fresh 96-well white, opaque, flat bottom plate. Catalase (Sigma Aldrich) was added to wells in triplicate to a final concentration of 1 x 104 U/L from a stock solution. Following this bor-DTZ (1 µL of a 100 µM solution) was added to wells and luminescence was measured immediately. For dose-response experiments 100X solutions of H_2O_2 were prepared in water and 1 µL of this was added to secNluc MDA-MB-231 cells 24 hours after plating as previously described. Bor-DTZ (1 µL of a 100 µM solution) was added to wells and luminescence was measured immediately.

Monitoring secNluc MDA-MB-231 response to cisplatin. Cells were plated at 10,000 cells per well in a 96-well, white, opaque flat-bottom plate. Eight hours later, the media was removed, and the cells were washed with pre-warmed (37 ºC) DPBS and 100 µL of OptiMem (Gibco) was added to each well. A 3 mM solution of cis-platin was prepared in water. 1 µL of this was added to the wells for a final concentration of 30 µM cisplatin. At the 16-hour time point solutions of 100 µM bor-DTZ and 100 µM DTZ (in ethanol) were prepared and 1 µL was added per well per treatment (n=3). Luminescence was immediately recorded as previously described. The area under the curve was calculated using GraphPad Prism software and the ratio of the A.U.C. from bor-DTZ to DTZ was calculated.

4.6 References

(1) Brandes, R. P.; Weissmann, N.; Schröder, K. Free Radical Biology and Medicine Nox Family NADPH Oxidases : Molecular Mechanisms of Activation. *Free Radic. Biol. Med.* **2014**, *76*, 208–226.

(2) Rojkind, M.; Domínguez-rosales, J.; Nieto, N.; Greenwel, P. Role of Hydrogen Peroxide and Oxidative Stress. *Cell. Mol. Life Sci.* **2002**, *59*, 1872–1891.

(3) Siddique, Y. H.; Ara, G.; Afzal, M. Estimation of Lipid Peroxidation Induced by Hydrogen Peroxide in Cultured Human Lymphocytes. *Dose-Response* **2012**, *10*, 1–10.

(4) Valverde, M.; Lozano-salgado, J.; Fortini, P.; Rodriguez-sastre, M. A.; Rojas, E.; Dogliotti, E. Hydrogen Peroxide-Induced DNA Damage and Repair through the Differentiation of Human Adipose-Derived Mesenchymal Stem Cells. *Stem Cells Int.* **2018**, *2018*.

(5) Liu, M.; Gong, X.; Alluri, R. K.; Wu, J.; Sablo, T.; Li, Z. Characterization of RNA Damage under Oxidative Stress in Escherichia Coli Min. **2012**, *393* (3), 123–132.

(6) Zhu, H.; Tamura, T.; Fujisawa, A.; Nishikawa, Y.; Cheng, R.; Takato, M.; Hamachi, I. Imaging and Profiling of Proteins under Oxidative Conditions in Cells and Tissues by Hydrogen-Peroxide-Responsive Labeling. *J. Clin. Exp. Hepatol.* **2020**, *142*, 15711–15721.

(7) Stone, J. R.; Yang, S. Hydrogen Peroxide: A Signaling Messenger. *Antioxid. Redox Signal.* **2006**, *8* (3), 243–270.

(8) Lennicke, C.; Cocheme, H. M. Review Redox Metabolism : ROS as Specific Molecular Regulators of Cell Signaling and Function. *Mol. Cell* **2021**, *81*, 3691–3707.

(9) Autréaux, B. D.; Toledano, M. B. REVIEWS ROS as Signalling Molecules : Mechanisms That Generate Specificity in ROS Homeostasis. *Nat. Rev. Mol. Cell Biol.* **2007**, *8*, 813–824.

(10) Cotter, T. G.; Gough, D. R. Hydrogen Peroxide : A Jekyll and Hyde Signalling Molecule. *Cell Death Dis.* **2011**, *2* (e213), 1–8.

(11) Antunes, F.; Brito, P. M. Redox Biology Quantitative Biology of Hydrogen Peroxide Signaling. *Redox Biol.* **2017**, *13*, 1–7.

(12) Rhee, S. G. H2O2, a Necessary Evil for Cell Signaling. *Science (80-.).* **2006**, *312* (5782), 1882–1884.

(13) Gupte, A.; Mumper, R. J. Elevated Copper and Oxidative Stress in Cancer Cells as a Target for Cancer Treatment. *Cancer Treat. Rev.* **2009**, *35* (1), 32–46.

(14) Finkel, T.; Serrano, M.; Blasco, M. A. The Common Biology of Cancer and Ageing. *Nat. Rev.* **2007**, *448*, 767–774.

(15) Wang, W.; Jiang, W.; Mao, G.; Tan, M.; Fei, J.; Li, Y.; Li, C. Monitoring the Fluctuation of Hydrogen Peroxide in Diabetes and Its Complications with a Novel Near-Infrared Fluorescent Probe. *Anal. Chem.* **2021**, *93*, 3301–3307.

(16) Houstis, N.; Rosen, E. D.; Lander, E. S. Reactive Oxygen Species Have a Causal Role in Multiple Forms of Insulin Resistance. *Nature* **2006**, *440*, 944–948.

(17) Wittmann, C.; Chockley, P.; Singh, S. K.; Pase, L.; Lieschke, G. J.; Grabher, C. Hydrogen Peroxide in Inflammation : Messenger , Guide , and Assassin. *Adv. Hematol.* **2012**, *2012*, 1–6.

(18) Mittal, M.; Siddiqui, M. R.; Tran, K.; Reddy, S. P.; Malik, A. B. Reactive Oxygen Species

in Inflammation and Tissue Injury. *Antioxid. Redox Signal.* **2014**, *20* (7), 1126–1167.
(19) Steinhorn, B.; Michel, T. Chemogenetic Generation of Hydrogen Peroxide in the Heart Induces Severe Cardiac Dysfunction. *Nat. Commun.* **2018**, *9*, 4044.
(20) Horwitz, D.; Sherman, N. A.; Horwitz, D. Hydrogen Peroxide Cytotoxicity in Cultured Cardiac Myocytes Is Iron Dependent. *Hear. Circ. Physiol.* **1994**, *226* (1), 121–127.
(21) Lampard, E. V; Sedgwick, A. C.; Sun, X.; Filer, K. L.; Hewins, S. C. Boronate-Based Fluorescence Probes for the Detection of Hydrogen Peroxide. *ChemistryOpen* **2018**, 262–265.
(22) Maeda, H.; Fukuyasu, Y.; Yoshida, S.; Fukuda, M.; Saeki, K.; Matsuno, H.; Yamauchi, Y.; Yoshida, K.; Hirata, K.; Miyamoto, K. Fluorescent Probes for Hydrogen Peroxide Based on a Non-Oxidative Mechanism**. *Angew. Chemie* **2004**, *43*, 2389–2391.
(23) Dickinson, B. C.; Huynh, C.; Chang, C. J. A Palette of Fluorescent Probes with Varying Emission Colors for Imaging Hydrogen Peroxide Signaling in Living Cells. *J. Am. Chem. Soc.* **2010**, *23*, 5906–5915.
(24) Chang, M. C. Y.; Pralle, A.; Isacoff, E. Y.; Chang, C. J. A Selective , Cell-Permeable Optical Probe for Hydrogen Peroxide in Living Cells. *J. Am. Chem. Soc.* **2004**, *2*, 15392–15393.
(25) Soh, N. Recent Advances in Fluorescent Probes for the Detection of Reactive Oxygen Species. *Anal. Bioanal. Chem.* **2006**, *386*, 532–543.
(26) Xie, X.; Wu, T.; Li, Y.; Li, M.; Tan, Q.; Wang, X.; Tang, B. Rational Design of an α -Ketoamide-Based Near-Infrared Fluorescent Probe Speci Fi c for Hydrogen Peroxide in Living Systems. *Anal. Chem.* **2016**, *88*, 8019–8025.
(27) Abo, M.; Urano, Y.; Hanaoka, K.; Terai, T.; Komatsu, T.; Nagano, T. Development of a Highly Sensitive Fluorescence Probe for Hydrogen Peroxide. *J. Am. Chem. Soc.* **2011**, *133*, 10629–10637.
(28) Carroll, V.; Michel, B. W.; Blecha, J.; Vanbrocklin, H.; Keshari, K.; Wilson, D.; Chang, C. J. A Boronate-Caged [18 F]FLT Probe for Hydrogen Peroxide Detection Using Positron Emission Tomography. *J. Am. Chem. Soc.* **2014**, *136* (42), 14742–14745.
(29) Miller, E. W.; Albers, A. E.; Pralle, A.; Isacoff, E. Y.; Chang, C. J. Boronate-Based Fluorescent Probes for Imaging Cellular Hydrogen Peroxide. *J. Am. Chem. Soc.* **2005**, *127* (47), 16652–16659.
(30) Manuscript, A. Peroxide in Living Systems. **2014**, 1–23.
(31) Lippert, A. R.; Bittner, G. C. V. A. N. D. E.; Chang, C. J. Boronate Oxidation as a Bioorthogonal Reaction Approach for Studying the Chemistry of Hydrogen Peroxide in Living Systems. *Acc. Chem. Res.* **2011**, *44* (9), 793–804.
(32) Purdey, M. S.; Mclennan, H. J.; Sutton-mcdowall, M. L.; Drumm, D. W.; Zhang, X.; Capon, P. K.; Heng, S.; Thompson, J. G.; Abell, A. D. Sensors and Actuators B : Chemical Biological Hydrogen Peroxide Detection with Aryl Boronate and Benzil BODIPY-Based Fluorescent Probes. *Sensors Actuators B. Chem.* **2018**, *262*, 750–757.
(33) Chen, Y.; Shi, X.; Lu, Z.; Wang, X.; Wang, Z. A Fluorescent Probe for Hydrogen Peroxide in Vivo Based on the Modulation of Intramolecular Charge Transfer. *Anal. Chem.* **2017**, *89*, 5278–5284.
(34) Hosogi, S.; Marunaka, Y.; Ashihara, E.; Yamada, T. Plasma Membrane Anchored Nanosensor for Quantifying Endogenous Production of H2O2 in Living Cells. *Biosens. Bioelectron.* **2021**, *179*, 113077.

(35) Zhang, T.; Gu, Y.; Li, C.; Yan, X.; Lu, N.; Liu, H.; Zhang, Z.; Zhang, H. Fabrication of Novel Electrochemical Biosensor Based on Graphene Nanohybrid to Detect H 2 O 2 Released from Living Cells with Ultrahigh Performance. *Appl. Mater. Interfaces* **2017**, *9*, 37991–37999.

(36) Shen, R.; Liu, P.; Zhang, Y.; Yu, Z.; Chen, X.; Zhou, L.; Nie, B.; Chen, J.; Liu, J. Sensitive Detection of Single-Cell Secreted H 2 O 2 by Integrating a Micro Fl Uidic Droplet Sensor and Au Nanoclusters †. *Anal. Chem.* **2018**, *90*, 4478–4484.

(37) Rathbun, C. M.; Prescher, J. A. Bioluminescent Probes for Imaging Biology beyond the Culture Dish. *Biochemistry* **2017**, *56*, 5178–5184.

(38) Mezzanotte, L.; van ‘t Root, M.; Karatas, H.; Goun, E. A.; Löwik, C. W. G. M. In Vivo Molecular Bioluminescence Imaging: New Tools and Applications. *Trends Biotechnol.* **2017**, *35* (7), 640–652.

(39) Li, J.; Chen, L.; Du, L.; Li, M. Cage the Firefly Luciferin! - A Strategy for Developing Bioluminescent Probes. *Chem. Soc. Rev.* **2013**, *42* (2), 662–676.

(40) Yang, X.; Li, Z.; Jiang, T.; Du, L.; Li, M. A Coelenterazine-Type Bioluminescent Probe for Nitroreductase Imaging. *Org. Biomol. Chem.* **2018**, *16*, 146–151.

(41) Bittner, G. C. Van De; Dubikovskaya, E. A.; Bertozzi, C. R.; Chang, C. J. In Vivo Imaging of Hydrogen Peroxide Production in a Murine Tumor Model with a Chemoselective Bioluminescent Reporter. *PNAS* **2010**, 21316–21321.

(42) Van de Bittner, G. C.; Bertozzi, C. R.; Chang, C. J. Strategy for Dual-Analyte Luciferin Imaging: In Vivo Bioluminescence Detection of Hydrogen Peroxide and Caspase Activity in a Murine Model of Acute In Fl Ammation. *J. Am. Chem. Soc.* **2013**, *135*, 1783–1795.

(43) Yeh, H.; Xiong, Y.; Wu, T.; Chen, M.; Ji, A.; Li, X.; Ai, H. ATP-Independent Bioluminescent Reporter Variants To Improve in Vivo Imaging. *ACS Chem. Biol.* **2019**, *14*, 959–965.

(44) Markova, S. V; Larionova, M. D.; Vysotski, E. S. Shining Light on the Secreted Luciferases of Marine Copepods : Current Knowledge and Applications. *Photochem. Photobiol.* **2019**, *95* (2), 705–721.

(45) Hall, M. P.; Unch, J.; Binkowski, B. F.; Valley, M. P.; Butler, B. L.; Wood, M. G.; Otto, P.; Zimmerman, K.; Vidugiris, G.; Machleidt, T.; Robers, M. B.; Benink, A.; Eggers, C. T.; Slater, M. R.; Meisenheimer, P. L.; Klaubert, D. H.; Fan, F.; Encell, L. P.; Wood, K. V. Engineered Luciferase Reporter from a Deep Sea Shrimp Utilizing a Novel Imidazopyrazinone Substrate. **2012**.

(46) Hall, M. P.; Unch, J.; Binkowski, B. F.; Valley, M. P.; Butler, B. L.; Wood, M. G.; Otto, P.; Zimmerman, K.; Vidugiris, G.; MacHleidt, T.; Robers, M. B.; Benink, H. A.; Eggers, C. T.; Slater, M. R.; Meisenheimer, P. L.; Klaubert, D. H.; Fan, F.; Encell, L. P.; Wood, K. V. Engineered Luciferase Reporter from a Deep Sea Shrimp Utilizing a Novel Imidazopyrazinone Substrate. *ACS Chem. Biol.* **2012**, *7* (11), 1848–1857.

(47) O’Sullivan, J. J.; Medici, V.; Heffern, M. C. A Caged Imidazopyrazinone for Selective Bioluminescence Detection of Labile Extracellular Copper(II). *Chem. Sci.* **2022**, *Advance Ar*.

(48) Yeh, H.; Karmach, O.; Ji, A.; Carter, D.; Martins-green, M. M.; Ai, H. Red-Shifted Luciferase – Luciferin Pairs for Enhanced Bioluminescence Imaging. *Nat. Methods* **2017**, *14* (10), 971–978.

(49) Chen, Q.; Liang, C.; Sun, X.; Chen, J.; Yang, Z.; Zhao, H.; Feng, L.; Liu, Z. H2O2-

Responsive Liposomal Nanoprobe for Photoacoustic Inflammation Imaging and Tumor Theranostics via in Vivo Chromogenic Assay. *PNAS* **2017**, *114* (21), 5343–5348.

(50) Chen, Q.; Feng, L.; Liu, J.; Zhu, W.; Dong, Z.; Wu, Y. Intelligent Albumin –MnO2 Nanoparticles as PH-/H2O2-Responsive Dissociable Nanocarriers to Modulate Tumor Hypoxia for Effective Combination Therapy. *Advanved Mater.* **2016**, *28*, 7129–7136.

(51) Szatrowski, T. P.; Nathan, C. F. Production of Large Amounts of Hydrogen Peroxide by Human Tumor Cells. *Cancer Res.* **1991**, *51*, 794–798.

(52) Castello, P. R.; Drechsel, D. A.; Patel, M. Mitochondria Are a Major Source of Paraquat-Induced Reactive Oxygen Species Production in the Brain *. *J. Biol. Chem.* **2007**, *282* (19), 14186–14193.

(53) Brown, N. S.; Bicknell, R. Hypoxia and Oxidative Stress in Breast Cancer Oxidative Stress: Its Effects on the Growth , Metastatic Potential and Response to Therapy of Breast Cancer. *Breast Cancer Res.* **2001**, *3* (5), 323–327.

(54) Polishchuk, R. S. Activity and Trafficking of Copper-Transporting ATPases in Tumor Development and Defense against Platinum-Based Drugs. *Cells* **2019**, *8*, 1080.

Chapter 5

Development of Raman Active Probes for Early-Stage Diagnosis of Ovarian Cancer*

*This chapter is adapted from a manuscript currently in preparation and in collaboration with Dr. Randy Carney and his lab in the UC Davis Biomedical Engineering department. The contributions from Justin O'Sullivan are the synthesis of the Raman tags and their conjugation to antibodies. Extensive work on the synthetic development of polyynes for surface enhanced Raman spectroscopy (SERS) applications was also done by Justin O'Sullivan but cannot be disclosed at this time. For the work presented here, Hanna J. Koster performed the bulk of the data acquisition including extracellular vesicle isolation and SERS analysis. Rachel Mizenko performed extracellular vesicle characterization and data analysis. Tatu Rojalin contributed to the design of the study. Randy Carney contributed to the conception and design of the study as well as custom software developed and used in the work.

5.1 Abstract

Cancer is a global health issue that researchers have been investigating for decades. To date, it remains one of the leading causes of death in the world. Early-stage diagnosis of cancers often lead to increased mortality rates and there is therefore a need to develop new screening tools for early-stage screening of various cancers. Ovarian cancer in particular has few screening methods, yet studies have shown that early-stage detection results in much more favorable patient outcome relative to late-stage detection. The clinical method of ovarian cancer screening is blood CA125 measurement. Here we report the use of Raman active tagged antibody conjugates for ovarian cancer specific biomarkers (including CA125) and apply them to extracellular vesicle (EV) analysis. We show that EVs isolated from patients undergoing clinically ordered CA125 screens contain useful diagnostic information through surface enhanced Raman spectroscopic analysis. Furthermore, we show that the inclusion of our in-house synthesized Raman-tagged antibody conjugates can pick up populations of EVs with unique chemical features and also increases the sensitivity, specificity, and accuracy towards distinguishing cancer and non-cancer derived exosomes.

5.2 Introduction

To date, cancer remains one of the most heavily researched diseases with the second leading cause of mortality worldwide with more than 277 different subtypes.[1] Researchers have identified different stages of cancer indicating that several gene mutations are involved in the pathology. Such genetic mutations result in the hallmark abnormal cell proliferation associated with cancer. Over recent years the prevalence of cancer has actually increased despite advances in medicine. In fact, recent studies revealed that the incidence of cancers of various organs (including breast, colorectum, endometrium, esophagus, gallbladder, head and neck, liver, bone, pancreas, prostate, stomach, and thyroid) has been rising in the under 50 years of age population in many parts of the world.[2–11]

Prior to the advent of new diagnostic technologies cancer was typically detected only after the development of clinical symptoms and subsequent biopsy. At this stage tumor development and metastasis are typically quite advanced. Because of this, late-stage diagnosis often results in much higher mortality rates relative to early-stage diagnosis.[12] Indeed, it has been shown that the earliest stages of cancer detection are when existing clinical interventions show the most success.[10] The detection of primary, pre-invasive tumors generally increases the rate of remission namely through the surgical removal of the cancerous mass. In fact, when accurate testing is available the general population is encouraged to undergo risk-based screenings such as with mammograms for breast cancer detection, colonoscopy for colon cancers, and Papanicolaou test (Pap test) for cervical cancer.[13–15] However, of over 250 cancer subtypes the vast majority of them do not have robust, non-invasive, and accurate methods of early-diagnosis screening creating an unmet challenge that can potentially be solved with current molecular imaging strategies.

The need for early-stage diagnosis and the vast diversity in subtypes of cancer has led researchers to try and identify cancer specific biomarkers. One of the most well-known examples for a blood-based cancer biomarker used in the clinic today is the prostate specific antigen which has been used to screen for prostate cancer (PSA).[16,17] However, it is worth noting that debate continues over if PSA based screens have resulted in decreased mortality rates.[18,19] In addition to PSA biomarker other biomarkers of interest include nucleic acids, peptides, proteins, lipids, and small molecule metabolites present in the blood or other biofluids.[20,21,30–35,22–29] Recent progress in the sequencing of cancer associated genes has resulted in significant strides in the use of circulating tumor DNA as a diagnostic handle.[36–38] However, the detection of tumor associated DNA in the blood often does not distinguish cancer subtype.

One cancer subtype of particular interest for developing early-stage diagnostic screening methods is ovarian cancer.[39] Ovarian cancer is a global disease that is typically diagnosed at late stage and currently has no effective screening methods. However, early-stage detection of ovarian cancer has been shown to result in a 5-year survival rate of over 90% where this rate is decreased to 29% for those diagnosed at late stage.[40,41] Because of the lack of specific biomarkers for ovarian cancer only about 15% of women are diagnosed at stage 1 where patient outcomes are more favorable.[42] Screening strategies to date for ovarian cancer have largely remained on the biomarker carbohydrate antigen 125 (CA125) (also known as mucin 16) and the use of transvaginal ultrasonography.[43,44] Combinations of these screenings have shown some success in detecting early-stage cancers, but they have not yet demonstrated definitive improvements in patient mortality.[45,46] Furthermore, the use of CA125 as a biomarker for ovarian cancer is below the acceptable accuracy and endogenous levels can be increased due to other factors such as endometriosis and pregnancy.[44] Because of this, there is a need for the development of new biomarkers that are highly specific to ovarian cancer and are at detectable levels at an early stage.

Recently, extracellular vesicles (EVs) have emerged as a potentially powerful biomarker for various cancers.[47–49] Exosomes are nanoscale, bilipid membrane particles ranging from 30-150 nm in size.[50] Though traditionally thought to only contain cellular "junk" and provide a means of getting rid of cellular debris, recent work has shown that EVs can be used to shuttle important information and cellular cargo from cell to cell.[51,52] EVs express various transmembrane proteins that are reflective of their parent cells. All cells in the body produce EVs including cancerous cells and indeed it has been seen that cancer derived EVs are capable of inducing metastasis and can promote secondary tumor growth.[53] Because of this there has been an increase in research trying to understand the potential of EVs as biomarker rich biomaterials. Regarding ovarian cancer researchers have found ovarian cancer derived exosomes express CA125, CA19-9, and HE4 in higher levels relative to non-ovarian cancer derived EVs making EVs an attractive new candidate for biomarker screening.[54,55]

Isolation of EVs from patients can routinely be performed through the processing of blood samples as EVs are constantly in circulation within our blood stream. Once isolated a variety of tools exist to study and characterize the collected EVs. Of particular interest is the use of Raman spectroscopy for the required biochemical analysis. Raman spectroscopy utilizes the physical phenomenon known as Raman scattering where photons can interact with molecules and inelastically scatter off them. The scattered photons, with a different wavelength then the incidence photons, can then be collected and analyzed. This vibrational technique results in a spectrum that can provide chemical fingerprinting of EVs being analyzed by giving insight into their composition including biomolecules such as proteins, lipids, and nucleic acids.[56–58] Because Raman is non-destructive, label free, and water silent it is an attractive modality for EV analysis and imaging of biomarkers. On the other hand, the Raman effect is inherently weak as there are a very low number of scattered photons produced and detected.

To ameliorate this weakness researchers discovered a phenomenon known as surface enhanced Raman spectroscopy where a metallic substrate is placed near the sample.[59] This effect results in a massive increase in signal intensity thereby allowing for much higher sensitivities. Typically metals like gold and silver are used. To date, SERS has been employed in a variety of uses for biomedical research and even for the analysis of EVs including cancer derived EVs.[60] Although SERS can provide useful information into the composition of cancer derived EVs it still struggles to achieve suitable specificity as EV populations are extremely heterogenous. However, the implementation of molecular Raman tags provides a potential avenue to increase the specificity of Raman based EV analysis. Typically, such tags are small molecules with unique Raman signals outside the region where biomaterials are Raman active. One of the most widely applied Raman active tags are alkyne based as they generate a strong signal outside the fingerprint region and can be synthesized and manipulated relatively easily.[61,62] The use of such molecules can help in making sure the sample is in focus of the laser by providing a diagnostic peak corresponding to the tag. Thus, tags can be attached to biomolecules of interest and allow researchers to ensure that they are measuring and probing desired analytes.

In the work described here we developed a library of three unique Raman tags based on the alkyne functionality and conjugated them to antibody biomarkers associated with ovarian cancer derived exosomes (CA125, CA19-0, and HE4). In the study, EVs were isolated from a cohort (cancer and control) undergoing CA125 ovarian cancer screening, then incubated the tagged antibodies with the EV samples (Figure 4.1a). After incubation of the EVs with the tagged antibodies the EVs underwent a washing step to remove any unbound tagged antibodies using size exclusion chromatography (SEC). The EVs were then placed on a gold substrate for SERS analysis and the resulting spectra were assessed for diagnostic ability. We demonstrate that the three unique tagged-antibody pairs were present in all EV samples and furthermore that the addition of the tag provided complimentary chemical information that allowed for increased sensitivity, specificity, and accuracy in identifying cancer derived from healthy EVs. This suggests a new potential non-invasive biomarker for Raman based screening of ovarian cancer.

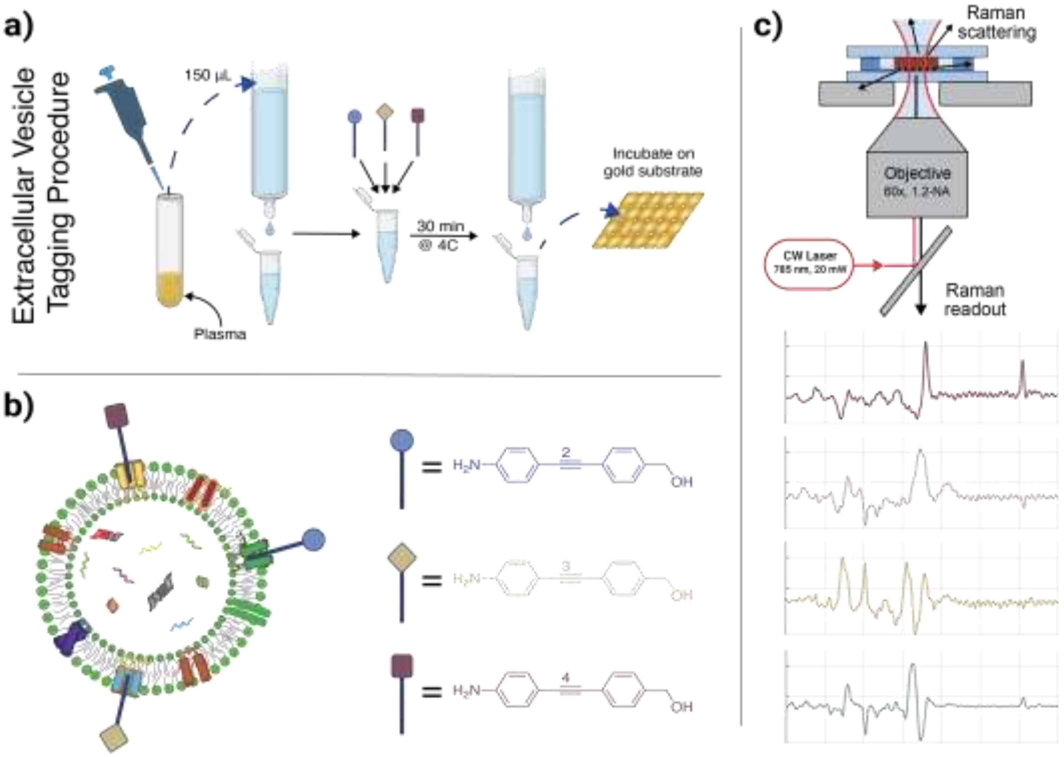

Figure 4.1 Extracellular vesicle (EV) isolation, incubation, and readout schematic. a) EVs are isolated using size-exclusion chromatography (SEC) then incubated with three Raman tag-antibody pairs. An additional SEC step removed unbound antibodies and samples are incubated on a gold substrate. b) Schematic showing the three alkyne tags attaching to specific surface proteins on the EV surface. c) Microscope set-up for Raman analysis of EV samples. Substrates are placed on the inverted confocal objective and spectra are acquired.

5.3 Results & Discussion

5.3.1 Design and Synthesis of Raman Tags

As previously mentioned, the alkyne functionality was chosen due to its unique Raman activity outside the biological fingerprint region and relatively straightforward incorporation into molecules of interest. In addition to these points, alkyne chain length can also be extended to produce polyynes such as diynes, triynes, tetraynes and so on and so forth. This extension in alkyne chains produces shifts in the Raman peak such that diynes and triynes will have signals at different wavenumbers. Indeed, researchers have previously demonstrated Raman resolved polyynes that enable multiplexed analysis. This library of polyynes produces a unique library of Raman active signals that has been dubbed the "carbow" by Wei Min et al.[63] We sought inspiration from this polyyne approach towards Raman active tags and sought out to synthesize a panel of three polyynes (Figure 4.1b) with functional amine and alcohol handles for facile conjugation to biomolecules such as the ovarian antibody biomarkers mentioned.

The synthesis of such polyynes typically occur through iterative alkyne cross couplings. Originally discovered by Glaser in 1869, by far the oldest alkyne coupling is the copper catalyzed homocoupling of terminal alkynes aptly named the Glaser coupling.[64,65] This reaction generally occurs efficiently but favors the homocoupling over heterocoupling product of two different alkynes. However, the generation of asymmetrical polyynes is of great importance as building blocks in drug discovery and materials sciences. To address this unmet need the Cadiot-Chodkiewicz coupling was developed where a haloalkyne can be coupled to a terminal alkyne under basic conditions and copper catalysis to obtain the desired asymmetric alkyne over the homocoupled products.[66,67] However, it should be noted that this is not a totally heteroselective reaction and often researchers are left with a mixture of two different homocoupled products in addition to the desired heterocoupling that must be separated. In this work the diyne and triyne tags were synthesized via Cadiot-Chodkiewicz coupling and the tetrayne was coupled under Glaser conditions (Scheme 4.1).

Scheme 4.1 Synthesis of diyne, triyne, and tetrayne Raman tags.[a]

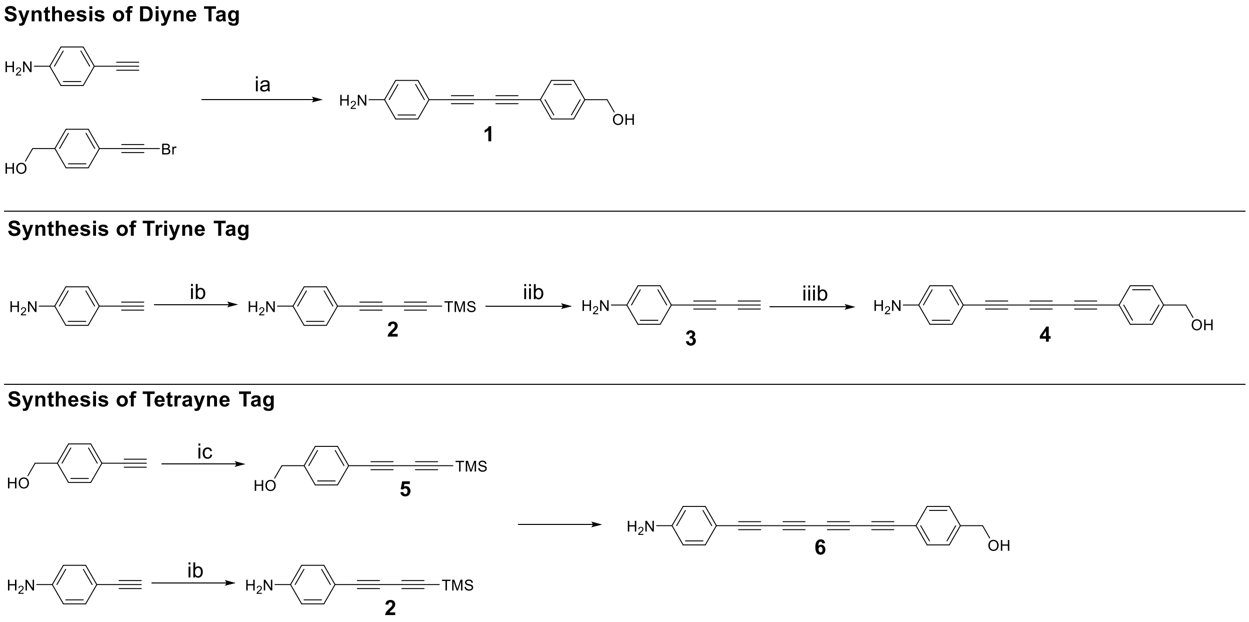

[a] **Synthesis of Diyne:** (ia) CuCl, n-BuNH$_2$, NH$_2$OH, H$_2$O/THF, 3hr. **Synthesis of Triyne:** (ib) TMSA, Cu-TMEDA, acetone, 6 hr; (iib) K$_2$CO$_3$, MeOH/DCM, 45 min; (iic) CuCl, n-BuNH$_2$, NH$_2$OH, H$_2$O/THF, 2 hr. **Synthesis of Tetrayne:** (ic) TMSA, Cu-TMEDA, acetone, 6 hr; (iic) Cu-TMEDA, acetone, 3 hr.

5.3.2 SERS Measurements of Raman Tags

Once the Raman tags were synthesized, they were initially assessed for their ability to multiplex based on their respective Raman signals prior to any testing with antibodies or EVs. SERS measurements were performed of each tag on a substrate (Figure 4.2). The diyne, triyne, and tetrayne all displayed unique Raman shifts in the spectra within the expected region for alkyne activity. Furthermore, additional measurements were taken off all three tags in the same solution to ensure that the unique shifts were still observable in a mixture which would be translatable to multiplexed environments. The three peaks were still observed in the spectra of the mixture suggesting that multiplexing could be successful with this system of tags. Notably though, when in a mixture we observed a shifting of the tetrayne from 2125 cm^{-1} to 2130 cm^{-1} and a shifting of the diyne from 2210 cm^{-1} to 2220 cm^{-1} as well as decreased signal intensity of the peak corresponding to the triyne.

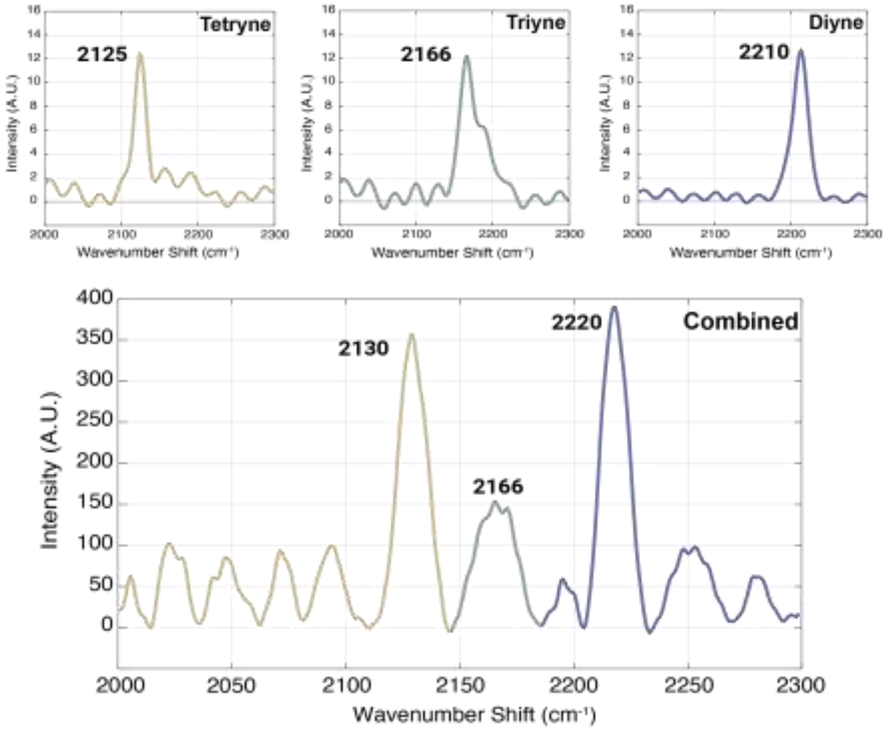

Figure 4.2 Distinct peaks are visible for all three tags. Unique peaks at 2125 cm^{-1} (Tetrayne), 2166 cm^{-1} (Triyne), and 2210 cm^{-1} (Diyne) show promise of multiplexing. A mixture of all three tags reveals peaks are still discrete and distinguishable from each other.

5.3.3 SERS of EVs Demonstrate Promising Diagnostic Ability

Having confirmed the ability of the tags to be applied towards multiplexing applications we moved forward with analysis of SERS on EVs that were isolated from the serum of patients after undergoing a clinician ordered CA125 test. Information about the patients can be found in table 4.1.

Table 4.1 Patient information for EV samples tested.

Label	**Age**	**Race**	**CA125 level (U/mL)**	**Diagnosis**
0001	90	White	79.8	Ovarian Cancer
0015	70	White	84.7	Carcinoma of ovary
0021	61	White	7.4	Malignant neoplasm
0024	75	White	17.6	Ovarian cancer
0033	63	White	13.5	Endometrial cancer
0051	63	Other	13.2	BRCA2 gene carrier
0058	55	Black	16.6	Bloating
0082	64	N/A	19.2	Adnexal mass
0087	52	White	33.1	Mass in ovary
0098	62	White	5.9	Family history of ovarian cancer

Size exclusion chromatography (SEC) was performed directly on serum samples and the isolated EVs were characterized using standard techniques to characterize size, morphology, and tetraspanin profiles.[68] Nanoparticle tracking analysis was used to visualize the size distribution of the isolated populations via Brownian motion tracking and provided additional information about the concentration of particles (Figure 4.3a). The isolated EVs fell within in the expected size distribution and were in high enough concentration to be usable for subsequent SERS analysis using antibody tagging. Isolates were also characterized using single particle interferometric reflectance imaging sensing (SP-IRIS) using the ExoView R100 platform. This system uses antibody coated spots for the common EV-associated tetraspanin proteins, CD63, CD9, and CD81 to assess their presence on the isolates being analyzed.[68] SP-IRIS on our isolates confirmed the presence of the three tetraspanins (Figure 4.3b) with the y-axis corresponding to the number of particles captured that express CD63 (red), CD9 (blue), and CD81 (green). Indeed, we see a good abundance of all three of these EV associated tetraspanin markers in our isolates. Taken together with the nanoparticle tracking analysis this demonstrated that our isolates contain strong EV populations that are suitable for further analysis.

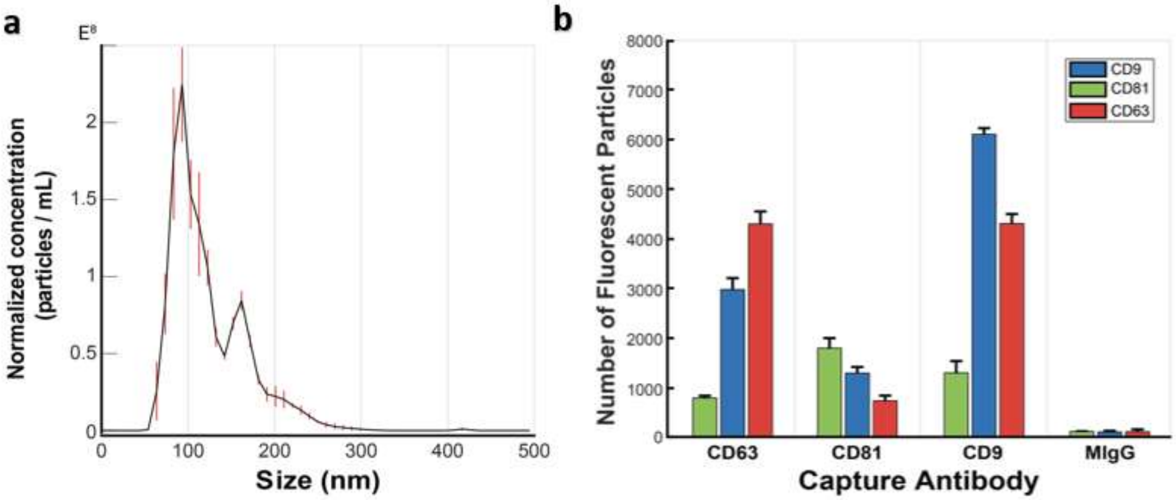

Figure 4.3 Characterization of EV isolates. a) NTA is used to measure particle concentration and size distribution. b) SP-IRIS demonstrates the presence of EVs captured in an antibody sandwich of tetraspanins CD9, CD63, and CD81, alongside mouse-IgG as a control. Particle counts from the fluorescently labeled detection antibodies are shown on the y-axis.

Before performing SERS analysis on the EVs including the Raman tags we wanted to see what diagnostic features were present in the EV signals themselves. Aside from the peaks corresponding to the alkyne functionality we also observed strong signal at 1600 cm^{-1} which corresponded to the antibodies themselves. To avoid including this in preliminary analysis of the EVs alone, SERS spectra for all samples were cropped from 800 cm^{-1} to 1550 cm^{-1} so as to remove any signal from the tagged antibodies in the analysis. After cropping, the spectral data and the first five principal components (Figure 4.4a) were saved and loaded into another MATLAB program for statistical analysis. A quadratic classifier was fitted to the dataset and used to generate a 3D plot (Figure 4.4b) and a confusion matrix (Figure 4c). This preliminary analysis demonstrated that the EVs themselves provide chemical fingerprints that allow for a decent job of separating cancer from non-cancer. Indeed, the sensitivity, specificity, and accuracy were calculated from the confusion matrix with values of 89.3%, 79%, and 83.3% respectively.

Following this the same analysis was performed using non-cropped spectra which included signal from the alkyne tagged antibodies. This analysis allows us to assess if there is any added value of the Raman tags. The first five principal components of the non-cropped data show distinct peaks in the 2000's cm^{-1} region corresponding to the alkynes (Figure 4.4d). The same quadratic classifier was applied to analyze the separation ability (Figure 4.4.e) and the sensitivity, specificity, and accuracy was determined to be 91%, 83.9%, and 87% respectively (Figure 4.4f). The increase in all three metrics demonstrates that the inclusion of the Raman tags indeed add diagnostic value relative to SERS analysis of EV isolates alone.

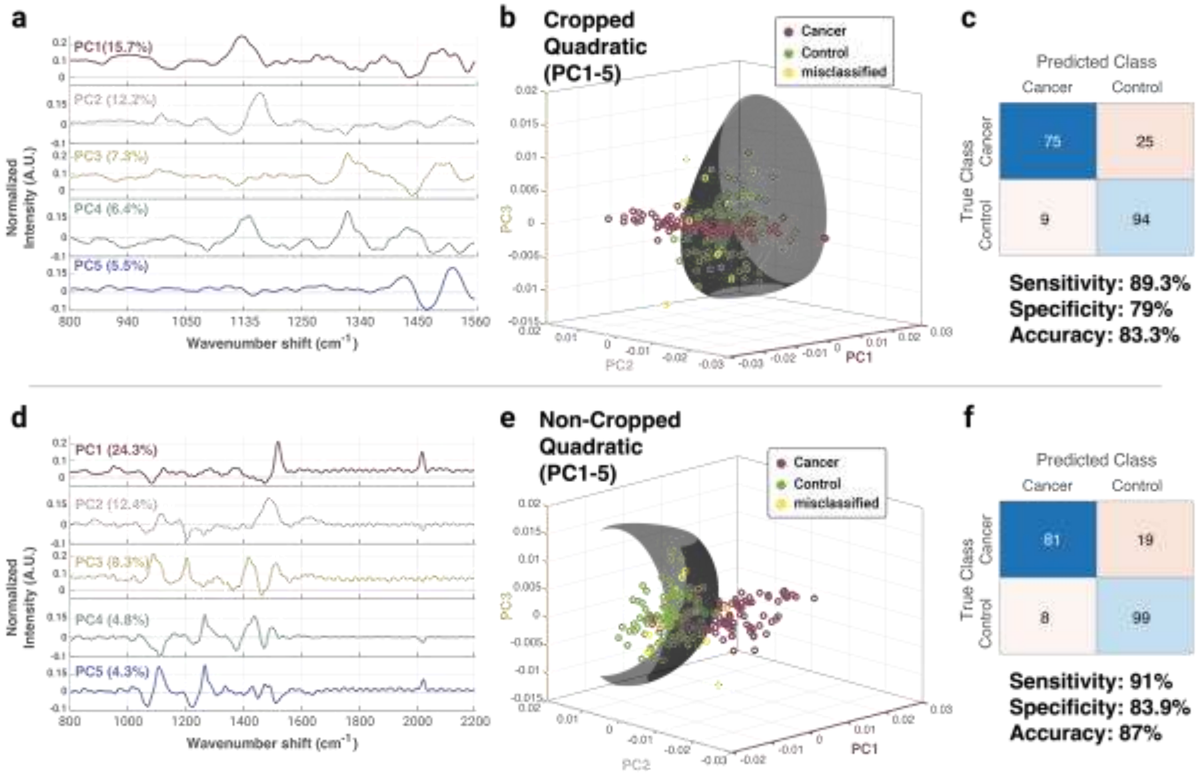

Figure 4.4: Analysis of cropped and non-cropped SERS spectra of EVs. a) First 5 principal components (PCs) with tag information cropped out. b) 3D plot of first 3 PCs with a quadratic classifier applied. Cancer spectra (purple), control spectra (green), and misclassified spectra (yellow) are projected with the classifier. c) Confusion matrix and calculated values for sensitivity (89.3%), specificity (79%), and accuracy (83.3%) d) First 5 PCs with tag information included. b) 3D plot of first 3 PCs with a quadratic classifier applied. Cancer spectra (purple), control spectra (green), and misclassified spectra (yellow) are projected with the classifier. c) Confusion matrix and calculated values for sensitivity (91%), specificity (83.9%), and accuracy (87%)

5.3.4 Analysis of Peaks from Principal Components

Although the general statistical analysis performed on the SERS measurements indeed showed an increase in the diagnostic ability when including the Raman tags in the analysis, identification of chemical components is also of interest. The first five principal components for both the cropped and tagged antibodies included data were analyzed and spectral features were identified. Table 4.2 displays the identified peaks and tentative chemical assignments and in Figure 4.5

peaks of interest are labeled. Analogous peaks that are present in both the cropped and uncropped data are highlighted in green. Interestingly, although we observe some overlap in the peaks present in both the cropped and uncropped data, the majority of chemical features in the principal components are unique.

Table 4.2 Peaks observed in both the cropped and uncropped Raman spectra and their respective chemical assignments

Dataset	PC	Wavenumber Shift	Peak Assignment
Cropped	1	1012	Si-O stretching
		1134	D-Mannose
		1350	Tryptophan
		1432	CH_2 lipids
		1493	Conjugated C=C vibrations in nucleic acids
		1536	Cytosine
	2	992	Phenylalanine
		1118	C-N stretching of protein backbone and lipids
		1167	Carbohydrate-related SERS vibrations
		1321	Carbohydrate-related SERS vibrations
		1510	Conjugated C=C vibrations in nucleic acids
	3	1126	D-mannose
		1286	CH_2, CH_3 deformation/C-N stretching
		1324	Nucleic acid bases
		1438	CH_2 bending and scissoring of glutamic acid
		1482	Amide II, C-N
		1503	Conjugated C=C vibrations in nucleic acids
	4	1075	C-C twisting, C-N stretching
		1150	Carbohydrate-related SERS vibrations

		1324	Nucleic acid bases
		1430	CH$_2$ lipids
		1475	CH$_2$ scissoring
		1522	Cytosine
	5	1426	COO$^-$ stretching
		1463	CH$_2$ (lipids)
		1510	Protein-related SERS vibration
Non-cropped	1	1133	D-Mannose
		1547	Protein vibrational modes (Amide II)
		1595	Raman Tag
		2125	Raman Tag
	2	1113	C-N stretching of protein backbone and lipids
		1167	Carbohydrate-related SERS vibrations
		1324	Nucleic acid bases
		1571	Guanine, Alanine
		2125	Raman Tag
	3	1139	D-mannose
		1267	NH^{3+} rocking and amide III vibrations
		1509	Adenine
		1597	Vibrations in nucleic acids
	4	1159	Carbohydrate-related SERS vibrations
		1324	Carbohydrate-related SERS vibrations
		1441	N-C-N asymmetric stretch
		1508	Adenine
		1544	Protein vibrational modes (Amide II)
		1568	Cytochrome in proteins

		2125	Raman Tag
	5	1115	C-N stretching of protein backbone and lipids
		1158	Carbohydrate-related SERS vibrations
		1282	CH_2, CH_3 deformation/C-N stretching
		1326	Nucleic acid bases
		1548	Protein vibrational modes (Amide II)
		2125	Raman Tag

Conserved peaks across both datasets include 1134 cm^{-1}, 1167 cm^{-1}, 1324 cm^{-1}, and 1520 cm^{-1}. 1134 and 1167 cm^{-1} correspond to D-mannose carbohydrate vibrations whereas peaks at 1324 and 1520 cm^{-1} correspond to nucleic acid bases and C=C conjugations in them respectively. The presence of these peaks in both the cropped and uncropped principal components would suggest they are inherently important information related to the pathology of the patient and are required for the correct diagnosis of the samples.

Interestingly, many of the peaks are unique to either the cropped or uncropped dataset suggesting the ability of the tags to pick up unique populations. The cropped samples showed more peaks corresponding to amino acids including tryptophan (1360 cm^{-1}), glutamic acid (1438 cm^{-1}), cytosine (1536 cm^{-1}), and phenylalanine (1536 cm^{-1}). We also observed additional peaks corresponding to conjugated C=C vibrations in nucleic acids at 1493 cm^{-1}, 1503 cm^{-1}, and 1510 cm^{-1}. Lastly, we detected more lipid content in the cropped data at 1430 cm^{-1} and 1464 cm^{-1}.

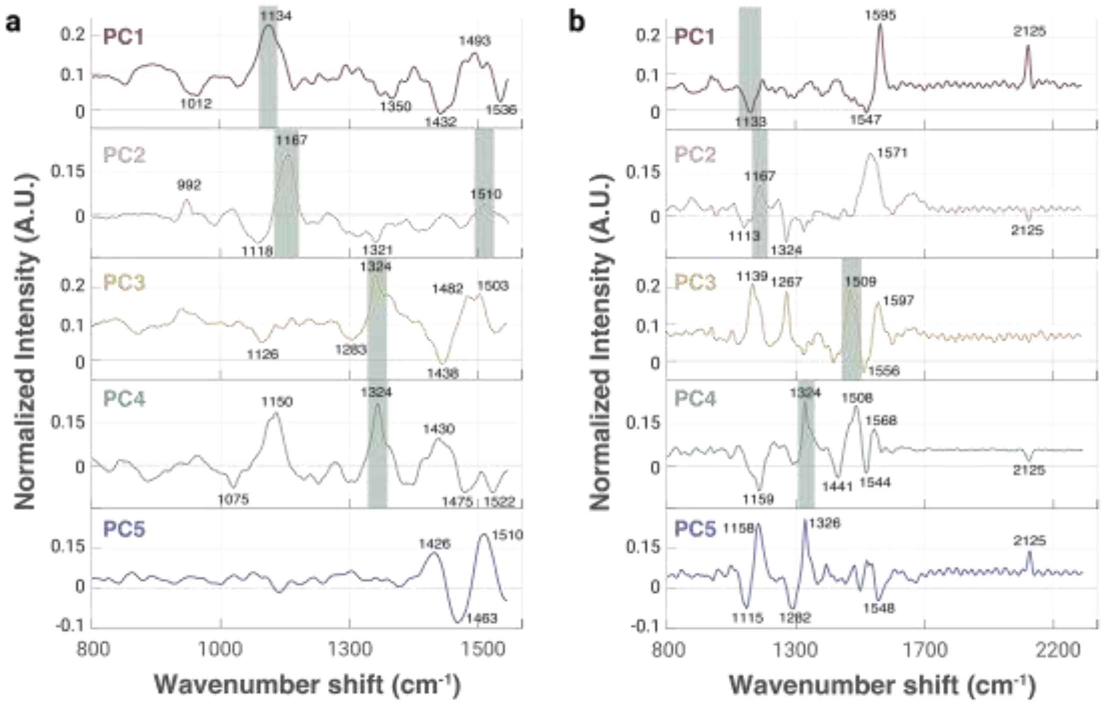

Figure 4.5 Peak identification for cropped (left) and non-cropped (right) datasets. Green highlights indicate conserved peaks seen in both datasets. a) Cropped dataset showed many peaks present and differing throughout the top 5 PCs. b) Non-cropped dataset has different peaks associated with the PCs.

In the spectra including the Raman tags many of the protein associated peaks were not amino acid specific but corresponded to vibrations for Amide II and Amide III (1267 cm^{-1}, 1544 cm^{-1}, and 1548 cm^{-1}). Furthermore, an increased number of peaks related to nucleic acids were observed corresponding to adenine directly as well as nucleic acid bases (1508 cm^{-1} along with 1324 and 1597 cm^{-1} respectively). The Raman tag signal at 2125 cm^{-1} was present in almost every principal component further supporting that the tagged antibodies aid in identifying populations that contain unique and important diagnostic information.

Lastly, we can relate which features are more or less present in samples that were captured by the tagged antibodies by identifying the sign (positive or negative) of the peaks when the tag peak is positive. Peaks that remain positive when the tag peak is positive suggest a correlation where there is more of that particular chemical signature in the tagged population. For example, the first principal component has the highest tag signature (1595 cm^{-1} and 2125 cm^{-1}) meaning it is one of the most important spectral features identified in the dataset. However, the other two peaks present corresponding to D-Mannose (1133 cm^{-1}) and Amide II (1547 cm^{-1}) are negative indicating that these chemical features are less present in the populations captured by the tagged-antibodies. Additionally in the second principal component we can see negative peaks (1113 cm^{-1}, 1324 cm^{-1}, and 2125 cm^{-1}) corresponding to lipid and carbohydrate signals and positive peaks (1167 and 1571 cm^{-1}) corresponding protein and nucleic acids.

The signals directly corresponding with the tag peaks (both either positive or negative) represent more carbohydrate and nucleic acids signatures then those peaks with the opposite signs. Lipid and protein signatures seemed to reflect more in the samples with weaker tag signals. Taken together, this would suggest that EV populations that are captured by the tagged antibodies contain more carbohydrate and nucleic acid materials. Given the inherent heterogeneity of EV populations this interesting but expected.

5.3.5 Enzyme-linked Immunosorbent Assays on Isolated EVs

In addition to the SERS analysis on the EVs, enzyme-linked immunosorbent assays (ELISA) were also performed in order to confirm the presence of the proteins being targeted by our Raman tagged antibodies. Notably, in the SERS analysis the HE4-tetrayne antibody conjugate was the only specific tag present in the principal component for the non-cropped data despite many spectra that showed multiple tags simultaneously (Figure 4.6).

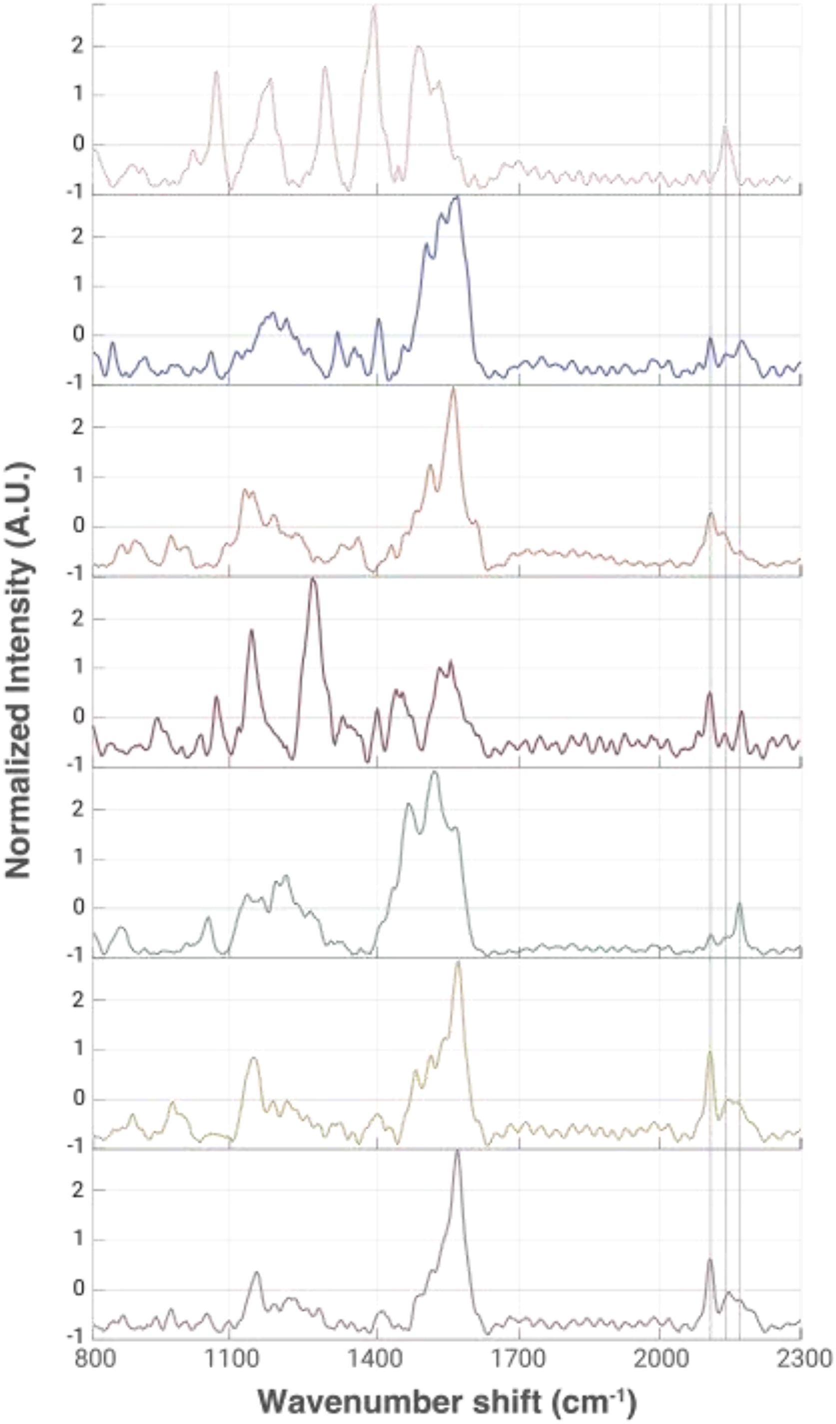

Figure 4.6 Representative spectra showing all three Raman tags could be seen throughout the samples. Vertical lines (right to left) show the peaks for HE4-tetryne, CA19-9-triyne, and CA125-diyne.

This indicates that HE4 was more highly expressed on the EVs than either CA125 or CA19-9 although all three proteins are expressed on the EVs. Indeed, the ELISA data does show the presence of HE4, CA125, and CA19-9 in most of the patient samples (Figure 4.7). CA125 showed the highest variability in expression level from patient to patient corresponding well to the data shown in Table 1. HE4 and CA19-9 showed more consistent expression levels across patients with HE4 showing slightly higher expression levels consistent with the observed tetrayne signal in the principal component analysis. Additionally, it is worth mentioning that the of all the antibody conjugates the diyne tagged one showed up the least in the Raman data. This is consistent with the ELISA data showing high levels of CA125 present in only two patient samples.

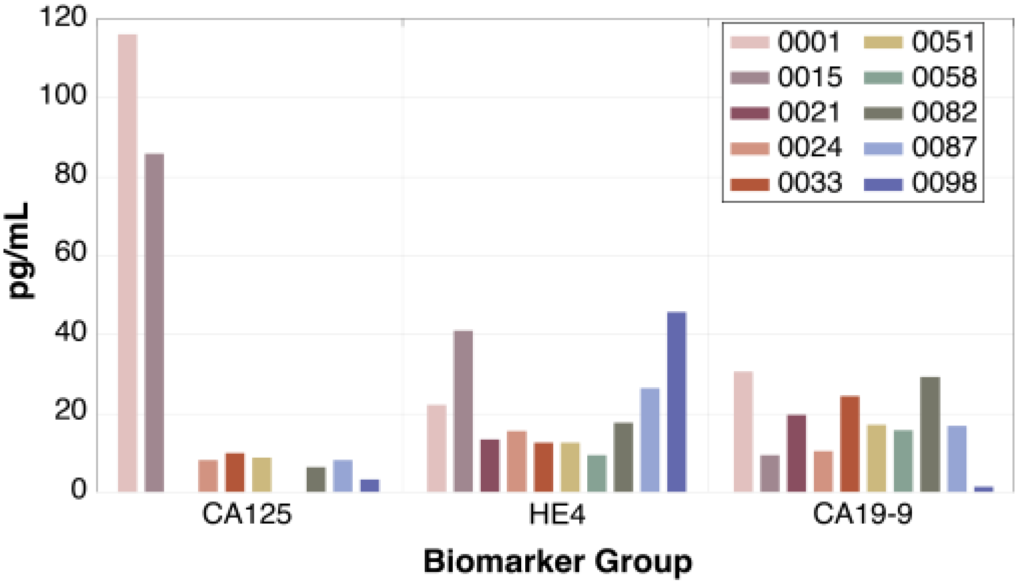

Figure 4.7 Relative protein expression for the three chosen biomarkers. Isolated EVs were tested using sandwich ELISAs to test the level of surface expression for CA125, HE4, and CA19-9.

5.4 Conclusions and Outlooks

In this study we reported robust Raman data demonstrating the ability of our in-house synthesized antibody-Raman tag conjugates to bind potential ovarian cancer biomarkers expressed on EVs isolated from patient biofluids. Surface expression of CA125, HE4, and CA19-9 were confirmed using sandwich ELISA assays. A set of three polyynes (diyne, triyne, and tetrayne) were synthesized using classic alkyne coupling reactions. The polyynes each contained a reactive amine handle for subsequent conjugation to anti-CA125, anti-HE4, and anti-CA19-9 antibodies. Subsequent SERS analysis of the isolated EVs incubated with the tagged antibodies revealed unique datasets from cropped (excluding the Raman tag) and uncropped (including the Raman tag) spectra. The inclusion of the Raman tag peaks resulted in higher sensitivity, specificity, and accuracy towards distinguishing cancer from non-cancer EV populations. We believe we have demonstrated an exciting new platform for identifying cancer derived EVs based on both their unique Raman spectral features as well as capturing and multiplexing based on specific EV surface biomarkers. This and future developments should aid in cancer detection and patient outcomes.

5.5 Materials & Methods

5.5.1 Synthesis of Raman Tags

Synthesis of 4-(bromoethynyl)phenyl methanol, 1. To a clean round bottom was added 4-ethynylbenzyl alcohol (2.00 g, 15.13 mmol), N-bromosuccinimide (2.82 g, 15.9 mmol), and silver nitrate (0.26 g, 1.51 mmol). The contents were then dissolved in acetone (120 mL) and allowed to stir under ambient conditions for three hours. Following this the reaction mixture was filtered through a Buchner funnel and an equal volume of water was added to the filtrate. The aqueous layer was extracted with ethyl acetate (3 X 25 mL) and the combined organic extract was washed with a saturated sodium bicarbonate solution. The organic extract was collected and dried with anhydrous magnesium sulfate and was then concentrated under reduced pressure to obtain the product as a pale-yellow solid (2.61 g, 81%). ^{1}H NMR (400 MHz, $CDCl_3$) δ 7.40-7.42 (d, 2H), 7.24-7.26 (d, 2H), 4.62 (s, 2H). ^{13}C NMR (101 MHz, $CDCl_3$) δ 141.51, 132.23, 126.83, 79.97, 64.76, 49.95. Low-resolution mass spectrometry (LRMS) (m/z): $[M+H]^+$ calculated for C_9H_6Br 192.9; found, 192.9.

Synthesis of Diyne, 2. To a clean round bottom was added CuCl (6 mg, 0.06 mmol) which was then dissolved in 30% aqueous n-butylamine (2 mL). The solution immediately turned blue. A few small crystals of hydroxylamine hydrochloride were added and the solution was stirred until the color changed from blue to clear suggesting reduction of Cu(II) to Cu(I). The solution was then placed in an ice bath. 4-ethynylaniline (333 mg, 2.85 mmol) was dissolved in anhydrous THF (1 mL) and added to the copper solution on ice. The color immediately changed from clear to bright yellow. The bromoalkyne,1, (602 mg, 2.85 mmol) was then dissolved in anhydrous THF (1 mL) and immediately added to the reaction mixture on ice. The reaction was allowed to come to room temperature and stirred for three hours. Hydroxylamine crystals were added roughly every 30 minutes to ensure cycling of Cu(II) to Cu(I). After three hours the reaction mixture was concentrated under reduced pressure and a silica gel column was run using 50/50 hexanes/ethyl acetate as eluent to afford the product as a yellowish powder (267 mg, 38% yield). ^{1}H NMR (400 MHz, DMSO-d6) δ 7.49-7.51 (d, 2H), 7.33-7.35 (d, 2H), 7.22-7.25 (d, 2H), 6.52-6.55 (d, 2H), 5.80 (br), 5.30 (br), 4.51 (s, 2H). ^{13}C NMR (151 MHz, DMSO-d6) δ 144.24, 133.89, 131.94, 126.66, 119.29, 113.58, 105.50, 84.27, 80.96, 74.24, 71.30, 62.45. Low-resolution mass spectrometry (LRMS) (m/z): $[M+H]^+$ calculated for $C_{17}H_{14}NO$ 248.1; found, 248.1.

Synthesis of TMS protected 4-ethynylaniline, 3. To a round bottom was added 4-ethynylaniline (500 mg, 4.27 mmol), trimethylsilylacetylene (TMSA) (2.09 g, 21.4 mmol), and Cu-TMEDA (1.9 g, 4.27 mmol). The contents of the round bottom were then dissolved in acetone (15 mL) and were allowed to stir at room temperature with air bubbling through the solution until full conversion of starting material was observed by LCMS. The reaction mixture was then concentrated under reduced pressure and purified by silica gel chromatography using 80/20 hexanes/ethyl acetate as the eluent. ^{1}H NMR (400 MHz, $CDCl_3$) δ 7.30-7.32 (d, 2H), 6.58-6.60 (d, 2H), 3.92 (br) 0.24 (s, 9H). ^{13}C NMR (101 MHz, $CDCl_3$) δ 147.67, 134.29, 114.59, 110.14, 89.46, 88.48, 78.07, 72.37, -0.27. Low-resolution mass spectrometry (LRMS) (m/z): $[M+H]^+$ calculated for $C_{13}H_{16}NSi$ 214.1; found, 214.1.

Synthesis of 4-(buta-1,3-diyn-1-yl)aniline, 4. Compound 3 (432 mg, 2.02 mmol) was added to a round bottom with potassium carbonate (1.12 g, 8.13 mmol) and they were dissolved in a 1:1 solution of MeOH:CH_2Cl_2 (25 mL). The reaction was allowed to stir under ambient conditions for 45 minutes. Following this the reaction was quenched in 100 mL of water and extracted into DCM (3 x 15 mL). The combined organic extract was dried over anhydrous magnesium sulfate and the solution was concentrated under reduced pressure to obtain a black oil. The crude material was used immediately for the following alkyne coupling.

Synthesis of Triyne, 5. To a round bottom was added CuCl (4 mg, 0.04 mmol) in 30% aqueous n-butylamine (2 mL) and allowed to stir until a deep blue solution was achieved. To this was added a few small crystals of hydroxylamine hydrochloride and the solution was stirred until it went from blue to colorless. The solution was placed in an ice bath and allowed to cool for ten minutes. To this was added compound 4 (286 mg, 2.02 mmol) dissolved in anhydrous THF (2 mL). The haloalkyne dissolved in anhydrous THF (2 mL) was immediately added to the reaction mixture and the solution was allowed to come to room temperature. The reaction was stirred until full conversion of the starting materials were observed by LCMS (about two hours). The reaction was then concentrated under reduced pressure and the crude mixture was purified by column chromatography using 80/20 hexanes/ethyl acetate as eluent. ^{1}H NMR (400 MHz, DMSO-d6) δ 7.56-7.58 (d, 2H), 7.36-7.38 (d, 2H), 7.28-7.30 (d, 2H), 6.52-6.54 (d, 2H), 5.96 (br), 5.33 (t, 1H), 4.52-4.54 (d, 2H). ^{13}C NMR (101 MHz, DMSO-d6) δ 151.80, 145.74, 135.22, 133.15, 127.16, 118.39, 114.09, 104.33, 82.85, 79.76, 74.26, 72.36, 67.86, 66.29, 62.87. Low-resolution mass spectrometry (LRMS) (m/z): $[M+H]^+$ calculated for $C_{19}H_{14}NO$ 272.1; found, 272.1.

Synthesis of TMS protected ethynylbenzyl alcohol, 6. To a round bottom was added 4-ethynylbenzyl alcohol (924 mg, 7.00 mmol), trimethylsilylacetylene (3.44 g, 35 mmol), and Cu-TMEDA (3.25 g, 7.00 mmol). The contents were dissolved in acetone (23 mL) and the reaction was allowed to stir under ambient conditions for two hours or until the reaction had gone to completion as observed by LCMS. Following full conversion of starting materials to product the reaction mixture was concentrated under reduced pressure and the crude solid was purified by silica gel chromatography using 60/40 hexanes/ethyl acetate as eluent. The product was afforded as a dark yellow solid (671 mg, 42%). ^{1}H NMR (400 MHz, $CDCl_3$) 7.48-7.50 (d, 2H), 7.32-7.34 (d, 2H), 4.70-4.72 (d, 2H), 0.25 (s, 9H). ^{13}C NMR (101 MHz, $CDCl_3$) δ 142.34, 133.00, 126.92, 120.67, 90.88, 87.93, 76.73, 74.32, 64.93, -0.26. Low-resolution mass spectrometry (LRMS) (m/z): $[M-OH]^+$ calculated for $C_{14}H_{15}NSi$ 211.1; found, 211.1.

Synthesis of Tetrayne, 7. To a round bottom was added TMS protected ethynylaniline **3** (262 mg, 1.23 mmol), TMS protected ethynylbenzyl alcohol **6** (187 mg, 0.820 mmol) and K_2CO_3 (453 mg, 3.28 mmol). The contents were dissolved in 1:1 MeOH/CH_2Cl_2 and the reaction was allowed to stir at room temperature for one hour. Following this the reaction was quenched with water and extracted three times with DCM (15 mL). The combined extracts were concentrated under reduced pressure and redissolved in acetone (10 mL). To this was added Cu-TMEDA (381 mg, 0.820 mmol). The coupling was allowed to proceed for two hours or until complete conversion was observed by LCMS. After this the reaction was concentrated under reduced pressure and the crude mixture was purified by silica gel chromatography using 20/80 hexanes/ethyl acetate as eluent to afford the desired product as a light-yellow power (121 mg, 50%). ^{1}H NMR (400 MHz, DMSO-d6) δ 7.60-7.62 (d, 2H), 7.37-7.39 (d, 2H), 7.31-7.33 (d, 2H), 6.53-6.55 (d, 2H), 6.08 (br), 5.33-5.36 (t, 1H), 4.53-4.55 (d, 2H). ^{13}C NMR (151 MHz, dmso) δ 151.80, 145.91, 135.30, 133.12, 126.74, 117.18, 113.67, 102.92, 82.26, 79.02, 73.45, 72.13, 67.14, 66.70, 65.27, 64.00, 62.39. Low-resolution mass spectrometry (LRMS) (m/z): $[M+H]^+$ calculated for $C_{21}H_{14}NO$ 296.1; found, 296.1.

Conjugation of Raman Tags to Antibodies. Generally, the Raman tag was coupled to Maleimide-PEG-COOH using DIC and Oxyma Pure (1 equivalent each) in DMF (0.4 M) with stirring overnight at room temperature. The following morning the reaction was quenched with water and extracted with DCM (3x). The combined DCM extract was concentrated under reduced pressure and the crude mixture was used without further purification for coupling to the antibodies. Molar excess (10 equivalents) of the Raman tag was dissolved in DMSO and added to the antibody solution in phosphate buffer (final concentration of DMSO <5%). The coupling was allowed to complete for one hour at room temperature without stirring. Following coupling any unreacted Raman tag was removed via 30 kDa spin column. The retained antibody was then washed three times with phosphate buffer before elution.

5.5.2 Extracellular Vesicle Isolation and Characterization

EV Isolation and Preparation. The EVs used in this study were isolated from clinical serum samples provided by the UC Davis Comprehensive Cancer Center (UCDCCC) following guidelines recognized by UC Davis Biorepository (IRB ID: XXX). Patient serum was given as deidentified remnants following a clinician ordered CA125 assay. Trained clinicians identified sample types by histopathology analysis. Approximately 1 mL of serum was obtained from each patient. EVs were isolated using size-exclusion chromatography (SEC) via an Automatic Fraction Collector (AFC) and prefabricated columns (qEV35, Izon Science). One 1.5 mL Eppendorf tube was loaded onto the AFC carousel and a single qEV35 column was inserted onto the mount. The column was flushed with 1 mL of filtered PBS then 150 μL of serum was loaded on the column. Once the sample had reached the upper frit of the column, 2 mL of filtered PBS was topped off and the machine proceeded to collect the void fraction. After the void fraction, the Eppendorf tube was filled with 800 μL of isolated EV material. Tubes were frozen at -80 when not in use.

Nanoparticle Tracking Analysis. Sample particle concentrations and size distributions were measured using a NanoSight LM10 (Malvern Panalytical) equipped with a 405 nm blue laser and sCMOS camera. 1000-fold dilutions of EV isolates were prepared. Filtered ultrapure water was also used to flush the NTA chamber and tubing before sample addition. 1 mL of each diluted sample was loaded into a syringe and placed on an automatic syringe pump for injection. Data was recorded as three 90 s videos containing a minimum of 200 particle tracks per video, recorded at camera level 13. NTA 3.1 software was used to analyze the data and track the Brownian motion of the individual particles recorded. Subsequently the software calculated hydrodynamic diameters (nm) of the tracked particles using the Einstein-Stokes relation, and the count-based concentrations (particles per mL) are simultaneously obtained as the number of particles and volume of the sample chamber are known.

Protein Concentration Measurement. Total protein content for each sample was measured using a BCA assay (Pierce BCA Protein Assay Kit, ThermoFisher Scientific) following the manufacturer’s instructions. 15 μL of SEC-isolated EVs were mixed with 8 μL of RIPA buffer (ThermoFisher Scientific) and 67 μL of ultra-pure water, vortexed briefly, and incubated on ice for 30 min prior to starting the assay.

ExoView Tetraspanin Assay. ExoView kits were used as purchased (NanoView Biosciences) to profile protein expression of EVs. Chips were stored at 4 °C when not in use and warmed to room temperature prior to use. Chips were pre-scanned using the manufacturer's protocol. For EV incubation, chips were placed in a 24-well plate. 5 μL of stock EVs were diluted in 45 μL incubation buffer then 35 μL of this solution was pipetted directly onto each respective chip. The plate was sealed and incubated overnight at room temperature. The following morning, chips were placed in the automatic chip washer and run according to manufacturer's instructions. After washing, chips were incubated with fluorescently labelled antibodies then washed again and finally dried before scanning. Chips were once again scanned for interferometric and fluorescence imaging.

5.5.3 SERS Analysis

Raman Tag Incubation. Isolated EVs were thawed on ice and 50 μL was pipetted into a fresh Eppendorf tube. 1 μL of each antibody-tag pair (HE4-tetrayne, CA19-9-triyne, and CA125-diyne) were added to the tube and mixture was briefly vortexed to mix. The tube was incubated at 4 °C, then unbound tags were removed with an additional SEC step as described above. 10 μL of the EV-tag solution was incubated on the SERS substrate (Silmeco) for 30 minutes, then inverted onto a glass coverslip and placed on our custom inverted confocal Raman microscope for subsequent measurements.

Raman Acquisition and Analysis. SERS spectra were acquired using a custom-built inverted Raman scanning confocal microscope with a 60X, 1.2 NA water immersion objected on an IX73 Olympus microscope. An excitation wavelength of 785 nm was used for measurements. Spectra were captured with an Andor Kymera-3281-C spectrophotometer and processed using Solis v.4.30.30034.0 software. Exposure time was set to 1 s per scan with a laser power of 15 mW.

Across all samples, SERS spectra were sampled in 20 different spatial locations with a 20-spectra kinetic series collected. Spots were selected when noticeable SERS peaks became visible and stable, as well as when the tag-specific peaks were seen. Spectral analysis was performed using custom software written in MATLAB (MathWorks, MA, USA). Spectral preprocessing included penalized least-squares (PLS) background correction, smoothing, and normalization. Processed datasets were subjected to principal component analysis (PCA) and hierarchical clustering analysis based on corresponding MATLAB built-in features. QDA analysis with the first 5 PCs and calculation of the confusion matrix, sensitivity, specificity, and accuracy were also carried out with the built-in MATLAB functions.

Enzyme-Linked Immunosorbent Assays. Sandwich ELISA kits were purchased for the three specific biomarkers. HE4 and CA125 (R&D Systems) and CA19-9 (Sigma Aldrich) kits were used to analyze the level of expression on EV surfaces. Each kit was used according to manufacturer's instructions. Absorbance readouts were taken at 450 nm using a SpectraMax i3 (Molecular Devices) and concentration was determined by fitting to standards.

5.5 References

(1) Hassanpour, S. H.; Dehghani, M. Review of Cancer from Perspective of Molecular. *J. Cancer Res. Pract.* **2017**, *4* (4), 127–129.

(2) Ward, E. M.; Sherman, R. L.; Henley, S. J.; Jemal, A.; Siegel, D. A.; Feuer, E. J.; Firth, A. U.; Kohler, B. A.; Scott, S.; Ma, J.; Anderson, R. N.; Benard, V.; Cronin, K. A. Annual Report to the Nation on the Status of Cancer, Featuring Cancer in Men and Women Age 20-49 Years. *J. Natl. Cancer Inst.* **2019**, *111* (12), 1279–1297.

(3) Fidler, M. M.; Gupta, S.; Soerjomataram, I.; Ferlay, J.; Steliarova-Foucher, E.; Bray, F. Cancer Incidence and Mortality among Young Adults Aged 20-39 Years Worldwide in 2012: A Population-Based Study. *Lancet. Oncol.* **2017**, *18* (12), 1579–1589.

(4) Codipilly, D. C.; Sawas, T.; Dhaliwal, L.; Johnson, M. L.; Lansing, R.; Wang, K. K.; Leggett, C. L.; Katzka, D. A.; Iyer, P. G. Epidemiology and Outcomes of Young-Onset Esophageal Adenocarcinoma: An Analysis from a Population-Based Database. *Cancer Epidemiol. biomarkers Prev. a Publ. Am. Assoc. Cancer Res. cosponsored by Am. Soc. Prev. Oncol.* **2021**, *30* (1), 142–149.

(5) Huang, J.; Lok, V.; Ngai, C. H.; Chu, C.; Patel, H. K.; Thoguluva Chandraseka, V.; Zhang, L.; Chen, P.; Wang, S.; Lao, X.-Q.; Tse, L. A.; Xu, W.; Zheng, Z.-J.; Wong, M. C. S. Disease Burden, Risk Factors, and Recent Trends of Liver Cancer: A Global Country-Level Analysis. *Liver cancer* **2021**, *10* (4), 330–345.

(6) Wong, M. C. S.; Huang, J.; Chan, P. S. F.; Choi, P.; Lao, X. Q.; Chan, S. M.; Teoh, A.; Liang, P. Global Incidence and Mortality of Gastric Cancer, 1980-2018. *JAMA Netw. open* **2021**, *4* (7), e2118457.

(7) Gupta, S.; Harper, A.; Ruan, Y.; Barr, R.; Frazier, A. L.; Ferlay, J.; Steliarova-Foucher, E.; Fidler-Benaoudia, M. M. International Trends in the Incidence of Cancer Among Adolescents and Young Adults. *J. Natl. Cancer Inst.* **2020**, *112* (11), 1105–1117.

(8) Heer, E.; Harper, A.; Escandor, N.; Sung, H.; McCormack, V.; Fidler-Benaoudia, M. M. Global Burden and Trends in Premenopausal and Postmenopausal Breast Cancer: A Population-Based Study. *Lancet. Glob. Heal.* **2020**, *8* (8), e1027–e1037.

(9) Lortet-Tieulent, J.; Ferlay, J.; Bray, F.; Jemal, A. International Patterns and Trends in Endometrial Cancer Incidence, 1978-2013. *J. Natl. Cancer Inst.* **2018**, *110* (4), 354–361.

(10) Siegel, R. L.; Miller, K. D.; Fuchs, H. E.; Jemal, A. Cancer Statistics, 2021. *CA. Cancer J. Clin.* **2021**, *71* (1), 7–33.

(11) Shah, R. R.; Millien, V. O.; da Costa, W. L. J.; Oluyomi, A. O.; Gould Suarez, M.; Thrift, A. P. Trends in the Incidence of Early-Onset Colorectal Cancer in All 50 United States from 2001 through 2017. *Cancer* **2022**, *128* (2), 299–310.

(12) Wang, F.; Luo, L.; McLafferty, S. Healthcare Access, Socioeconomic Factors and Late-Stage Cancer Diagnosis: An Exploratory Spatial Analysis and Public Policy Implication. *Int. J. Public Pol.* **2010**, *5* (2–3), 237–258.

(13) Farrell, K.; Bennett, D. L.; Schwartz, T. L. Screening for Breast Cancer: What You Need to Know. *Mo. Med.* **2020**, *117* (2), 133–135.

(14) Bevan, R.; Rutter, M. D. Colorectal Cancer Screening-Who, How, and When? *Clin. Endosc.* **2018**, *51* (1), 37–49.

(15) Sachan, P. L.; Singh, M.; Patel, M. L.; Sachan, R. A Study on Cervical Cancer Screening

Using Pap Smear Test and Clinical Correlation. *Asia-Pacific J. Oncol. Nurs.* **2018**, *5* (3), 337–341.

(16) David, M. K.; Leslie, S. W. Prostate Specific Antigen. In *StatPearls*; Treasure Island (FL), 2022.

(17) Stephan, C.; Rittenhouse, H.; Hu, X.; Cammann, H.; Jung, K. Prostate-Specific Antigen (PSA) Screening and New Biomarkers for Prostate Cancer (PCa). *EJIFCC* **2014**, *25* (1), 55–78.

(18) Merrill, R. M.; Otto, S. A.; Hammond, E. B. Prostate-Specific Antigen Screening According to Health Professional Counseling and Age in the United States. *Prostate Cancer* **2022**, *2022*, 8646314.

(19) Fridriksson, J.; Gunseus, K.; Stattin, P. Information on Pros and Cons of Prostate-Specific Antigen Testing to Men Prior to Blood Draw: A Study from the National Prostate Cancer Register (NPCR) of Sweden. *Scand. J. Urol. Nephrol.* **2012**, *46* (5), 326–331.

(20) Schwarzenbach, H.; Hoon, D. S. B.; Pantel, K. Cell-Free Nucleic Acids as Biomarkers in Cancer Patients. *Nat. Rev. Cancer* **2011**, *11* (6), 426–437.

(21) Cirmena, G.; Dameri, M.; Ravera, F.; Fregatti, P.; Ballestrero, A.; Zoppoli, G. Assessment of Circulating Nucleic Acids in Cancer: From Current Status to Future Perspectives and Potential Clinical Applications. *Cancers (Basel).* **2021**, *13* (14).

(22) Xi, X.; Li, T.; Huang, Y.; Sun, J.; Zhu, Y.; Yang, Y.; Lu, Z. J. RNA Biomarkers: Frontier of Precision Medicine for Cancer. *Non-coding RNA* **2017**, *3* (1).

(23) Lu, Z.-L.; Chen, Y.-J.; Jing, X.-Y.; Wang, N.-N.; Zhang, T.; Hu, C.-J. Detection and Identification of Serum Peptides Biomarker in Papillary Thyroid Cancer. *Med. Sci. Monit. Int. Med. J. Exp. Clin. Res.* **2018**, *24*, 1581–1587.

(24) Martorella, A.; Robbins, R. Serum Peptide Profiling: Identifying Novel Cancer Biomarkers for Early Disease Detection. *Acta bio-medica : Atenei Parmensis*. Italy 2007, pp 123–128.

(25) Murgan, S. S.; Abd Elaziz, F. J.; Nasr, A. M. A.; Elfaki, M. E. E.; Khalil, E. A. G. Ovarian Cancer: Tumor-Specific Urinary Micro-Peptides Profiling as Potential Biomarkers for Early Diagnosis. *Proteomes* **2020**, *8* (4).

(26) Heo, C.-K.; Hwang, H.-M.; Lim, W.-H.; Lee, H.-J.; Yoo, J.-S.; Lim, K.-J.; Cho, E.-W. Cyclic Peptide Mimotopes for the Detection of Serum Anti-ATIC Autoantibody Biomarker in Hepato-Cellular Carcinoma. *Int. J. Mol. Sci.* **2020**, *21* (24).

(27) Liang, S.-L.; Chan, D. W. Enzymes and Related Proteins as Cancer Biomarkers: A Proteomic Approach. *Clin. Chim. Acta.* **2007**, *381* (1), 93–97.

(28) Gam, L.-H. Breast Cancer and Protein Biomarkers. *World J. Exp. Med.* **2012**, *2* (5), 86–91.

(29) Hristova, V. A.; Chan, D. W. Cancer Biomarker Discovery and Translation: Proteomics and Beyond. *Expert Rev. Proteomics* **2019**, *16* (2), 93–103.

(30) El-Khoury, V.; Schritz, A.; Kim, S.-Y.; Lesur, A.; Sertamo, K.; Bernardin, F.; Petritis, K.; Pirrotte, P.; Selinsky, C.; Whiteaker, J. R.; Zhang, H.; Kennedy, J. J.; Lin, C.; Lee, L. W.; Yan, P.; Tran, N. L.; Inge, L. J.; Chalabi, K.; Decker, G.; Bjerkvig, R.; Paulovich, A. G.; Berchem, G.; Kim, Y. J. Identification of a Blood-Based Protein Biomarker Panel for Lung Cancer Detection. *Cancers (Basel).* **2020**, *12* (6).

(31) Yan, F.; Zhao, H.; Zeng, Y. Lipidomics: A Promising Cancer Biomarker. *Clin. Transl. Med.* **2018**, *7* (1), 21.

(32) Perrotti, F.; Rosa, C.; Cicalini, I.; Sacchetta, P.; Del Boccio, P.; Genovesi, D.; Pieragostino, D. Advances in Lipidomics for Cancer Biomarkers Discovery. *Int. J. Mol. Sci.* **2016**, *17* (12).

(33) Chandler, P. D.; Song, Y.; Lin, J.; Zhang, S.; Sesso, H. D.; Mora, S.; Giovannucci, E. L.; Rexrode, K. E.; Moorthy, M. V.; Li, C.; Ridker, P. M.; Lee, I.-M.; Manson, J. E.; Buring, J. E.; Wang, L. Lipid Biomarkers and Long-Term Risk of Cancer in the Women's Health Study. *Am. J. Clin. Nutr.* **2016**, *103* (6), 1397–1407.

(34) Park, J.; Shin, Y.; Kim, T. H.; Kim, D.-H.; Lee, A. Plasma Metabolites as Possible Biomarkers for Diagnosis of Breast Cancer. *PLoS One* **2019**, *14* (12), e0225129.

(35) Wu, X.; Ao, H.; Gao, H.; Zhu, Z. Metabolite Biomarker Discovery for Human Gastric Cancer Using Dried Blood Spot Mass Spectrometry Metabolomic Approach. *Sci. Rep.* **2022**, *12* (1), 14632.

(36) Uesato, Y.; Sasahira, N.; Ozaka, M.; Sasaki, T.; Takatsuki, M.; Zembutsu, H. Evaluation of Circulating Tumor DNA as a Biomarker in Pancreatic Cancer with Liver Metastasis. *PLoS One* **2020**, *15* (7), e0235623.

(37) Cheng, F.; Su, L.; Qian, C. Circulating Tumor DNA: A Promising Biomarker in the Liquid Biopsy of Cancer. *Oncotarget* **2016**, *7* (30), 48832–48841.

(38) Yang, J.; Hui, Y.; Zhang, Y.; Zhang, M.; Ji, B.; Tian, G.; Guo, Y.; Tang, M.; Li, L.; Guo, B.; Ma, T. Application of Circulating Tumor DNA as a Biomarker for Non-Small Cell Lung Cancer. *Front. Oncol.* **2021**, *11*, 725938.

(39) Nash, Z.; Menon, U. Ovarian Cancer Screening: Current Status and Future Directions. *Best Pract. Res. Clin. Obstet. Gynaecol.* **2020**, *65*, 32–45.

(40) Lheureux, S.; Gourley, C.; Vergote, I.; Oza, A. M. Epithelial Ovarian Cancer. *Lancet* **2019**, *393* (10177), 1240–1253.

(41) Torre, L. A.; Trabert, B.; DeSantis, C. E.; Miller, K. D.; Samimi, G.; Runowicz, C. D.; Gaudet, M. M.; Jemal, A.; Siegel, R. L. Ovarian Cancer Statistics, 2018. *CA. Cancer J. Clin.* **2018**, *68* (4), 284–296.

(42) *Ovarian Cancer Strategies, Survival Rate, and Prognosis OCRA*. https://ocrahope.org/patients/about-ovarian-cancer/staging/.

(43) Kamal, R.; Hamed, S.; Mansour, S.; Mounir, Y.; Abdel Sallam, S. Ovarian Cancer Screening-Ultrasound; Impact on Ovarian Cancer Mortality. *Br. J. Radiol.* **2018**, *91* (1090), 20170571.

(44) Charkhchi, P.; Cybulski, C.; Gronwald, J.; Wong, F. O.; Narod, S. A.; Akbari, M. R. CA125 and Ovarian Cancer: A Comprehensive Review. *Cancers (Basel).* **2020**, *12* (12).

(45) Menon, U.; Ryan, A.; Kalsi, J.; Gentry-Maharaj, A.; Dawnay, A.; Habib, M.; Apostolidou, S.; Singh, N.; Benjamin, E.; Burnell, M.; Davies, S.; Sharma, A.; Gunu, R.; Godfrey, K.; Lopes, A.; Oram, D.; Herod, J.; Williamson, K.; Seif, M. W.; Jenkins, H.; Mould, T.; Woolas, R.; Murdoch, J. B.; Dobbs, S.; Amso, N. N.; Leeson, S.; Cruickshank, D.; Scott, I.; Fallowfield, L.; Widschwendter, M.; Reynolds, K.; McGuire, A.; Campbell, S.; Parmar, M.; Skates, S. J.; Jacobs, I. Risk Algorithm Using Serial Biomarker Measurements Doubles the Number of Screen-Detected Cancers Compared With a Single-Threshold Rule in the United Kingdom Collaborative Trial of Ovarian Cancer Screening. *J. Clin. Oncol. Off. J. Am. Soc. Clin. Oncol.* **2015**, *33* (18), 2062–2071.

(46) Jacobs, I. J.; Menon, U.; Ryan, A.; Gentry-Maharaj, A.; Burnell, M.; Kalsi, J. K.; Amso, N. N.; Apostolidou, S.; Benjamin, E.; Cruickshank, D.; Crump, D. N.; Davies, S. K.;

Dawnay, A.; Dobbs, S.; Fletcher, G.; Ford, J.; Godfrey, K.; Gunu, R.; Habib, M.; Hallett, R.; Herod, J.; Jenkins, H.; Karpinskyj, C.; Leeson, S.; Lewis, S. J.; Liston, W. R.; Lopes, A.; Mould, T.; Murdoch, J.; Oram, D.; Rabideau, D. J.; Reynolds, K.; Scott, I.; Seif, M. W.; Sharma, A.; Singh, N.; Taylor, J.; Warburton, F.; Widschwendter, M.; Williamson, K.; Woolas, R.; Fallowfield, L.; McGuire, A. J.; Campbell, S.; Parmar, M.; Skates, S. J. Ovarian Cancer Screening and Mortality in the UK Collaborative Trial of Ovarian Cancer Screening (UKCTOCS): A Randomised Controlled Trial. *Lancet* **2016**, *387* (10022), 945–956.

(47) Dai, J.; Su, Y.; Zhong, S.; Cong, L.; Liu, B.; Yang, J.; Tao, Y.; He, Z.; Chen, C.; Jiang, Y. Exosomes: Key Players in Cancer and Potential Therapeutic Strategy. *Signal Transduct. Target. Ther.* **2020**, *5* (1), 145.

(48) Logozzi, M.; Mizzoni, D.; Di Raimo, R.; Fais, S. Exosomes: A Source for New and Old Biomarkers in Cancer. *Cancers (Basel).* **2020**, *12* (9).

(49) Huang, T.; Deng, C.-X. Current Progresses of Exosomes as Cancer Diagnostic and Prognostic Biomarkers. *Int. J. Biol. Sci.* **2019**, *15* (1), 1–11.

(50) Li, M.; Zeringer, E.; Barta, T.; Schageman, J.; Cheng, A.; Vlassov, A. V. Analysis of the RNA Content of the Exosomes Derived from Blood Serum and Urine and Its Potential as Biomarkers. *Philos Trans R Soc L. B Biol Sci.* **2014**, *369* (1652).

(51) Zhang, Y.; Liu, Y.; Liu, H.; Tang, W. H. Exosomes: Biogenesis, Biologic Function and Clinical Potential. *Cell Biosci.* **2019**, *9*, 19.

(52) Gurung, S.; Perocheau, D.; Touramanidou, L.; Baruteau, J. The Exosome Journey: From Biogenesis to Uptake and Intracellular Signalling. *Cell Commun. Signal.* **2021**, *19* (1), 47.

(53) Jiang, C.; Zhang, N.; Hu, X.; Wang, H. Tumor-Associated Exosomes Promote Lung Cancer Metastasis through Multiple Mechanisms. *Mol. Cancer* **2021**, *20* (1), 117.

(54) Croft, P. K.; Sharma, S.; Godbole, N.; Rice, G. E.; Salomon, C. Ovarian-Cancer-Associated Extracellular Vesicles: Microenvironmental Regulation and Potential Clinical Applications. *Cells* **2021**, *10* (9).

(55) Chen, Z.; Liang, Q.; Zeng, H.; Zhao, Q.; Guo, Z.; Zhong, R.; Xie, M.; Cai, X.; Su, J.; He, Z.; Zheng, L.; Zhao, K. Exosomal CA125 as A Promising Biomarker for Ovarian Cancer Diagnosis. *J. Cancer* **2020**, *11* (21), 6445–6453.

(56) Dietzek, B.; Cialla, D.; Schmitt, M.; Popp, J. Introduction to the Fundamentals of Raman Spectroscopy BT - Confocal Raman Microscopy; Toporski, J., Dieing, T., Hollricher, O., Eds.; Springer International Publishing: Cham, 2018; pp 47–68.

(57) Short, K. W.; Carpenter, S.; Freyer, J. P.; Mourant, J. R. Raman Spectroscopy Detects Biochemical Changes Due to Proliferation in Mammalian Cell Cultures. *Biophys. J.* **2005**, *88* (6), 4274–4288.

(58) Chen, Y.; Dai, J.; Zhou, X.; Liu, Y.; Zhang, W.; Peng, G. Raman Spectroscopy Analysis of the Biochemical Characteristics of Molecules Associated with the Malignant Transformation of Gastric Mucosa. *PLoS One* **2014**, *9* (4), e93906.

(59) Li, P.; Long, F.; Chen, W.; Chen, J.; Chu, P. K.; Wang, H. Fundamentals and Applications of Surface-Enhanced Raman Spectroscopy–Based Biosensors. *Curr. Opin. Biomed. Eng.* **2020**, *13*, 51–59.

(60) Guerrini, L.; Garcia-Rico, E.; O'Loghlen, A.; Giannini, V.; Alvarez-Puebla, R. A. Surface-Enhanced Raman Scattering (SERS) Spectroscopy for Sensing and Characterization of Exosomes in Cancer Diagnosis. *Cancers (Basel).* **2021**, *13* (9).

(61) Yamakoshi, H.; Dodo, K.; Palonpon, A.; Ando, J.; Fujita, K.; Kawata, S.; Sodeoka, M. Alkyne-Tag Raman Imaging for Visualization of Mobile Small Molecules in Live Cells. *J. Am. Chem. Soc.* **2012**, *134* (51), 20681–20689.

(62) Chen, Y.; Ren, J.-Q.; Zhang, X.-G.; Wu, D.-Y.; Shen, A.-G.; Hu, J.-M. Alkyne-Modulated Surface-Enhanced Raman Scattering-Palette for Optical Interference-Free and Multiplex Cellular Imaging. *Anal. Chem.* **2016**, *88* (12), 6115–6119.

(63) Hu, F.; Zeng, C.; Long, R.; Miao, Y.; Wei, L.; Xu, Q.; Min, W. Supermultiplexed Optical Imaging and Barcoding with Engineered Polyynes. *Nat. Methods* **2018**, *15* (3), 194–200.

(64) Glaser, C. Beiträge Zur Kenntniss Des Acetenylbenzols. *Berichte der Dtsch. Chem. Gesellschaft* **1869**, *2* (1), 422–424.

(65) Glaser, C. Untersuchungen Über Einige Derivate Der Zimmtsäure. *Justus Liebigs Ann. Chem.* **1870**, *154* (2), 137–171.

(66) Chodkiewicz, W. No Title. *Ann. Chim. Paris* **1957**, *2*, 819–869.

(67) Chodkiewics, W.; Cadiot, P. No Title. *C. R. Hebd. Seances Acad. Sci.* **1955**, *241*, 1055.

(68) Théry, C.; Witwer, K. W.; Aikawa, E.; Alcaraz, M. J.; Anderson, J. D.; Andriantsitohaina, R.; Antoniou, A.; Arab, T.; Archer, F.; Atkin-Smith, G. K.; Ayre, D. C.; Bach, J.-M.; Bachurski, D.; Baharvand, H.; Balaj, L.; Baldacchino, S.; Bauer, N. N.; Baxter, A. A.; Bebawy, M.; Beckham, C.; Bedina Zavec, A.; Benmoussa, A.; Berardi, A. C.; Bergese, P.; Bielska, E.; Blenkiron, C.; Bobis-Wozowicz, S.; Boilard, E.; Boireau, W.; Bongiovanni, A.; Borràs, F. E.; Bosch, S.; Boulanger, C. M.; Breakefield, X.; Breglio, A. M.; Brennan, M. Á.; Brigstock, D. R.; Brisson, A.; Broekman, M. L.; Bromberg, J. F.; Bryl-Górecka, P.; Buch, S.; Buck, A. H.; Burger, D.; Busatto, S.; Buschmann, D.; Bussolati, B.; Buzás, E. I.; Byrd, J. B.; Camussi, G.; Carter, D. R.; Caruso, S.; Chamley, L. W.; Chang, Y.-T.; Chen, C.; Chen, S.; Cheng, L.; Chin, A. R.; Clayton, A.; Clerici, S. P.; Cocks, A.; Cocucci, E.; Coffey, R. J.; Cordeiro-da-Silva, A.; Couch, Y.; Coumans, F. A.; Coyle, B.; Crescitelli, R.; Criado, M. F.; D'Souza-Schorey, C.; Das, S.; Datta Chaudhuri, A.; de Candia, P.; De Santana, E. F.; De Wever, O.; Del Portillo, H. A.; Demaret, T.; Deville, S.; Devitt, A.; Dhondt, B.; Di Vizio, D.; Dieterich, L. C.; Dolo, V.; Dominguez Rubio, A. P.; Dominici, M.; Dourado, M. R.; Driedonks, T. A.; Duarte, F. V; Duncan, H. M.; Eichenberger, R. M.; Ekström, K.; El Andaloussi, S.; Elie-Caille, C.; Erdbrügger, U.; Falcón-Pérez, J. M.; Fatima, F.; Fish, J. E.; Flores-Bellver, M.; Försönits, A.; Frelet-Barrand, A.; Fricke, F.; Fuhrmann, G.; Gabrielsson, S.; Gámez-Valero, A.; Gardiner, C.; Gärtner, K.; Gaudin, R.; Gho, Y. S.; Giebel, B.; Gilbert, C.; Gimona, M.; Giusti, I.; Goberdhan, D. C.; Görgens, A.; Gorski, S. M.; Greening, D. W.; Gross, J. C.; Gualerzi, A.; Gupta, G. N.; Gustafson, D.; Handberg, A.; Haraszti, R. A.; Harrison, P.; Hegyesi, H.; Hendrix, A.; Hill, A. F.; Hochberg, F. H.; Hoffmann, K. F.; Holder, B.; Holthofer, H.; Hosseinkhani, B.; Hu, G.; Huang, Y.; Huber, V.; Hunt, S.; Ibrahim, A. G.-E.; Ikezu, T.; Inal, J. M.; Isin, M.; Ivanova, A.; Jackson, H. K.; Jacobsen, S.; Jay, S. M.; Jayachandran, M.; Jenster, G.; Jiang, L.; Johnson, S. M.; Jones, J. C.; Jong, A.; Jovanovic-Talisman, T.; Jung, S.; Kalluri, R.; Kano, S.-I.; Kaur, S.; Kawamura, Y.; Keller, E. T.; Khamari, D.; Khomyakova, E.; Khvorova, A.; Kierulf, P.; Kim, K. P.; Kislinger, T.; Klingeborn, M.; Klinke, D. J. 2nd; Kornek, M.; Kosanović, M. M.; Kovács, Á. F.; Krämer-Albers, E.-M.; Krasemann, S.; Krause, M.; Kurochkin, I. V; Kusuma, G. D.; Kuypers, S.; Laitinen, S.; Langevin, S. M.; Languino, L. R.; Lannigan, J.; Lässer, C.; Laurent, L. C.; Lavieu, G.; Lázaro-Ibáñez, E.; Le Lay, S.; Lee, M.-S.; Lee, Y. X. F.; Lemos, D. S.; Lenassi, M.; Leszczynska, A.; Li, I.

T.; Liao, K.; Libregts, S. F.; Ligeti, E.; Lim, R.; Lim, S. K.; Linē, A.; Linnemannstöns, K.; Llorente, A.; Lombard, C. A.; Lorenowicz, M. J.; Lörincz, Á. M.; Lötvall, J.; Lovett, J.; Lowry, M. C.; Loyer, X.; Lu, Q.; Lukomska, B.; Lunavat, T. R.; Maas, S. L.; Malhi, H.; Marcilla, A.; Mariani, J.; Mariscal, J.; Martens-Uzunova, E. S.; Martin-Jaular, L.; Martinez, M. C.; Martins, V. R.; Mathieu, M.; Mathivanan, S.; Maugeri, M.; McGinnis, L. K.; McVey, M. J.; Meckes, D. G. J.; Meehan, K. L.; Mertens, I.; Minciacchi, V. R.; Möller, A.; Møller Jørgensen, M.; Morales-Kastresana, A.; Morhayim, J.; Mullier, F.; Muraca, M.; Musante, L.; Mussack, V.; Muth, D. C.; Myburgh, K. H.; Najrana, T.; Nawaz, M.; Nazarenko, I.; Nejsum, P.; Neri, C.; Neri, T.; Nieuwland, R.; Nimrichter, L.; Nolan, J. P.; Nolte-'t Hoen, E. N.; Noren Hooten, N.; O'Driscoll, L.; O'Grady, T.; O'Loghlen, A.; Ochiya, T.; Olivier, M.; Ortiz, A.; Ortiz, L. A.; Osteikoetxea, X.; Østergaard, O.; Ostrowski, M.; Park, J.; Pegtel, D. M.; Peinado, H.; Perut, F.; Pfaffl, M. W.; Phinney, D. G.; Pieters, B. C.; Pink, R. C.; Pisetsky, D. S.; Pogge von Strandmann, E.; Polakovicova, I.; Poon, I. K.; Powell, B. H.; Prada, I.; Pulliam, L.; Quesenberry, P.; Radeghieri, A.; Raffai, R. L.; Raimondo, S.; Rak, J.; Ramirez, M. I.; Raposo, G.; Rayyan, M. S.; Regev-Rudzki, N.; Ricklefs, F. L.; Robbins, P. D.; Roberts, D. D.; Rodrigues, S. C.; Rohde, E.; Rome, S.; Rouschop, K. M.; Rughetti, A.; Russell, A. E.; Saá, P.; Sahoo, S.; Salas-Huenuleo, E.; Sánchez, C.; Saugstad, J. A.; Saul, M. J.; Schiffelers, R. M.; Schneider, R.; Schøyen, T. H.; Scott, A.; Shahaj, E.; Sharma, S.; Shatnyeva, O.; Shekari, F.; Shelke, G. V.; Shetty, A. K.; Shiba, K.; Siljander, P. R.-M.; Silva, A. M.; Skowronek, A.; Snyder, O. L. 2nd; Soares, R. P.; Sódar, B. W.; Soekmadji, C.; Sotillo, J.; Stahl, P. D.; Stoorvogel, W.; Stott, S. L.; Strasser, E. F.; Swift, S.; Tahara, H.; Tewari, M.; Timms, K.; Tiwari, S.; Tixeira, R.; Tkach, M.; Toh, W. S.; Tomasini, R.; Torrecilhas, A. C.; Tosar, J. P.; Toxavidis, V.; Urbanelli, L.; Vader, P.; van Balkom, B. W.; van der Grein, S. G.; Van Deun, J.; van Herwijnen, M. J.; Van Keuren-Jensen, K.; van Niel, G.; van Royen, M. E.; van Wijnen, A. J.; Vasconcelos, M. H.; Vechetti, I. J. J.; Veit, T. D.; Vella, L. J.; Velot, É.; Verweij, F. J.; Vestad, B.; Viñas, J. L.; Visnovitz, T.; Vukman, K. V; Wahlgren, J.; Watson, D. C.; Wauben, M. H.; Weaver, A.; Webber, J. P.; Weber, V.; Wehman, A. M.; Weiss, D. J.; Welsh, J. A.; Wendt, S.; Wheelock, A. M.; Wiener, Z.; Witte, L.; Wolfram, J.; Xagorari, A.; Xander, P.; Xu, J.; Yan, X.; Yáñez-Mó, M.; Yin, H.; Yuana, Y.; Zappulli, V.; Zarubova, J.; Žėkas, V.; Zhang, J.-Y.; Zhao, Z.; Zheng, L.; Zheutlin, A. R.; Zickler, A. M.; Zimmermann, P.; Zivkovic, A. M.; Zocco, D.; Zuba-Surma, E. K. Minimal Information for Studies of Extracellular Vesicles 2018 (MISEV2018): A Position Statement of the International Society for Extracellular Vesicles and Update of the MISEV2014 Guidelines. *J. Extracell. vesicles* **2018**, *7* (1), 1535750.

Chapter 6

Investigation of Metal Modulation of Oxytocin Structure Receptor-Mediated Signaling*

---

*The following chapter is adapted from a manuscript that has been submitted for publication entitled Investigation of Metal Modulation of Oxytocin Structure-Receptor Mediated Signaling. Justin O'Sullivan collected circular dichroism data on native oxidized oxytocin and performed cell studies. Kylie S. Uyeda and Michael J. Stevenson collected the electronic absorption spectra shown and the circular dichroism spectra of the oxytocin analogs. They also aided in the design of the study and analysis of data as well as provided feedback on the written manuscript. Though not directly related to molecular imaging this chapter explores the roles of metal ion peptide hormone interactions in the extracellular space.

6.1 Abstract

Oxytocin is a 9-amino acid peptide hormone. Since its discovery in 1954 it has most commonly been studied in relation to its role in stimulating parturition and lactation. However, it is now known that oxytocin has a widely diverse set of functions throughout the body including neuromodulation, bone growth, and inflammation. Previous research has suggested that divalent metal ions may be required for oxytocin activity, but the exact metal species and specific pathways have yet to be fully elucidated. In this work, we focus on characterizing copper and zinc bound forms of oxytocin and related analogs through far-UV circular dichroism. We report that Cu(II) and Zn(II) bind uniquely to oxytocin and all analogs investigated. Furthermore, we investigated how these metal bound forms may affect downstream signaling of MAPK activation upon receptor binding. We find that both Cu(II) and Zn(II) bound oxytocin attenuates the activation of the MAPK pathway upon receptor binding relative to oxytocin alone. Interestingly, we observed that Zn(II) bound forms of linear oxytocin facilitate increased MAPK signaling. This study lays the foundation for future work on elucidating the metal effects on oxytocin's diverse bioactivity.

6.2 Introduction

Oxytocin (OT) is a peptide hormone that is most widely known for its clinical applications in stimulating childbirth as well as its role in stimulating parturition and lactation. OT and its synthetic analogs have been extensively used in clinical applications since the 1960s; however, the dosing and side effects are often unpredictable in large part due to an incomplete understanding of its regulation and mechanism of action. Several decades ago, in an effort to understand the drivers of OT action, divalent metal ions were found to influence the hormonal activities of OT.[1] However, it remains unclear how metals influence OT function at the molecular level and the downstream bioactivity.

Early studies suggested that divalent metals could enhance the binding of OT to the OT receptor (OTR) on mammary gland tissues.[2] Researchers initially postulated that the enhanced receptor binding was due to metal ions interacting with the OTR to increase the affinity and concentration of OT binding sites, though the molecular nature of these sites were not elucidated.[1] However, several studies in the 1990s began investigating divalent metal interactions directly with the OT peptide itself, primarily employing mass spectrometry, computational calculations, or a combination thereof. These studies demonstrated that both Cu(II) and Zn(II) can coordinate to OT and change its conformation, albeit with different binding modes.[3–6]

Zn(II) is posited to interact with OT through interaction of backbone carbonyls under acidic, but not basic, conditions.[3,4] Bowers and coworkers used Cross Section and Hydration Energy Mass Spectrometry (MS) alongside Chemistry at Harvard Macromolecular Mechanics (CHARMM) force field and Density Functional Theory (DFT) calculations to predict that Zn(II) binds to OT via six of the backbone carbonyl oxygens to form a near-perfect octahedral complex that stabilizes a near-planar surface ideal for OTR binding and pinpointed these six backbone carbonyls to those of the Tyr2, Ile3, Gln4, Cys6, and Lys8 and Gly9.[3]

Cu(II) has been shown to stably coordinate OT in the gas phase under both acidic and basic conditions, with evidence pointing to a highly stable, planar 4N coordination mode.[3,4] This was initially demonstrated with both spectroscopic and potentiometric studies by Danyi et al.[7] and Bal et al.[8] While collective data on Zn(II)-binding is generally in good agreement with respect to which residues are involved, reports on Cu(II)-binding show some disparity as to the exact location of binding. While the early spectroscopic studies revealed that Cys1, Tyr2, Ile3, and Gln4 are involved in copper coordination[8], later studies by collision-induced dissociation (CID) mass spectrometry pointed to complexation involving Cys1, Cys6, Leu8, and Gly9[3]. These discrepancies may be in part due to the strong pH-dependence of Cu(II) complexation.[4,9,10] CID and electron-capture dissociation (ECD) MS measurements alongside calculations have shown that at pH 10, Cu(II) coordinates the backbone nitrogens of Cys1, Cys6, Leu8, and Gly9.[11] Lowering the pH to pH 5 allows Cu(II) to coordinate the backbone nitrogens of the Cys1, Tyr2, Ile3, Gln4 segment.[8] As the pH is lowered further to pH 3, Cu(II) coordination shifts to 4O involving the Tyr2, Ile3, Cys6, and Gly9.[12] Calculations have predicted that at pH 7, Cu(II) coordinates to the backbone nitrogens of Ile3, Gln4, Asn4, Cys6.[3] Very recently, further NMR analysis with paramagnetic relaxation enhancement (PRE) indicated that a free amine of Cys1 is required, with Cu(II) binding at that -NH2 first, followed by Tyr2, Ile3, and Gln4.[13] The low-energy ensemble from this analysis showed structural rigidity at the Tyr2 side chain ring, indicating the possible presence of pi-cation interaction. Taken together, this would suggest that the binding mode of copper is heavily influenced by solvent environments and pH.

Despite the repeated observations that Cu(II) and Zn(II) can bind OT and that their binding modes are distinct, it remains unclear how these molecular interactions alter peptide conformation with respect to receptor interactions and downstream hormone regulatory pathways. Majority of the studies that have investigated the consequences of OT/metal on bioactivity assess physiological effects at the whole tissue rather than the molecular or biochemical level. Moreover, such studies focus on the metal effects on OT-induced uterine contractions. Recent years have revealed new and divergent functions of OT in different tissues including neuromodulation, metabolic regulation, and inflammation, opening up new questions as to the what effectors, allosteric modulators, and regulators might be involved directing or tuning OT signaling pathways.[14–17] In particular, many of these functions are associated with activation of the ERK1/2 MAPK pathway.[18–22]

To this end, we hypothesize that Zn(II) and Cu(II) play differential roles in modulating and directing OT towards the various signaling pathways that it can activate, and that a closer investigation of the molecular components that govern OT/metal interactions is warranted. In this work, we assess the impact of Zn(II) and Cu(II) on peptide secondary structure under biologically relevant conditions not only with native oxytocin, but in both cyclic and linear analogs where potential binding regions are perturbed (Figure 6.1).

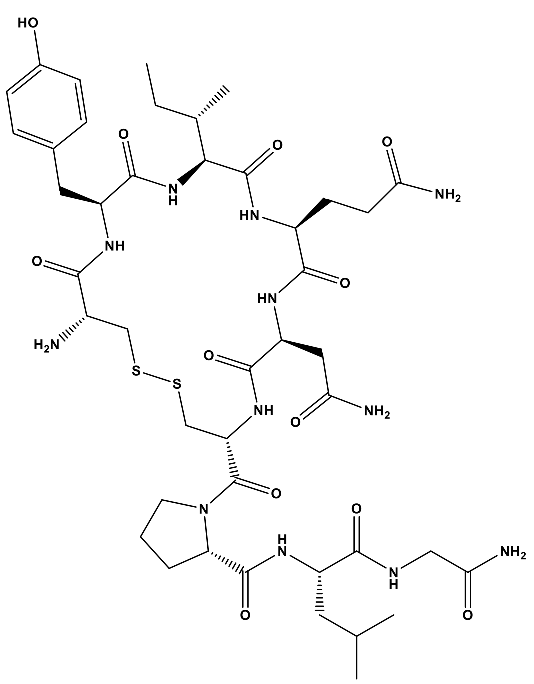

OT

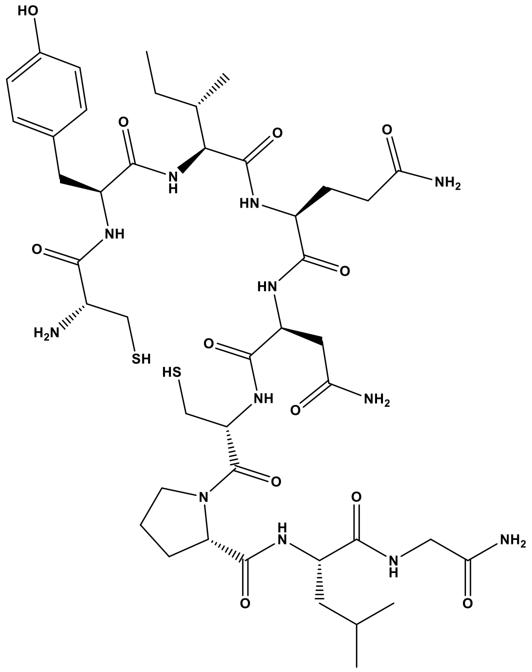

rOT

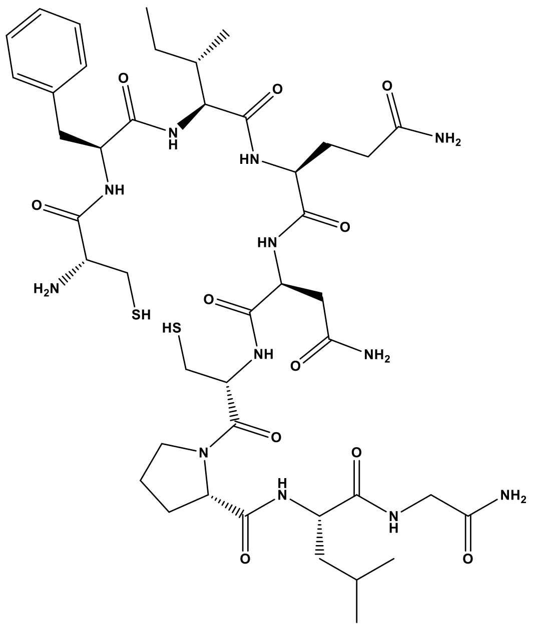

rOTF

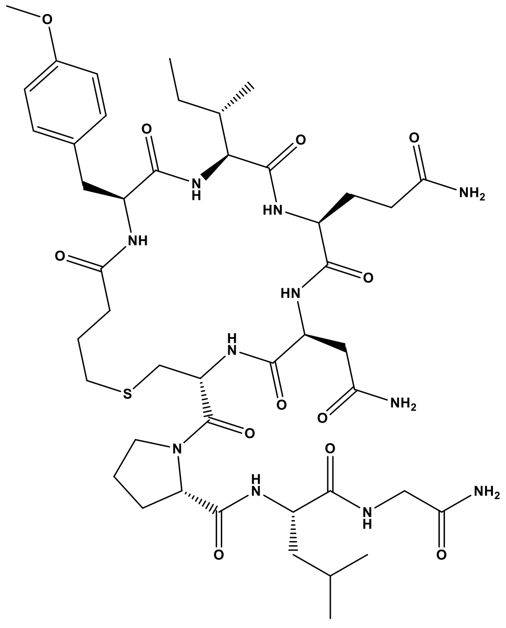

Carbetocin

Figure 6.1 Chemical structures of oxidized oxytocin (oxOT), reduced oxytocin (rOT), Y2F-oxytocin (rOTF), and carbetocin.

While the most-studied form of OT is its cyclized 9-amino acid form wherein the Cys1 and Cys6 are oxidized to form a disulfide bond (termed here oxOT for oxidized OT), emerging studies suggest that modified analogs, including its linear reduced form, may exert differing functions from the canonical oxOT form.[23] In addition to studying both oxOT and reduced OT (rOT), we investigated carbetocin, a synthetic analogue used clinically, where the disulfide linkage is replaced with a thioether and methoxy-tyrosine at Tyr2 position. Additionally, carbetocin is deaminated at the C-terminus whereas oxytocin has is c-terminus amidated. Furthermore, we synthesized and studied the mutant OT Y2F with reduced cysteines (rOTF) where the tyrosine is replaced with a phenyalanine to determine if the tyrosine hydroxyl is required for binding.

Our spectroscopic studies find that both Cu(II) and Zn(II) can bind to all analogs, but the binding modes and conformational consequences differ between the two metals ions and the analogs. We find the native Tyr2 residue is involved in conformational dynamics associated with Cu(II) binding, as evidenced by large perturbations in the spectroscopic signatures corresponding to the aromatic side chain. In contrast, Zn(II) does not appear to bind near the Tyr2. In contrast, Zn(II) induces more notable changes in the spectroscopic region of the peptide that corresponds to the backbone and tail, particularly with rOT. Furthermore, we demonstrate that binding of Cu(II) or Zn(II) to oxOT is competitive. We extend these studies to investigate how the two metals influence ERK1/2 MAPK activation. Our data shows that both Zn(II)- and Cu(II)-bound OT decrease MAPK activation relative to OT alone, suggesting that these metal bound forms have differing interactions with the oxytocin receptor in association with the MAPK signaling pathway. In contrast, Zn(II) enhances MAPK activation by linear OT, suggesting that the metal ion may stabilize the receptor recognition site on an otherwise less-ordered linear form.

6.3 Results and Discussion

6.3.1 Selection of OT Analogs

We aimed to first assess and compare how Cu(II) and Zn(II) binding to oxOT affects the peptide's structure under buffered aqueous conditions at physiologically relevant pH. We applied circular dichroism (CD) spectroscopy, a common technique for evaluating protein and peptide structure via optical activity. Most reports on oxytocin structure have evaluated the CD spectra of the peptide and related peptides in the near-UV region (250 nm – 400 nm), or, in the case of Cu(II)-binding, in the d-d transition region (400 nm – 800 nm). The focus on the near-UV region may be attributed to the presence of the chromophoric amino acid, tyrosine (at Tyr2), and a disulfide bond, which both have intense optical activities in this spectral region. However, this region may also exhibit sensitives to charge-transfer transitions with Cu(II) that may not occur with the d^{10} configuration of Zn(II). To allow for direct comparisons between the two metal ions, we instead investigated the impact of Cu(II) and Zn(II) on the far-UV region of the CD. To facilitate spectral interpretation, the CD spectra of additional analogs were acquired. Three were selected wherein either putative metal ion binding site or the optically-active features are altered: reduced OT (rOT), which lacks the disulfide bond and instead has two free thiols at Cys1 and Cys6; reduced OTF (rOTF), which similarly lacks the disulfide bond but also has a phenylalanine substituted for Tyr2; and carbetocin, which has a methylated Tyr2 and a thioether bond instead of a disulfide bond bridging positions 1 and 6 (Figure 1). Carbetocin is of added interest as it is a clinically used analogue that is reportedly more shelf-stable and resistant to degradation once administered than OT. Despite the increased chemical robustness of carbetocin, research shows that the effect on potency can vary by application. For instance, while potency is increased with respect to prevention of post-partum hemorrhage, decreased potency in single-dose induction of uterine contractions is observed.[24,25] This may suggest tissue-specific or co-factor differences in the action of oxOT as compared to carbetocin. Indeed, molecular pharmacology studies have shown that OT including carbetocin can elicit functionally different effects despite interactions with the same receptor.[26,27]

6.3.2 Far-UV Circular Dichroism of Oxytocin and Analogs

As previously reported in literature, the spectrum of oxOT in the absence of metals (apo-oxOT) shows a positive band centered at 225 nm and a positive shoulder (Figure 6.2), which has previously been attributed primarily to a Tyr2 transition, but with possible contributions from the amide backbone and disulfide bond.[28]

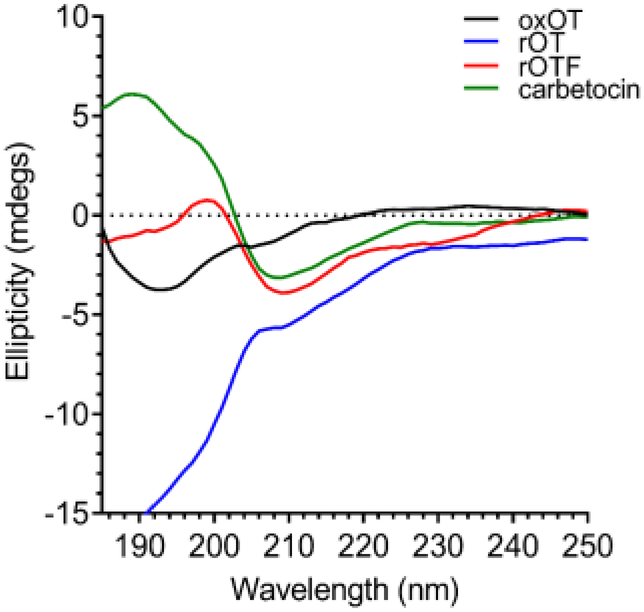

Figure 6.2 Circular dichroism spectra of 40 µM oxOT, rOT, rOTF, and carbetocin (15 mM phosphate, pH 7.4).

The spectrum also exhibits a minimum centered at 196 nm, which may represent the disordered region of three C-terminal amino acid tail that is excluded from the tocin ring. In comparing the CD spectra of the apo forms of oxOT and redOT the peak profiles look similar at wavelengths higher than 200 nm, but redOT adapts a more negative ellipticity at >200 nm, which influences the relative values of the remainder of the spectrum. Negative ellipticity values below 200 nm are frequently suggestive of random coil formations as might be expected with redOT when the cyclic structure is no longer stabilized by the disulfide linkage. The 225 nm band is both reduced and red-shifted in the CD spectra of rOTF as would be expected for a Phe substitution, further corroborating the strong contribution of Tyr2 transitions to this peak. Interestingly, rOTF exhibits a less negative ellipticity below 200 nm, possibly indicating that this analogue exhibits less disorder than rOT. Surprisingly, carbetocin shows marked differences <200 nm despite having the same tail region as oxOT as well the structural constraints of cyclization. Given that the thioether bond of carbetocin that replaces the disulfide bond of oxOT is proximal to the tail region, it is possible that conformational changes to the tocin ring that stems from the -CH2 replacement may reorient the tail region to restrict structural disorder. The carbetocin CD spectrum shows additional differences in the 225 nm band, suggesting that tyrosine methylation red-shifts and reduces the molar ellipticity of this transition.

6.3.3 Effects of Cu(II) and Zn(II) Binding to oxOT Structure

Using the far-UV CD spectroscopy, we probed how Cu(II) and Zn(II) affects the secondary structural features of oxOT. Both Cu(II) and Zn(II) increase the molar ellipticity of the band at 196 nm (Figure 6.3).

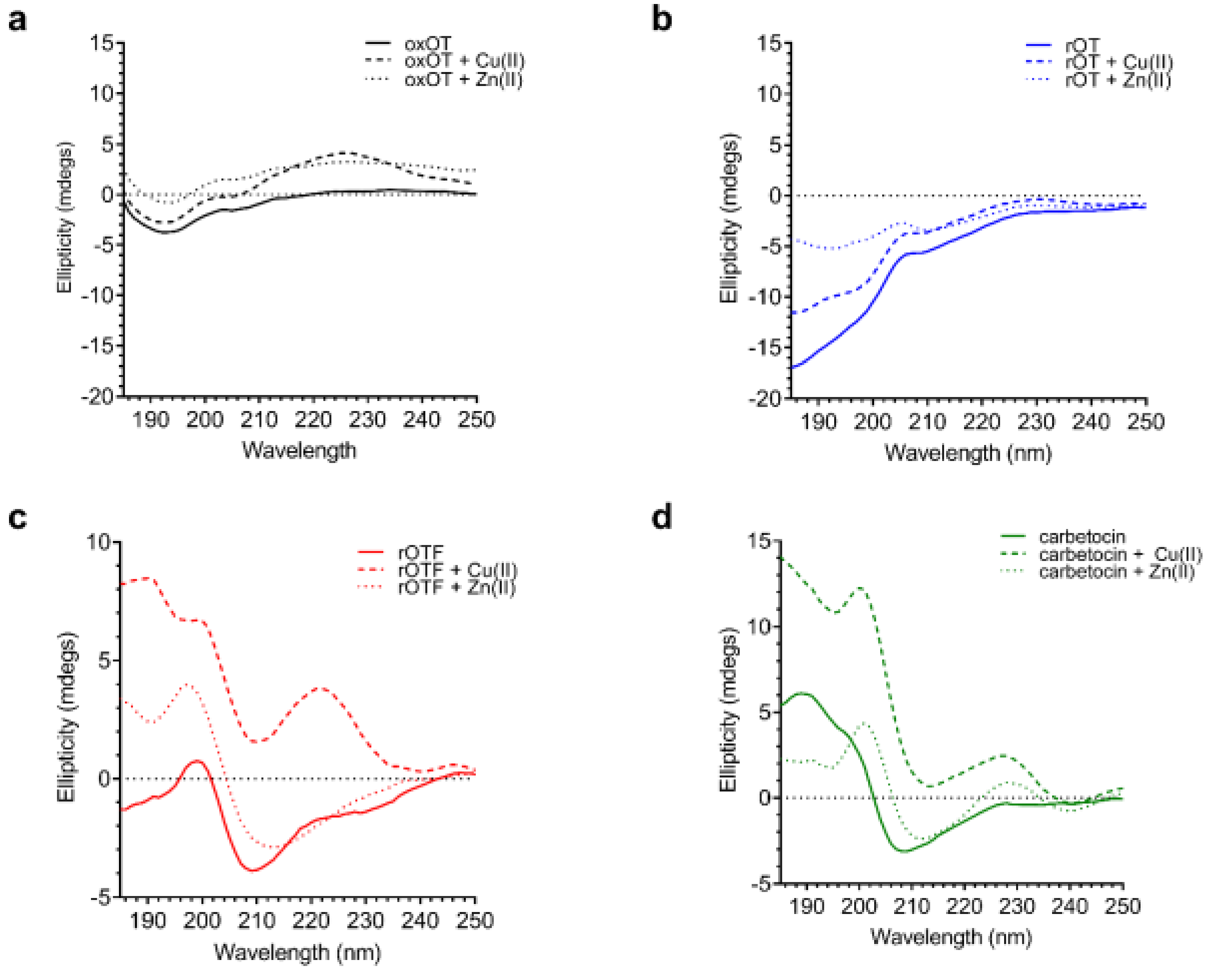

Figure 6.3 Circular dichroism spectra of 40 µM oxOT, rOT, rOTF, and carbetocin in the absence or presence of one equivalent of either Cu(II) or Zn(II) (15 mM phosphate, pH 7.4).

Cu(II) increases the molar ellipticity value relative to apo-oxOT from -3 to -1 millidegrees, in contrast to Zn(II) which increases it from -3 to 0 millidegrees, suggesting that metal ion binding may alter the conformation of the tail region. Stoichiometric addition of Cu(II) also increases the intensity of the band centered at 225 nm. Zn(II) has a similar but less pronounced effect on this 225-nm band (Figure 6.3) suggesting that Zn(II) does not induce the same structural effects as Cu(II) which are likely on the Tyr2 transition. Previous works done at pH 10.3 in the gas phase suggest that Zn(II) binding orients Ile3, Gln4, and Asn5 differently than apo and Cu(II)-oxOT, but changes to these residues may not be observable by CD. Titration of sub- (0.5 equivalents) to super- (4.0 equivalents) of Cu(II) into OT show the increase at 225 nm up to 1.0 equivalents of Cu(II) (Figure 6.4a), suggesting a 1:1 Cu(II) to OT ratio in the complex. Titration of Zn(II) into oxOT also suggests a 1:1 binding ratio (Figure 6.4b).

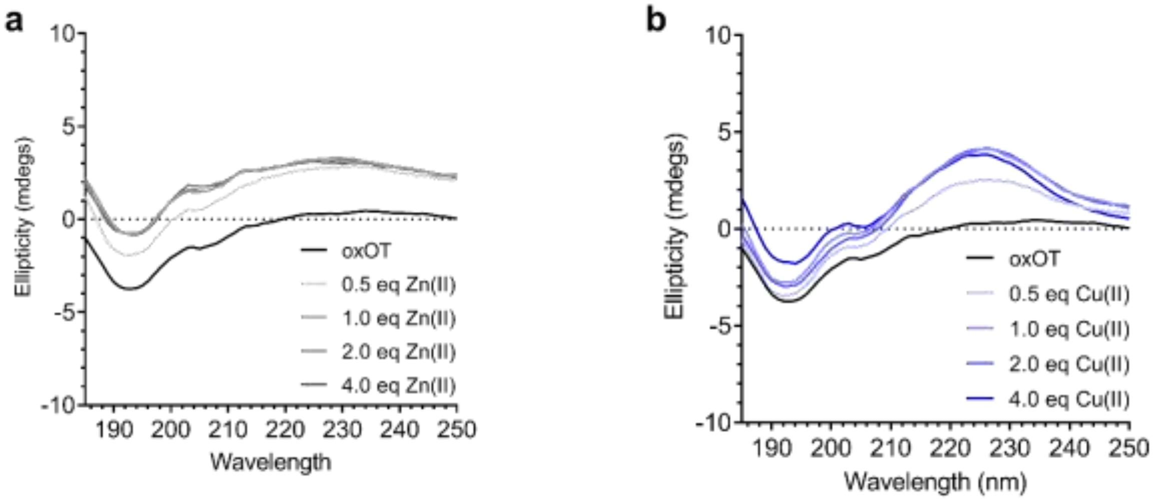

Figure 6.4 Titration of A) Zn(II) and B) Cu(II) into 40 µM oxytocin. Spectra averaged over eight scans and collected with 1 mm path length.

We further applied CD spectroscopy to assess binding competition between the two metal ions. Understanding binding competition would provide insight into how these metals could influence, and possibly regulate, oxOT function *in vivo*. When added to oxOT pre-incubated with one equivalent of Zn(II) (Zn(II)-oxOT), Cu(II) addition increases the band at 225 nm (Figure 6.5a), but additional Cu(II) equivalents (2.0 equivalents) are required to reach the maximum change relative to apo-oxOT. At 2.0 equivalents of Cu(II) to Zn(II)-oxOT, the spectrum resembles that of oxOT pre-incubated with stoichiometric amounts of Cu(II). In contrast, while addition of Zn(II) to Cu(II)-oxOT at one equivalent of Cu(II) leads to a increase in the band at

196 nm (Figure 6.5b), even 4.0 equivalents of Zn(II) does not restore the spectrum to that of Zn(II)-oxOT.

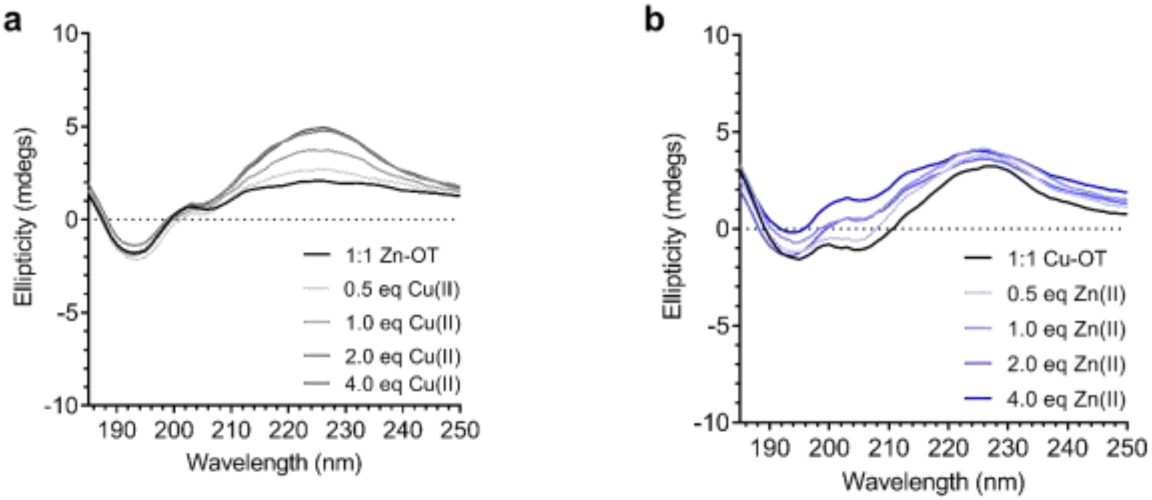

Figure 6.4 Circular dichroism spectra of the competition between Cu(II) and Zn(II) for oxytocin binding. A) Cu(II) titration into the preformed Zn(II)-oxOT complex (1:1 Zn(II) to oxOT), and B) Zn(II) titration into the preformed Cu(II)-oxOT complex (1:1 Cu(II) to oxOT). Spectra averaged over eight scans and collected with 40 µM oxOT and 1 mm path length. The increase in the band at 229 nm from Cu(II) titrated into Zn(II)-oxOT and the increase in the band at 205 nm from Zn(II) titrated into Cu(II)-oxOT indicates binding competition between the two metal ions for oxOT.

These data show that both metal ions bind to oxOT at neutral pH and either compete with each other for the same ligand set or preclude the other metal ion from binding. Moreover, Cu(II) binding seems to drastically impact the ability of Zn(II) to complex to the peptide, suggesting a shared region of binding with preferential affinity for Cu(II).

Given the ability of Cu(II) to change the 225 nm band in the CD spectrum of oxOT alongside the recent paramagnetic relaxation enhancement nuclear magnetic resonance (PRE NMR) studies pointing to pi-cation interactions, we applied electronic absorption spectra to assess the impact of the metal ion on the Tyr phenolic absorption spectrum. Apo-oxOT exhibits characteristic bands at 220-230 nm from the peptide backbone and 280 nm due to absorption by the Tyr2 ring (Figure 6.5). Ionization of tyrosine hydroxyl groups has been shown to red-shift the spectrum of the amino acid to 295 nm.[29,30] Stoichiometric addition of Cu(II), however, induces a blue-shift from 275 nm to 270 nm alongside a notable increase in intensity. This spectral change is accompanied by a rise in a band centered at 515 nm, which is consistent with a d-d transition at the Cu(II) center (Figure 6.5).

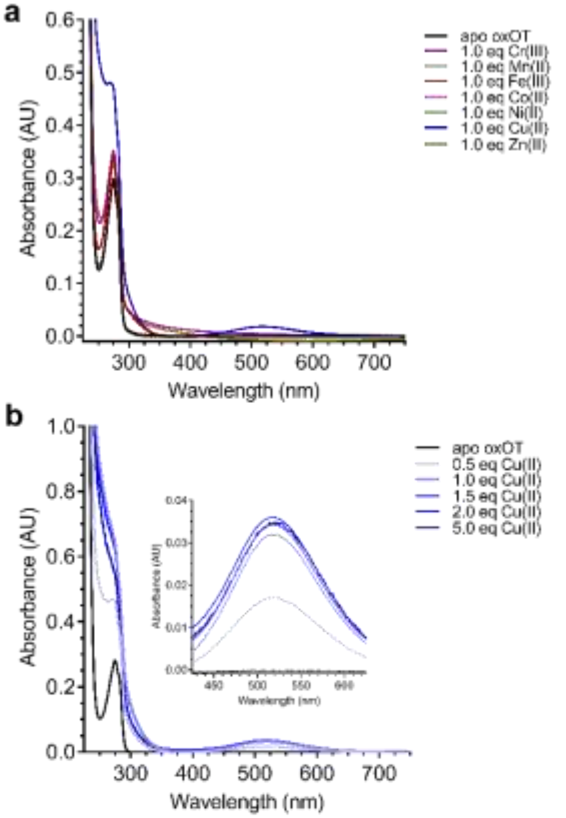

Figure 6.5 Electronic absorption spectra of A) 200 µM oxOT (15 mM phosphate, pH 7.4) in the absence (apo) and presence of 200 µM $CrCl_3$, $MnCl_2$, $FeCl_3$, $CoCl_2$, $NiCl_2$, $CuCl_2$, $ZnCl_2$ and B) $CuCl_2$ titrated into 200 µM oxOT (15 mM MOPS, pH 7.4) from sub- (0.5 eq) to super-stoichiometric (5.0 eq) ratios. $CrCl_3$, $MnCl_2$, $FeCl_3$, $CoCl_2$, and $NiCl_2$ have negligible changes to the spectrum of oxytocin, whereas $CuCl_2$ alters the spectrum of oxytocin by blue-shifting the tyrosine band from 275 to 270 nm and forming a d-d band centered at 515 nm. Arrow denotes increase in d-d band.

This energy and extinction coefficient correlate well with backbone amide coordination, which is consistent with previously published findings.[12] Addition of one stoichiometric equivalent of Zn(II) or other d-block transition metals (Cr(III), Mn(II), Fe(III), Co(II), and Ni(II)) does not yield changes to the UV-Vis spectra of apo-oxOT indicating a lack of detectable metal binding interaction with oxOT that would perturb either the Tyr2 residue or the peptide backbone absorbances. We further probed the binding by titration of sub- (0.5 equivalents) to super- (5.0 equivalents) stoichiometric Cu(II) into oxOT (Figure 6.5b). The resulting spectra show both the increase and blue-shift of the tyrosine band and the increase of the d-d transition up to 1 equivalent Cu(II), corroborating the presence of a 1:1 Cu(II):OT complex that was observed in the CD spectra (Figure 6.5b). It should be noted that at higher copper stoichiometries (4 equivalents) the baseline in the absorption spectrum appears to be floated indicating possible aggregation under high copper concentration. We also measured the emission spectra of oxOT attributed to the tyrosine residue through excitation at 275 nm (Figure 6.6). We measured oxOT's emission spectra in the presence and absence of Cu(II) and observed fluorescence quenching but no shift in the spectrum upon addition of Cu(II). This would further indicate that Cu(II) binding is not directly interacting with the tyrosine ring system.

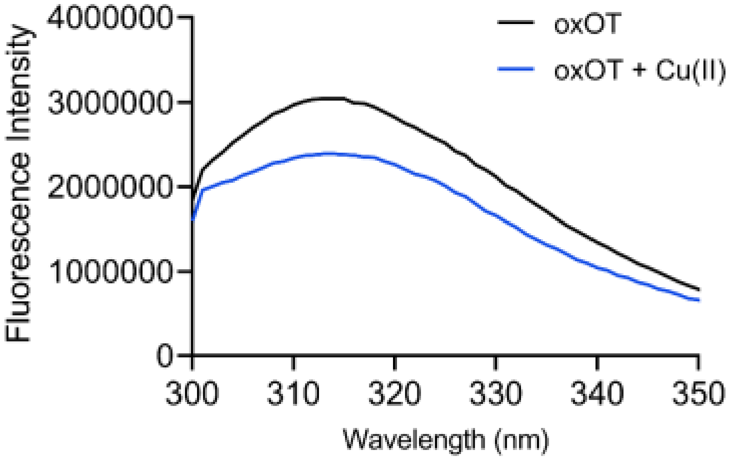

Figure 6.6 Emission spectra of oxOT and Cu(II) added to 30 µM oxOT. Excitation wavelength of 275 nm was used. Cu(II) quenches fluorescence but does not alter the wavelength of maximum emission suggesting that Cu(II) does not directly interact with the tyrosine ring system.

We investigated whether the modifications present in the analogs would affect their metal-binding capacity relative to oxOT. Surprisingly, the CD spectra are shifted with the addition of Cu(II) or Zn(II) for all the analogs, suggesting that these can still interact with the metal ions. This supports the notion that the peptide backbone plays a significant role in binding to both metal ions. For the reduced analogs (rOT and rOTF) an Elman’s test showed that addition of Cu(II) results in oxidation of the free thiols and formation of a disulfide bridge as could be expected given the redox potentials (Tables 6.1 & 6.2).

Table 6.1 Standard curve for absorbance measurements of cysteine concentration range after incubation with Ellman's reagent. Linear fit was then applied and the resulting equation was used to determine the free thiol content of rOT and rOTF before and after addition of Cu(II).

[Cysteine] mM	**Absorbance$_{412}$**
0.0	0.0434
0.1	0.0765
0.2	0.1088
0.4	0.1738
0.8	0.2977
1.6	0.5703

Table 6.2 Experimentally determined concentrations of free thiol content of rOT and rOTF before and after addition of Cu(II) using an Ellman's test. Theoretical concentration of free thiol content prior to addition of Cu(II) was 1 mM. Addition of Cu(II) significantly decreases the free thiol content of rOT and rOTF suggesting oxidation to disulfides.

	Absorbance$_{412}$	**Calculated [Free Thiols] mM**
rOT	0.3465	0.9274
1:1 Cu-rOT	0.0758	0.1021
rOTF	0.3341	0.8895
1:1 Cu-rOTF	0.0992	0.1735

Mass spectrometry analysis was consistent with intra-disulfide bonding as opposed to dimerized inter-disulfide bonding or other oxidation products (Figure 6.7). However, the CD spectra of rOT after Cu(II) addition does not look like that of oxOT alone suggesting that there is likely a subsequent Cu(I) oxOT interaction following disulfide formation.

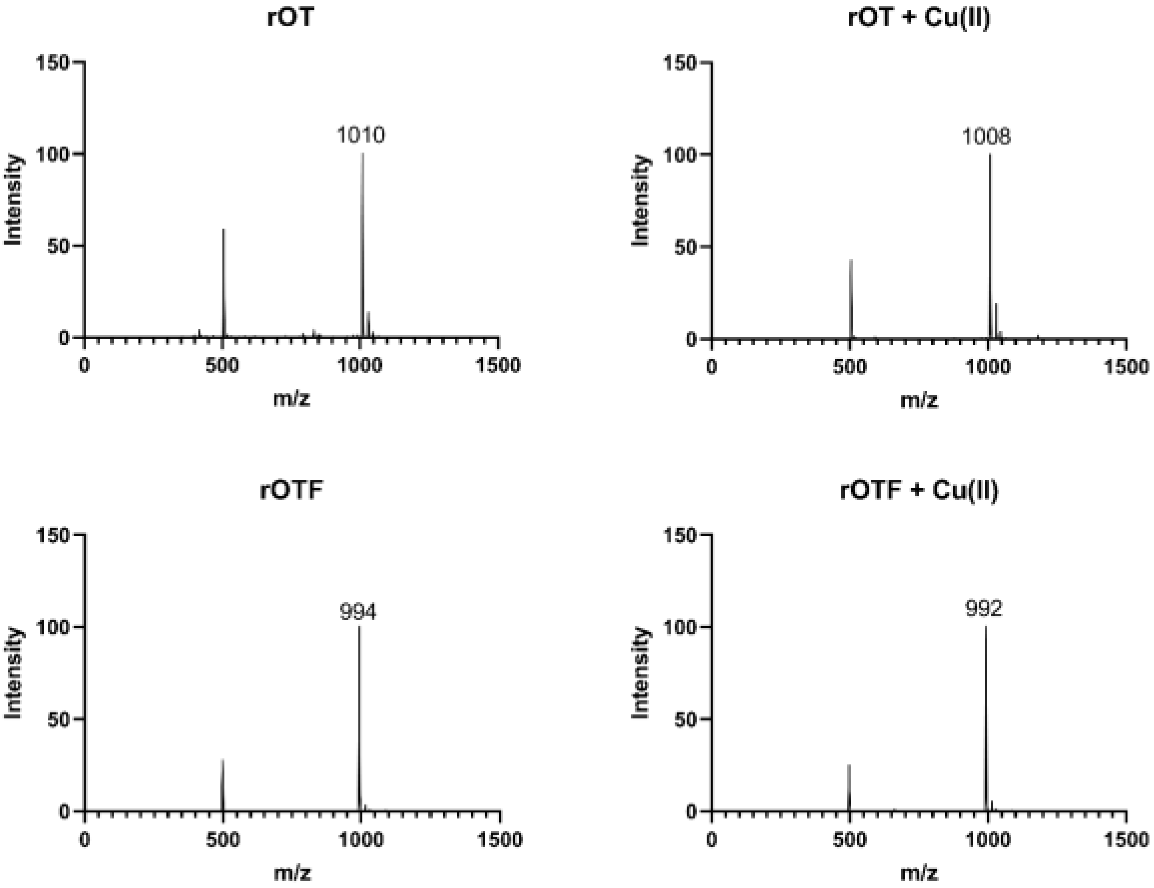

Figure 6.7 Mass spectra of 50 µM rOT and rOTF before and after addition of Cu(II) (1 equivalent) reveal a loss of two protons upon Cu(II) addition consistent with formation of disulfide bridge.

6.3.4 Metal Effects on Oxytocin/Receptor-Mediated MAPK Signaling

Ligand binding to the oxytocin receptor can elicit a variety of signaling pathways in tissue-specific ways including increased cytosolic calcium, cAMP activation, and activation of MAP kinases. The mechanistic or structural underpinnings of this pathway divergence remain unclear but may point to distinct active conformations of the ligand-receptor complex.[31] Whether metal ions are involved in activating the oxOT/OTR axis remains unexplored. The CD data strongly support that both Cu(II) and Zn(II) interactions with oxOT and its induce structural changes in distinct manners. We thus investigated the potential consequences of the metal-induced structural changes on their receptor-mediated bioactivity. We focused on the ability of oxOT/OTR binding to activate MAPK to begin querying the influence of metals on receptor interactions. HEK293T cells were transiently transfected to express a GFP-tagged human OTR. Cells were stimulated for five minutes with the apo peptides or peptides preincubated with Cu(II) or Zn(II). Lysates were collected and western blots were used to analyze total and phosphorylated MAPK expression. Densitometry was performed to quantify the ratio of phosphorylated MAPK to total MAPK where increased phosphorylation indicates activation of the MAPK pathway (Figure 6.8). Representative blots can be seen in Figure 6.9.

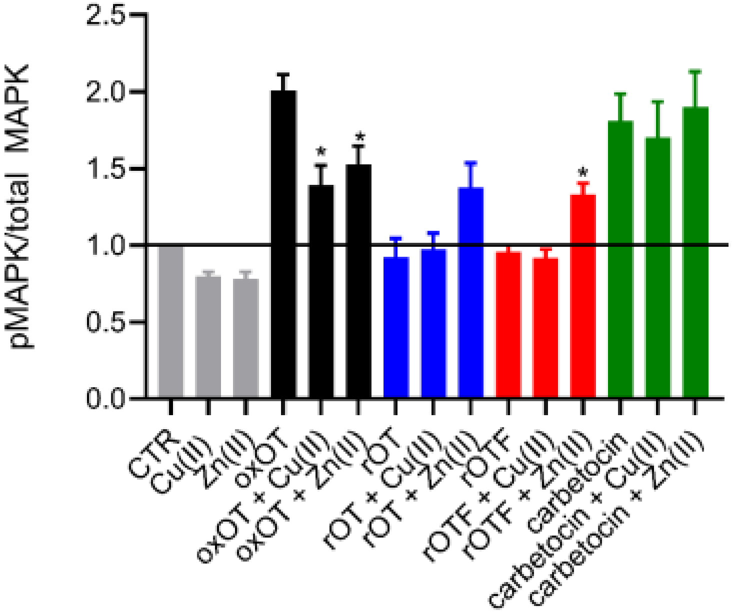

Figure 6.8 Densitometry of western blots for total and phosphorylated MAPK reveal metal-dependent modulation of MAPK activation by oxytocin (n = 3 to 4). Statistical significance of peptide alone compared to metal bound peptide was assessed by calculating *p*-values using unpaired t-test, * $p < 0.05$

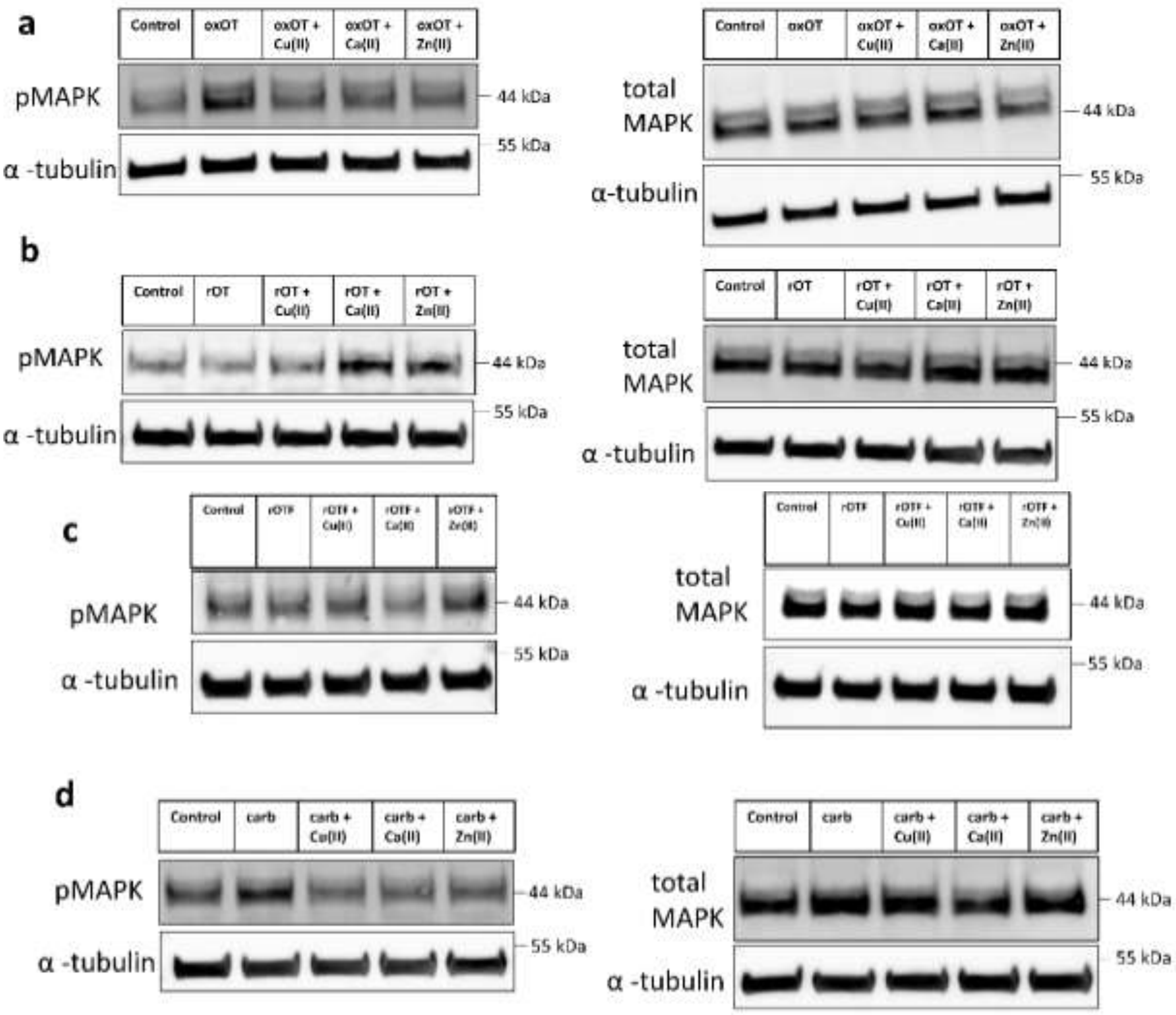

Figure 6.9 Representative MAPK blots for oxOT (a), rOT (b), rOTF (c), and carbetocin (d).

As expected, we observe strong activation of the MAPK pathway by oxOT alone relative to the no-peptide control. Interestingly, Cu(II) and Zn(II) addition to oxOT both attenuate this activation, suggesting that the metal-bound forms of oxOT either do not interact with the OT receptor as strongly or that the receptor-ligand conformation does not mediate MAPK signaling. Consistent with the traditional dogma that oxidized OT is the bioactive form, we observe that neither rOT nor rOTF activate MAPK signaling. However, both reduced OT and reduced OTF show an increase in activation when bound by Zn(II) but no change relative to peptide alone when bound by Cu(II). Alongside the CD data (Figure 3), the Zn(II)-dependent gain-of-function of the linear peptides may suggest that Zn(II) may reduce the disorder of the linear peptide towards a more rigid structure like the cyclic peptides, facilitating receptor binding. Further future studies should be performed in order to substantiate this hypothesis. While carbetocin promotes MAPK activation, it does so to a lesser degree than oxOT, and Zn(II) showed no effect on its activity. While a modest decrease in activation was observed with the addition of Cu(II) relative to apo-carbetocin, the difference was not statistically significant. Thus, while metal-binding is indeed observed for carbetocin, the lack of effects on MAPK activation may suggest that any induced conformational change by Cu(II) or Zn(II) does not significantly alter the synthetic analogue's interaction with the receptor.

6.4 Conclusion & Outlooks

This work offers molecular insight into how metal ions bind to a peptide hormone and alters its structure as well as bioactivity. We first used electronic absorption spectroscopy to show a direct interaction between Cu(II) and OT in a 1:1 binding stoichiometry. Circular dichroism then showed that Cu(II) induces structural changes by means of reorienting the disulfide bond and the phenol ring of Tyr2 and Zn(II) induces structural changes in the carboxy terminal tail. In conjunction with fluorescence spectrometry and of OT we show that the hydroxyl group of Tyr2 most likely coordinates to Cu(II) and alters the structure of the 20-membered ring formed by the disulfide bond. Furthermore, the competition studies show that Cu(II) is able to out-compete Zn(II) for OT. We then showed a metal-modulated effect on downstream signaling upon oxytocin receptor binding of oxytocin and where both Cu(II) and Zn(II) bound OT attenuate

MAPK signaling relative to OT alone. Additionally, we note that Zn(II) bound rOT shows an increase in signaling from rOT alone and carbetocin with and without metal bound shows no significant changes in MAPK activation and lower MAPK signaling overall relative to oxytocin. Taken together, this lays a foundation for future research at the receptor level of oxytocin and metal mediated bioactivity.

Metal-induced structural changes to a peptide hormone may have a number of effects on storage, secretion, stability, and/or signaling. In this case, it is possible that both Zn(II) and Cu(II) lend different structural integrities to OT at different points in OT lifetime. Physiologically, it is possible that Cu(II) is bound to OT in serum but, because the concentrations of metal ions surrounding specific tissues are believed to fluctuate, Zn(II) may be able to displace Cu(II) under specific concentrations. It still remains to be seen how Cu(II) would affect OT in serum, however, metal binding may be a key player in prevention of degradation; further studies in our lab are underway to test this hypothesis. The binding of metal ions to peptide hormones, particularly OT, may provide an additional source for regulation, and this study provides the foundation for future studies.

6.5 Materials & Methods

6.5.1 Chemicals and Reagents

All chemicals and reagents were purchased from Fisher Scientific, Spectrum Chemicals or Sigma-Aldrich Oxidized, unless otherwise noted. Oxytocin (OT) was purchased through Fisher from Alfa Aesar. Dimethylformamide (DMF), 4-methylpiperidine, N,N,N’,N’-tetramthyl-O-(1Hbenzotriazol-1-yl)uronium hexafluorophosphate (HBTU), N,N-diisopropylethylamine

(DIEA), dichloromethane (DCM), 2,2,2-trifloroacetic acid (TFA), diethyl ether, acetonitrile, methanol, formic acid (FA), CrCl3·6H2O, MnCl2, (NH4)2Fe(SO4)2·6H2O, CoCl2, NiCl2, CuCl2, NaOH, HCl, tris(2-carboxyethyl)phosphine (TCEP) resin, and ethylenediaminetetraacetic acid (EDTA), were purchased from ThermoFisher. ZnCl2 and FeCl3 were purchased from Sigma-Aldrich. 5,5'-Dithiobis(2-nitrobenzoic acid) (DTNB) and glutathione (GSH) were purchased from ThermoFisher but manufactured by Acros Organics. Piperidine was purchased from Spectrum Chemicals. Wang resin preloaded with Fmoc-Gly-OH and Fmoc-protected amino acids were purchased from ThermoFisher but manufactured by ChemImplex. Buffered solutions and metal salt solutions were made using Direct-Q 3 deionized water (>18 MΩ, Millipore).

6.5.2 Solid-phase Peptide Synthesis of oxOT and Analogs

Human oxytocin (sequence CYIQNCPLG) and an analogs(OTF; sequence CFIQNCPLG) were synthesized via Fmoc-based solid-phase peptide synthesis (SPPS) method. For a 0.2 mmol synthesis, Wang resin preloaded with Fmoc-Gly-OH was swelled for 2 hours in 5x DMF. Resin was washed 5 times with 2x resin volume of DMF. The Fmoc-Gly-OH residue was deprotected with 20% piperidine in DMF or 25% 4-methylpiperidine in DMF by shaking for 1 minute then repeating for 10 minutes. The deprotected resin was washed 10x with 2x resin volume DMF. Amino acids (4.0 equivalents) and HBTU (3.9 equivalents) were dissolved in minimal DMF and DIEA (10.0 equivalents) was added. Washed resin was then suspended in amino acid/HBTU/DIEA solution and shaken at room temperature for 40 minutes. The resin was again washed 10x with 2x resin volume DMF. This process was repeated from the deprotection step for each amino acid addition. After addition of final amino acid, the resin was washed 10x with 2x resin volume DMF, then washed 10x with 2x resin volume DCM and allowed to dry overnight. To cleave peptide from resin, resin was saturated with 95:5 TFA:water solution and allowed to shake for 1-4 hours. The solution was separated from resin, and crude product was precipitated in chilled diethyl ether and the suspension was centrifuged at 3900 rpm for 10 minutes at 4°C. The pellet was washed thrice with chilled diethyl ether followed by centrifugation after each wash. The pellet was dried under a stream of nitrogen overnight.

Purification was performed with RP-HPLC on an Agilent Technologies 1260 Infinity II HPLC with coupled Agilent Technologies 1260 Infinity II UV-Vis detection system. Purification of crude OT was performed using an Agilent Zorbax SB-C3 column (9.4 x 250 mm) at a flow rate of 3.75 mL/min using a gradient of water with 0.1% FA (Solvent A) and acetonitrile with 0.1% FA (Solvent B). The column was equilibrated and crude OTF loaded onto the column with 10% Solvent B held constant for 5 minutes. Solvent B increased from 10% to 20% from 5-6 minutes, then from 20% to 80% from 6-26 minutes. Solvent B was decreased back to 10% from 26-27 minutes then held constant at 10% from 27-30 minutes. OTF elutes off column at 41% Solvent B. Fractions containing OTF were confirmed by electrospray ionization mass spectrometry (ESI-MS) using an Agilent Technologies 1260 Infinity II coupled with an Agilent Technologies InfinityLab LC/MSD, dried, and stored at -20°C.

6.5.3 Oxidation & Reduction of Oxytocin

OT was purchased through ThermoFisher from Alfa Aesar. The concentration of reduced and oxidized OT were determined by DTNB assay in 15 mM phosphate, pH 7.4 using the molar extinction coefficient of 5-thionitrobenzoic acid, which absorbs strongly at 412 nm (ε=14,150 M-1 cm-1). It was found that ≤10% of OT (Alfa Aesar) was reduced, i.e. ≥90% of the thiols are oxidized in disulfide bonds.

6.5.4 UV-Visible Spectroscopy

All measurements were recorded on either a Shimadzu UV-1800 or Shimadzu UV-1900 at room temperature using Starna Cells quartz cuvettes with a 1 cm path length.

To determine actual concentrations of oxidized and reduced OT or OTF in the sample, a DTNB assay was performed. Absorbance of dilutions of known concentration of GSH and DTNB in 15 mM phosphate buffer pH 7.4 were measured at 412 nm yielding a linear graph. Absorbance of 10 μM OT or OTF and DTNB in 15 mM phosphate buffer pH 7.4 was measured at 412 nm and the concentration of free thiols in the OT or OTF solution could be extrapolated from the linear graph.

For metal titrations into apo-peptide (OT oxidized, OT reduced, OTF, Carbetocin), peptide was dissolved to 25 μM in 15 mM phosphate buffer pH 7.4. All metal and EDTA solutions were dissolved in Milli-Q water. Varying equivalents (12.5-125 μM) of metal salts were added to peptide, allowed to equilibrate at room temperature for 5 minutes, and measured with water as a spectral reference. Following data collection, buffer spectrum was subtracted from all spectra and all spectra were normalized to account for dilution.

6.5.5 Circular Dichroism Spectroscopy

. All measurements were recorded on a Chirascan Circular Dichroism spectrophotometer (Applied Photophysics) at room temperature using Starna Cells quartz cuvettes with a 1 mm path length. For metal titrations into apo-peptide, peptide was dissolved to 40 μM in 15 mM phosphate buffer pH 7.4. All metal salts were dissolved in Milli-Q water. Varying equivalents (20-200 μM) of metal salts were added to peptide, allowed to equilibrate at room temperature for 5 minutes, and measured. For each metal addition, 8 scans were averaged with a bandwidth of 0.5 nm. Following data collection, buffer spectrum was subtracted from all spectra.

For metal competition studies apo-OT was dissolved to 40 μM in 15 mM phosphate buffer pH 7.4. All metal salts were dissolved in Milli-Q water. OT was incubated with 1.0 equivalents (40 μM) CuCl2 or ZnCl2 for 10 minutes at room temperature. Then varying equivalents (20-200 μM) of competing metal salts were added, allowed to equilibrate for 5 minutes at room temperature, and measured. For each metal addition, 8 scans were averaged with a bandwidth of 0.5 nm. Following data collection, buffer spectrum was subtracted from all spectra.

6.5.6 Fluorescence Spectroscopy

All measurements were recorded on a SpectraMax i3x Multi-Mode Microplate Reader (Molecular Devices) at room temperature using Corning half-area, black-wall, clear-bottom 96-well plates. Peptide was dissolved to 30 μM in 15 mM phosphate buffer pH 7.4. For the measurement of a copper oxOT complex, copper was titrated into oxOT for a 1:1 complex and this was incubated for 5 minutes prior to recording the emission spectra. Excitation at 275 nm was used and emission was recorded from 300 to 350 nm.

6.5.7 Plasmid Amplification & Purification

GFP tagged human oxytocin receptor open reading frame clone was purchased from Origene and transformed into E. coli. Amplified plasmid was extracted and purified using a QIAGEN plasmid maxi prep kit. Purified plasmid was then sequenced (GENEWIZ).

6.5.8 Cell Culture

HEK293T cells were maintained in Dulbecco's modified medium (DMEM) supplemented with 10% fetal bovine serum (FBS) (Gibco) 1x penicillin-streptomycin (Corning), 2 mM L-glutamine (Gibco), 1 mM sodium pyruvate (Gibco) at 37 °C and 5% CO2. HEK293T cells were plated and grown to 60-70% confluence before transfection with GFP tagged human oxytocin receptor clone (Origene) using Attractene transfection agent (QIAGEN). 12 hours post-transfection cells were examined under a fluorescent microscope for GFP expression to confirm successful transfection. Media was then replaced and cells were stimulated 12 hours later.

For cell stimulations with metal bound peptide, peptide hormones and metal chloride salts (1:1 molar ratio) were incubated at 37 °C for 10 minutes in DPBS and then added to plated cells at a final concentration of 1 μM for 5 minutes before lysing.

6.5.9 Western Blot Analysis & Densitometry

HEK293T cells were transfected and stimulated as previously described and then lysed at 5 minutes in RIPA buffer (150 mM NaCl, 1% NP-40, 0.5% sodium deoxycholate, 0.1% SDS, 50 mM Tris pH 7.4) with EDTA free protease inhibitor (ThermoFisher) and phosphatase inhibitor

(Sigma). Lysates were put one ice for 15 minutes before being vortexed and centrifuged at 15000 x G at 4 °C. Protein was quantified after freezing the lysates by BCA assay (Invitrogen). Samples were then made using 10 μg of protein with PBS (Gibco), sample buffer (Invitrogen), and 2-mercaptoethanol (BioRad). Samples were loaded into a 4-12% bis-tris 12 well gel (Invitrogen) and run for one hour at 100 V and then was transferred on to a PVDF membrane using a Trans-Blot Turbo Transfer System (BioRad). The membranes were blocked for one hour in 5% BSA in TBST buffer. Membranes were then incubated overnight at 4 °C with primary antibodies and washed three times the following day with TBST buffer before incubating secondary antibodies for one hour. Membranes were imaged on a Chemidoc MP Imager (BioRad). Primary antibodies used were p44/42 MAPK (Erk1/2) (1:2,000 Cell Signaling Technologies), Phospho-p44/42 MAPK (Erk1/2) (Thr202/Tyr204) (1:1,000 Cell Signaling Technologies), and tubulin.

For densitometry, two separate gels were run and stained for either total MAPK and tubulin or phosphorylated MAPK and tubulin. Fluorescence of the bands was quantified using Image Lab software (Biorad). First the ratio of tubulin bands to total MAPK bands was calculated from one gel and then the ratio of phosphorylated MAPK to tubulin was calculated from a second gel. The ratio of tubulin normalized phosphorylated MAPK to tubulin normalized total MAPK was then calculated.

6.6 References

(1) Pearlmutter, A. F.; Soloff, M. S. Characterization of the Metal Ion Requirement for Oxytocin-Receptor Interaction in Rat Mammary Gland Membranes *. *J. Biol. Chem.* **1979**, *254* (10), 3899–3906.

(2) Soloff, M. S.; Swartz, T. L. Characterization Receptor in Rat of a Proposed Oxytocin Mammary Gland *. *J. Biol. Chem.* **1973**, *248* (18), 6471–6478.

(3) Wyttenbach, T.; Liu, D.; Bowers, M. T. Interactions of the Hormone Oxytocin with Divalent Metal Ions. *J. Am. Chem. Soc.* **2008**, *130* (17), 5993–6000.

(4) Wei, H.; Luo, X.; Wu, Y.; Yao, Y.; Guo, Z.; Zhu, L. Compositions and Conformations of Several Tranistion Metal Complexes with a Nonapeptide Hormone Oxytocin. *J. Chem. Soc., Dalt. Trans.* **2000**, 4196–4200.

(5) Mervinetsky, E.; Alshanski, I.; Tadi, K. K.; Dianat, A.; Buchwald, J.; Gutierrez, R.; Cuniberti, G.; Hurevich, M.; Yitzchaik, S. A Zinc Selective Oxytocin Based Biosensor. *J. Mater. Chem. B* **2020**, *8*, 155–160.

(6) Kleinnijenhuis, A. J.; Mihalca, R.; Heeren, R. M. A.; Heck, A. J. R. Atypical Behavior in the Electron Capture Induced Dissociation of Biologically Relevant Transition Metal Ion Complexes of the Peptide Hormone Oxytocin. *Int. J. Mass Spectrom.* **2006**, *253*, 217–224.

(7) Danyi, P.; Varnagy, K.; Sovago, I.; Schon, I.; Sanna, D.; Micera, G. Potentiometric and Spectroscopic Studies on the Copper (II) Complexes of Peptide Hormones Containing Disulfide Bridges. *J. Inorg. Biochem.* **1995**, *78*, 69–78.

(8) Bal, W.; Kozlowski, H.; Lammek, B.; Pettit, L. D. Potentiometric and Spectroscopic Studies of the Cu(II) Complexes of Ala-Arg8 -Vasopressin and Oxytocin: Two Vasopressin-Like Peptides. *J. Inorg. Biochem.* **1992**, *45*, 193–202.

(9) Jeong, H.; Kim, H. Determination of a Binding Site of Cu and Ni Metal Ions with Oxytocin Peptide by Electrospray Tandem Mass Spectrometry and Multiple Mass Spectrometry. *Eur. J. Mass Spectrom.* **2009**, *15*, 67–72.

(10) Joly, L.; Antoine, R.; Allouche, A.; Broyer, M. Optical Properties of Isolated Hormone Oxytocin Dianions : Ionization , Reduction , and Copper Complexation Effects. *J. Phys. Chem. A* **2009**, *113*, 6607–6611.

(11) Liu, D.; Seuthe, A. B.; Ehrler, O. T.; Zhang, X.; Wyttenbach, T.; Hsu, J. F.; Bowers, M. T. Oxytocin-Receptor Binding: Why Divalent Metals Are Essential. *J. Am. Chem. Soc.* **2005**, *127*, 2024–2025.

(12) Joly, L.; Antoine, R.; Albrieux, F.; Ballivian, R.; Broyer, M.; Chirot, F.; Dugourd, P.; Greco, C.; Mitric, R. Optical and Structural Properties of Copper - Oxytocin Dications in the Gas Phase. *J. Phys. Chem. B* **2009**, *113*, 11293–11300.

(13) Alshanski, I.; Shalev, D. E.; Yitzchaik, S.; Hurevich, M. Determining the Structure and Binding Mechanism of Oxytocin - Cu 2 + Complex Using Paramagnetic Relaxation Enhancement NMR Analysis. *J. Biol. Inorg. Chem.* **2021**, *26* (7), 809–815.

(14) Chatterjee, O.; Patil, K.; Sahu, A.; Gopalakrishnan, L.; Prasad, T. S. K. An Overview of the Oxytocin-Oxytocin Receptor Signaling Network. *J. Cell Commun. Signal.* **2016**, *10*, 355–360.

(15) Carter, C. S.; Caldwell, H. K.; Bosch, O. J.; Carter, C. S. The Oxytocin – Vasopressin Pathway in the Context of Love and Fear. *Front. Endocrinol. (Lausanne).* **2017**, *8* (356).

(16) Carter, C. S.; Kenkel, W. M.; Maclean, E. L.; Wilson, S. R.; Perkeybile, A. M.; Yee, J. R.; Ferris, C. F.; Nazarloo, H. P.; Porges, S. W.; Davis, J. M.; et al. Is Oxytocin " Nature ' s Medicine " ? *Pharmacol. Rev.* **2020**, *72*, 829–861.

(17) Camerino, C. Oxytocin Involvement in Body Composition Unveils the True Identity of Oxytocin. *Int. J. Mol. Sci.* **2021**, *22*, 6383.

(18) Koike, K.; Nohara, A.; Zhang, Z. X.; Hirota, K. Oxytocin Stimulates Mitogen-Activated Protein Kinase in Cultured Human Puerperal Uterine Myometrial Cells. *Endocrinology* **1995**, *136* (5), 2082–2087.

(19) Rimoldi, V.; Reversi, A.; Taverna, E.; Rosa, P.; Francolini, M.; Parenti, M.; Chini, B. Oxytocin Receptor Elicits Different EGFR / MAPK Activation Patterns Depending on Its Localization in Caveolin-1 Enriched Domains. *Oncogene* **2003**, *22*, 6054–6060.

(20) Sanborn, B. M.; Yang, M.; Zhong, M. Myometrial Oxytocin Receptor Involves GG and Epidermal Growth Factor Receptor Tyrosine. *Endocrinology* **2003**, *144* (7), 2947–2956.

(21) Blume, A.; Bosch, O. J.; Miklos, S.; Torner, L.; Wales, L.; Waldherr, M.; Neumann, I. D. Oxytocin Reduces Anxiety via ERK1 ⁄ 2 Activation : Local Effect within the Rat Hypothalamic Paraventricular Nucleus. *Eur. J. Neurosci.* **2008**, *27*, 1947–1956.

(22) Wei, J.; Ma, L.; Ju, P.; Yang, B.; Wang, Y.; Wang, Y. Involvement of Oxytocin Receptor / Erk / MAPK Signaling in the MPFC in Early Life Stress-Induced Autistic-Like Behaviors. *Front. Cell Dev. Biol.* **2020**, *8*, 564485.

(23) Uvnäs-moberg, K.; Ekström-bergström, A.; Berg, M.; Buckley, S.; Pajalic, Z. Maternal Plasma Levels of Oxytocin during Physiological Childbirth – a Systematic Review with Implications for Uterine Contractions and Central Actions of Oxytocin. *BMC Pregnancy Childbirth* **2019**, *9*, 285.

(24) Rath, W. Prevention of Postpartum Haemorrhage with the Oxytocin Analogue Carbetocin. *Eur. J. Obstet. Gynecol. Reprod. Biol.* **2009**, *147*, 15–20.

(25) Patel, A. B.; Carroli, G.; Fawole, B.; Goudar, S. S.; Pujar, Y. V; Neilson, J.; Hofmeyr, G. J. Heat-Stable Carbetocin versus Oxytocin to Prevent Hemorrhage after Vaginal Birth. *N. Engl. J. Med.* **2018**, *379*, 743–752.

(26) Passoni, I.; Leonzino, M.; Gigliucci, V.; Chini, B.; Busnelli, M. Carbetocin Is a Functional Selective Gq Agonist That Does Not Promote Oxytocin Receptor Recycling After Inducing b -Arrestin-Independent Internalisation Neuroendocrinology. *J. Neuroendocrinol.* **2016**, *28* (12), 12363.

(27) Busnelli, M.; Chini, B. Molecular Basis of Oxytocin Receptor Signalling in the Brain: What We Know and What We Need to Know. In *Behavioral Pharmacology of Neuropeptides: Oxytocin*; Hurlemann, R., Grinevich, V., Eds.; Springer, 2018; pp 3–30.

(28) Beychok, S.; Breslow, E. Circular Oxytocin Dichroism Analogues * of Oxytocin and Several. *J. Biol. Chem.* **1968**, *243* (1), 151–154.

(29) Antosiewicz, J. M.; Shugar, D. UV – Vis Spectroscopy of Tyrosine Side-Groups in Studies of Protein Structure . Part 2 : Selected Applications. *Biophys. Rev.* **2016**, *8*, 163–177.

(30) Shugar, D.; Antosiewicz, J. M. UV – Vis Spectroscopy of Tyrosine Side-Groups in Studies of Protein Structure . Part 1 : Basic Principles and Properties of Tyrosine Chromophore. *Biophys. Rev.* **2016**, *8*, 151–161.

(31) Rousseau, G.; Kohout, T.; Bouvier, M.; Azzi, M.; Charest, P. G. Arrestin-Mediated Activation of MAPK by Inverse Agonists Reveals Distinct Active Conformations for G Protein-Coupled Receptors. *PNAS* **2003**, *100* (20), 11406–11411.

Appendix 1

A Combinatorial Approach Towards Discovering Metal Binding Peptides

The rest is still unwritten.

- Natasha Bedingfield (*Unwritten*, New York, **2004**)

A1.1 Introduction

Natural peptides are short biopolymers composed of L-amino acids that are linked together via amide bonds. They are widely used in basic research as well as in the pharmaceutical and biotechnology industries.[1–4] At a fundamental level, researchers have long studied endogenous peptides in organisms across all walks of life to better understand how amino acid sequence and subsequent structure affects downstream biological activity. More recently, they have been heavily investigated for their use as effective therapeutics since they lie between small molecules and large biomolecules like proteins and antibodies.[5,6] Because of this, they possess highly desirable properties including favorable tissue penetration, high potency, and high selectivity for their targets.[7] However, it is worth noting that native peptides often possess unique drawbacks such as poor oral bioavailability as well as short plasma half-lives as they are easily degraded by endogenous proteases.[8,9] In addition to their applications in drug discovery and therapeutics peptides have also been used in biotechnology for biosensor applications as both recognition elements and enzyme substrates for activity-based readouts.[10–12]

One highly common approach in the development of peptide design is the use of combinatorial libraries which are comprised of totally random or partially randomized peptide variants.[13,14] Combinatorial methods gained enormous amounts of attraction from the pharmaceutical industry in the late 1980’s and 1990’s because of their potential to greatly expedite the drug discovery process using high-throughput screening of billions of different compounds at once.[15,16] Though originally implemented to build peptide and oligonucleotide libraries combinatorial methods have since advanced to applications in small molecule libraries, protein libraries, and oligosaccharide libraries and have seen tremendous success in both fundamental research and drug discovery.[17–19] Such combinatorial peptide libraries can be build using biological (e.g. phage display) or synthetic methods (traditionally performed on resin supports). Of the synthetic methods to build combinatorial peptide libraries the one used and discussed here is the one-bead-one-compound (OBOC) method first recognized by Lam et al. where the split-pool synthesis method is employed (Figure 1.1).[20]

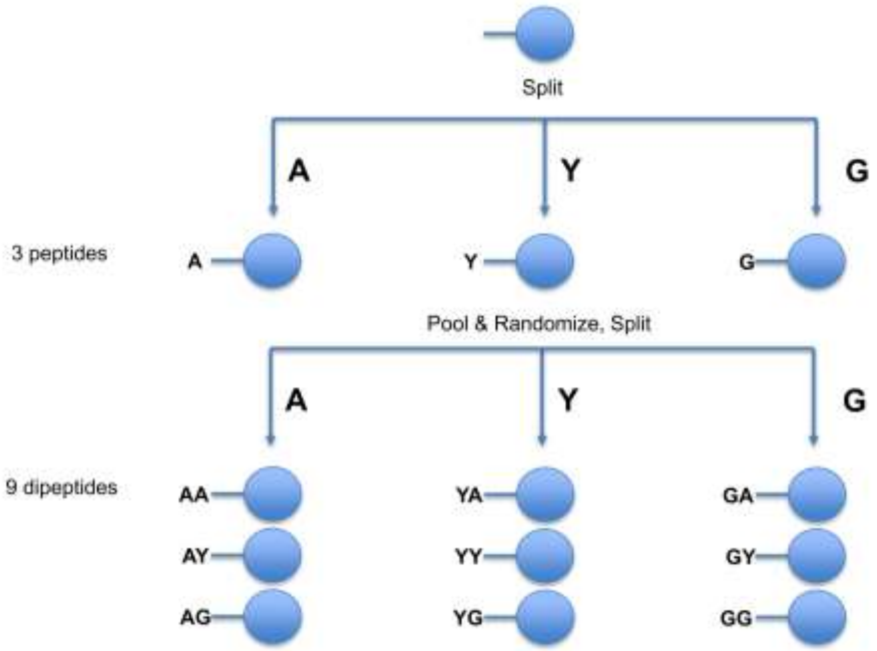

Figure 1.1 Schematic for the split-pool method used in the one-bead-one-compound combinatorial library synthesis.

The split-pool synthesis employs an iterative approach consisting of three steps: (i) the division of a compound mixture into equal portions, (ii) the coupling of one amino acid (or building block) to each portion and, (iii) the pooling and homogenous mixing of the portions. Using this approach, a peptide library can be produced where each resin bead contains up to 10^{13} copies of one single peptide.[20] The advantages of using the OBOC method include the rapid synthesis of large libraries, the ease of incorporation of unnatural amino acids into the library, and the compounds are spatially separated on resin beads making the screening extremely high throughput.

This appendix describes some of the preliminary work done by our lab in applying the OBOC method towards discovering new metal binding peptides. We have used the OBOC approach to synthesize a unique peptide library and applied high throughput screening methods using live-cell assays as well as a colorimetric assay for identifying non-canonical metal-binding hits. We belief that the discovery of such motifs could correlate to endogenous protein and peptide sequences previously not known to interact with metal ions and provide rational for therapeutic advancements in either targeted design or chelation therapies. Additionally, such metal binding frameworks could serve to provide structural motifs that can be used towards biosensing and molecular imaging platforms. As the work discussed is largely preliminary and no sequences have been determined at this stage, I will discuss only the library design and methods of screening used to date.

A1.2 Discussion

A1.2.1 Library Design

The use of the OBOC method allows for a high level of control over peptide library design in that the user can choose which amino acids to incorporate or exclude from the library as well as whether any unnatural amino acids are to be included. For the purposes of this library, we sought to uncover non-canonical metal binding motifs that have not been identified in nature to date. In general, it is well established that majority of known peptide metal binding motifs rely on cysteine and histidine residues for their metal binding affinity.[21–28] For example, the amino-terminus Cu(II) and Ni(II) binding (ATCUN) motif is a well-known motif which can be present in proteins or peptides.[29,30] The structure of the ATCUN motif is defined as containing a free N-terminal amine, a histidine residue in the third position, and two intervening peptide nitrogens. The ATCUN motif has been observed in various albumins including human serum albumins and is heavily conserved across the histatins.[29] Aside from the ATCUN motif histidines and cysteines have been well documented as necessary residues in various proteins, peptides, and metalloenzymes.[31,32]

For this reason, we chose to synthesize a library of 8-mer peptides containing all 20 natural amino acids except for histidine and cysteine. Furthermore, we included a cleavable linker in the library design which serves as a chemical handle to selectively cleave positive hits off bead for subsequent *de novo* sequencing after screening. We synthesized two separate libraries with two different cleavable linkers: (i) a photocleavable linker based on the *o*-nitrobenzyl moiety and (ii) a disulfide-based linker which can be cleaved under reducing conditions (Figure 1.2). Notably, the disulfide linker can only be incorporated into libraries without cysteines. We chose a length of 8-mer amino acids as it would provide a high level of chemical diversity to sample a vast chemical space but also be a length that would allow for more facile *de novo* sequencing using tandem MS/MS.

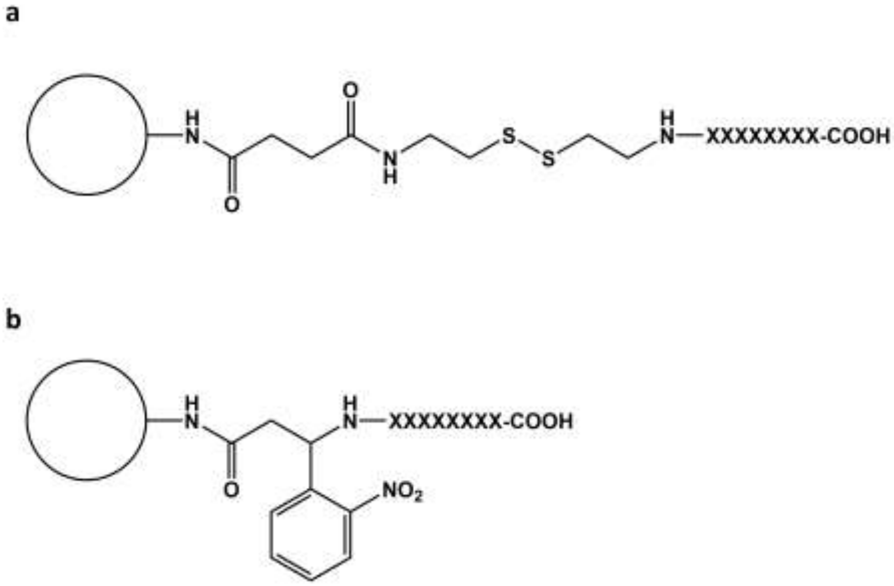

Figure 1.2 Library design of 8-mer peptides using either a) a disulfide based cleavable linker or b) a *o*-nitrobenzyl-based photocleavable linker.

A.1.2.2 Library Screening

With the libraries in hand, we were ready to screen them to identify metal-binding peptides. For the purposes of preliminary studies, we focused on screening for copper binding affinity of the peptides. Two methods of screening were employed, cell binding assays and a colorimetric assay. Live cell assays have commonly been employed in OBOC screening methods to either identify peptides that bind the cell membrane generally or for peptides that bind a particular receptor over-expressed on the membrane surface of the cell.[33–35] In this study we sought to employ live cell assays to identify metal-mediated peptide membrane binding. The general design of the screening assay was to incubate the peptide library with copper for 30 minutes at room temperature, wash the peptides to remove any unbound metals, incubate the peptides with live-cells (both HEK293 and MDA-MB-232 cell lines were used) for 30 minutes at 5% CO_2 and 37 °C, wash the peptides to remove any unbound cells, and lastly image the library (Figure 1.3). A control was first done on the library without any metal incubation to remove false positives.

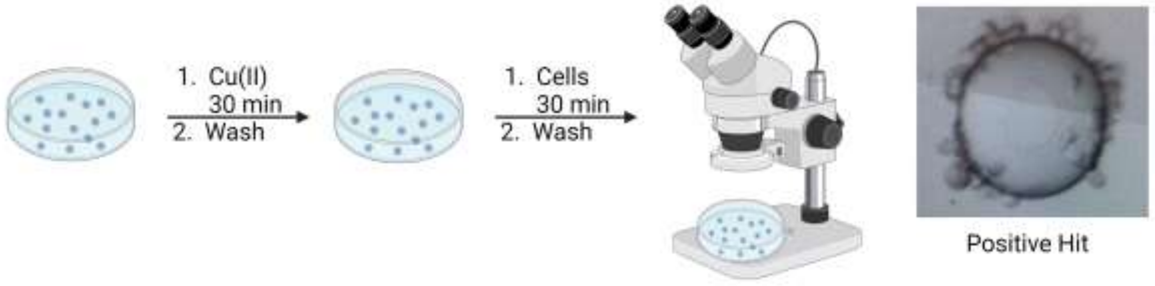

Figure 1.3 Library screening design for identifying metal-mediated membrane binding peptides and an example of a positive hit showing a PEGA bead covered in live cells. (Figure made with Biorender)

In addition to live cell assays a colorimetric assay was also developed in our lab. Previous examples of colorimetric chelators being used to detect metal binding peptides on bead have been reported in the past. The general design here is that a chelator that undergoes a colorimetric change upon metal binding can chelate to metals that are bound by peptide on bead and then become trapped in the matrix of the bead resulting in a color change of positive hit beads. Indeed, this method of metal detection has proven successful in the past with one example being the use of a diphenylcarbazide dye to stain beads with chromium bound peptides by Knight et al. in 2013.[36] In this way, researchers can quickly identify positive metal binding hits based on a color change. In this work we sought to find a suitable colorimetric chelator to detect copper bound peptides on bead. We employed Zincon which is a chelator that undergoes a strong color change from reddish brown to deep blue upon binding with copper. In this assay the workflow was similar to the live cell assays where we incubate the peptide library for 30 minutes with copper followed by a washing step to remove any unbound metals however, we then incubate the peptide with 500 µM Zincon for 2 minutes after this and then wash the library three times with PBS and image them under the microscope to identify hits (Figure 1.4). This screening method proved to be successful in identifying copper binding hits where positive hits are beads colored deeply purple/blue and nonhits either colorless or brownish in color.

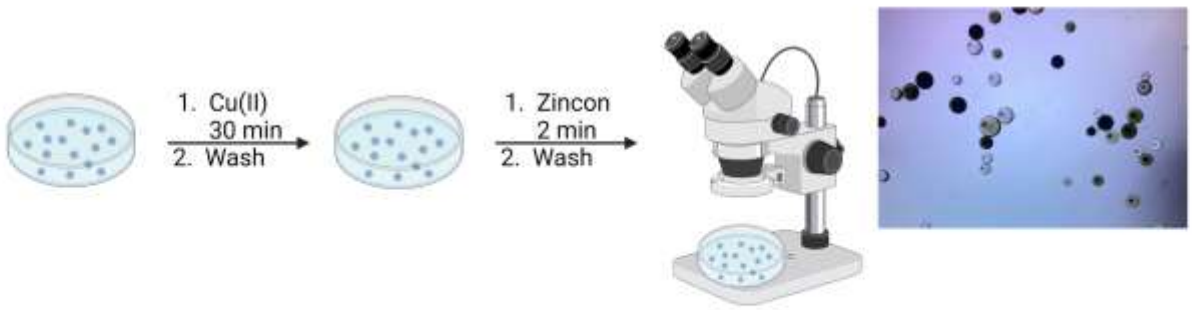

Figure 1.4 Library screening design for identifying copper binding peptides using the colorimetric chelator, Zincon, to detect copper-bound peptide hits. Positive hits are shown deeply colored whereas non-hits are colorless or lightly colored brown. (Figure made using Biorender)

A1.3 Conclusions and Future Studies

The OBOC method of combinatorial screening provides a powerful platform from which we are able to sample a vast chemical space for huge variety of targets and applications. Our preliminary studies alone have shown that this platform can be uniquely suited for the discovery of novel metal binding peptides. Through careful library design there is the potential to discover natural metal binding motifs previously not reported in the literature. With the current work in our lab, we have shown two methods of screening, live cell and colorimetric chelation, then can be employed in a high throughput manner to identify hits quickly.

Future work in our lab will focus on optimizing cleavage conditions for the two cleavable linkers in order for adequate peptide for MALDI MS analysis. After the identification and *de novo* sequencing of the peptide hits, they will be resynthesized, and metal binding ability will then be characterized in solution phase. We will also search the BLAST database for any sequence alignment against the human proteome.

A1.4 Materials and Methods

A1.4.1 Library Synthesis

The OBOC peptide library was prepared using standard solid phase peptide synthesis procedures using Fmoc-protected amino acids (Novabiochem) with Oxyma Pure (Sigma) and N,N'-Diisopropylcarbodiimide (DIC) (Spectrum) to synthesize the linear peptides on PEGA resin (Sigma). The disulfide linker was synthesized in house using previously reported methods.[37] The photocleavable linker, Fmoc-(S)-3-amino-3-(2-nitrophenyl)propionic acid, was purchased from Fisher Scientific. The two linkers were coupled to PEGA resin (0.4 mmol/mg loading) in 4 equivalent excess using Oxyma/DIC (4 equivalent excess) overnight. After this the reaction liquid was drained and the beads were washed with DMF, MeOH, and DCM three times each. Fmoc-deprotection was then performed using 25% 4-methylpiperidine in DMF for 5 minutes at 95 °C. The beads were then washed and separated into 18 aliquots and were reacted with 4 molar excess of one of 18 Fmoc-amino acids using Oxyma/DIC activators (also at 4 molar excess). Coupling was allowed to proceed for twenty minutes at 95 °C. Complete coupling was ensured by Kaiser testing. Following complete coupling the beads were drained and washed as previously described and Fmoc-deprotected. The beads were then combined and washed again and re-divided for the next cycle of coupling. This was done a total of 8 times for the synthesis of the 8-mer library. After Fmoc-deprotection of the final amino acid the side chains were cleaved under acidic conditions using TFA/H_2O/TIPS/Thioanisole (95:3:1:1) for two hours at room temperature. The beads were then washed with 5% DIEA in DMF, (DMF, MeOH, DCM) three times, PBS twice, water twice, and lastly DMF.

A1.4.2 Live-cell Screening

The library beads were suspended in 90% DMF/water, and then added onto a polystyrene 6-well plate and allowed to sit for 30 minutes. Afterwards the solution was removed with a pipette and the immobilized library beads were washed with 50% DMF/water, water, PBS, and then incubated with 1 mM $CuCl_2$ for 30 minutes at room temperature with shaking. Following this the beads were washed five times with water. HEK293T cells or MDA-MB-231 cells were plated in a 6 well plate the following day to reach 90% confluency at the time of the assay. They were trypsinized using Tryp-LE (Gibco) and resuspended in 10 mL of DMEM supplemented with 10% FBS, 1% glutamine, 1% sodium pyruvate and 1% pen/strep at 37 °C. Two milliliters of cell suspension were added to each well of the peptide libraries and they were allowed to incubate for 30 minutes at 37 °C with shaking. Following incubation, the wells were immediately washed with PBS five times to remove any unbound cells. Cell media (DMEM as previously described) was added to the wells, and they were immediately imaged under a microscope (EVOS1000) using an automated tiling feature to provide an image of the entire well. Similar control experiments were done without metal incubation to remove false positives from the library.

A1.4.3 Colorimetric Based Screening

The library beads were suspended in 90% DMF/water, and then added onto a polystyrene 6-well plate and allowed to sit for 30 minutes. Afterwards the solution was removed with a pipette and the immobilized library beads were washed with 50% DMF/water, water, PBS, and then incubated with 1 mM $CuCl_2$ for 30 minutes at room temperature with shaking. Following this the beads were washed five times with water. After this a solution of Zincon (500 µM) in water was added to the peptide library and shaken for 2 minutes. The Zincon solution was then removed, and the well was washed 5x with water. It was then imaged under a microscope as previously described to identify hits which appear deep blue/purple in color. Non-hits appear colorless to brown in color.

A1.5 References

(1) Martínez-Villaluenga, C.; Hernández-Ledesma, B. Peptides for Health Benefits 2019. *International journal of molecular sciences*. April 2020.

(2) Cabral, H. Peptides: Molecular and Biotechnological Aspects. *Biomolecules*. January 2021.

(3) Apostolopoulos, V.; Bojarska, J.; Chai, T.-T.; Elnagdy, S.; Kaczmarek, K.; Matsoukas, J.; New, R.; Parang, K.; Lopez, O. P.; Parhiz, H.; Perera, C. O.; Pickholz, M.; Remko, M.; Saviano, M.; Skwarczynski, M.; Tang, Y.; Wolf, W. M.; Yoshiya, T.; Zabrocki, J.; Zielenkiewicz, P.; AlKhazindar, M.; Barriga, V.; Kelaidonis, K.; Sarasia, E. M.; Toth, I. A Global Review on Short Peptides: Frontiers and Perspectives. *Molecules* **2021**, *26* (2).

(4) Gentilucci, L.; Tolomelli, A.; Squassabia, F. Peptides and Peptidomimetics in Medicine, Surgery and Biotechnology. *Curr. Med. Chem.* **2006**, *13* (20), 2449–2466.

(5) de la Torre, B. G.; Albericio, F. Peptide Therapeutics 2.0. *Molecules (Basel, Switzerland)*. May 2020.

(6) Wang, L.; Wang, N.; Zhang, W.; Cheng, X.; Yan, Z.; Shao, G.; Wang, X.; Wang, R.; Fu, C. Therapeutic Peptides: Current Applications and Future Directions. *Signal Transduct. Target. Ther.* **2022**, *7* (1), 48.

(7) Fosgerau, K.; Hoffmann, T. Peptide Therapeutics: Current Status and Future Directions. *Drug Discov. Today* **2015**, *20* (1), 122–128.

(8) Renukuntla, J.; Vadlapudi, A. D.; Patel, A.; Boddu, S. H. S.; Mitra, A. K. Approaches for Enhancing Oral Bioavailability of Peptides and Proteins. *Int. J. Pharm.* **2013**, *447* (1–2), 75–93.

(9) Werle, M.; Bernkop-Schnürch, A. Strategies to Improve Plasma Half Life Time of Peptide and Protein Drugs. *Amino Acids* **2006**, *30* (4), 351–367.

(10) Liu, Q.; Wang, J.; Boyd, B. J. Peptide-Based Biosensors. *Talanta* **2015**, *136*, 114–127.

(11) Wasilewski, T.; Szulczyński, B.; Wojciechowski, M.; Kamysz, W.; Gębicki, J. A Highly Selective Biosensor Based on Peptide Directly Derived from the HarmOBP7 Aldehyde Binding Site. *Sensors (Basel).* **2019**, *19* (19).

(12) Sfragano, P. S.; Moro, G.; Polo, F.; Palchetti, I. The Role of Peptides in the Design of Electrochemical Biosensors for Clinical Diagnostics. *Biosensors* **2021**, *11* (8).

(13) Gray, B. P.; Brown, K. C. Combinatorial Peptide Libraries: Mining for Cell-Binding Peptides. *Chem. Rev.* **2014**, *114* (2), 1020–1081.

(14) Bozovičar, K.; Bratkovič, T. Evolving a Peptide: Library Platforms and Diversification Strategies. *Int. J. Mol. Sci.* **2019**, *21* (1).

(15) Carroll, J. Will Combinatorial Chemistry Keep Its Promise? *Biotechnol. Healthc.* **2005**, *2* (3), 26–32.

(16) Liu, R.; Li, X.; Lam, K. S. Combinatorial Chemistry in Drug Discovery. *Curr. Opin. Chem. Biol.* **2017**, *38*, 117–126.

(17) Jemth, P.; Kreuger, J.; Kusche-Gullberg, M.; Sturiale, L.; Giménez-Gallego, G.; Lindahl, U. Biosynthetic Oligosaccharide Libraries for Identification of Protein-Binding Heparan Sulfate Motifs. Exploring the Structural Diversity by Screening for Fibroblast Growth Factor (FGF)1 and FGF2 Binding. *J. Biol. Chem.* **2002**, *277* (34), 30567–30573.

(18) Matsuura, T.; Ernst, A.; Plückthun, A. Construction and Characterization of Protein

Libraries Composed of Secondary Structure Modules. *Protein Sci.* **2002**, *11* (11), 2631–2643.

(19) Dandapani, S.; Rosse, G.; Southall, N.; Salvino, J. M.; Thomas, C. J. Selecting, Acquiring, and Using Small Molecule Libraries for High-Throughput Screening. *Curr. Protoc. Chem. Biol.* **2012**, *4*, 177–191.

(20) Lam, K. S.; Lebl, M.; Krchňák, V. The "One-Bead-One-Compound" Combinatorial Library Method. *Chem. Rev.* **1997**, *97* (2), 411–448.

(21) Isarankura-Na-Ayudhya, P.; Thippakorn, C.; Pannengpetch, S.; Roytrakul, S.; Isarankura-Na-Ayudhya, C.; Bunmee, N.; Sawangnual, S.; Prachayasittikul, V. Metal Complexation by Histidine-Rich Peptides Confers Protective Roles against Cadmium Stress in Escherichia Coli as Revealed by Proteomics Analysis. *PeerJ* **2018**, *6*, e5245.

(22) Peris-Díaz, M. D.; Guran, R.; Zitka, O.; Adam, V.; Krężel, A. Mass Spectrometry-Based Structural Analysis of Cysteine-Rich Metal-Binding Sites in Proteins with MetaOdysseus R Software. *J. Proteome Res.* **2021**, *20* (1), 776–785.

(23) Peris-Díaz, M. D.; Guran, R.; Zitka, O.; Adam, V.; Krężel, A. Metal- and Affinity-Specific Dual Labeling of Cysteine-Rich Proteins for Identification of Metal-Binding Sites. *Anal. Chem.* **2020**, *92* (19), 12950–12958.

(24) Cun, S.; Li, H.; Ge, R.; Lin, M. C. M.; Sun, H. A Histidine-Rich and Cysteine-Rich Metal-Binding Domain at the C Terminus of Heat Shock Protein A from Helicobacter Pylori: Implication for Nickel Homeostasis and Bismuth Susceptibility. *J. Biol. Chem.* **2008**, *283* (22), 15142–15151.

(25) Lukács, M.; Csilla Pálinkás, D.; Szunyog, G.; Várnagy, K. Metal Binding Ability of Small Peptides Containing Cysteine Residues. *ChemistryOpen* **2021**, *10* (4), 451–463.

(26) Potocki, S.; Rowinska-Zyrek, M.; Valensin, D.; Krzywoszynska, K.; Witkowska, D.; Luczkowski, M.; Kozlowski, H. Metal Binding Ability of Cysteine-Rich Peptide Domain of ZIP13 Zn2+ Ions Transporter. *Inorg. Chem.* **2011**, *50* (13), 6135–6145.

(27) Zeng, Y.-B.; Yang, N.; Sun, H. Metal-Binding Properties of an Hpn-like Histidine-Rich Protein. *Chemistry* **2011**, *17* (21), 5852–5860.

(28) Brewer, D.; Lajoie, G. Evaluation of the Metal Binding Properties of the Histidine-Rich Antimicrobial Peptides Histatin 3 and 5 by Electrospray Ionization Mass Spectrometry. *Rapid Commun. Mass Spectrom.* **2000**, *14* (19), 1736–1745.

(29) Harford, C.; Sarkar, B. Amino Terminal Cu(II)- and Ni(II)-Binding (ATCUN) Motif of Proteins and Peptides: Metal Binding, DNA Cleavage, and Other Properties. *Acc. Chem. Res.* **1997**, *30* (3), 123–130.

(30) Sankararamakrishnan, R.; Verma, S.; Kumar, S. ATCUN-like Metal-Binding Motifs in Proteins: Identification and Characterization by Crystal Structure and Sequence Analysis. *Proteins* **2005**, *58* (1), 211–221.

(31) Holeček, M. Histidine in Health and Disease: Metabolism, Physiological Importance, and Use as a Supplement. *Nutrients* **2020**, *12* (3).

(32) Pace, N. J.; Weerapana, E. Zinc-Binding Cysteines: Diverse Functions and Structural Motifs. *Biomolecules* **2014**, *4* (2), 419–434.

(33) Cho, C.-F.; Behnam Azad, B.; Luyt, L. G.; Lewis, J. D. High-Throughput Screening of One-Bead-One-Compound Peptide Libraries Using Intact Cells. *ACS Comb. Sci.* **2013**, *15* (8), 393–400.

(34) Xiao, W.; Ma, W.; Wei, S.; Li, Q.; Liu, R.; Carney, R. P.; Yang, K.; Lee, J.; Nyugen, A.;

Yoneda, K. Y.; Lam, K. S.; Li, T. High-Affinity Peptide Ligand LXY30 for Targeting A3β1 Integrin in Non-Small Cell Lung Cancer. *J. Hematol. Oncol.* **2019**, *12* (1), 56.

(35) Miyamoto, S.; Liu, R.; Hung, S.; Wang, X.; Lam, K. S. Screening of a One Bead-One Compound Combinatorial Library for Beta-Actin Identifies Molecules Active toward Ramos B-Lymphoma Cells. *Anal. Biochem.* **2008**, *374* (1), 112–120.

(36) Knight, A. S.; Zhou, E. Y.; Pelton, J. G.; Francis, M. B. Selective Chromium(VI) Ligands Identified Using Combinatorial Peptoid Libraries. *J. Am. Chem. Soc.* **2013**, *135* (46), 17488–17493.

(37) Townsend, J. B.; Shaheen, F.; Liu, R.; Lam, K. S. Jeffamine Derivatized TentaGel Beads and Poly(Dimethylsiloxane) Microbead Cassettes for Ultrahigh-Throughput in Situ Releasable Solution-Phase Cell-Based Screening of One-Bead-One-Compound Combinatorial Small Molecule Libraries. *J. Comb. Chem.* **2010**, *12* (5), 700–712.